Low-energy Plasma–Surface Interactions at Airless Icy Bodies

Thesis by

Robert W. Grayson

In Partial Fulfillment of the Requirements for the degree of
Doctor of Philosophy in Chemical Engineering

CALIFORNIA INSTITUTE OF TECHNOLOGY
Pasadena, California

2024
(Defended 5/30/2024)

Robert W. Grayson
ORCID: 0000-0002-8044-9654

ACKNOWLEDGEMENTS

First, let me thank my advisor, Prof. Konstantinos Giapis, for his direction over the past five years. This thesis would not have been possible without his support. I am particularly grateful for his practical skill with vacuum and mechanical work, without which experiments would never have gotten off the ground. Prof. Bill Goddard I thank for his infinite patience as I've tried to balance simulation and experiment efforts over the years. Without the involvement of Dr. Tom Nordheim, this would undoubtably be a very different thesis. I count myself exceedingly lucky that our collaboration materialized and endured, founded as it was on a chance encounter. I am thankful as well for the other members of my thesis committee, Prof. Zhen-Gang Wang and Prof. Mitchio Okumura, for their insights and advice. All of these have been generous with their time and resources beyond professional expectations.

To be more specific, I thank Prof. Bill Goddard for his supervision of the simulation work described in Chapters 4, 5, 7, and 8. Dr. Tom Nordheim was the Co-I for work funded by the JPL/Caltech PDRDF, which includes Chapters 2, 3, and 6. I am also grateful to Dr. Ben Teolis of SWRI for useful discussions during the PDRDF effort. Tom Nordheim was also the primary supervisor of the work described in Chapter 7, undertaken during an internship at JPL with funding from NASA. Prof. Konstantinos Giapis' supervision spanned all chapters. Thanks to Ricardo Zarazua of the Caltech Machine Shop for fabrication related to Chapter 6 and to Joe Drew for keeping Spalding Lab upright.

For the past five years, the Caltech Chemical Engineering department has been my most local professional ecosystem. I am profoundly grateful to Mike Vicic and Allison Kinard for striving to improve it, even at their cost. The members of my cohort, especially Gennady Gorin, Andrew Friedman, and Dan Wackelin, have been lab mates in the second (and highest) degree. Their support, both technical and moral, has been indispensable. The Keck Institute for Space Studies (KISS) has been a home (office) away from home (lab) for the past year. Thank you, Antonio Soriano and Janet Seid, for the coffee and conversation, and thanks to KISS more broadly for the affiliate program.

I am indebted to my undergraduate research advisor, William Ducker, and to mentor and friend, Prudvi Gaddam, for encouraging me toward research. I could not have persisted through the many trials of this program without my family and dear friends, Kat Grayson, Susan Grayson, Livvy Call, and Robert Blake, who, even at a distance of 2,000 miles, have been close. Finally, to many other friends and family: you can be sure that I am grateful for you. Without you all, graduate school would have been nothing more than a quiet basement with a loud machine.

ABSTRACT

Low-energy plasma surface interactions occur in many solar system environments and are especially important in the magnetospheres of gas giants. Within these magnetospheres orbit a catalogue of icy moons, some of which famously host interior liquid-water oceans. They are continuously exposed to a cold, corotating plasma "wind," resulting in bombardment by heavy reactive ions, with peak number fluxes in the hyperthermal energy regime (10s to 100s of eV). Despite their abundance, these low-energy ions have been mostly overlooked in planetary science because they are poor drivers of radiolysis. In this thesis we take a combined experimental-theoretical approach to understanding the interaction of hyperthermal water group molecules/ions with relevant surfaces, motivated by some specific solar system observations, mostly from the Saturn system.

We begin with experimental case studies of water-group ion scattering on carbonaceous (Chapter 2) and chloride-salt surfaces (Chapter 3), focusing on the emission of secondary negative ions. For carbonaceous surfaces, we detect surprisingly energetic carbon fragments, apparently emitted by near-threshold sputtering processes. The most abundant products (O^-, C_2^-, C_2H^-) are consistent with mass range for negative PUIs of unknown origin observed near Dione and Rhea. The reported mass ranges, however, have been estimated for pick-up of initially stationary ions, which is a poor assumption for the products we observe. Our experiments with chloride salts (relevant to Jupiter's moon Europa) are complicated by surface charging but provide kinematic evidence of reactive scattering and single knock-on sputter processes. Specifically, we observe abstraction of Cl from Pt to form chlorine monoxide anions. We then describe a modification of our scattering apparatus to enable exposure of ice targets, developing a one-of-a-kind experimental facility (Chapter 6). Some limited and preliminary results for Ar^+ and O^+ bombardment of amorphous water ice follow, which are more revealing of experimental challenges than of surface chemistry and dynamics.

Our theoretical efforts include Reactive Molecular Dynamics simulations of collision-induced chemistry in ices using the ReaxFF formalism. These reveal a novel non-radiolytic process (an Eley-Rideal reaction) for formation of molecular oxygen in low-energy (2−50 eV) water-group molecule bombardment of crystalline water ice, relevant to the maintenance of O_2 exospheres at Saturn's moons Dione and Rhea (Chapter 4). With the addition of CH_4 to the ice (as a clathrate), bombardment results in formation of methanol and formaldehyde at yields as great as 10% and 5%, respectively (Chapter 5). Two mechanisms are observed for methanol synthesis: one a typical radiolysis process and the second a two-step non-radiolytic mechanism. We provide preliminary results for an $HCN/CH_4/H_2O$

ice target in Chapter 8 to motivate further study of the role that hyperthermal reactive ions play in synthesis of prebiotic organics. Finally, in Chapter 7, we describe a Monte-Carlo model for the production and transport of H_2 in the Enceladus due to plasma-surface interactions. Radiolysis by suprathermal electrons is the primary contributor, but the calculated mixing ratio falls several orders of magnitude short of the reported ~1%, which lends credibility to the notion that H_2 is being emitted from Enceladus' internal ocean.

PUBLISHED CONTENT AND CONTRIBUTIONS

Grayson, R. W., Goddard, W. A. & Giapis, K. P. Reactive scattering of water group ions on ice surfaces with relevance to Saturn's icy moons. *Icarus* **379**, 114967 (2022). DOI: 10.1016/j.icarus.2022.114967

RWG participated in conception of the work, performed all calculations, prepared the data and analysis, and coauthored the manuscript with W.A.G. and K.P.G.

TABLE OF CONTENTS

LIST OF TABLES AND FIGURES

NOMENCLATURE

Acronyms and Abbreviations

a.u.	Arbitrary units
aC	Amorphous carbon
ASW	Amorphous solid water
AU	Astronomical units
BCA	Binary collision approximation
BEC	Binary elastic collision
BO	Bond order
CAPS	Cassini Plasma Spectrometer
CAPS-ELS	CAPS Electron Spectrometer
CB	Conduction band
CCCBDB	Computational Chemistry Comparison and Benchmark Database
CDA	Cosmic Dust Analyzer
CHON	Carbon, hydrogen, oxygen, nitrogen
CI	Confidence interval
COM	Center of mass
DEA	Dissociative electron attachment
DFT	Density Functional Theory
DI	Deionized
DS	Double scattering
EA	Electron affinity
EEA	Electrostatic energy analyzer
ER	Eley-Rideal
ESD	Electron stimulated desorption
FWHM	Full width at half maximum
HA	Hot atom
HOPG	Highly-oriented pyrolytic graphite
HRD	High Rate Detector
ICP	Inductively coupled plasma
IE	Ionization energy
INMS	Ion and Neutral Mass Spectrometer
ISS	Ion scattering spectroscopy
ISS	Imaging Science Subsystem
K	Kinematic factor
KE	Kinetic energy
LAMMPS	Large-scale Atomic/Molecular Massively Parallel Simulator
LEIS	Low-energy ion scattering
LEO	Low Earth orbit

LH	Langmuir-Hinshelwood
MC	Monte Carlo
MD	Molecular dynamics
MIBSA	Molecular Ion Beamline and Scattering Apparatus
ML	Monolayer
MS	Multiple scattering
NIMS	Near-infrared mapping spectrometer
NVE	Microcanonical ensemble
NVT	Canonical ensemble
OS	Open source
PAH	Polycyclic aromatic hydrocarbon
PES	Potential energy surface
POI	Plane of incidence
PUI	Pick-up ion
Q1	First quartile
Qeq	Charge equilibration method
QM	Quantum mechanics
QMS	Quadrupole mass spectrometer
RCT	Resonant charge transfer
RF	Radio frequency
RGA	Residual gas analyzer
RIS	Reactive ion scattering
RMD	Reactive molecular dynamics
ROS	Reactive oxygen species
RPWS	Radio and Plasma Wave Science
SA	Surface area
SCA	Semi-classical approximation
SIMS	Secondary ion mass spectroscopy
SNMS	Secondary neutral mass spectroscopy
SNR	Signal to noise ratio
SRS	Stanford Research Systems
SS	Single scattering
SZA	Solar zenith angle
TPD	Temperature-programmed desorption
UHV	Ultra-high vacuum
VB	Valence band
VIMS	Visual and Infrared Mapping Spectrometer
W^+	Water group ions (not tungsten)

Symbols

$\mathbf{a}$	Grain radius
$\mathbf{E}$	Particle kinetic energy
$\boldsymbol{e}$	Elementary charge
$\mathbf{E_0}$	Incident energy
$\mathbf{E_0'}$	Incident energy after modification by surface potential
$\mathbf{E_f}$	Fermi level
$\mathbf{E_{out}}$	Exit energy
$\mathbf{E_{out}'}$	Exit energy before modification by surface potential
$\mathbf{E_U}$	Truncation energy
$\mathbf{G}$	Universal gravitation constant
$\mathbf{K}$	Kinematic factor
$\mathbf{k_b}$	Boltzmann constant
$\mathbf{L_{coll}}$	Characteristic collision length
$\mathbf{M}$	Mach number
$\mathbf{M_E}$	Enceladus mass
$\mathbf{m_i}$	Mass of species *i*
$\mathbf{q}$	particle charge
$\mathbf{R_E}$	Enceladus radius
$\mathbf{r_s}$	Source region radius
$\mathbf{s}$	Inelasticity
$\mathbf{U}$	Binding energy
$\mathbf{U_{co}}$	Cohesive energy
$\mathbf{V_p}$	External plasma bias
$\mathbf{Vs}$	Surface potential
$\mathbf{V_{sp}}$	Plasma self-bias
$\mathbf{X_{H2}}$	H_2 mixing ratio
$\mathbf{Y_i}$	Yield of species *i*
$\mathbf{Z_m}$	Cassini measurement altitude
$\mathbf{Z_{max}}$	z-position of highest atom in slab
$\boldsymbol{\beta}$	Sticking probability
$\boldsymbol{\varepsilon_0}$	Vacuum permittivity
$\boldsymbol{\theta_0}$	Incident angle
$\boldsymbol{\theta_i}$	Lab-frame scattering angle for i^{th} collision
$\boldsymbol{\theta_T}$	Total lab-frame scattering angle
$\boldsymbol{\kappa}$	Power law parameter
$\boldsymbol{\lambda_D}$	Debye length
$\boldsymbol{\tau}$	Residence time

Chapter 1

INTRODUCTION

1.1 Overview

Several features make the hyperthermal energy regime (kinetic energies of 10s to 100s of eV) distinct from lower- and higher-energy regimes. The sticking probability reaches a minimum at hyperthermal impact energies.[1] Charge exchange is facilitated by small apsis distances and relatively lengthy surface interactions.[2] The stopping range of atoms and ions at these energies is very short, making the scattering interaction highly surface selective.[1] Due to this combination of factors, Eley-Rideal surface reactions, direct reactions between gas-phase molecules and chemisorbed surface species, have been unambiguously demonstrated in this regime.[3] For the very same reasons, these reactive and nonreactive scattering processes have been developed in the past few decades into powerful surface-analytical tools, Reactive Ion Scattering (RIS)[4] and Low-Energy Ion Scattering (LEIS, also known as Ion Scattering Spectroscopy or ISS).[5] In the latter method, fine detail of surface structure and composition is revealed through the angular and energy distribution of scattered non-reactive ions. In the former, Cs^+ ions abstract surface atoms and molecules, which are identified mass spectroscopically, while causing minimal surface damage.[4]

Outside of the laboratory, these low-energy[1] ion–surface interactions are quite uncommon on Earth, occurring almost nowhere in terrestrial nature. Their main relevance is to semiconductor processing, where they have enormous importance in plasma etching. With increasing altitude, though, they become more common. In atmospheric reentry, for instance, gas-surface relative velocities enter the hyperthermal regime.[6] In low Earth orbit (LEO), atomic oxygen escaping the thermosphere interacts with materials of spacecraft and satellite construction at orbital velocities, very efficiently degrading surfaces.[6,7]

Beyond LEO, the trend continues. Low-energy solar wind protons scatter from the Lunar surface[8] and have been implicated in the maintenance of Lunar water.[9] Farther still, molecules outgassed from

[1] Terminology differs from field to field. This thesis is primarily concerned with kinetic energies of 10−300 eV, which in surface science are called "hyperthermal." The threshold between the hyperthermal regime and the "low-energy" regime is not, however, precisely defined (fluctuating in the range of 100 and 1000 eV). In planetary science the distinction is not as careful — hyperthermal ions are frequently called "low-energy" or, even less precisely, "cold." Going forward, we will use the terms low-energy and hyperthermal interchangeably.

comets are ionized and accelerated by the solar wind, becoming hyperthermal pick-up ions (PUIs),[10] which can re-impact the nucleus and drive unexpected chemistry.[11] Perhaps nowhere in the solar system are hyperthermal ion–surface interactions more important, however, than in the magnetospheres of the gas-giants. Here dwell the so-called Ocean Worlds, a lengthening catalogue of icy satellites that harbor global subsurface oceans. Although these airless bodies are protected from the solar wind by the giant magnetospheres of their host planets, they are exposed to intense irradiation by energetic electrons and reactive heavy ions. A major component of this radiation environment is the corotating "cold" plasma, which is dragged along by rotation of the planets' magnetic fields and overtakes the moons in their orbits, a continuous hyperthermal wind.[12,13]

This magnetospheric plasma bombardment appears to have important ramifications for the composition of both the condensed and rarefied phases (*vide infra*). Unfortunately, the development of LEIS/RIS (the techniques) in the laboratory largely overlooked materials of astrophysical relevance in favor of more facile targets. Unfortunately again, LEIS/RIS (the phenomena) have been largely overlooked in planetary science, where research on ion–surface interactions has overwhelmingly focused on much higher kinetic energies. The overarching goal of this thesis is to fill some of the void. We take mixed experimental–theoretical approach to understanding the chemical weathering astrophysical surfaces by low-energy plasma. Our experiments focus on hyperthermal reactive ions (specifically, water group ions) scattering from surfaces relevant to the Saturnian and Jovian moons and how the scattering interaction populates the plasma phase with ions (Chapters 2, 3, and 6). Our theoretical efforts include modelling of plasma–surface chemistry in the Enceladus plume (Chapter 7) and Reactive Molecular Dynamics (RMD) simulations of water-group molecules[2] bombarding ices (pure H_2O and clathrates) toward identifying novel mechanisms for forming small molecules (Chapters 4, 5, and 8).

The following sections will provide some basic background for low-energy plasma–surface interactions in the Solar System, specifically in the Saturnian magnetosphere (§1.2), and in the laboratory (§1.3), focusing on reactive scattering. A summary of our general experimental and simulation methods will follow (§1.5−1.6).

---

[2] Although this thesis is about low energy *plasma* surface interactions, our simulations model impacts of *neutral* molecules. Neutralization is typically very efficient for ion-surface collisions in this regime because of the long interaction times,[5] and, moreover, gas phase charge exchange reactions can occur which neutralize energetic ions with little loss of kinetic energy.[14,15] Hyperthermal impacts are, therefore, within the scope of plasma-surface interactions.

1.2 Solar system plasma-surface interactions

1.2.1 Plasma environment of icy moons

Nowhere in our solar system are hyperthermal ion–surface interactions more abundant and persistent than inside the magnetospheres of the gas giants. These planets host moons that orbit perpetually within their giant magnetospheres, where they are exposed to a variety of radiations sources. The Cassini mission, active around Saturn from 2004−2017, revealed this environment in great detail. Heavy ion bombardment is a major element, and the largest ion fluxes onto Saturn's midsized icy moons (Mimas, Enceladus, Tethys, Dione, and Rhea) come from the cold, corotating plasma.[16] One of Saturn's moons, Enceladus, famously hides a liquid water ocean beneath its frozen surface and emits a plume of water vapor into space through fissures in its ice crust.[17] The Enceladus plume populates the magnetosphere with water group ions (O^+, OH^+, H_2O^+, H_3O^+; abbreviated collectively W^+), which are swept up by Saturn's rotating magnetic field, accelerating them to velocities that far exceed the Keplerian velocities of the icy moons.[18] The relative motion of the corotating plasma and the moons results in a continuous bombardment of the surface by ions at hyperthermal energies (Figure 1-1).

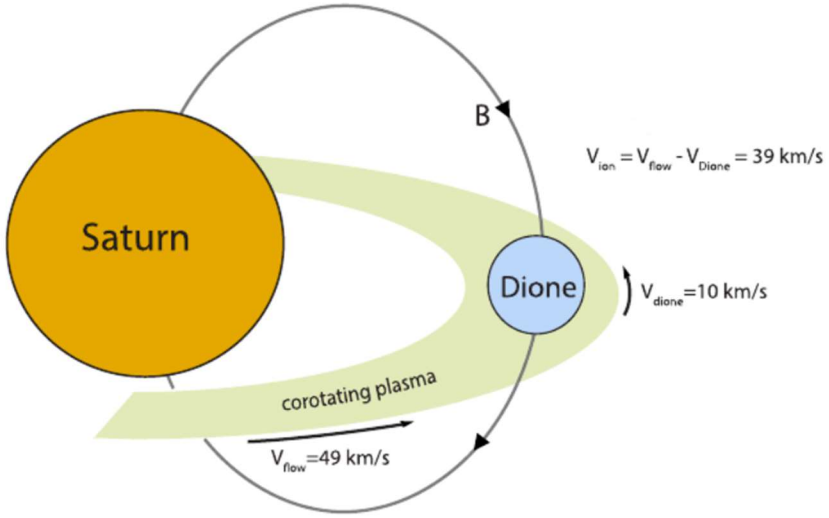

Figure 1-1: Illustration of the corotating plasma-moon interaction for Dione. Reproduced with publisher permission from Nordheim et al. (2020).[19] The corotating plasma flows at V_{flow}=49 km/s, overtaking Dione at a relative velocity of $V_{flow}-V_{Dione}$ = 39 km/s.

The kinetic energy of the impacting heavy ions is distributed over many orders of magnitude, with the mode falling in the hyperthermal regime.[16] Over the past decades, the contributions of high-energy ions to sputtering and radiolysis have been well characterized.[20] In contrast, the predominating cold plasma ions have been generally neglected because they are relatively radiolytically inert—much of

the collision cascade fails to meet the threshold for bond dissociation. Critically, however, the ion kinetic energy is greater than activation energies for chemical reactions, meaning that these ions can drive chemistry that would ordinarily be prohibited by lack of thermal energy at the cold ice surface.

1.2.2 Surface composition

The influence of these low-energy ions on the surface composition of icy satellites is not well understood, but it is apparent that they play an important role. The hemispheric color asymmetry seen at several of Saturn's icy moons[21] provides a clear illustration of this (Figure 1-2). The large moons of Saturn (and Jupiter) are tidally locked, so that the corotating plasma impinges primarily on the trailing hemisphere (the side facing opposite the direction of orbit). A darkening/reddening of this hemisphere is common to Tethys, Dione, and Rhea and evinces plasma induced chemical changes to the ice,[21] yet its mechanism remains unresolved.[12] It has been attributed to a variety of species including carbonaceous materials, possibly organics, although conclusive identification has not been possible through spectroscopy.[22]

Since one of our goals in this thesis is to address plasma interactions at astrophysically relevant surfaces, it is useful to give a brief overview of what these surfaces look like. By and large, the icy satellites of Saturn are just that. Their surfaces are composed overwhelmingly of crystalline water ice.[17] The second most abundant ice is CO_2, which, together with radiolytically produced O_2, sustains a seasonal exosphere (a tenuous, collisionless atmosphere) at Dione and Rhea.[16] Molecular oxygen is readily formed in energetic particle (heavy ions, electrons, cosmic rays, etc.) bombardment of water ice via radiolysis, the collision induced dissociation of ice into radicals and their subsequent barrierless or near-barrierless recombination into other molecules.[20] Molecular hydrogen is also produced by this mechanism, which is highly relevant to Chapter 7. Besides these two ices, the surfaces contain trace amounts of organics (methanol, PAH), ammonia hydrate, and another water ice radiolysis product, hydrogen peroxide (see Table 1-1). Other surface constituents are plausible because they have been identified in the vapor of the Enceladus plume or in its entrained ice grains, which populate the diffuse E-ring and deposit eventually on the other satellites.[23] These include sodium-bearing salts (NaCl, $NaHCO_3$ or Na_2CO_3),[24] silica nanograins,[25] and methane.[26]

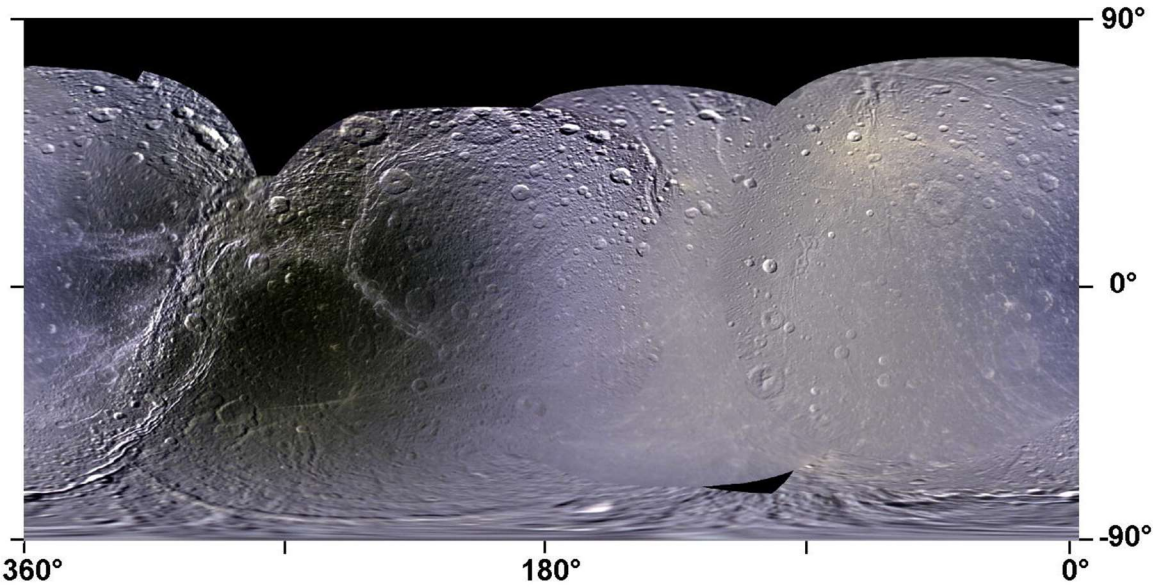

Figure 1-2: Enhanced Cassini false-color (IR-Green-UV) global map for Dione reproduced from Schenk et al. (2011) with publisher permission.[21] The map is cylindrically projected with the trailing hemisphere centered at 270° longitude and leading hemisphere at 90°. A change in the surface spectral properties for the plasma bombarded trailing hemisphere is apparent, but the mechanism is unknown.[12]

Table 1-1. Table summarizing detected and hypothesized constituents of the surfaces of icy moons in the Saturn system. Credit: Tom Nordheim

Surface constituent	**Present on**	**Concentration**	**Refs.**
H_2O (crystalline)	All moons	90+%	
H_2O (amorphous)	Enceladus (tiger stripes), Dione (partial)	Unclear, but low	[27,28]
CO_2	All moons. Abundant at Enceladus South Pole. Enhanced on Dione's trailing hemisphere.	Enceladus South Polar Terrain: ~10s of %. Otherwise: Trace (~1% level or less)	[22,29]
NH_3 hydrate/NH_4OH	Possibly present at Enceladus, Tethys, Dione, Iapetus	Trace (~1% level or less)	[22]
Amorphous carbon	All satellites. Prominent on Iapetus and Dione. Speculated carbonaceous lag layer at Dione and Rhea.	Unclear	[22,30]
"Short-chain organics"	Enceladus, Iapetus, Phoebe, Hyperion	Trace (~1%) level	[31]
PAH	Iapetus, Phoebe, Hyperion	Trace (~1%) level	[22,32–34]
CH_3OH	Enceladus	~1%	[35]
Nanophase iron or nanophase hematite	All satellites. Prominent on Iapetus and Dione.	Trace (~1% level)	[22,30]
Trapped H_2	Iapetus and Hyperion	Trace (~1%) level	[22,30]
"Triton tholin"	Rhea	Trace (0.4%)	[36]
H_2O_2	Mimas	Trace (0.13%)	[37]
Hydrazine monohydrate	Rhea	Minor (~5%)	[38]

1.2.3 Negative Pick-Up Ions

The neglected low-energy plasma–surface interaction is associated with a several *Cassini* observations that continue to defy explanation. One is the mechanism of the hemispheric color dichotomy introduced above. A second is the detection of negative ion signatures by the Cassini Plasma Spectrometer (CAPS) during flybys[3] of Saturn's large moons Dione, Rhea, and Enceladus. Gas-phase mechanisms of negative ion formation fail to reproduce the observed abundances, suggesting an as yet undetermined, surface mediated formation pathway.[16] Back-tracing of negative pick-up ion (PUI) trajectories from the point of observation in the plasma wake of Dione and Rhea locates their source at the surface of moons, supporting the hypothesis of a surface origin (Fig. 2).[39,40] Due to limitations in the capabilities of CAPS-ELS, the mass of negative PUIs near Saturn's moons could only be constrained to a broad range, 23−29 amu and 15−25 amu[40] at Rhea and Dione, respectively.[19,39] Resonant charge transfer (RCT) during low energy scattering interactions is known to efficiently produce negative ions,[41] but there is a dearth of research with relevant surfaces and projectiles.[42] Negative ion formation by this mechanism is facilitated by lengthy interactions of scattered ions with the continuum of electronic states in the solid ice and the near-surface enhancement of the electron affinity due to image charge attraction.[2]

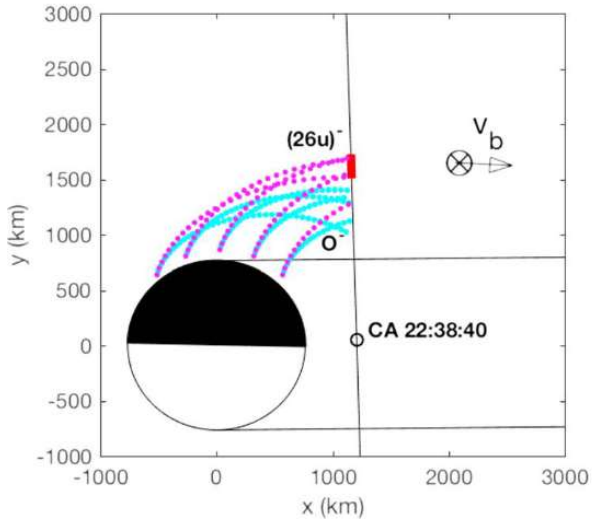

Figure 1-3: Trajectories of negative PUIs detected near Rhea, from source (near surface) to point of detection (Cassini flight path). Trajectories are shown for two candidate ion masses, 26 amu and 16 amu. The results are consistent with a surface mediated process for negative ion formation. Figure reproduced with permission from Desai et al. (2018).[39]

[3] A "flyby" is a close encounter of a natural satellite by *Cassini*. These are referenced by a short abbreviation of the moon's name and a number assigned chronologically. For instance, the 22 flybys of Enceladus are numbered E1−E22 and the single targeted flyby of Tethys is called Te1.

RCT is thus a promising candidate for the PUI source, especially in light of the low sticking probabilities generic to the hyperthermal regime, which allow projectiles to sample the electronic states of the surface and scatter back into the vacuum. The Moon furnishes an excellent illustration of plasma scattering at airless bodies, with reflection of 0.1%−1% of solar wind protons (~750 eV) from the surface having been detected by the polar orbiter *SELENE*.[8]

Negative ions have also been observed in several other solar system environments (see Table 1-2), where they are also associated with hyperthermal ion scattering. For instance, they were detected decades ago in the coma of comets,[43] but only recently did the *Rosetta* mission to Comet 67P reveal a connection to low-energy ion exposure. In the coma, *Rosetta* discovered a population of water group ions accelerated by interaction with the solar wind to a mean energy of several hundred eV.[44] This population impinges on the nucleus at fluxes comparable to or even exceeding the solar wind flux.[44] In tandem with this discovery, *Rosetta* detected molecular oxygen in the coma at unexpectedly large abundance.[45] Following these discoveries, researchers demonstrated experimentally that hyperthermal water ions undergo an Eley-Rideal reaction with a variety of metal oxide and silicate surfaces, in which an oxygen atom is abstracted from the surface to form molecular oxygen as a negative ion. [11] In the Jovian system, the presence of Cl^- pick-up ions near Europa was inferred from *Galileo* observations of cyclotron waves, providing indirect evidence for chloride bearing salts on the moon's surface.[46,47] Like Saturn's satellites, the Galilean moons are exposed to corotating magnetospheric plasma, although here the composition (sulfur and oxygen ions sourced from Io's volcanism) differ and energies are somewhat higher due to larger corotation velocities.[48]

The mass range for negative PUIs at Dione and Rhea, interestingly, is compatible with small carbon bearing molecules with high EA (C_2, C_2H).[39,40] This brings us to a third lingering mystery. Although these moons are predominately water ice and radiolytic O_2 production is very well studied,[20] efforts to quantitatively model the exospheres at Dione and Rhea predict O_2 source rates 50 and 300 times greater than observed.[16] This has led to speculation that an angstroms-thick lag layer of refractory carbonaceous material exists on the surface and suppresses radiolysis/sputtering,[16] although there is no direct evidence for such a feature. Together these observations (color dichotomy, negative PUIs, O_2 source rate discrepancy) raise questions about low-energy plasma ions' unknown influence on the surface and gas-/plasma-phase composition.

Table 1-2. Table of past negative ion/plasma scattering observations.

Body	Parent	Type of scattering signal observed	Candidate species	Ref.
Rhea	Saturn	Direct detection of negative PUIs	O^-, CN^-, C_2H^-, C_2^-, HCO^-	39,49
Dione	Saturn	Direct detection of negative PUIs	O^-, other species possible	40
Enceladus	Saturn	Direct detection of negative PUIs	$(H_2O)_nOH^-$ and other negative water clusters, loosely constrained	50,51
Titan	Saturn	Direct detection of ionospheric negative ions	CN^-, NH_2^-, O^-, NCN^-, $HNCN^-$, C_3H^-, etc., very massive ions up to 10,000 amu/q	51,52
Europa	Jupiter	Indirect detection of negative pick-up ions via ion cyclotron waves	Cl^-	46,47
Comet 67P	Sun	Direct detection of negative PUIs	H^-	53
Comet 1P/Halley	Sun	Direct detection of negative ions	O^-, OH^-, C^-, CH^-, CN^- and heavier complex CHO molecular ions	43
Moon	Earth	Direct detection of scattered solar wind protons	H^+	8

1.3 Reactive ion scattering - Binary Collision Approximation

In the absence of inelastic energy losses, such as those related electron and vibrational excitations, the energy of a scattered particle can be determined from the conservation of momentum and energy. Assuming that the scattering interaction is between only two moieties (the "binary collision approximation" or BCA), the ratio of the impactor[4] exit energy (E_{out}) to the incident energy (E_0) is a constant, the so-called kinematic factor (K), which depends only on the scattering geometry and mass ratio of the two particles ($A=m_1/m_2$):[54]

$$K = \left(\frac{\cos\theta \pm \sqrt{A^2 - \sin^2\theta}}{1 + A} \right)^2 \qquad 1\text{-}1$$

[4] The "impactor" being the hyperthermal ion or molecule impacting the surface. We use the terms impactor and projectile interchangeably throughout this work.

where θ is the lab-frame scattering angle, that is, the angle between the impactor's incident and exit velocity vectors. The maximum energy transfer from the impactor to its collision partner occurs for a head-on collision (impact parameter = 0) and is a fraction T of E_0 depending only on the mass ratio:

$$T = \frac{4A}{(1+A)^2} \qquad 1\text{-}2$$

For consecutive elastic collisions, the impactor's fractional energy retention is the product of the kinematic factors for each collision.

$$\frac{E_{out,n}(\theta_T)}{E_0} = \prod_{i=1}^{n} K(\theta_i, A_i) \qquad 1\text{-}3$$

where the total scattering angle (θ_T) is given by the sum of the scattering angles for each collision:

$$\theta = \sum_{i=1}^{n} \theta_i \qquad 1\text{-}4$$

The above Binary Elastic Collision (BEC) model is readily extended to more realistic systems by including an inelastic energy loss (s). So long as the energy loss does not occur during momentum exchange between the particles, the BEC conservation equations are still observed but now apply to the incident and exit energies just before and after the collisional interaction, as distinguished from the energies at greater interatomic distances. We will denote these local energies E_0' and E_{out}'. If the inelasticity is not a function of E_0, the incident and exit energies are now related by:

$$E_{out} = KE_0 - s \qquad 1\text{-}5$$

Despite its many assumptions, this very simple result holds for a variety of scattering systems in the hyperthermal energy regime. Variations on the basic BEC model have been applied successfully to scattering of diatomic molecules (N_2, O_2),[55] triatomics (namely H_2O^+),[56] and Eley-Rideal abstraction reactions.[57] In the simplest variation of the last, the projectile atom/ion abstracts an atom adsorbed on a substrate atom. Although the collision complex is actually ternary, the recoiling bodies are only two, the diatomic product and the substrate atom. From the conservation equations underpinning BCA, Yao & Giapis (2016) derive the kinematic factor:[57]

1-11

$$K_{ER}(\theta) = \frac{\left[\sqrt{m_P(m_P + m_A)}\cos\theta \pm \sqrt{(m_P + m_A + m_S)(m_S - m_P) + m_P(m_P + m_A)\cos^2\theta}\right]^2}{(m_P + m_A + m_S)^2} \quad \text{1-6}$$

where the mass of the projectile, adsorbate, and substrate atoms are m_p, m_a, and m_s, respectively. The linear relationship of Eq. 1-5 holds for a variety of reactions, including abstraction of O from Pt and Pd by N^+ and O^+.[57] It also holds for more complex reaction systems, like the abstraction of adsorbed oxygen by H_2O^+ impactors, forming a transient oxywater state ($H_2O{-}O$).[11] The transient state in this case dissociates rapidly into fragments with equal lab-frame velocity, that of the scattered transient predicted by Eq. 1-6 and Eq. 1-5. For this reaction and for the collision-induced intramolecular reaction $H_2O \rightarrow O + H_2$, the H_2O^+ impactor is effectively described as a single moiety of mass $m_P = 18$ amu for the sake of Eq. 1-6 and Eq. 1-1.[11]

Although deviations from BCA do occur,[54] the relatively simple equations above provide a great deal of insight into the scattering/reaction mechanisms. In particular, the linearity of Eq. 1-5 is strong evidence in favor an ER reaction mechanism, as opposed to a Langmuir-Hinshelwood (LH) reaction mechanism.[57] In the LH mechanism, reaction is preceded by adsorption and diffusion of the reactants on a surface, which results in their thermalization with the solid such that the incident energy is "forgotten".[58] This forgetfulness is also characteristic of sputtering in the linear cascade regime and at high kinetic energies.[59] In contrast, at low impact energies (in the "near-threshold" regime), the ejection of surface atoms is possible only for a limited set of well-defined collision sequences, which can be described by BCA.[60] We will refer to the above equations for the calculation of kinematic factors later on, sometimes using an abbreviated notation of the form $K(P \rightarrow AS \rightarrow PA)$ to reference a particular collision system (in this example, abstraction of A from S by P to form molecule PA).

1.4 General experimental methods

Our experiments leverage a unique home-built molecular ion beamline and scattering apparatus (MIBSA). One of the main experimental challenges in the study of hyperthermal ions is that high current densities necessitate high number densities of mutually repulsive ions, making it difficult to maintain a beam for steering, focusing, and mass filtering. Our MIBSA avoids this problem by utilizing the accel-decel schema. Ions (monoatomic or molecular) extracted from an inductively coupled plasma (ICP) are immediately accelerated to energies of 10-15 keV, at which energy they are magnetically mass filtered, focused, and steered. As near to the target surface as practicable, they

are decelerated to the intended incident energy (10-600 eV). In this way, it is possible to deliver ML/s fluxes a variety of mass- and energy-selected ions to a target surface. An extremely thorough description of this MIBSA is included in the dissertation of its primary architect, Michael Gordon.[61] A more concise description is also published in Review of Scientific Instruments.[62] With the exception of modifications to the target holder (described in Chapter 6) and to the detection system, the apparatus is essentially unchanged. Nevertheless, a brief recapitulation is provided here for convenience of the reader.

The primary ions are sourced from an inductively coupled plasma with gas pressures typically in the range of 1-5 millitorr and driven by 400-600 W. Hyperthermal ion beams are very sensitive to stray electric fields, which necessitates that the scattering chamber and target surface are earthed. Without external biasing, ions extracted from the plasma and reaching ground would be accelerated on passing through the plasma sheath to a kinetic energy of $e \times V_{sp}$, where V_{sp} is the plasma self-bias, typically 5-20 V. We control the ultimate kinetic energy of the ions by applying an external bias to an electrode embedded in the plasma. The ions are extracted, accelerated, and focused by a series of cylindrical electrostatic lenses (Figure 1-4a). The lens voltages are manually tuned to ensure optimal extraction conditions and to correctly focus the beam prior to magnetic mass filter. In order to maintain a coherent beam during the mass filtration operation, the flight tube is electrically isolated from the rest of the vacuum apparatus by dielectric standoffs, which allows it to float at ~15 kV. The high voltage beamline passes through a 60° magnetic sector and a second, 10° magnetic sector (Figure 1-4b). The first accomplishes mass filtration by imaging ions of the target mass onto a narrow exit slit. The second ensures that fast neutrals formed at the heavily gas-loaded exit slit do not reach the scattering surface. The first magnetic filtering step introduces a beam astigmatism which is corrected downstream of the exit slit by a pair of electrostatic quadrupole lenses, refocusing the beam ahead of the 10° sector. Before reaching the target surface, the ions are decelerated by a cylindrical Einzel lens triplet and pass through a final quadruple lens, which is used for fine steering corrections.

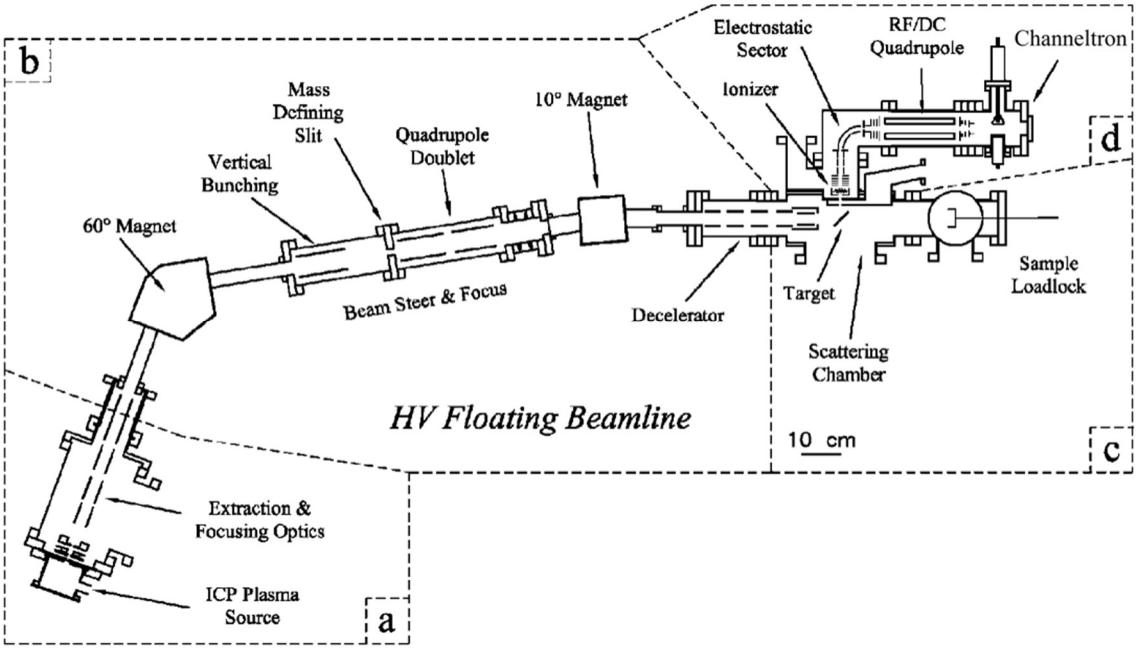

Figure 1-4: Schematic of the MIBSA, reproduced (with very slight modification and with permission) from Gordon & Giapis (2005).[62]

After exiting the beamline, the ions beam passes through a grounded, rotatable flag with a 2 mm aperture, establishing field-free conditions near the target by screening stray electric fields from the beamline's terminal electrostatic optics. The detector line of sight is perpendicular to the beamline optical axis, nominally fixing the lab-frame scattering angle at 90 degrees (Figure 1-4c). Small displacements of the target surface (due for instance to a variable sample thickness) or the flag aperture can cause the actual scattering angle to deviate from 90°. In order to account for this deviation, we extract the scattering angle from the energetics of primary ion recoils from heavy surface atoms, when possible, using BCA. That is, we measure the kinematic factor for a known projectile and surface and solve Eq. 1-1 for θ.

Broadly speaking, two types of targets are considered in our work: refractory and volatile. These two classes of targets require very different accommodations, the primary consideration being the sample temperature. One of the goals of this thesis was to establish an experimental capacity for the study of astrophysical ices. This effort and its preliminary results will be discussed in Chapter 6. Otherwise, our experiments utilized refractory surfaces. The target surface is mounted in a sample holder, which is transferred in and out of the scattering chamber via load-lock, allowing facile target switching. The base of the sample holder is a stainless-steel platen which can be twist-locked onto the target stage in

vacuo using a coaxial linear/rotary feedthrough. The platen also includes electrical contacts for a K-type thermocouple which provides both temperature monitoring of the sample and a metered ground connection, although not simultaneously. The target stage is mounted on a three-axis translational manipulator and a differentially pumped rotary manipulator, which enables us to adjust the incident angle. It also features a nude filament heater behind the platen. The sample itself is electrically isolated from the platen by a sapphire disc on the bottom side and a sapphire washer on the top. A molybdenum retaining ring with four screws secures the assembly to the platen and covers the sapphire washer. A thin copper foil is sandwiched between the sapphire disc and the back of the sample to provide more uniform charge dissipation through the attached thermocouple.

The target stage can be moved vertically, clear of the beam axis, which allows us to characterize the beam energetically and spatially using a miniaturized electrostatic energy analyzer (EEA) and a wire profiler. Alternatively, we obtain the primary ion energy using our main detector system and a special positioning of the target that results in a conservative deflection of the beam into the detector. This modality also enables direct verification of the primary ion mass.

The detection system (Figure 1-4d) comprises a continuous dynode electron multiplier (Channeltron) coupled to an electrostatic energy filter, with an interposed quadrupole mass filter (Extranuclear Laboratories, Inc.). The EEA and QMS float at variable DC-voltage while the EEA pass energy is maintained at 15 eV. In this way, ions can be detected over a wide range of kinetic energies without a confounding change in the transmission coefficient or yield of the detection system. At the entrance to the EEA, a commercial electron impact ionizer assembly (Extranuclear Laboratories, Inc.) provides an optional secondary neutral mass spectrometry capability (SNMS). Due to the low efficiency electron impact ionization, we do not use this capability in the work presented here, except as described in Chapter 6 for a preliminary temperature programmed desorption (TPD) test. The detection apparatus communicates with the scattering chamber via two 2 mm apertures with line of sight to the target surface across a differentially pumped stage. This interstitial space also contains parallel electrodes, which can be biased to prevent transmission of primary and secondary ions during SNMS operation.

The MIBSA requires that a pressure differential of 7 to 8 orders of magnitude be maintained between the plasma source and the detector while gas is being actively transported down the beamline. For this reason, the beam is differentially pumped in at least six stages. Pressures of $\sim 2\times10^{-8}$ torr can be maintained in the scattering chamber during beam exposure because of the combined pumping speed

of a large turbomolecular pump and cryopump. A residual gas analyzer (SRS RGA-200) is installed in the scattering chamber to monitor the background pressure and composition.

1.5 General simulation methods

Molecular dynamics (MD) is a classical simulation method that follows the motion of particles (typically atoms, molecules). ReaxFF is a formalism for "reactive" molecular dynamics (RMD), which models the dynamic formation and breakage of chemical bonds. In ReaxFF, there is no prescribed bond topology. Covalent bonding is captured via a bond distance–bond order relationship, which is parameterized to reproduce more expensive quantum mechanics (QM) calculations, such as reaction coordinates from Density Functional Theory (DFT). A complete description of the methodology can be found in Chenoweth et al. (2008),[63] but, in brief, the total energy is a sum of contributions from various interactions:

$$E_{total} = E_{bond} + E_{over} + E_{angle} + E_{tors} + E_{vdw} + E_{coul} + E_{spec} \qquad 1\text{-}7$$

The first term (E_{bond}) relates to covalent bonding via the bond order (BO_{ij}), which is a continuous function of the interatomic distance (r_{ij}):

$$BO_{ij} = BO_{ij}^{\sigma} + BO_{ij}^{\pi} + BO_{ij}^{\pi\pi} = \qquad 1\text{-}8$$
$$exp\left(p_{bo1}\left(\frac{r_{ij}}{r_0^{\sigma}}\right)^{P_{bo2}}\right) + exp\left(p_{bo3}\left(\frac{r_{ij}}{r_0^{\pi}}\right)^{P_{bo4}}\right) + exp\left(p_{bo5}\left(\frac{r_{ij}}{r_0^{\pi\pi}}\right)^{P_{bo6}}\right)$$

The angle and torsion terms (E_{over} and E_{angle}) are three- and four-body strains governing the geometry of polyatomic molecules. The E_{vdw} and E_{coul} are a Morse potential and shielded coulomb potential, respectively, accounting for long-range attraction due to dispersion, short-range Pauli repulsion, and coulombic interaction. E_{coul} depends on the partial charges of interacting atoms/ions, which can be obtained via the QEq charge equilibration method of Rappe & Goddard (1991). In QEq, charge is distributed among atoms based on their ionization potentials (IP), electron affinities (EA), and the system geometry in order to establish equality of atomic-scale chemical potentials.[64] The E_{over} term penalizes the energy of over coordinated atoms, that is, atoms with more bonds than preferred by its valence. Finally, the E_{spec} term subsumes a variety of contributions, including hydrogen bonding and resonance, and some molecule-specific corrections (for C_2 and CO).

The parameters ($p_{bo1}, p_{bo2}, p_{bo3}, p_{bo4}, p_{bo5}, p_{bo6}, r_0^{\sigma}, r_0^{\pi}, r_0^{\pi\pi}$) of Eq. 1-8 and the other terms of Eq. 1-7 are optimized to reproduce DFT results for the system of interest. This fitting is generally done for the ground state, the lowest potential energy surface (PES) for the system. ReaxFF is a remarkably flexible paradigm and has been applied to a wide variety of systems, including hypervelocity impacts of materials,[65,66] aqueous chemistry, combustion, detonation of high-energy materials, and hyperthermal oxygen impacts (see Senftle et al. (2016) and references therein).[67] Despite not explicitly handling electronic states, ReaxFF is able to capture most of the phenomena relevant to condensed H_2O phases, including autoionization, homolytic and heterolytic bond dissociation of water, and structural diffusion of H^+ and OH^-.[68] For these reasons, it is an excellent tool for understanding the collision-induced chemistry of ices.

1.7 References

1. Rabalais, J. W. & Marton, D. Atomic collisions in surface chemistry and film deposition. *Nuclear Instruments and Methods in Physics Research Section B: Beam Interactions with Materials and Atoms* **67**, 287–295 (1992).
2. Shao, H., Langreth, D. & Nordlander, P. Chapter 3 Theoretical Description of Charge Transfer in Atom-Surface Collisions. in *Low energy ion-surface interactions* (ed. Rabalais, J. W.) 118–186 (J. Wiley & sons, Chichester New York Brisbane [etc.], 1994).
3. Kuipers, E. W., Vardi, A., Danon, A. & Amirav, A. Surface-molecule proton transfer: A demonstration of the Eley-Rideal mechanism. *Phys. Rev. Lett.* **66**, 116–119 (1991).
4. Kang, H. Reactive Ion Scattering of Low Energy Cs+ from Surfaces. A Technique for Surface Molecular Analysis. *Bulletin of the Korean Chemical Society* **32**, 389–398 (2011).
5. Rabalais, J. W. *Low Energy Ion-Surface Interactions*. (J. Wiley & sons, Chichester New York Brisbane [etc.], 1994).
6. *Chemical Dynamics in Extreme Environments*. (World Scientific, Singapore River Edge, NJ, 2001).
7. Banks, B. A., De Groh, K. K. & Miller, S. K. Low Earth Orbital Atomic Oxygen Interactions with Spacecraft Materials. *MRS Proc.* **851**, NN8.1 (2004).
8. Saito, Y. *et al.* Solar wind proton reflection at the lunar surface: Low energy ion measurement by MAP-PACE onboard SELENE (KAGUYA). *Geophysical Research Letters* **35**, (2008).
9. Jones, B. M., Aleksandrov, A., Hibbitts, K., Dyar, M. D. & Orlando, T. M. Solar Wind-Induced Water Cycle on the Moon. *Geophysical Research Letters* **45**, 10,959-10,967 (2018).
10. Nilsson, H. *et al.* Birth of a comet magnetosphere: A spring of water ions. *Science* **347**, aaa0571 (2015).
11. Yao, Y. & Giapis, K. P. Dynamic molecular oxygen production in cometary comae. *Nature Communications* **8**, 15298 (2017).

12. Howett, C. J. A. *et al.* Ring and Magnetosphere Interactions with Satellite Surfaces. in *Enceladus and the Icy Moons of Saturn* (The University of Arizona Press, 2018). doi:10.2458/azu_uapress_9780816537075-ch017.
13. Pappalardo, R. T., McKinnon, W. B., Khurana, K., & Lunar and Planetary Institute. *Europa*. (University of Arizona Press, Tucson, 2009).
14. Lishawa, C. R., Dressler, R. A., Gardner, J. A., Salter, R. H. & Murad, E. Cross sections and product kinetic energy analysis of H2O+–H2O collisions at suprathermal energies. *J. Chem. Phys.* **93**, 3196–3206 (1990).
15. Haythornthwaite, R. P., Coates, A. J., Jones, G. H. & Waite, J. H. Fast and Slow Water Ion Populations in the Enceladus Plume. *Journal of Geophysical Research: Space Physics* **125**, e2019JA027591 (2020).
16. Teolis, B. D. & Waite, J. H. Dione and Rhea seasonal exospheres revealed by Cassini CAPS and INMS. *Icarus* **272**, 277–289 (2016).
17. Postberg, F. *et al.* Plume and Surface Composition of Enceladus. in *Enceladus and the Icy Moons of Saturn* (The University of Arizona Press, 2018). doi:10.2458/azu_uapress_9780816537075-ch007.
18. Teolis, B., Tokar, R., Cassidy, T., Khurana, K. & Nordheim, T. Exospheres and Magnetospheric Currents at Saturn's Icy Moons: Dione and Rhea. in *Enceladus and the Icy Moons of Saturn* (The University of Arizona Press, 2018). doi:10.2458/azu_uapress_9780816537075-ch018.
19. Nordheim, T. A. *et al.* Detection of Negative Pickup Ions at Saturn's Moon Dione. *Geophysical Research Letters* **47**, e2020GL087543 (2020).
20. Teolis, B. D., Plainaki, C., Cassidy, T. A. & Raut, U. Water Ice Radiolytic O_2, H_2, and H_2O_2 Yields for Any Projectile Species, Energy, or Temperature: A Model for Icy Astrophysical Bodies: Ice O_2, H_2, and H_2O_2 Radiolysis Yields. *Journal of Geophysical Research: Planets* **122**, 1996–2012 (2017).
21. Schenk, P. *et al.* Plasma, plumes and rings: Saturn system dynamics as recorded in global color patterns on its midsize icy satellites. *Icarus* **211**, 740–757 (2011).
22. Clark, R. N. *et al.* Compositional mapping of Saturn's satellite Dione with Cassini VIMS and implications of dark material in the Saturn system. *Icarus* **193**, 372–386 (2008).
23. Hendrix, A. R. *et al.* Surface Composition of Icy Moons. in *Enceladus and the Icy Moons of Saturn* (The University of Arizona Press, 2018). doi:10.2458/azu_uapress_9780816537075-ch015.
24. Postberg, F. *et al.* Sodium salts in E-ring ice grains from an ocean below the surface of Enceladus. *Nature* **459**, 1098–1101 (2009).
25. Hsu, H.-W. *et al.* Ongoing hydrothermal activities within Enceladus. *Nature* **519**, 207–210 (2015).
26. Waite, J. H. *et al.* Cassini finds molecular hydrogen in the Enceladus plume: Evidence for hydrothermal processes. *Science* **356**, 155–159 (2017).
27. Newman, S. F. *et al.* Photometric and spectral analysis of the distribution of crystalline and amorphous ices on Enceladus as seen by Cassini. *Icarus* **193**, 397–406 (2008).
28. Newman, S. F. *et al.* Water ice crystallinity and grain sizes on Dione. *Icarus* **203**, 553–559 (2009).

29. Combe, J.-P. *et al.* Nature, distribution and origin of CO2 on Enceladus. *Icarus* **317**, 491–508 (2019).
30. Clark, R. N. *et al.* The surface composition of Iapetus: Mapping results from Cassini VIMS. *Icarus* **218**, 831–860 (2012).
31. Brown, R. H. *et al.* Composition and Physical Properties of Enceladus' Surface. *Science* **311**, 1425–1428 (2006).
32. Dalton, J. B., Cruikshank, D. P. & Clark, R. N. Compositional analysis of Hyperion with the Cassini Visual and Infrared Mapping Spectrometer. *Icarus* **220**, 752–776 (2012).
33. Dalle Ore, C. M., Cruikshank, D. P. & Clark, R. N. Infrared spectroscopic characterization of the low-albedo materials on Iapetus. *Icarus* **221**, 735–743 (2012).
34. Clark, R. N. *et al.* Compositional maps of Saturn's moon Phoebe from imaging spectroscopy. *Nature* **435**, 66–69 (2005).
35. Hodyss, R. *et al.* Methanol on Enceladus. *Geophys. Res. Lett.* **36**, L17103 (2009).
36. Ciarniello, M. *et al.* Hapke modeling of Rhea surface properties through Cassini-VIMS spectra. *Icarus* **214**, 541–555 (2011).
37. Hendrix, A. R. *et al.* Mimas' far-UV albedo: Spatial variations. *Icarus* **220**, 922–931 (2012).
38. Elowitz, M. *et al.* Possible detection of hydrazine on Saturn's moon Rhea. *Sci. Adv.* **7**, eaba5749 (2021).
39. Desai, R. T. *et al.* Cassini CAPS Identification of Pickup Ion Compositions at Rhea. *Geophysical Research Letters* (2018) doi:10.1002/2017GL076588.
40. Nordheim, T. A. *et al.* Detection of negative pickup ions at Saturn's moon Dione. *Geophysical Research Letters* 1–9 (2020) doi:10.1029/2020gl087543.
41. Marbach, J., Bronold, F. X. & Fehske, H. Resonant charge transfer at dielectric surfaces. *Eur. Phys. J. D* **66**, 106 (2012).
42. Millar, T. J., Walsh, C. & Field, T. A. Negative Ions in Space. *Chemical Reviews* **117**, 1765–1795 (2017).
43. Chaizy, P. *et al.* Negative ions in the coma of comet Halley. *Nature* **349**, 393–396 (1991).
44. Nilsson, H. *et al.* Evolution of the ion environment of comet 67P/Churyumov-Gerasimenko: Observations between 3.6 and 2.0 AU. *A&A* **583**, A20 (2015).
45. Bieler, A. *et al.* Abundant molecular oxygen in the coma of comet 67P/Churyumov–Gerasimenko. *Nature* **526**, 678–681 (2015).
46. Volwerk, M., Kivelson, M. G. & Khurana, K. K. Wave activity in Europa's wake: Implications for ion pickup. *J. Geophys. Res.* **106**, 26033–26048 (2001).
47. Desai, R. T. *et al.* Hybrid Simulations of Positively and Negatively Charged Pickup Ions and Cyclotron Wave Generation at Europa. *JGR Space Physics* **122**, (2017).
48. Vorburger, A. & Wurz, P. Europa's ice-related atmosphere: The sputter contribution. *Icarus* **311**, 135–145 (2018).
49. Teolis, B. D. *et al.* Cassini finds an oxygen-carbon dioxide atmosphere at Saturn's icy moon Rhea. *Science (New York, N.Y.)* **330**, 1813–5 (2010).
50. Coates, A. J. *et al.* Negative ions in the Enceladus plume. *Icarus* **206**, 618–622 (2010).
51. Coates, A. J. *et al.* Negative ions at Titan and Enceladus: recent results. *Faraday Discussions* **147**, 293 (2010).

52. Coates, A. J. *et al.* Discovery of heavy negative ions in Titan's ionosphere. *Geophysical Research Letters* **34**, (2007).
53. Burch, J. L. *et al.* Charge exchange in cometary coma: Discovery of H^- ions in the solar wind close to comet 67P/Churyumov-Gerasimenko: NEGATIVE H IONS NEAR COMET C-G. *Geophys. Res. Lett.* **42**, 5125–5131 (2015).
54. Bertrand, P. G. & Rabalais, J. W. Chapter 2 Ion Scattering and Recoiling for Elemental Analysis and Structure Determination. in *Low energy ion-surface interactions* (ed. Rabalais, J. W.) 55–116 (J. Wiley & sons, Chichester New York Brisbane [etc.], 1994).
55. Yao, Y. & Giapis, K. P. Direct Hydrogenation of Dinitrogen and Dioxygen via Eley-Rideal Reactions. *Angewandte Chemie International Edition* **55**, 11595–11599 (2016).
56. Yao, Y. & Giapis, K. P. Intramolecular water-splitting reaction in single collisions of water ions with surfaces. *Chemical Science* **8**, 2852–2858 (2017).
57. Yao, Y. & Giapis, K. P. Kinematics of Eley-Rideal Reactions at Hyperthermal Energies. *Physical Review Letters* **116**, (2016).
58. Prins, R. Eley–Rideal, the Other Mechanism. *Topics in Catalysis* **61**, 714–721 (2018).
59. Thompson, M. W. II. The energy spectrum of ejected atoms during the high energy sputtering of gold. *Philosophical Magazine* **18**, 377–414 (1968).
60. Yamamura, Y., Takiguchi, T. & Kimura, H. Ion-induced desorption in the near-threshold regime. *Nuclear Instruments and Methods in Physics Research Section B: Beam Interactions with Materials and Atoms* **78**, 337–341 (1993).
61. Gordon, M. J. Low-Energy Ion Beamline-Scattering Apparatus with Application to Charge Exchange Collisions at Surfaces. ([object Object], 2004). doi:10.7907/W315-SR88.
62. Gordon, M. J. & Giapis, K. P. Low-energy ion beamline scattering apparatus for surface science investigations. *Review of Scientific Instruments* **76**, 083302 (2005).
63. Chenoweth, K., van Duin, A. C. T. & Goddard, W. A. ReaxFF Reactive Force Field for Molecular Dynamics Simulations of Hydrocarbon Oxidation. *J. Phys. Chem. A* **112**, 1040–1053 (2008).
64. Rappe, A. K. & Goddard, W. A. Charge equilibration for molecular dynamics simulations. *J. Phys. Chem.* **95**, 3358–3363 (1991).
65. Jaramillo-Botero, A. *et al.* Hypervelocity Impact Effect of Molecules from Enceladus' Plume and Titan's Upper Atmosphere on NASA's Cassini Spectrometer from Reactive Dynamics Simulation. *Phys. Rev. Lett.* **109**, 213201 (2012).
66. Jaramillo-Botero, A., An, Q., Theofanis, P. L. & Goddard, W. A. Large-scale Molecular Simulations of Hypervelocity Impact of Materials. *Procedia Engineering* **58**, 167–176 (2013).
67. Senftle, T. P. *et al.* The ReaxFF reactive force-field: development, applications and future directions. *npj Comput Mater* **2**, 15011 (2016).
68. van Duin, A. C. T., Zou, C., Joshi, K., Bryantsev, V. & Goddard, W. A. CHAPTER 6. A Reaxff Reactive Force-field for Proton Transfer Reactions in Bulk Water and its Applications to Heterogeneous Catalysis. in *Catalysis Series* (eds. Asthagiri, A. & Janik, M. J.) 223–243 (Royal Society of Chemistry, Cambridge, 2013). doi:10.1039/9781849734905-00223.

Chapter 2

SCATTERING OF WATER GROUP IONS FROM CARBON SURFACES

2.1 Introduction

Carbonaceous materials are often invoked as surface darkening agents at airless bodies throughout the solar system. In the Saturn system, for instance, darkening of the trailing hemispheres of the inner icy satellites has been variously attributed to nanoscopic iron oxide or amorphous carbon particles.[1,2] Polycyclic aromatic hydrocarbons (PAHs) were detected by Cassini VIMS at Saturn's moons Iapetus, Phoebe, and Hyperion.[1,3–5] Refractory carbon phases are of particular interest at the Saturnian moons Dione and Rhea, where they have been invoked to explain the apparent discrepancy between predicted and observed O_2 exosphere source rates.[6] While incident magnetospheric charged particles are expected to readily produce O_2 through radiolysis of water ice on the surface, a putative lag layer of only a few angstroms thickness could substantially interfere with radiolytic O_2 production. Yet such a surface layer would be undetectable by the optical remote sensing instruments carried by *Cassini*,[6] as those are sensitive to photons that sample much deeper into the surface (typically on the order of 1 μm to 1 mm). Negative pick-up ion (PUI) observations near Dione and Rhea lend some credence to this idea, being potentially consistent with C_2^- or C_2H^- produced by charged particle interactions with the putative surface lag layer, although the ion mass could not be determined directly with Cassini's instrumentation.[7,8] PUI observations such as these may be useful to infer the surface composition of airless bodies generally.[9] But translation of surface composition into gas phase ion abundances (particularly negative ions) is poorly characterized for the relevant scattering species and energies.[10] Here, we undertake laboratory scattering experiments for one such system: carbonaceous surfaces (graphite and amorphous carbon) under bombardment by hyperthermal water group ions, focusing on secondary negative ion emission.

Bombardment of carbonaceous surfaces by hyperthermal oxygen has garnered much experimental attention because of its direct relevance to spacecraft in low-Earth orbit (LEO),[11] beginning in the early 1980s with the first orbital spaceflights of NASA's Space Shuttle program.[12] But, in accord with their practical motivations, most studies have focused on erosion (chemical sputtering) rates of engineering materials (e.g. polymers) and on the energy range relevant to LEO (3.9–7.0 eV).[11,13] Fewer studies have addressed the formation of secondary negative ions during heavy ion

scattering/sputtering (e.g. refs. [14–22]) and these generally use much higher projectile kinetic energies (>2 keV). Especially notable are the several and thorough experiments of Hubert Gnaser, which resolved the energy distributions of atomic and molecular anions sputtered from a variety of carbon-bearing surfaces by 14.5 keV Cs^+,[19,23,24] and a report by Silva et al. (1999) of the C^- energy distribution in 4 keV Ar^+ bombardment of graphite.[14] Concerning hyperthermal reactive ions, Deng and Souda undertook SIMS studies of graphite under nitrogen (atomic and molecular) ion bombardment at 10s to 100s of eV, focusing on the production of CN anions.[25–27] At the intersection of these topics, where there is a conspicuous lack of research, we find the system relevant to Saturn's moons, a putative carbonaceous surface bombarded by the abundant water group ions of Saturn's cold, corotating magnetospheric plasma.

2.2 Methods

2.2.1 Sample preparation

An amorphous carbon target for the beam experiments was deposited onto a copper foil (4N5, ESPI metals) using a commercial Cressington Carbon Coater 108carbon/A in its continuous supply mode without purge gas. The copper substrate was prepared by manual sanding with 600 grit sandpaper, followed by alumina, and an iron oxide crocus paper. After sanding, the sample was rinsed and sonicated with DI water for 20 minutes, sonicated in acetone for 20 minutes, rinsed with MeOH, sonicated in MeOH, rinsed with acetone, and rinsed with MeOH. The deposition consisted of six thirty-second cycles of the evaporator, between which it was necessary to break vacuum and replace the Bradley-type evaporation source (graphite ≤5ppm impurities, Ted Pella). Each deposition was preceded by a 10-minute pump-down to ~8×10^{-5} torr. After the first coating, the carbon film was blue in color, indicating a thickness of 90–100 nm at a refractive index of 2.5,[28] which suggests a final film thickness of approximately 570 nm. The film thickness is not a critical parameter in our experiments, so further characterization was not undertaken.

Ions are extracted from plasmas fed by a combination of oxygen (industrial grade, Airgas), neon (research plus grade, Air Liquide), and argon (UHP grade, Airgas) with or without humidification by DI water. Since the beam itself is mass-filtered en route to the target, the purity of the plasma source gas is not critical.

2.2.2 Measurement of secondary ion energetics and relative yields

Energy distributions for several negative ions were collected following stepwise changes in the beam energy from 54 eV to 212 eV, during 20−30 minutes' exposure at each condition. Due to

erosion of the thin carbon film, data for the highest beam energy (244 eV) were collected in a different location on the same sample, following a 10-minute pre-exposure. The ion beam for this experiment was O^+ sourced from a 575 W Ar/Ne/O_2 (3:2:2) inductively coupled plasma.

Establishing relative yields requires that identical exposure conditions be established for two targets. Given the tendency for hyperthermal ion beams to bloom due to coulombic repulsion, changing the beam energy generally requires adjustment of electrostatic steering and focusing to maximize flux to the target "sweet spot" (that is, the location sighted by the detector aperture) and thus the scattered/sputtered ion signal. The beam tuning process is particularly sensitive at low incident energies, making it difficult repeatably establish a precise surface flux. To measure relative yields in spite of this experimental difficulty, we collect data for two targets at once. The target arrangement for this experiment comprises a graphite planchet (<2ppm total impurities, Ted Pella) with an amorphous carbon coated thin Cu foil masking a disk segment of the graphite. Since negative ion yields were consistently larger for the amorphous carbon (due to the combination of higher density and lower work function[29]), we establish the beam tuning for the aC and then switch targets via a vertical displacement of the sample by ~0.25". The energy distributions for several products were collected up to 40 eV following stepwise increases in E_0, as in the experiment to measure secondary ion energetics. Without changing the sample, the stepping protocol was repeated from the beginning using a different beamline transport voltage twice more. The effect of this change in transport voltage is to necessitate non-trivial refocusing of the beam. This set of three technical replicates was itself repeated four times, replacing the amorphous carbon surface between each set (due to the risk of eroding through the aC film), for a total of twelve replicates. An initial exposure time of 10 minutes was observed for each change of the amorphous carbon film. The beam for this experiment was H_3O^+ sourced from a 400 W Ar/H_2O plasma and the current ranged from 5 to 13 μA, depending on the beamline transport voltage.

2.3 Secondary Negative Ion Energetics of Amorphous Carbon under O^+ Exposure

We begin with an investigation of secondary ion energetics for an amorphous carbon film under exposure to a hyperthermal O^+ beam. The dominant negative ion is O^-, which exits at relatively high kinetic energies (Figure 2-1). At E_0 = 194 eV, the O^- exit energy distribution peaks at 30 eV, with a tail reaching as high as 90 eV. The mean energy of O^- shows a relatively strong scaling with the beam energy (see Fig. 2-2), a memory of the incident energy which is more consistent with scattering or single knock-on processes than with the linear cascade model. Although our amorphous carbon film is nominally hydrogen-free, we observed a signal at mass 17 amu, which

is too strong (lower than ^{16}O by only 1−2 decades) to be attributed to ^{17}O ($^{17}O/^{16}O = 3.8\times10^{-4}$).[30] The 17 amu anion is most likely OH^-, due to flux of residual hydrogen in the scattering chamber. In this experiment, the flux of O^+ delivered by the beam is greater than the expected flux of residual H_2 by a factor of around ~90, based on residual gas analysis of the scattering chamber. It is unlikely that the hydrogen was incorporated at the time of deposition, given that the carbon flux would have exceeded the residual H_2 flux by at least some four orders of magnitude. In any case, the energy distribution for the HO^- product mirrors that of O^-, implying a mechanistic relation.

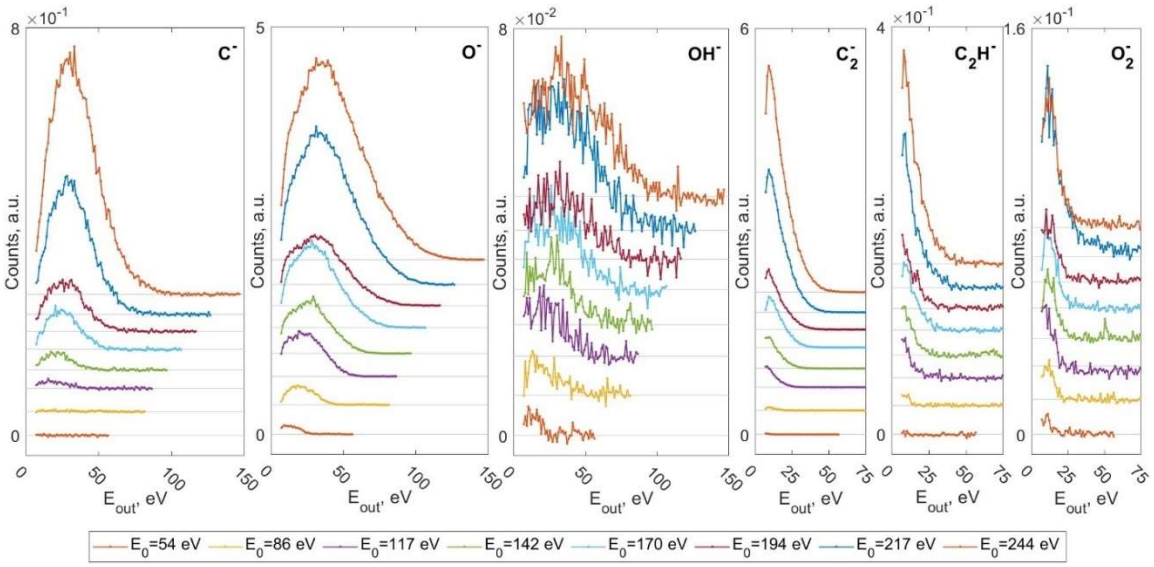

Figure 2-1. Staggered energy distribution for negative ion products emitted during O^+ bombardment of amorphous carbon. For readability, the signal baselines are staggered along the y-axis. Background counts (mean of last 5 data points) have been subtracted and each signal normalized to the beam current. For products with low signal intensity (OH^-), this makes a considerable difference in the readability of the figure.

The total scattering angle of our system cannot be satisfied by a single collision of the projectile with a surface atom due to the mass ratio being less than one. Scattered products must therefore be redirected through a series of at least two collisions. Due again to the mass ratio, even several consecutive collisions in an efficient geometry result in the loss of most of the projectile kinetic energy. Under BCA, for any lab-frame total scattering angle (θ_L), a series of collisions with identical scattering angles (e.g. three O−C collisions, each with $\theta=\theta_L/3$) effect the maximum preservation of the projectile KE. In a consecutive double collision with surface carbon atoms, an oxygen ion can scatter into the detector with at most 9% of its initial kinetic energy (for a 90° scattering angle). For

a triple collision, this fraction rises to 29% of E_0. The triple-collision is sufficient to account for most of the scattered O^-, but either higher-order scattering processes or double collisions involving implanted or chemisorbed oxygen are needed to account for higher exit energies. In the latter case, replacing a single carbon-atom collision partner with oxygen could raise the maximum exit energy for the double and triple scattering process to $0.18\times E_0$ and $0.34\times E_0$. At suitably high O surface coverages, the triple scattering process involving only O atoms becomes feasible and can produce exit energies as high as $0.42\times E_0$, still insufficient to account for the observed maximum exit energy of $0.53\times E_0$ (at 244 eV, see Fig. 2-2). Clearly, within the BCA framework, higher order scattering processes are required.

Although, it was not our objective to make a quantitative measurement of the total sputtering yield, it is valuable at this point to note that over the course several hours' beam exposure during this experiment we did completely erode the carbon film, exposing bare copper. This resulted in the eventual appearance of a well-defined peak in the O^- energy distribution near the expectation for scattering off single Cu atoms per BCA. There is no evidence for Cu exposure in the distributions shown in Figure 2-1, which were collected 30 minutes prior to the appearance of the Cu BCA peak. Based on our estimate of the aC film thickness and the integrated O^+ fluence, we loosely estimate that the average sputter yield during the experiment was ~2 C/O^+. This figure is quite comparable with sputtering of aC:H by 200 eV Ar^+ with coexposure to O_2.[31] Such a low sputtering yield would certainly allow for the accumulation of considerable O surface coverages, accounting for the observation of sputtered O_2 and potentially contributing to the high-energy tail of the O^- energy distribution.

The C^- product energy distribution is qualitatively similar to O^- and OH^-, but it neither peaks at nor tails to energies as high as the scattered products. The mean exit energy for this subpopulation also scales strongly with E_0, suggesting that the C^- ions are the products of single knock-on sputtering events (see Fig. 2-2). Exit energies as high as 30% of E_0 are observed. Transfer of kinetic energy in a head on-collision (impact parameter = 0) is very efficient for mass ratios near unity. For atomic oxygen colliding head-on with a carbon atom, 98% of the lab-frame kinetic energy is transferred to the carbon. Carbon atom ejection by the projectile after one or more redirecting collisions can thus produce secondary ions with energies comparable to scattered products. The C^- peak exit energy increases with the incident energy, reaching as high as 30 eV for C^- at E_0 = 244 eV.

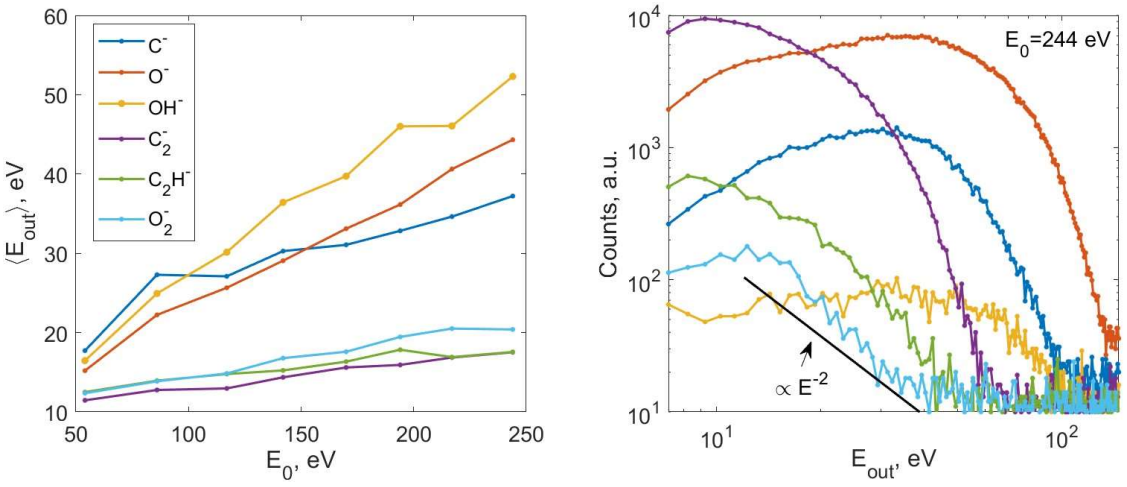

Fig. 2-2: Left) Mean energy for negative ion products vs the incident energy. Right) Energy distributions (*f*) for the same products at an incident energy of 244 eV. The solid black line depicts the E^{-2} behavior expected for a linear cascade.

In contrast, heavier molecular anions, C_2^-, C_2H^-, and O_2^- show energy distributions more typical of sputtering, with peak energies near or below the minimum scan energy. The measured energy distribution (*f*) for C_2 in particular shows a strong deviation from Thompson's result for the differential energy distribution *g*:

$$g(E,\phi) = \frac{C\cos\phi\left(1-\sqrt{(U+E)/E_{max}}\right)}{E^2(1+U/E)^3} \qquad 2\text{-}1$$

where U is the binding energy, C a normalization constant, ϕ the ejection angle, and E_{max} is the maximum recoil energy. In the BCA framework, E_{max} is proportional the incident energy E_0 with constant of proportionality related to the masses (M_1 and M_2) of the collision partners (projectile and surface atom):

$$E_{max} = E_0 4\, M_1M_2/(M_1+M_2)^2 \qquad 2\text{-}2$$

In the limit of $E_{max} \gg E \gg U$, Eq. 2-1 prescribes a sputtered flux proportional to E^{-2}. As the exit energy approaches the maximum reoil energy, the distribution is driven to zero by the factor of $1-\sqrt{(U+E)/E_{max}}$. This result is known to fail at low energies.[32] Zhou et al. (2005), for instance, observe in simulated sputtering of nickel by 600 eV Xe^+ ions a truncation of the energy distribution

around 40 eV, well below the 512 eV precited by linear cascade theory.[33] Zhou et al. proposed an empirical truncation (at energy E_u) of the linear cascade result by a factor of $1-(E/E_u)^4$, which captures our results adequately but unsatisfyingly.[33,34] We note that for O_2, no truncation is apparently necessary, but this is simply a consequence of the tail being overwhelmed by background counts. O_2 formation via an Eley-Rideal mechanism has been observed for many oxide surfaces experimentally[35,36] and in hyperthermal atomic oxygen bombardment of diamond surfaces in ReaxFF MD simulations.[37] The product energy distributions in this case provide no direct evidence to confirm an ER O_2 production mechanism, but could be consistent with formation and subsequent sputtering of peroxide or 1,2-dioxetane surface moieties, as seen in the ReaxFF simulations.[37]

Because we are observing secondary ions rather than secondary neutrals, the dynamics of resonant charge transfer can also cause a deviation from the Thompson result. For sputtered molecules, the charge state depends only on the exit trajectory and molecular/surface properties. If the deviations of the measured energy distribution from Eq. 2-1 are due exclusively to charge transfer dynamics, we should expect, then, that the deviation be independent of the impactor energy, neglecting any variation in the surface properties (binding energy U, work function). To assess whether this is the case, we will assume that the total sputtered flux obeys the Thompson energy distribution (g). The negative ion fraction P^- is related to the distributions g and f as $P^-(E)/\langle P^-\rangle = f(E)/g(E)$, where $\langle P^-\rangle = \int P^- g\, dE$. The results of this exercise are shown in Fig. 4.3-3.

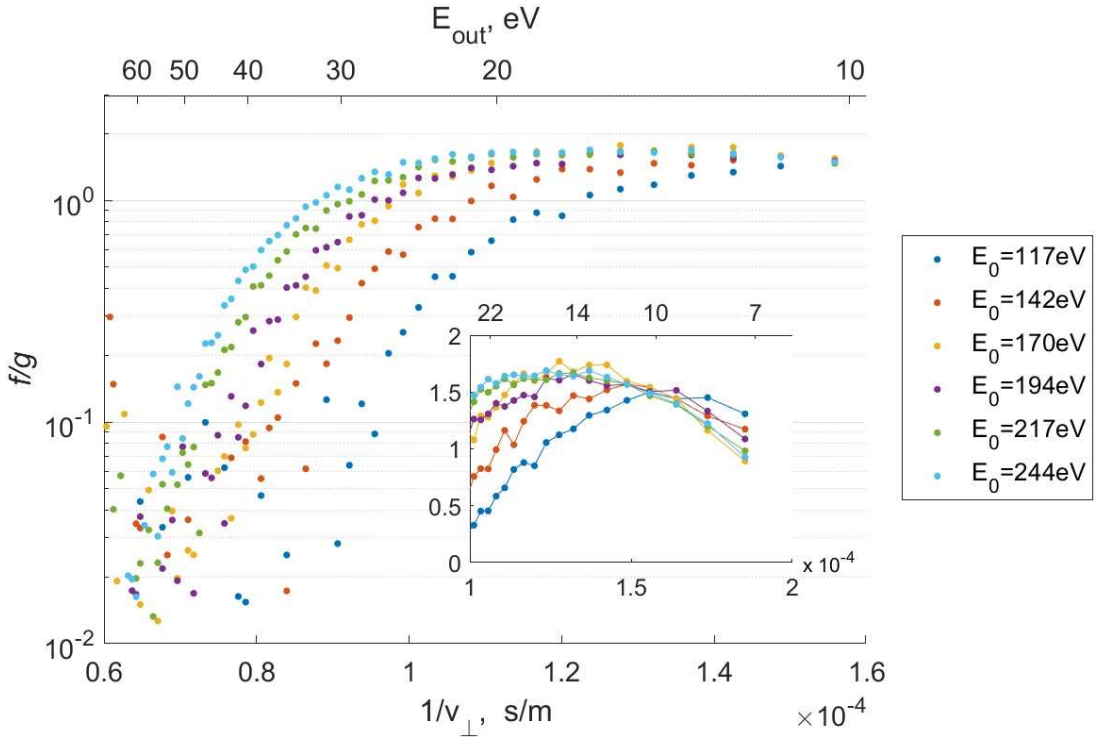

Fig. 2-3: Ratio of the measured C_2^- energy distribution to that of Thompson vs the inverse perpendicular exit velocity (bottom axis) for our 45° detection angle. We have taken U = 7 eV and M_2 = 24 amu. A nonlinear energy scale is provided on the top axis. The elevated points at the highest plotted energies are the noise floor enhanced by the falling value of $g(E_{out})$. The ordinate is equivalent to $P^-/\langle P^-\rangle$, where P^- is the negative ion fraction, if the total sputtered flux is described by g. The inset axis is a magnification of the low energy range, with the same axis definitions, showing the nonmonotonicity.

It is immediately apparent that the deviation is not constant with respect to the impactor energy, which implies that the total sputtered flux does not obey g. The deviation therefore is not due solely to charge transfer dynamics. At low energies, where the deviation of the actual energy distribution from Eq. 2-1 is expected to be small, the negative ion fraction is evidently nonmonotonic with respect to kinetic energy (see Fig. 2-3 inset) for reasonable choices of U (i.e. ~7 eV)[14]. This behavior has been observed in sputtering of C^- from graphite.[14] The nonmonotonicity is inconsistent with the neutralization of a frozen equilibrium ion distribution, and instead reflects kinetically limited charge transfer both above and below the crossing distance.[38] Given the magnitude of $v_\perp(\leq 1.7\times10^4$ m $s^{-1})$ relative to expected tunneling rates of order 10^{14} s^{-1},[38] this explanation is plausible.

At high sp^3/sp^2 hybridization ratios, amorphous carbon behaves as a semiconductor,[39] with a bandgap ~0.5 eV.[29,40] This results in a suppression of the tunneling rate while the image-shifted EA crosses the gap.[41] With the Fermi level at the bottom of this gap[29] and the sharpness of the Fermi function, the occupancy factors for the CB and VB are approximately 0 and 1, respectively. Ionization of C_2 can thus be conceptualized as occurring in two steps: 1) electron acquisition while the image-shifted EA is resonant with valence band states (below the crossing distance Z_c) and 2) neutralization at greater distances, where the EA is resonant with CB states (above Z_c). For an image-like shift in the EA, the crossing occurs where $E_f = E_a - 1/4Z_c$ (atomic units). For C_2 (EA 3.27 eV[42]), Z_c is 1.4 to 2.9 Å, depending on the degree of hybridization.

Since all sputtered C_2 originates from within the solid, negative ion formation is certainly expected. At low exit velocities and near the surface, the tunneling rate is large enough that the ion fractions attain equilibrium. At greater distance, the negative ion population decays into resonant CB states. As the velocity increases, the time for this decay is reduced, resulting in larger negative ion fractions, with an exponential dependence on the inverse velocity: $P^- \propto \exp(-a_1/v_\perp)$.[14] At large velocities, however, the negative ion fraction will become kinetically limited by residence time of C_2 below the crossing distance.[43] In this limit, neglecting neutralization above Z_c, the tunneling dynamics provide for an exponential dependence of the negative ion fraction on the inverse of the perpendicular velocity component: $1 - P^- \propto \exp(-a_2/v_\perp)$.[43] These exponential limits emerge from the semi-classical approximation (SCA) of charge transfer between an atom and a metallic substrate on the level of the so-called simple master equations (SME).[43,44] In the high energy limit, our data do evince an exponential decay, but since we lack a direct measurement of the sputtered energy distribution for all charge states ($\Phi(E)$), we cannot conclusively say whether this is due to deviation of Φ from *g,* due to charge transfer kinetics, or both.

Finally, we note that the features discussed above are not artifacts of surface roughness. Scattering of O^+ on highly oriented pyrolytic graphite (HOPG) shows qualitatively similar behavior for the scattered O^- and sputtered C_2^- (Figure 2-4). The main difference is the appearance of high energy scattering peak at E_0<143 eV. Although the high degree of surface uniformity makes HOPG an appealing substrate for scattering studies, due to its higher work function and lower surface density, the scattering signal is relatively poor. It is thus less facile and less relevant (to our application) than amorphous carbon.

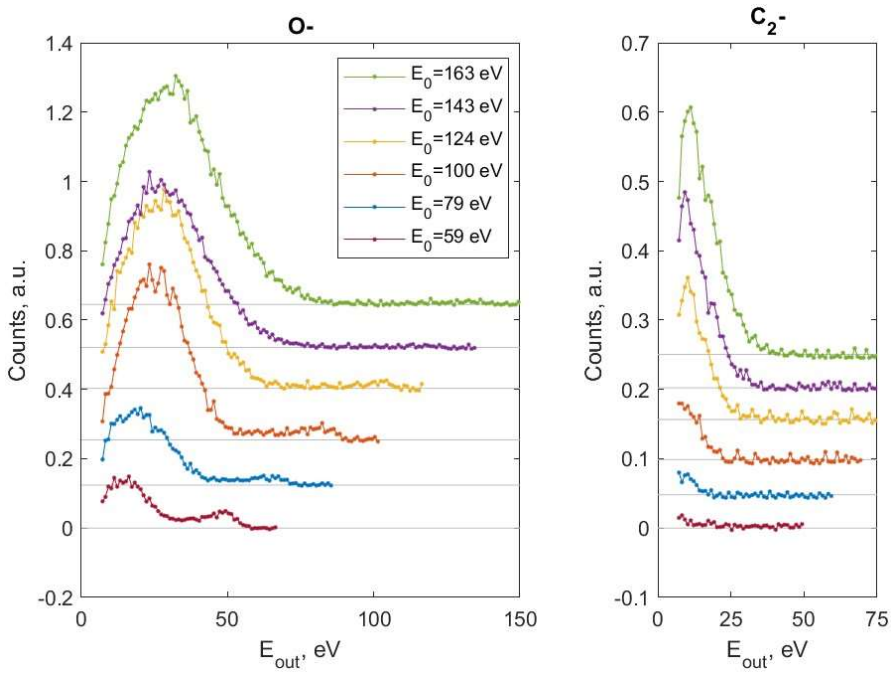

Figure 2-4: Staggered energy distribution for negative ion products emitted during O^+ bombardment of HOPG. For readability, the signal baselines are staggered along the y-axis. Background counts (mean of last 5 data points) have been subtracted and each signal normalized to the beam current.

2.4 Secondary Positive Ion Energetics of Amorphous Carbon under O+ Exposure

We detect several species as positive secondary ions, among them CO^+, HCO^+, and CO_2^+ (Figure 2-5). Notably, O^+ could not be resolved among the positive ions. The 39 amu species can be attributed to either C_3H_3 or NaO since Na^+ was also detected as a surface or detector contaminant. The C_3H_3 identification seems more likely, given that we were able to detect the corresponding anion at abundances comparable to O_2^-, which would be quite unexpected for a minor surface impurity with similar EA (0.45 eV[45]) but very plausible for the 1-propynyl radical (EA of 2.74[46]). Additionally, a rather strong signal (comparable intensity to CO^+) is seen at 56 amu. There are several possibilities for oxocarbon or hydrocarbon species massing 56 amu (e.g. butene, propenal, propargyl alcohol, cyclobutane, ethylene dione), so conclusive identification was not possible. Repeated attempts to detect the corresponding 56 amu anion failed. Given that our amorphous carbon target is nominally hydrogen free, the notoriously elusive ethylene dione (OCCO) is a particularly interesting possibility.[47]

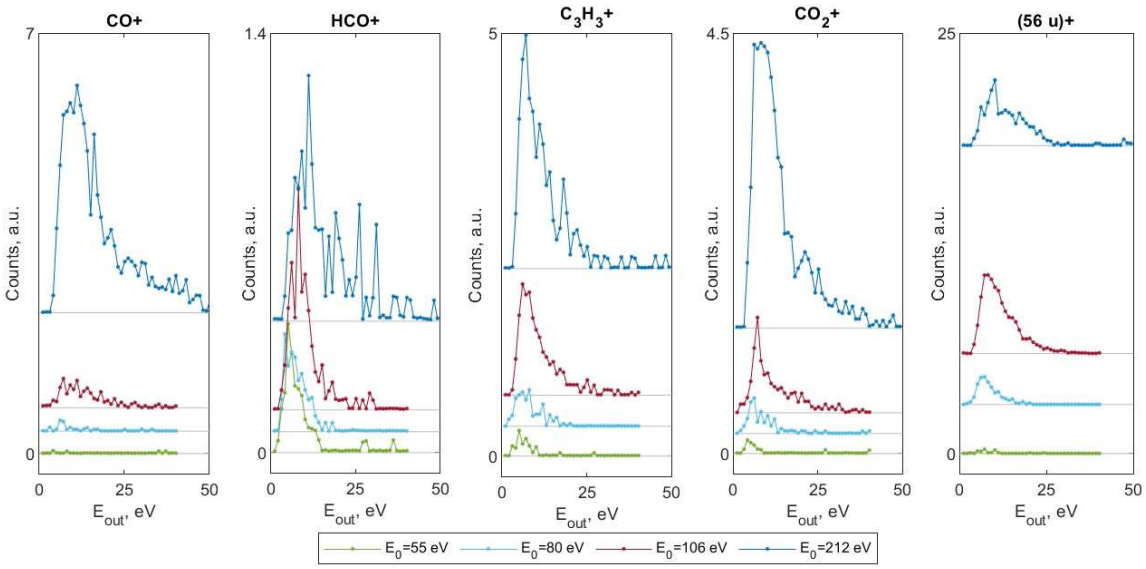

Figure 2-5: Staggered energy distributions for the most abundant positive ion products emitted during O^+ bombardment of amorphous carbon with baselines staggered. The E_0 = 212 eV scan for $(56\ u)^+$ was conducted at a higher mass resolution than the other $(56\ u)^+$. To improve readability, that trace has been scaled by a factor of two. Otherwise, all scans for a given species were conducted at the same resolution and the signal normalized by the integration time and beam current.

In contrast to the negative ions, the positive ion energy distributions do not lend themselves to any obvious typology, possibly due to the poorer dynamic range, which makes interrogation of the high-energy tails impossible. At E_0 = 212 eV, where the SNR is highest, the CO^+ energy distribution appears to show more weight in the tail than $C_3H_3^+$, perhaps indicating a different formation mechanism (an ER abstraction reaction?). Some evidence for an ER formation mechanism has indeed been reported,[13] but the reaction is nearly kinematically ambiguous with single-knockon sputtering processes, making it difficult prove a mechanism.[1]

2.4 Relative Yields of Negative Ions: Graphite vs Amorphous Carbon

To be of relevance to astrophysical environments, we must address two further degrees of freedom in the scattering system. One is the chemical and physical structure of the surface, namely the sp^2/sp^3 hybridization ratio and the roughness. We have already seen that sputtering/scattering of negative ions is sustained for HOPG. Now, we will contrast negative ion emission from amorphous carbon with that of a rough graphite surface. The second consideration is the degree of

[1] We ourselves have observed the ER abstraction reaction in Reactive MD simulations of atomic oxygen impacting amorphous carbon at 33 eV and may elaborate on it in future work.

hydrogenation of our projectile. Oxygen ions are present in several solar system environments, where they are often derived from water molecules. The corotating plasma of Saturn's magnetosphere comprises the whole array of water group ions (O^+, HO^+, H_2O^+, H_3O^+), in roughly equal abundance.[48] H_3O^+ becomes relatively important in denser plasma environments, like the plume of Enceladus or cometary comae.[49,50] To bracket the full range of projectile oxidations states, we will provide scattering results for an H_3O^+ beam in this section.

In contrast to the O^+ beam results, for H_3O^+ bombardment hydrogenated secondary ions OH^-, CH^-, and C_2H^- appear at abundances comparable O^-, C^-, and C_2^- (Figure 2-6). In light of its lower EA (see Table 2-1), the preference for O^- scattering relative to OH^- reflects a high probability for complete collision induced dissociation of the projectile at the 113 eV impact energy. The abundance of hydrogenated secondary testifies to the effective delivery of hydrogen from the projectile to the surface. Chemisorption of hydrogen at unsaturated carbon atoms results in C−C bond rupture and reduces the binding energy of the carbon fragments, making them more susceptible to sputtering.[51–53] The abundance of CH^- relative to C^- is particularly telling, since the EA of formation, which governs the exiting ion fraction, is virtually identical for these anions.[54,55] Supposing that these species are sputtered from vinylidene or vinyl radical surface groups, the difference in binding energy (i.e. the C=C BDE) is very small (~0.1 eV).[56] The difference in abundance, then, suggests a surface stoichiometry on the order of 1 H/C.

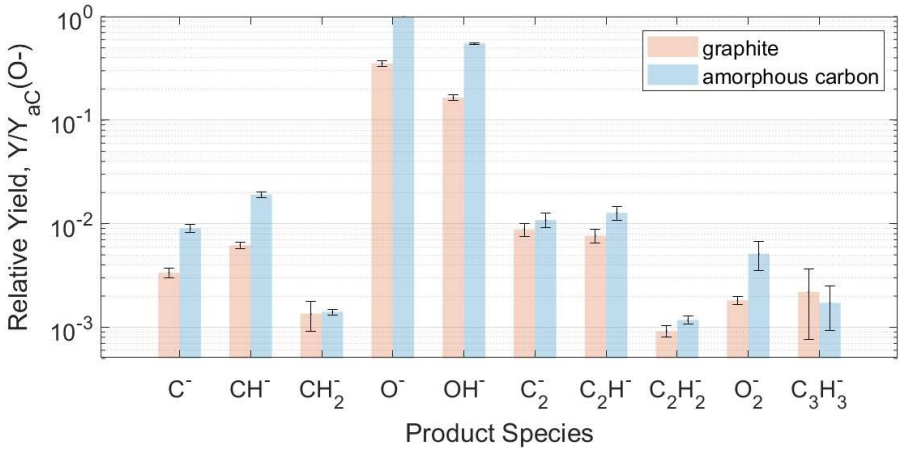

Figure 2-6: Relative yields of secondary negative ions from a graphite target and an amorphous carbon target under H_3O^+ bombardment at 113 eV. The yields are normalized to the O^- signal from amorphous carbon. The yields before normalization are integrated over the product energy range 6 eV to 56 eV. Error bars represent standard error across 12 technical replicates.

Compared to the graphite target, amorphous carbon target shows significantly higher yields of the main secondary negative ions, which is expected given the lower density and higher work function.[29] The graphite target has a porosity of 28−30% to which some of the deficit can be attributed. Assuming no secondary ions reach our detector from the surface voids, the differences in intrinsic yields between the two surfaces are mitigated, although for C^-, CH^-, O^-, OH^-, and O_2^- they remain significant. After accounting for the surface porosities, the yields of the diatomic fragments C_2^- and C_2H^- are not significantly different across the two surfaces, whereas sputtering C^- and CH^- is disfavored for graphite. A preference for even numbered carbon fragments (C_n, n even and <9) is typical of sputtering from graphite and amorphous carbon surfaces, a consequence of the larger EA for these fragments (see Table 2-1).[17,18]

As concerns the surface bonding topology, impact induced amorphization and implantation/chemisorption of oxygen and hydrogen are likely to overwrite much of the bulk hybridization, resulting in a convergent surface morphology. MD simulations of low-energy (500 eV) ion bombardment of carbon surfaces reported by Tran & Chew (2023) demonstrate that the surface hybridization ratio converges (after a dose of $\sim 1\times10^{15}$ cm^{-2}) to the same saturation value whether the target surface is diamond or multi-layer graphene.[57] It is therefore unlikely that the difference in secondary ion emission between graphite and amorphous carbon is due to a difference in the surface binding energy.

Table 2-1. Electron affinities of selected species

Species	EA, eV	Reference
C	1.26	Scheer et al. 1998[54]
CH	1.26	Goebbert 2012[55]
CH_2	0.65	Leopold et al. 1985[58]
O	1.44	Joiner et al. 2011[59]
OH	1.83	Celotta et al. 1973[60]
C_2	3.27	Arnold et al. 1991[42]
C_2H	2.94	Janousek et al. 1979[61]
C_2H_2 (vinylidene)	0.49	Ervin et al. 1989[62]
O_2	0.45	Ervin et al. 2003[63]
C_3H_3 (1-propynyl radical)	2.74	Zhou et al. 2007[46]
C_3H_3 (propargyl radical)	0.92	Robinson et al. 1995[64]
C_3	2.00	Arnold et al. 1991[42]
HCO (formyl radical)	0.31	Murray et al. 1986[65]
OC_3H_4 (oxyallyl radical)	1.94	Ichino et al. 2011[66]
C_2O_2	1.94	Dixon et al. 2015[47]

2.5 Discussion

As introduced in Chapter 1, these experiments have been motivated specifically by the observation of surface-originating negative pick-up ions at Saturn's moons Dione and Rhea,[7,8] where a refractory carbonaceous lag layer has been invoked to explain unexpectedly low exospheric source rates.[6] At Rhea, the negative PUIs signals detected by the *Cassini* CAPS instrument during the R1 flyby encounter were initially identified with O^- and later with a species massing 26±3 amu.[7,67] Desai et al. (2018) offer CN^-, C_2H^-, C_2^-, or HCO^- as candidates on the basis of their electron affinities and the notion of a carbonaceous surface-darkening agent. They also comment that the signal could be consistent instead with accelerated or reflected O^- ions. [7] Our limited results for carbon scattering certainly do not resolve the ambiguity. They do, however, lend more credence to the second explanation, which was disfavored, in part, due to the implausibility of O^- primary ions in the corotating plasma. Our experiments demonstrate that reversal of the impactor polarity is efficient (compared to negative ionization of sputtered molecules) for O^+ scattering on carbon, and, furthermore, that resulting O^- ions scatter with a relatively large portion of their initial kinetic energy (up to ∼50%). Near threshold sputtering processes similarly can eject C^- ions with considerable excess kinetic energies.

At Dione, a negative PUI signal appeared during Cassini's crossing of the plasma wake (D2 flyby), which Nordheim et al. (2020) found consistent with O^-.[8] Here, the signal spans a wide range of kinetic energies (400–1000 eV), which the authors attribute to a spread of gyrophases or, possibly, PUIs masses.[8] An alternative explanation is that the spread in PUI energy is due to the sputtering or scattering energy distribution. As an illustration of this point, we provide some PUI trajectories (Figure 2-7), computed as in Nordheim et al. (2020), except with a nonzero starting velocity in the Dione frame. An O^- ion leaving the surface with 10 eV of kinetic energy and initial velocity directly opposed to corotation, has a peak KE ∼150 eV greater than the same ion with zero initial KE. For ions ejected along other bearings, the maximum appearance energy is reduced (relative to $\theta = 180^\circ$) and the PUI trajectory deviates substantially from the zero KE case.

Although the Dione and Rhea PUI detections are apparently consistent with a surface-mediated process, the precise origin has not been resolved due to the limitations of CAPS. Gas phase processes seem, at least at Rhea, to be insufficient to account for the negative PUI abundance.[6,68] But, the CAPS data themselves have not allowed for differentiation between a surface process and a near-surface process (i.e. in the exosphere).[8] Surface originating ions will almost certainly have considerable excess kinetic energy before pick-up, if not intrinsic to the ejection mechanism (i.e.

sputter, scatter, and ESD to a lesser extent), then due to surface charging, which at Dione (Rhea) can reach -40 V (-90 V).[69] In contrast, negative ions formed in the exosphere will have lower excess energy at formation (see e.g. Illenberger 1981)[70] and will not be accelerated by the surface potential, so long as they form at altitudes greater than several Debye lengths (Rhea: $\lambda_D = 12$ m, Dione: $\lambda_D = 3$ m)[69]. The spatial and energetic dispersion of negative PUIs may thus provide insight into their formation mechanism, at least where other fields (i.e. the ambipolar wake field) do not interfere.

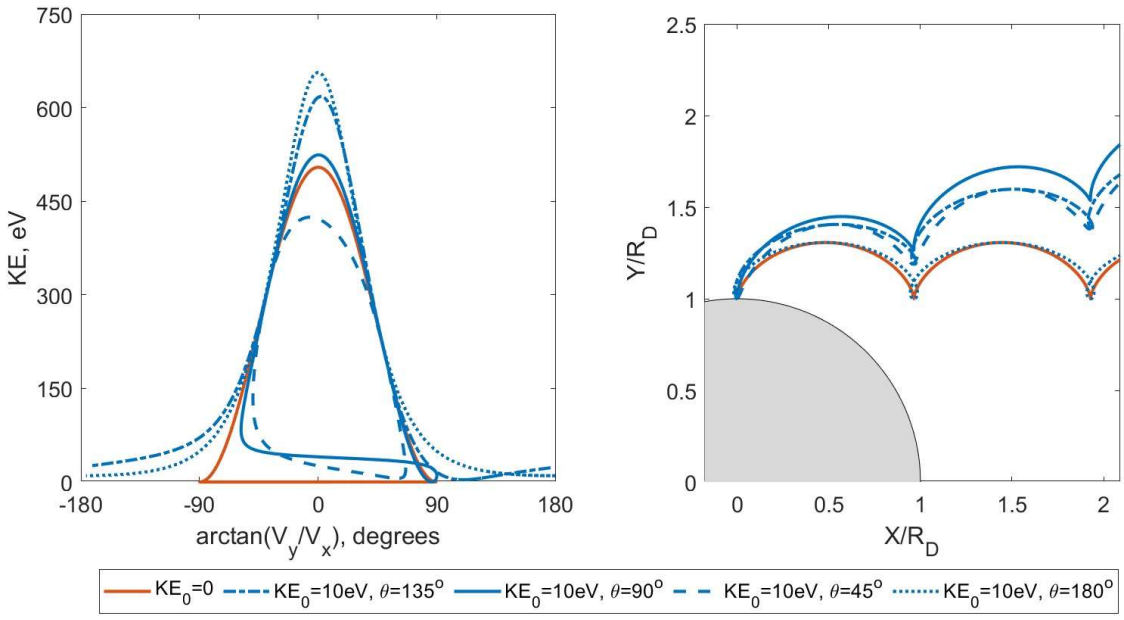

Figure 2-7: Negative PUI trajectories and energies at Dione. Right) Negative PUI trajectories (16 amu) in the Dione rest frame subject to different initial starting energies (KE_0) and launch directions (θ) relative to the x-axis. Corotation is in the +X direction and Saturn is in the +Y direction. The launch vector is in the XY plane. Left) PUI kinetic energy in the Dione rest frame versus the PUI instantaneous bearing in the XY plane (relative to +X). For $\theta = 180^o$, the launch velocity is directly opposed to corotation.

2.6 Conclusion

We have conducted measurements of secondary ion emission for a scattering system of astrophysical relevance, carbonaceous surfaces exposed to hyperthermal water group ions. These impact energies (50 to 250 eV) are in the near threshold sputtering regime, where atomic/molecular ejection is only feasible for a small set of well-defined collision sequences. The product energy distributions consequently show significant deviations from the linear cascade theory. Specifically, the dominant (under O^+ bombardment) sputtered product C_2^- displays a sharp truncation of the exit energy at 10s of eV, well below the constraint posed the maximum recoil energy. We show that this

truncation is not exclusively due to charge transfer dynamics, but instead reflects an actual failure to eject energetic products. The C^- product energetics are more similar to scattered O^- than to sputtered C_2^-, with the mode of the exit energy distribution falling at relatively high KE and the mean exit energy scaling strongly with E_0. Regardless of the surface hybridization (graphite vs amorphous carbon) and the projectile hydrogenation (O^+ vs H_3O^+) the predominating negative ion product is energetic O^-. Our results do not disambiguate the identity of negative PUIs observed near Dione and Rhea but do lend more credibility to the notion of O^- PUIs with high kinetic energy. We note, however, that excess KE at formation will produce a different spatial and energetic dispersion of PUIs downstream of the source (i.e. as seen by the spacecraft).

2.6 References

1. Clark, R. N. *et al.* Compositional mapping of Saturn's satellite Dione with Cassini VIMS and implications of dark material in the Saturn system. *Icarus* **193**, 372–386 (2008).
2. Clark, R. N. *et al.* The surface composition of Iapetus: Mapping results from Cassini VIMS. *Icarus* **218**, 831–860 (2012).
3. Clark, R. N. *et al.* Compositional maps of Saturn's moon Phoebe from imaging spectroscopy. *Nature* **435**, 66–69 (2005).
4. Dalle Ore, C. M., Cruikshank, D. P. & Clark, R. N. Infrared spectroscopic characterization of the low-albedo materials on Iapetus. *Icarus* **221**, 735–743 (2012).
5. Dalton, J. B., Cruikshank, D. P. & Clark, R. N. Compositional analysis of Hyperion with the Cassini Visual and Infrared Mapping Spectrometer. *Icarus* **220**, 752–776 (2012).
6. Teolis, B. D. & Waite, J. H. Dione and Rhea seasonal exospheres revealed by Cassini CAPS and INMS. *Icarus* **272**, 277–289 (2016).
7. Desai, R. T. *et al.* Cassini CAPS Identification of Pickup Ion Compositions at Rhea: Pickup Ions at Rhea. *Geophys. Res. Lett.* **45**, 1704–1712 (2018).
8. Nordheim, T. A. *et al.* Detection of Negative Pickup Ions at Saturn's Moon Dione. *Geophys. Res. Lett.* **47**, e2020GL087543 (2020).
9. Desai, R. T., Zhang, Z., Wu, X. & Lue, C. Photodetachment and Test-particle Simulation Constraints on Negative Ions in Solar System Plasmas. *Planet. Sci. J.* **2**, 99 (2021).
10. Millar, T. J., Walsh, C. & Field, T. A. Negative Ions in Space. *Chem. Rev.* **117**, 1765–1795 (2017).
11. Minton, T. K. & Garton, D. J. Dynamics of atomic-oxygen-induced polymer degradation in low earth orbit. in *Chemical Dynamics in Extreme Environments* vol. Volume 11 420–489 (WORLD SCIENTIFIC, 2001).
12. Leger, L. J. Oxygen Atom Reaction with Shuttle Materials at Orbital Altitudes. *NASA Tech. Memo.* (1982).
13. Minton, T. K., Nelson, C. M., Brinza, D. E. & Liang, R. H. *Inelastic and Reactive Scattering of Hyperthermal Atomic Oxygen from Amorphous Carbon*. https://ntrs.nasa.gov/citations/19920004547 (1991).

14. Silva, J. A. M. C., Henriques, C. M. R., Teodoro, O. M. N. D. & Moutinho, A. M. C. The negative ionization of sputtered carbon atoms. *Appl. Surf. Sci.* **144–145**, 208–211 (1999).
15. Lienemann, J. *et al.* Negative ion formation during scattering of fast ions from diamond-like carbon surfaces. *Nucl. Instrum. Methods Phys. Res. Sect. B Beam Interact. Mater. At.* **269**, 915–918 (2011).
16. Guo, X. *et al.* Unexpected Negative-Ion Conversion in Grazing Scattering of Negative Ions on HOPG. *J. Phys. Chem. C* **125**, 13997–14005 (2021).
17. Schauer, S. N., Williams, P. & Compton, R. N. Production of small doubly charged negative carbon cluster ions by sputtering. *Phys. Rev. Lett.* **65**, 625–628 (1990).
18. Iyer, I. S., Mehta, R., Kanjilal, D. & Roy, A. Sputter emission of negatively charged carbon clusters. *Radiat. Eff. Defects Solids* **138**, 145–152 (1996).
19. Gnaser, H. Singly- and doubly-negative carbon clusters in sputtering: Energy spectra, abundance distributions and unimolecular fragmentation. *Nucl. Instrum. Methods Phys. Res. Sect. B Beam Interact. Mater. At.* **149**, 38–52 (1999).
20. Gnaser, H., Dreuw, A. & Cederbaum, L. S. Discovery of a new class of stable gas-phase dianions: Mixed oxygen–carbon cluster OC_n^{2-} (n=5–19). *J. Chem. Phys.* **117**, 7002–7009 (2002).
21. Gnaser, H. Ionization probability of sputtered negative cluster ions: Dependence on surface work function and emission velocity. *Phys. Rev. B* **63**, 045415 (2001).
22. Matsunaga, T., Yoshikawa, S. & Tsukamoto, K. Secondary ion yields of C, Si, and Ge in InP, and Cs surface density and concentration, in SIMS. *Surf. Sci.* **515**, 390–402 (2002).
23. Gnaser, H. Formation of molecular doubly charged anions in sputtering. *Nucl. Instrum. Methods Phys. Res. Sect. B Beam Interact. Mater. At.* **212**, 407–413 (2003).
24. Gnaser, H. Negative cluster ions in sputtering of Si, SiC and graphite: Abundance distributions, energy spectra and fragmentation processes. *Nucl. Instrum. Methods Phys. Res. Sect. B Beam Interact. Mater. At.* **164–165**, 705–714 (2000).
25. Deng, Z. W. & Souda, R. A SIMS study on positive and negative ions sputtered from graphite by mass-separated low energy Ne^+, N_2^+ and N^+ ions. *Nucl. Instrum. Methods Phys. Res. Sect. B Beam Interact. Mater. At.* **183**, 260–270 (2001).
26. Deng, Z. W. & Souda, R. Eley-Rideal abstraction of carbon from graphite by hyperthermal N^+ ions. *J. Chem. Phys.* **117**, 6235–6238 (2002).
27. Deng, Z.-W. & Souda, R. Dynamics of CN^- ion emission during hyperthermal N_2^+ion irradiation of graphite. *Phys. Rev. B* **65**, 144108 (2002).
28. Zhou, X. *et al.* Structural analysis of amorphous carbon films by spectroscopic ellipsometry, RBS/ERDA, and NEXAFS. *Appl. Phys. Lett.* **110**, 201902 (2017).
29. Liu, L., Lu, F., Tian, J., Xia, S. & Diao, Y. Electronic and optical properties of amorphous carbon with different sp3/sp2 hybridization ratio. *Appl. Phys. A* **125**, 366 (2019).
30. Berglund, M. & Wieser, M. E. Isotopic compositions of the elements 2009 (IUPAC Technical Report). *Pure Appl. Chem.* **83**, 397–410 (2011).
31. Hopf, C., Schlüter, M., Schwarz-Selinger, T., Von Toussaint, U. & Jacob, W. Chemical sputtering of carbon films by simultaneous irradiation with argon ions and molecular oxygen. *New J. Phys.* **10**, 093022 (2008).

32. Gnaser, H. Chapter 2: Interaction of Low-Engery Ions with Solids. in *Low-energy ion irradiation of solid surfaces* 7–83 (Springer, Berlin ; New York, 1999).
33. Zhou, X. W., Wadley, H. N. G. & Sainathan, S. Low energy sputtering of nickel by normally incident xenon ions. *Nucl. Instrum. Methods Phys. Res. Sect. B Beam Interact. Mater. At.* **234**, 441–457 (2005).
34. Thompson, M. W. Atomic collision cascades in solids. *Vacuum* **66**, 99–114 (2002).
35. Yao, Y. & Giapis, K. P. Dynamic molecular oxygen production in cometary comae. *Nat. Commun.* **8**, 15298 (2017).
36. Yao, Y. & Giapis, K. P. Reply to "On the origin of molecular oxygen in cometary comae". *Nat. Commun.* **9**, 2581 (2018).
37. Goverapet Srinivasan, S. & van Duin, A. C. T. Direction dependent etching of diamond surfaces by hyperthermal atomic oxygen: A ReaxFF based molecular dynamics study. *Carbon* **82**, 314–326 (2015).
38. Xiong, F. *et al.* Dynamical resonant charge transfer of fast C−, O−, F− ions and water covered Si(111) surface. *Vacuum* **137**, 23–30 (2017).
39. Stephan, U., Frauenheim, Th., Blaudeck, P. & Jungnickel, G. π bonding versus electronic-defect generation: An examination of band-gap properties in amorphous carbon. *Phys. Rev. B* **50**, 1489–1501 (1994).
40. Robertson, J. & O'Reilly, E. P. Electronic and atomic structure of amorphous carbon. *Phys. Rev. B* **35**, 2946–2957 (1987).
41. Borisov, A. G., Kazansky, A. K. & Gauyacq, J. P. Finite Time Effect in the Charge Transfer Process during an Ion-Metal Surface Collision. *Phys. Rev. Lett.* **80**, 1996–1999 (1998).
42. Arnold, D. W., Bradforth, S. E., Kitsopoulos, T. N. & Neumark, D. M. Vibrationally resolved spectra of C2–C11 by anion photoelectron spectroscopy. *J. Chem. Phys.* **95**, 8753–8764 (1991).
43. Shao, H., Langreth, D. & Nordlander, P. Chapter 3 Theoretical Description of Charge Transfer in Atom-Surface Collisions. in *Low energy ion-surface interactions* (ed. Rabalais, J. W.) 118–186 (J. Wiley & sons, Chichester New York Brisbane [etc.], 1994).
44. Nordlander, P., Shao, H. & Langreth, D. C. Intra-atomic correlation effects in charge transfer. *Nucl. Instrum. Methods Phys. Res. Sect. B Beam Interact. Mater. At.* **78**, 11–19 (1993).
45. Bauschlicher, C. W., Partridge, H. & Pettersson, L. G. M. Franck–Condon factors for photodetachment from LiO−, NaO−, and KO−. *J. Chem. Phys.* **99**, 3654–3658 (1993).
46. Zhou, J., Garand, E., Eisfeld, W. & Neumark, D. M. Slow electron velocity-map imaging spectroscopy of the 1-propynyl radical. *J. Chem. Phys.* **127**, 034304 (2007).
47. Dixon, A. R., Xue, T. & Sanov, A. Spectroscopy of Ethylenedione. *Angew. Chem. Int. Ed.* **54**, 8764–8767 (2015).
48. Young, D. T. *et al.* Composition and Dynamics of Plasma in Saturn's Magnetosphere. *Science* **307**, 1262–1266 (2005).
49. Fuselier, S. A. *et al.* Ion chemistry in the coma of comet 67P near perihelion. *Mon. Not. R. Astron. Soc.* **462**, S67–S77 (2016).
50. Cravens, T. E. *et al.* Plume ionosphere of Enceladus as seen by the Cassini ion and neutral mass spectrometer. *Geophys. Res. Lett.* **36**, (2009).

51. Salonen, E., Nordlund, K., Keinonen, J. & Wu, C. H. Swift chemical sputtering of amorphous hydrogenated carbon. *Phys. Rev. B* **63**, 195415 (2001).
52. Zhang, Y., Zhang, D., Zhang, L., Yang, B. & Gan, Z. The Etching Mechanisms of Diamond, Graphite, and Amorphous Carbon by Hydrogen Plasma: A Reactive Molecular Dynamics Study. *Adv. Theory Simul.* **6**, 2300371 (2023).
53. Aussems, D. U. B., Bal, K. M., Morgan, T. W., Van De Sanden, M. C. M. & Neyts, E. C. Atomistic simulations of graphite etching at realistic time scales. *Chem. Sci.* **8**, 7160–7168 (2017).
54. Scheer, M., Bilodeau, R. C., Brodie, C. A. & Haugen, H. K. Systematic study of the stable states of C^-, Si^-, Ge^-, and Sn^- via infrared laser spectroscopy. *Phys. Rev. A* **58**, 2844–2856 (1998).
55. Goebbert, D. J. Photoelectron imaging of CH−. *Chem. Phys. Lett.* **551**, 19–25 (2012).
56. Blanksby, S. J. & Ellison, G. B. Bond Dissociation Energies of Organic Molecules. *Acc. Chem. Res.* **36**, 255–263 (2003).
57. Tran, H. & Chew, H. B. Surface morphology and carbon structure effects on sputtering: Bridging scales between molecular dynamics simulations and experiments. *Carbon* **205**, 180–193 (2023).
58. Leopold, D. G., Murray, K. K., Miller, A. E. S. & Lineberger, W. C. Methylene: A study of the $\tilde{X}\ ^3B_1$ and $\tilde{a}\ ^1A_1$ states by photoelectron spectroscopy of CH_2^- and CD_2^-. *J. Chem. Phys.* **83**, 4849–4865 (1985).
59. Joiner, A., Mohr, R. H. & Yukich, J. N. High-resolution photodetachment spectroscopy from the lowest threshold of O^-. *Phys. Rev. A* **83**, 035401 (2011).
60. Celotta, R. J., Bennett, R. A. & Hall, J. L. Laser photodetachment determination of the electron affinities of OH, NH2, NH, SO2, and S2. *J. Chem. Phys.* **60**, 1740–1745 (1974).
61. Janousek, B. K., Brauman, J. I. & Simons, J. An experimental and theoretical determination of the electron affinity of the ethynyl radical, HC2·. *J. Chem. Phys.* **71**, 2057–2061 (1979).
62. Ervin, K. M., Ho, J. & Lineberger, W. C. A study of the singlet and triplet states of vinylidene by photoelectron spectroscopy of H2C=C−, D2C=C−, and HDC=C−. Vinylidene–acetylene isomerization. *J. Chem. Phys.* **91**, 5974–5992 (1989).
63. Ervin, K. M., Anusiewicz, I., Skurski, P., Simons, J. & Lineberger, W. C. The Only Stable State of O2- Is the X 2Πg Ground State and It (Still!) Has an Adiabatic Electron Detachment Energy of 0.45 eV. *J. Phys. Chem. A* **107**, 8521–8529 (2003).
64. Robinson, M. S., Polak, M. L., Bierbaum, V. M., DePuy, C. H. & Lineberger, W. C. Experimental Studies of Allene, Methylacetylene, and the Propargyl Radical: Bond Dissociation Energies, Gas-Phase Acidities, and Ion-Molecule Chemistry. *J. Am. Chem. Soc.* **117**, 6766–6778 (1995).
65. Murray, K. K., Miller, T. M., Leopold, D. G. & Lineberger, W. C. Laser photoelectron spectroscopy of the formyl anion. *J. Chem. Phys.* **84**, 2520–2525 (1986).
66. Ichino, T. *et al.* Photoelectron Spectroscopic Study of the Oxyallyl Diradical. *J. Phys. Chem. A* **115**, 1634–1649 (2011).
67. Teolis, B. D. *et al.* Cassini Finds an Oxygen-Carbon Dioxide Atmosphere at Saturn's Icy Moon Rhea. *Science* **330**, 1813–1815 (2010).

68. Itikawa, Y. Cross Sections for Electron Collisions with Oxygen Molecules. *J. Phys. Chem. Ref. Data* **38**, 1–20 (2009).
69. Roussos, E., Krupp, N., Krüger, H. & Jones, G. H. Surface charging of Saturn's plasma-absorbing moons. *J. Geophys. Res. Space Phys.* **115**, (2010).
70. Illenberger, E. Measurement of the translational excess energy in dissociative electron attachment processes. *Chem. Phys. Lett.* **80**, 153–158 (1981).

Chapter 3

SCATTERING OF WATER GROUP IONS FROM CHLORIDE SALTS

3.1 Introduction

In contrast to the relative pristine icy bodies of the Saturn system, Jupiter's moon Europa has abundant non-ice material on its surface. Spectroscopic ambiguities have stymied many efforts to definitively identify this material, but on the basis of measurements by *Galileo's* Near-infrared Mapping Spectrometer (NIMS) sulfate salts have been suggested.[1] More recently, ground-based observations have provided evidence in favor of sodium chloride, potentially brine from an NaCl dominated ocean.[2] Surface chlorides would be consistent with the presence of Cl^- pick-up ions inferred from cyclotron waves near Europa.[3,4] Since many postulated surface species are difficult to distinguish by existing and currently planned remote sensing spectrometers, and upcoming missions to Europa (*Juice* and *Europa Clipper*) do not involve landers, determination of the surface composition will rely in large part on the gas and ion abundances measured from orbit. As we have seen in the previous chapter, there is reason to believe that the low-energy plasma–surface interaction can produce negative pick-up ions (PUIs) detectable by spacecraft. But in order to relate remote PUI observations to the surface composition, one must understand how hyperthermal impactors modify the surface composition and translate it into the plasma phase. For this reason, we undertake an experimental study of two chloride surfaces (AgCl and NaCl), with emphasis on reactive scattering and the emission of secondary negative ions.

Ionic crystals are particularly recalcitrant targets for scattering studies on account of their low conductivities.[5] The problem of surface charging is especially acute for experiments at hyperthermal energies, where mild surface potentials can cause deviations in the impactor trajectory and distortions of the product energy distribution.[5] Still, several studies have reported on sputtering of ionic crystals, overwhelmingly with primary ion energies >1 keV. Early work (neatly summarized in Postawa (1994)[6]) showed that sputtering by heavy ions produces predominately thermal neutrals, with a secondary population of mostly atomic species ejected by the collision cascade.[6,7] Ions are also emitted in a collision cascade, with energy distributions typical of sputtering from metals (exhibiting the E^{-2} power-law tail).[8] Later studies have focused on the phenomenon of potential sputtering, in which multiply charged ions are rapidly neutralized, creating holes in the surface valence band that then decay, resulting in emission of neutrals.[9–13]

These studies concern themselves chiefly with quantitatively capturing the depended of sputter yield on charge state.[14] Research on high-angle scattering/sputtering of these surface apparently stalls in the early 2000s, although grazing-incidence investigations of charge transfer mechanisms continue.[15,16] The scattering of atomic oxygen on LiF has been studied for these purposes, at grazing incidence and at kinetics energy of 10 keV.[17] As for the hyperthermal reactive ion bombardment of salts relevant to astrophysical systems, to our knowledge, there is no published work.

3.2 Methods

3.2.1 Target preparation

The silver chloride target discussed in §3.3 was prepared by anodization of a 0.01" thick silver foil from (5N, ESPI metals). Prior to anodization, the foil was cleaned sonication in DI water and in acetone and then rinsed with ethanol. The foil was then electroreduced at −1 V against a graphite counter electrode in sodium chloride (0.1 M) solution for twenty minutes. The foil was then anodized for 10 minutes at 0.5 V, subsequently rinsed with copious DI water and dried for 15 minutes in air at 200 ºC. Test samples prepared in this way showed the anticipated reactivity toward aluminum foil. The anodized scattering target sample was immediately installed into the scattering apparatus. In order to minimize photodegradation of the AgCl, all steps after the electroreduction were performed under safelight and viewports into the vacuum chamber were masked.

For §3.4, our target surfaces comprise sputter coated freshly cleaved, single-crystalline NaCl surfaces. The (100) NaCl surfaces were cleaved from high purity (<1% impurities) single crystal NaCl from Ted Pella in air immediately prior to sputter coating using a Cressington 208HR sputter coater with its mtm20 thickness controller. Sputter coating was preceded by an Argon purge cycle. The sputter target was platinum (99.95%) supplied by Ted Pella and the coating thickness was 40 nm. Cleaved salt samples were approximately 2mm thick and 10 mm in length and width. The sample (hereafter, "Pt−NaCl") was secured mechanically to the target holder by an elastically deformed copper (99.995%, ESPI metals, 0.004") foil, which also provided the sole electrical connection (dry) to earth ground, via an ammeter monitoring the beam current.

For a follow-on experiment assessing surface charge effects (§3.4.3) we patterned the sputtered film using a TEM grid (gilder parallel bar grid, 400 lines/inch, Ladd Research Industries). Coating was performed as before, but from a gold sputter target (99.99%, Ted Pella) and in two steps. For the first, 15 nm of Au was deposited with a TEM grid shadow mask, producing parallel bars of gold disconnected from the continuous film. A second 15 mm coating step with the deposited bar pattern

masked connects the bars to an otherwise continuous coating, so that we are left with parallel bars of exposed NaCl (~24 μm wide) spanning a circle of diameter ~2.7 mm (this sample hereafter "Au−NaCl").

During scattering experiments, surface temperature was controlled using a nude filament heater positioned behind the scattering target. Because the thermocouple wire used to measure the sample temperature is also used to ground the target surface, the sample temperature could not be placed under closed loop control during scattering. Consequently, the temperature was prone to drift by up to +10 K as the sample stage and manipulator warmed slowly during the course of an experiment (several hours). For this reason, sample temperatures reported below are approximate.

3.2.2 Beam preparation

For a general description of the scattering apparatus, see Chapter 1. The beam is extracted from an inductively coupled plasma fed by oxygen (industrial grade, Airgas), neon (research plus grade, Air Liquide), and/or argon (UHP grade, Airgas) with or without humidification by DI water. For experiments with an O^+ beam, the feed gas was a 25:75:35 mixture of Ne, O_2, and Ar without humidification, and the ICP was driven at 600 W. Where an H_2O^+ beam is used, the feed gas is humidified argon, and the ICP was driven at 400 W. The beam species was confirmed for each experiment by deflecting primary ions into the detection system. Also in this way, the primary ion energy (E_0) was obtained at the end of each experiment (except as noted) for several settings of the external plasma bias (V_p). The plasma self-bias, which dictates the beam energy at an external bias of zero volts, is obtained as the intercept of the E_0 vs V_p line (see, as an example, Appendix Fig. A-11A).

3.2.3 SIMS energetics and mass spectra

The mass spectra of §3.4.3 were collected for the Pt−NaCl negative and positive secondary ions at a fixed product kinetic energy of 15 eV and 30 eV, respectively, during exposure to an H_2O^+ beam at 113 eV. The sample was exposed to this beam for a cumulative 3 hours prior to collecting the mass spectra. The sample current during this period ranged between 3 and 5 μA. The beam focusing was adjusted to maximize the Na^+ signal. Given the narrow acceptance angle of our detector, this tuning is expected to align the beam spot to the detector-sighted position on the sample.

Secondary ion energetics (§3.4.3) were measured using a fresh sample at 412 °C (in order to facilitate charge dissipation). Following a 30-minute exposure to 120 eV O^+ at 2−4 μA, we obtain kinetic energy distributions of four product anions (O^-, O_2^-, $^{35}Cl^-$, $^{35}ClO^-$) as a function of beam

incident energy over the range 59 to 139 eV, stepping E_0 in 5 eV increments. A 5-minute exposure period was observed before acquiring energy distributions, and the total duration of exposure at each energy level was 10−11 minutes. The beam current increased with E_0, rising by a factor of ~1.7 over the course of the experiment. The negative ion energy distributions are truncated below 6 eV due to a voltage offset in power supply. This similar procedure was also observed to obtain the secondary ion energetics for AgCl (350 °C) but stepping E_0 in ~30 eV increments over the range 63−208 eV (§3.2.2).

A calibration/control scattering experiment with an O^+ beam and a polycrystalline gold target (99.999%, ESPI metals) heated to 200 °C provides verification the scattering geometry and the single-scattering (SS) peak shape (width), which is used in §3.4 to interpret the Pt−NaCl data.

3.3 Results – AgCl

Surface charging presents a substantial obstacle to the interpretation of hyperthermal scattering energetics. All ionic crystals present this difficulty. Among the metal halides, the silver halides exhibit exceptional ionic conductivity, due to the small cation size and large polarizability. Indeed, solid silver iodide is known to exhibit "superionic" conductivity above 147 °C due to a sublattice melting phase transition, in which the Ag cations become highly mobile.[18,19] Although, silver chloride does not undergo this interesting phase transition, it still exhibits impressive ionic conductivity among halide crystals (~0.1 S cm^{-1} at 350 °C). This scattering system will be a useful starting point in understanding low energy reactive ion scattering from salts.

3.3.1 Surface charging effects

The AgCl sample provides a much clear illustration of how the products energy distributions are distorted by surface charging. In Figure 3-1, we show product energy distributions under comparable H_2O^+ exposure conditions for the AgCl target with and without heating. The scans were obtained on different days using the same sample and similar plasma conditions. The external plasma bias, which controls the beam energy, was the same to within 1 V on both days, but the plasma self-bias was not measured directly when the unheated (RT) data were acquired. Consequently, the beam energy for the RT experiment may differ by several electronvolts from that of the 350 °C experiment (114 eV). Without sample heating, the Cl^- energy distribution (Figure 3-1, right) shows truncation of the sputtered peak due to trapping by positive surface potentials. The O^- energy distribution for the uncharged sample displays a much longer tail to low exit

energies. A single, nearly symmetric peak is observed for the heated sample, reflecting the elimination of surface charge effect.

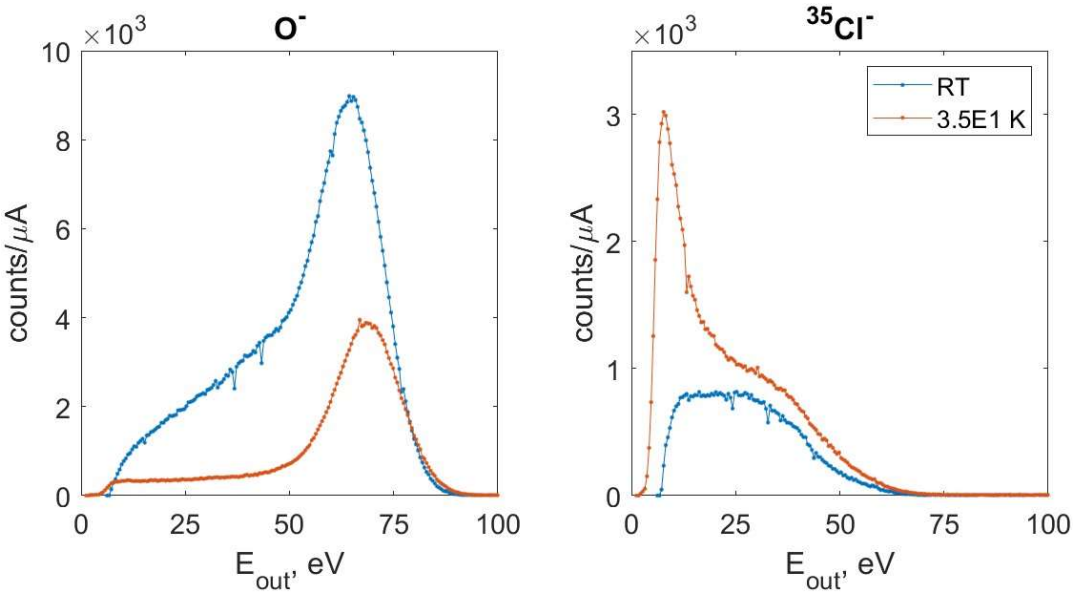

Figure 3-1: Energy distributions for O^- and Cl^- products at different AgCl target temperatures (unheated=RT vs heated to 350 ºC) under similar exposure conditions to H_2O^+ ions (~114 eV).

3.3.2 Energetics of O^-

Under exposure to O^+ ions, the heated AgCl provides very clean energy distributions for the scattered O^- product (Figure 3-2). The O^- scattering peak is much narrower for the O^+ beam than for H_2O^+, due to the absence of collision induced dissociation of the projectile. On the basis of the exit kinetic energy, we attribute the dominant peak in the O^- signal to scattering from single silver atoms/ions. We obtain the energy distributions for Cl^- and O^- products as a function of the incident beam energy, E_0. We begin with a verification of the scattering angle, by comparing the placement of the O^- peak to the BCA prediction. We can fit the prominent O^- peak with high confidence, and the linearity of the peak exit energy is with respect to E_0 excellent (adj. R^2=0.9998). The linear fit yields an inelasticity of 0.95 (−0.91, 2.8) eV and a slope, K, of 0.712 (0.699, 0.724). Solving Eq. 1-1 for the total scattering angle, θ_T, we obtain 97.8º (95, 101). This angle is not significantly different from what we measure in scattering from a clean Au surface in the calibration experiment. The small peak on the rising tail is attributable to scattering off of single Cl atoms. With a cubic polynomial subtraction of the tail, we obtain their peak energies from gaussian fits. The linearity is

very good (adj. R^2=0.9965), and fitting yields a slope of 0.362 (0.336, 0.389), within 10% of the expected kinematic factor of 0.3297.

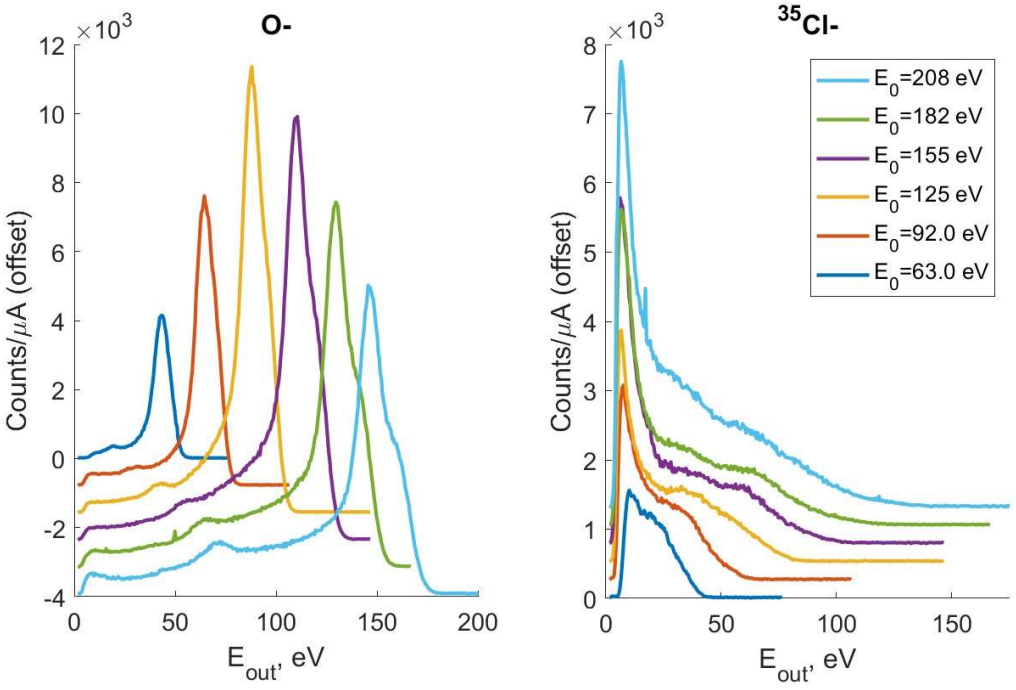

Figure 3-2: Energy distributions for O^+ scattering on AgCl (350 ºC) with baselines staggered.

Notably, a shoulder appears at the highest several E_0. At the highest E_0 (208 eV) the peak separation between the two abundant Ag isotopes should amount less than 1 eV at our deduced scattering angle, whereas the shoulder is suggestive of a peak at least 10 eV higher in energy. In fact, at a peak separation of 1 eV, two peaks would not be distinguishable, since the interval of our scan is 0.5 eV and the peak is width is much greater (~10 eV FWHM). Furthermore, the amplitude of the shoulder is lower than expected based on the representative isotopic composition of silver. The energy is more consistent with double scattering (DS) than an isotope effect. In the optimal geometry, DS from silver atoms/ions could produce O^- at energies 22 eV greater than the single collision process at E_0=208 eV. So-called zig-zag DS events, which involve excursions of the projectile out of specular plane, are also possible and produce exit energies intermediate between the single scattering (SS) and specular DS processes. These have been observed experimentally on single crystalline targets, where they present as a distinct peak in the energy spectrum.[20,21]

In a polycrystalline or surface amorphized target (such as ours), the total scattering angle can be satisfied by a continuum of double zig-zag trajectories. These range from the least lossy double

collision of the chain model to extremely lossy double backscattered trajectories. The left skew of the scattered O^- peak is suggestive of such a continuum. It is apparently a generic feature for O^- scattered from polycrystalline metal surfaces, occurring also for the clean Au target. In accordance with differential scattering cross-section, the probability of a given geometry increases with the exit energy, that is, less lossy collisions (smaller individual scattering angles) are more probable than more lossy ones. The expectation for E_{out} corresponds to trajectories which include small excursions out of the specular plane at the cost of some energy.*

3.3.3 Energetics of Cl^-

In contrast to O^-, Most of the $^{35}Cl^-$ signal is sharply peaked at low energy, consistent with sputtering. At all E_0, there is a clear shoulder, which separates distinctly into two shoulders for E_0>125 eV. Extracting the peak positions from the Cl^- data is less facile. It is apparent at a glance that the higher energy population is exiting at mean kinetic energies as great a ~60 eV, atypical of sputtering in the linear cascade regime, where energies are distributed as $\sim E^{-2}$.[22] Neither are these ejection energies consistent with potential sputtering. A coulomb explosion would be unexpected for a singly charged projectile at such low energies,[10] although ejecta energies as high as 40 times the cohesive energy (U_{co}) have been observed in simulations of the phenomenon.[23] Sudden neutralization of a single silver cation in the surface could impart a portion of the cohesive energy (U_{co} = 8.67 eV per ion pair[24]) to the Cl^- in the COM frame, but this falls well short of the observed energies.

Because the fast Cl^- peaks are not prominent enough to fit directly, any closer analysis requires a model for the superimposed energy distribution from sputtering. In the near-threshold regime (at E_0 not far exceeding the sputtering threshold), the collision cascade model is known to fail in prediction of product energy distributions.[22] As discussed in Chapter 2, Thompson's well-known result, $E \sim E/(E+U)^3$, fails at low impact energies.[25,26] Zhou et al. (2005) undertook MD simulations of Ni sputtering by hyperthermal Xe^+ and found that their results were adequately captured by a pragmatic truncation:

* The exact shape of the energy distribution depends on the scattering potential, in particular on the steepness of the internuclear repulsion. For a screened coulomb potential, the resulting distribution is a sharply rising and left-skewed. Potentials with a harder inner wall (e.g. Mie) produce a stronger skew.

$$\rho(E) \propto \frac{E}{(E+U)^{\alpha}}\left[1-\left(\frac{E}{E_U}\right)^{4}\right] \qquad 3\text{-}1$$

where E_U is the truncation energy.[26] The need for truncation is apparent in our data, so we adopt this approach, taking α=3, which reproduces Thompon's distribution at higher energies. Unfortunately, the parameter E_U cannot be obtained directly by fitting since the tail of the sputtered distribution is subsumed. Sputtering in this near-threshold regime is governed by a relatively limited set of well-defined collision sequences.[27] We set our truncation energy based on one of these: two consecutive collisions of the projectile with Ag atoms/ions preceding a direct knock-out collision, ejecting Cl along a bearing that satisfies our scattering geometry. The potential geometries (and thus energies) are various in our surface-amorphized target surface.[27] For E_U, we choose the most efficient DS geometry in BCA (for an O projectile, each collision deflecting O by $\theta_T/2$), resulting in $E_U \propto E_0$. For O^+ projectiles, this truncation is satisfactory. For H_2O^+ projectiles, we presume dissociation on the first impact and find it necessary to include an inelasticity (5 eV). The free parameters, U and a scaling factor, are obtained by fitting to the falling slope of the sputtered peak up to E_{out}=15 eV. After subtracting the background and the sputtered population, we are left with a bimodal distribution, increasingly right-skewed toward high E_0 (Figure *3-3*).

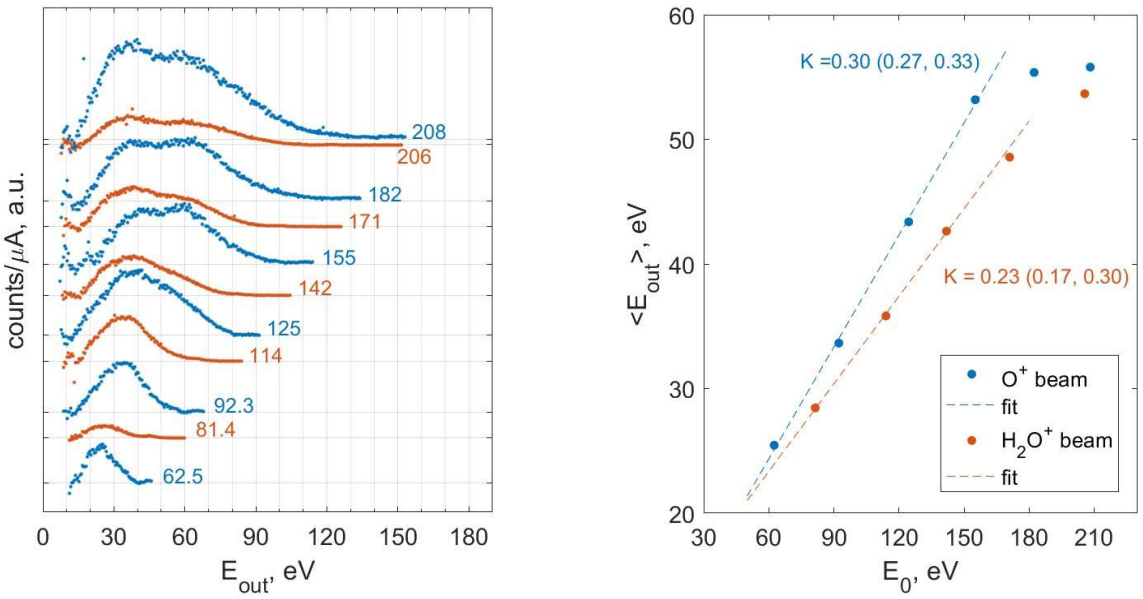

Figure 3-3: Energetics of fast Cl^- emitted from AgCl. Left) Staggered energy distributions for the fast Cl^- product after subtracting the sputtered component and background. Baselines are offset in proportion to the beam energy E_0, which is indicated beside each trace. Right) Mean exit energy of the fast Cl^- population vs the beam energy. Red points are for an H_2O^+ beam, and blue are for

an O^+ beam. Linear fits to the data are shown as dashed lines, with the slope, K (95% CI), annotated beside. Data points with E_0>180 are excluded from the fits because plateauing is apparent.

The current-normalized signal for Cl^- is larger for O^+ than for H_2O^+ projectile, which is consistent with our expectation that H_2O^+ is the less efficient sputterer due to its rotational and internal degrees of freedom. The energetic remainder comprises a variable fraction of the total signal, ranging from 14% to 38%, but it is also consistently higher for the O^+ projectile. Although the bimodality is obvious, without additional constraints on the peak shapes, we cannot separate the subpopulations with any confidence. We can, however, readily compute the mean exit energy. We find that it scales linearly with E_0 before plateauing (definitively in the case of O^+, less-so for H_2O^+). This scaling suggests that the peaks are due to consistent kinematic sequences, though, unfortunately, it does little to clarify which.

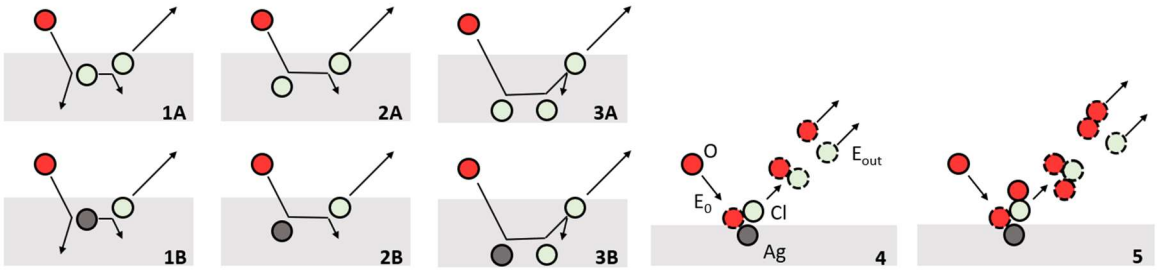

Figure 3-4: Various mechanisms to generate fast Cl^-. Circles with solid outlines show initial positions of the atoms and are colored to indicate species (red = O, green = Cl, gray = Ag). Circles with broken outlines show their positions at subsequent times. Arrows depict displacements. 1A(B) – recoil of surface Cl (Ag) ejects Cl. 2A(B) - recoil of projectile from surface Cl (Ag) ejects Cl. 3A/B – double-scattering projectile ejects Cl. 3C (not depicted) – As 3A but with both surface atoms as Ag instead of Cl. 4 – ER abstraction of Cl from Ag to from ClO, which dissociates into fragments with equal lab-frame velocity. 5 – ER abstraction of OCl from Ag to from ClO_2, which dissociates into fragments with equal velocity.

We can, however, rule out some processes. First, we note that, whatever their origin, the separation of the peaks cannot be due to an isotope effect alone — whether the collision partner is Ag or Cl, the dual isotopes of the surface atom provide for an energy difference of ≤12 meV/E_0 for the abstraction scenario (Mech. 4&5), and ≤20 meV/E_0 in the DS knockon scenario (Mech. 3ABC). They must instead be owed to distinct kinematic sequences. At E_0=155 eV, where the mean exit energy is yet to plateau, the peaks are well enough separated to confidently determine the modes of the energy distribution. These energies place a lower limit on the kinematic factor for the corresponding trajectories (equivalent to assuming zero inelasticity). The high-energy mode

suggests a limit of K≥0.39. We can therefore rule out the single-collision abstraction-dissociation mechanisms (Mech. 4&5), the single-knockon collision mechanisms 1A and 1B, and the DS knockon ejection involving only Cl atoms/ions (Mech. 2A). The lower-energy mode provides a limit of K≥0.2710, ruling out these same processes except for dissociation of ClO formed by abstraction of Cl from Ag (Mech. 4) and mechanism 2A. Several possibilities remain for both peaks, including the type-2 single-knockon process (Cl ejected by projectile after a single collision) involving Ag (Mech 2B) or Cl (Mech 2A), DS knockon ejection involving one or two Ag atoms/ions (Mech. 3BC), DS abstraction-dissociation, and higher order processes.

Table 3-1: Maximum fractional Cl exit energy for various mechanisms at the total scattering angle of this experiment (θ_T =97.8°). Surface atom masses $m_{\overline{Ag}}$ and $m_{\overline{Cl}}$ are taken to be the standard atomic weights, otherwise the masses are for the relevant isotopes of the experiment (^{35}Cl, ^{16}O, $^{35}Cl^{16}O_2$, $^{35}Cl^{16}O$). The angles θ_i (i= 1−3) are chosen for each sequence to satisfy the total scattering angle.

Mechanism	Cl^- K_{max}	Expression
1A	0.243	$\left(1-K\left(m_{Cl}/m_{\overline{Cl}},\theta_2\right)\right)(1-K(m_{\overline{Cl}}/m_O,\theta_1))$
1B	0.069	$\left(1-K\left(m_{Cl}/m_{\overline{Ag}},\theta_2\right)\right)(1-K\left(m_{\overline{Ag}}/m_O,\theta_1\right))$
2A	0.361	$\left(1-K\left(m_{Cl}/m_O,\theta_2\right)\right)K(m_{\overline{Cl}}/m_O,\theta_1)$
2B	0.627	$\left(1-K\left(m_{Cl}/m_O,\theta_2\right)\right)K\left(m_{\overline{Ag}}/m_O,\theta_1\right)$
3A	0.507	$\left(1-K\left(m_{Cl}/m_O,\theta_2\right)\right)K(m_{\overline{Cl}}/m_O,\theta_1/2)^2$
3B	0.658	$\left(1-K\left(m_{Cl}/m_O,\theta_2\right)\right)K(m_{\overline{Cl}}/m_O,\theta_1)\,K\left(m_{\overline{Ag}}/m_O,\theta_3\right)$
3C	0.711	$\left(1-K\left(m_{Cl}/m_O,\theta_2\right)\right)K\left(m_{Ag}/m_O,\theta_1/2\right)^2$
4	0.372	$K_{ER}\left(m_O,m_{Cl},m_{\overline{Ag}},\theta_T\right)m_{Cl}/m_{OCl}$
5	0.256	$K_{ER}\left(m_O,m_{OCl},m_{\overline{Ag}},\theta_T\right)m_{Cl}/m_{ClO_2}$

A double-scattering knockon process could produce Cl^- exit energies as high as 0.711×E_0, if both scattering partners are Ag (Mech. 3C). Such a process would be sufficient to account for the high energy tail. DS trajectories involving two Ag atoms would be facilitated by the formation of a Ag-enriched overlayer, analogous to the nonstoichiometric overlayers seen in electron stimulated desorption (ESD) of alkali halides at low temperature[28,29] and in potential sputtering of SiO_2.[9] Given the double-scattering feature seen in the O^- energy distributions, this scenario is plausible.

3.4 Results – NaCl Scattering

3.4.1 H_2O^+ bombardment

Surface charging is a much greater obstacle for macroscopically thick NaCl targets than for the AgCl surface, and heating alone (to temperatures ~400 ºC) could not mitigate the issue enough to make experiments tractable. Our analysis of the scattering behavior of NaCl targets is performed using a heated (~400 ºC) NaCl target with a thin (40 nm) platinum coating, which, among other combinations of coating materials (Ni, Au), thicknesses, and temperatures, provided the most intense and stable secondary ion signals. The surface microstructure of the target after exposure to hyperthermal ions was evaluated using optical microscopy at 500× magnification, revealing one- and two-dimensional domains of exposed NaCl with characteristic widths around 10 μm (Figure 3-5). The point-like domains exhibit branching, fractal character, which is consistent with diversion of the ion current to the perimeter of exposed NaCl. The two-dimensional domains are likely owed to differential thermal expansion as the target was heated. For comparison, a freshly coated, unexposed sample was also imaged and exhibited a relatively uniform morphology. This film showed rectangular domains (~40 μm) separated by linear faults, which do not expose uncoated NaCl.

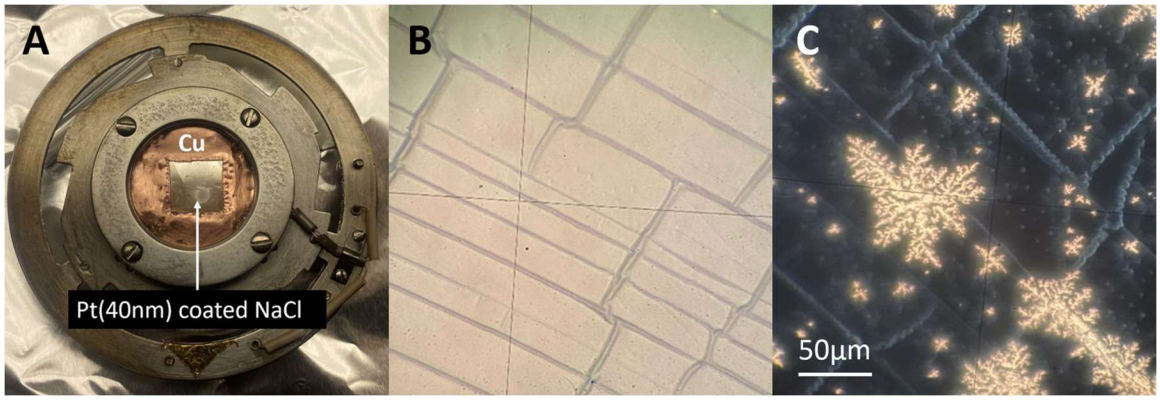

Figure 3-5: A) Photo of the target surface after exposure, showing the Cu shroud and Pt−NaCl. B) Microscope image of unexposed Pt−NaCl. B) Microscope image of Pt−NaCl after exposure to the beam.

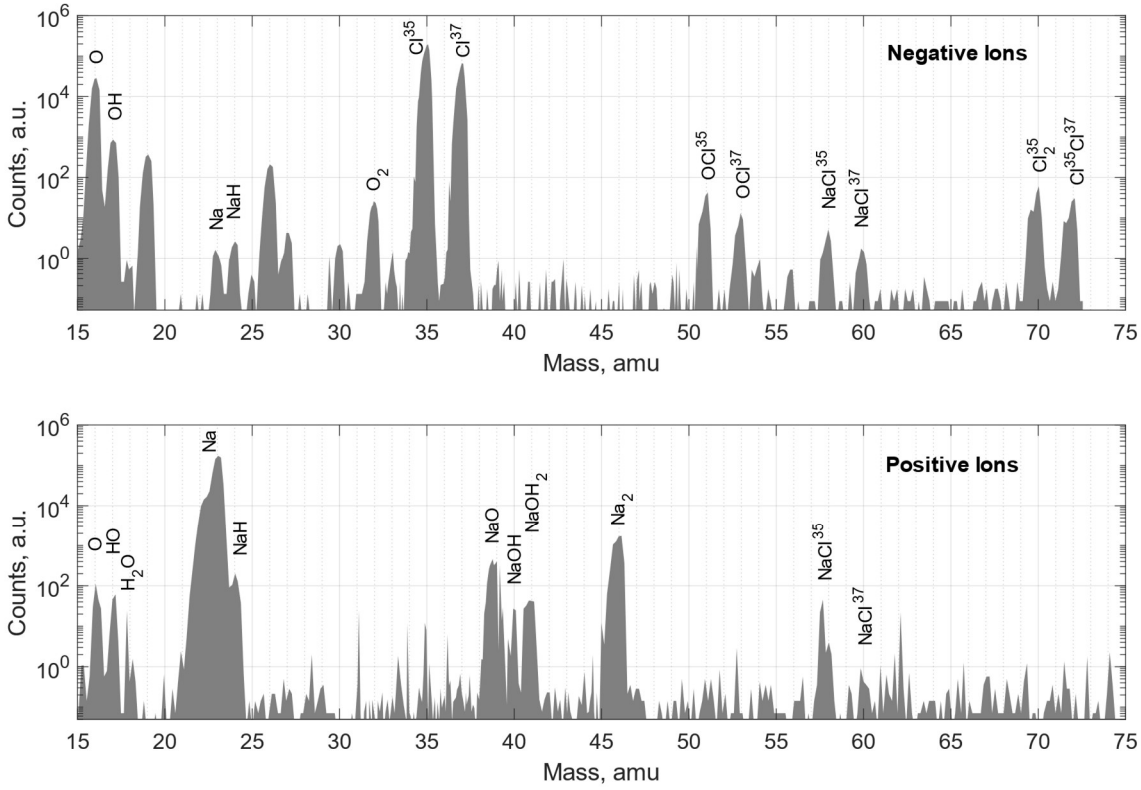

Figure 3-6: Mass spectra for negative (top) and positive (bottom) ions for platinum coated NaCl under 113 eV H_2O^+ bombardment. The spectra were taken at fixed product kinetic energies of 15 eV and 30 eV for the negative and positive ions, respectively.

Mass spectra for negative and positive secondary ion products of H_2O^+ (113 eV) scattering on Pt−NaCl are shown in Figure 3-6. An important consideration with these data is that they represent the ion mass distribution subject at a single scattering angle and product kinetic energy (15 eV and 30 eV for the negative and positive ions, respectively). Due to surface charging effects, the energy distributions of secondary ions are offset, in this case, by approximately four electron volts. Consequently, conducting the mass sweeps at the identical product energy would favor scattered over sputtered products for one polarity and vice versa for the other. For this reason, the product kinetic energy was selected for each polarity relative to the peak energy of the dominant sputtered ions (Na^+, Cl^-), offset to a higher energy, in an effort to capture both scattered and sputtered ions species simultaneously. For the positive ions, this energy was 30 eV, about 35% higher than the median Na^+ energy and 50% lower than the O^+ median energy. For the negative ions, the energy was 15 eV, 15% lower than the median Cl^- energy and 60% lower than the O^- median energy. Because the sputtered product energy distribution in right skewed, this choice of scan energy favors sputtered over scattered ions.

Negative product ions are dominated by the sputtered isotopes of Cl^-, followed by O^- and OH^- ions, whose energy distributions are consistent with scattering. Based on the energy distributions of the Cl^- and O^- ions, we can estimate the relative yields for these species (integrated over all energies). Making this correction (a ~4.2× enhancement of the O^- yield), we find that a relative yield of 1.25 for $O^-/^{35}Cl^-$. The relative yield for molecular ions fell at least two orders of magnitude below that of the atomic species, consistent with low-energy sputtering results for LiF.[12] The primary molecular negative ions were Cl_2^-, OCl^-, and O_2^-. These later two species are possibly the products of reactive scattering, which we will discuss in more detail shortly. Also apparent in the mass spectrum is F^-, a consequence of known fluorine contamination in our EEA accumulated during previous work.

The positive ion product distribution is dominated by Na^+, with all other species, including fragments of the projectile ion, falling at least two orders of magnitude lower in yield. The primary molecular ions were Na_2^+, NaO^+, and NaH^+. Water group ions (excepting H_3O^+) and the cluster $NaOH_2^+$ appear at lower abundances. The ions H_2O^+, HO^+, and O^+ occur in increasing abundance, reflecting the high probability of projectile dissociation at this energy.

Ejecta of both polarities show unusual energy distributions, qualitatively similar to the Cl^- energy distributions, but with much higher probability density in the energetic population. In the case of Cl^- and OCl^-, a high-energy peak is prominent against the tail of the sputtered population. In the next sections, we focus on analyzing the production mechanisms for the energetic Cl^- and OCl^- ions.

3.4.2 O^+ Bombardment

In order to investigate the origin of this high energy population, we conduct a follow up experiment with an O^+ beam and a fresh Pt-coated (40 nm) NaCl surface. Again, we observe bimodal energy distributions for the Cl^- and OCl^- products, with a sputtering peak at constant energy and a second peak which rises with beam energy before plateauing around 55 eV (Fig. 4.4.3). The Cl^- energy distributions are strikingly similar. The O_2^- product shows somewhat different behavior, with a much weaker contribution from sputtering and a high-energy peak which, above E_0=104 eV, continues to scale with E_0 but is “smeared” down to approximately 60 eV. This behavior follows that of O^-, except that the latter scales more steeply with E_0. This smearing of the scattered peak is similar to the surface charging effect seen for AgCl (see Figure 3-1), although here it is more dramatic.

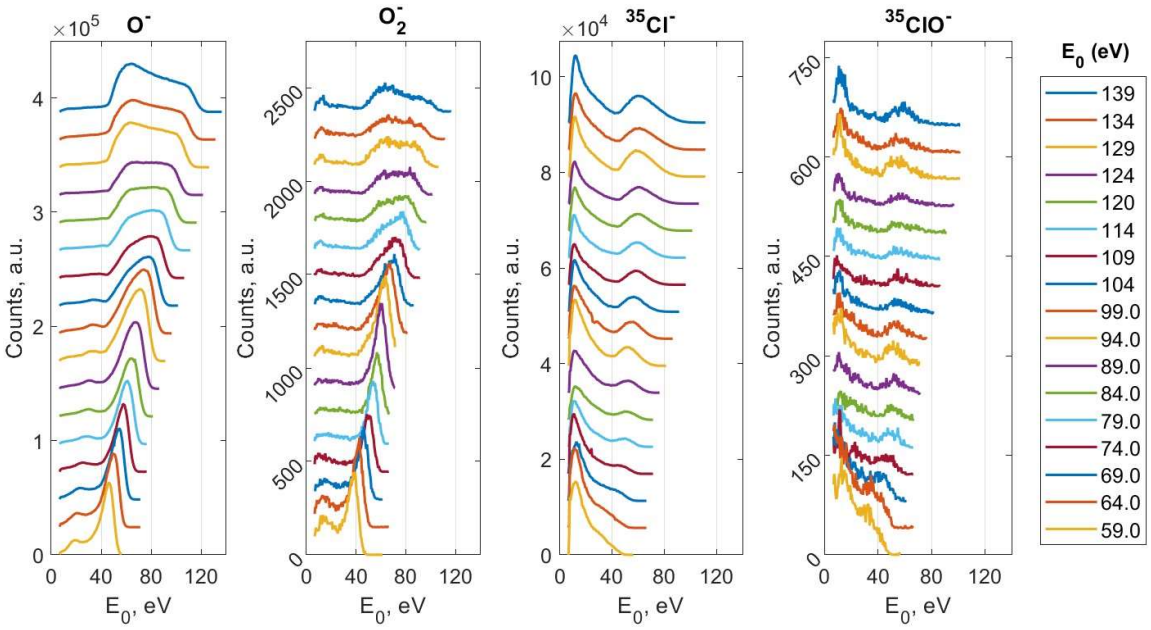

Figure 3-7. Energy distributions for negative ion products of O^+ scattering on Pt-coated (40 nm) NaCl at 412 °C at various beam energies. The baseline of each energy distribution is offset in proportion to the beam energy for convenience of viewing. The signal intensity is reported in arbitrary units, but the peak amplitudes are comparable across beam energies and product species.

3.4.3 Surface charging effects

Due to potential charging effects, the scattering angle is not known *a priori*, but must be extracted from the O^- scattering kinematics. Unfortunately, despite our mitigation efforts, surface charging is severe enough that this is not an entirely trivial exercise. On a neutral surface, we expect the O^- kinematics to follow binary collision approximation (BCA), which we confirmed in O^+ scattering experiments on a clean Au target and reaffirmed with the AgCl experiment. Assuming that the O^- signal is not sourced from negatively charged regions, we expect that the highest energy component of the distribution comes from binary collisions of O with Pt atoms at a neutral surface — a positive surface charge would be double-acting to reduce the kinetic energy, retarding the incident O^+ and the exiting O^-. We extract the O–Pt scattering energy from the falling inflection point of the high-energy shoulder. The control experiment scattering O^+ from a 200 °C polycrystalline Au target enables us to relate the inflection point position to the peak position. The control experiment demonstrates that the $O^+ \rightarrow Au \rightarrow O^-$ BCA peak is sharper than gaussian, well captured by a generalized gaussian distribution with shape parameter ~1.5. We also observe a slight widening of the peak with increasing E_0. The FWHM increases by 5×10^{-2} (95% CI: $\pm 2\times10^{-2}$) eV per additional eV of incident energy. Since there is only a single stable Au isotope and the dispersion of our beam

energy is constant, this result is not anticipated directly in BCA for single collisions. Widening is, however, anticipated for a Pt surface because of the multiplicity of Pt isotopes — at our experimental energies the peaks are not well separated and merge into one. Without dispersion in the beam energy, the merged peak width should scale in proportion to the difference in kinematic factors for the heaviest and lightest abundant Pt isotopes. Similarly, an apparent widening can occur within the BCA framework due to the superposition of a SS and DS peak, as seen in the AgCl data.

Accounting for the peak shape and widening, we obtain the peak position from the falling inflection point at each E_0. The outstanding linearity of the E_{peak} vs E_0 data (adjusted $R^2 = 0.9996$) is reassuring. From fitting we find, the slope, K, as 0.7811 (0.7733, 0.7889) and the intercept as 2.5 (1.7, 3.3) eV, where the parenthetical figures are the 95% CI. From the BCA model, we extract the total scattering angle from the slope, obtaining $\theta_T = 120 \pm 4$ degrees. Here, we have taken the surface atom mass to be that of isotopically average Pt and the projectile as ^{16}O. The various Pt isotope peaks are well-merged at the energies of our experiment, and the error in peak position incurred by using the standard atomic weight is small ($O(1\times10^{-3})$ %). This scattering angle is roughly 20° more acute than expected for our apparatus geometry, consistent with the influence of an electric field. The regression indicates a slightly negative inelasticity for the scattering interaction, which suggests that the fast shoulder of the O^- signal may be influenced by a small negative surface potential, contrary to our initial assumption. Extra widening of the merged Pt peak due to the multiplicity of isotopes would displace the calculated peak positions by <3 meV, far from enough to account for the inelasticity.

In order to assess our assumptions about the surface charge distribution, we refer to the results of a second experiment, in which we monitor the scattering energy of O^- and Cl^- under different surface charging conditions. To produce more dramatic surface charge effects, we utilize a NaCl target with a micropatterned Au coating. We regulate the effects of surface charging by adjusting the temperature of this target under constant O^+ exposure conditions, with higher temperatures effecting greater charge dissipation via the improved ionic conductivity. The bulk conductivity of undoped NaCl increases by a factor of 6.8 over this temperature range.[30] We observe dramatic increase in the signal intensity for both Cl^- and O^- as the temperature increases (Figure 3-8). The increase in signal is especially pronounced for Cl^- (17× at 50 eV). Without an independent measurement of the work function, we cannot conclude with certainty whether this is an effect of the decreased work function or increased fluence to the beam spot. As in our Pt−NaCl experiment,

we see the O^- energy distribution dominated by two bridged peaks. The high energy peak we identify as scattering from Au where V_s is near zero. The position of this peak does not move more than 0.5 eV as the temperature is varied, confirming that its energy is not regulated by charging effects. In contrast, the sputtered Cl^- peak shifts toward higher energy by 5.5 eV as the temperature increases from 300 °C to 400 °C. This we attribute to a positive V_s of increasing magnitude as the NaCl is cooled, which results in trapping of low-energy sputtered Cl^-. The left-skew of the high-energy O^- peak decreases as the temperature is raised, and its amplitude increases relative the peak between 50 and 60 eV. We interpret this as an indication that the surface charge distribution is becoming increasingly neutral as the temperature is raised.

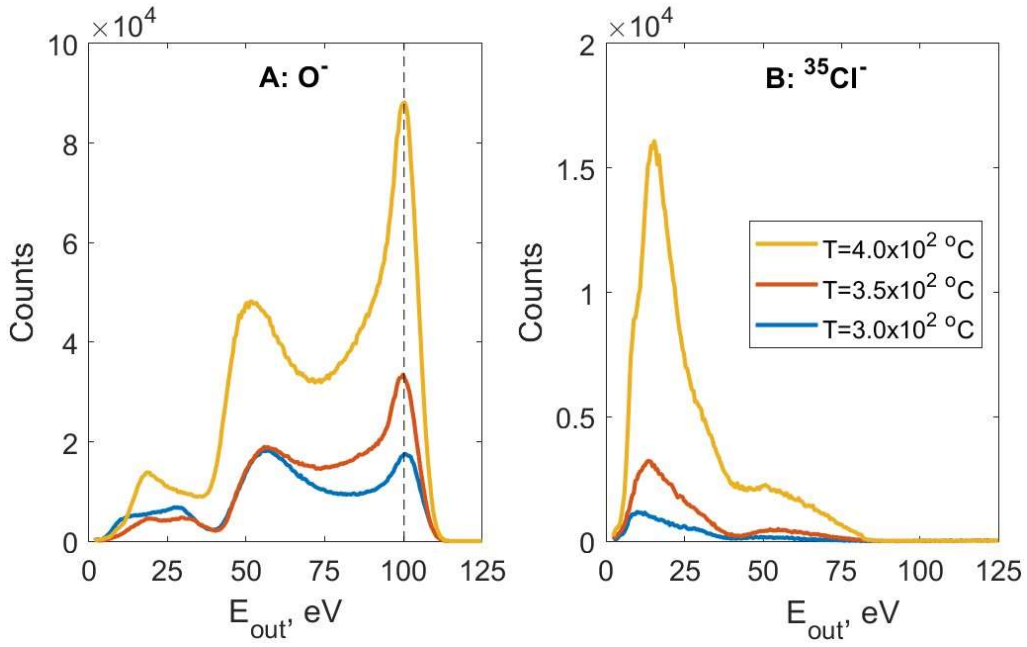

Figure 3-8. Energy distributions two products (A: O^-, B: Cl^-) for micropatterned Au−NaCl under identical exposure conditions but different surface temperatures.

Resuming our discussion of the Pt−NaCl results, with the scattering angle known, we can place upper limits on the locations of BCA peaks for scattering from the other main surface species. Neglecting the inelasticity, these are 7.0%, 22.3%, and 24.5% of E_0 for Na, ^{35}Cl, and ^{37}Cl, respectively. In view of Figure 3-7, the low-energy mode of the dominant O^- peak cannot be attributed to these other species without considerable negative surface charging. There is good evidence against a strong negative surface charge. Sputtered negative ions, for instance would be "kicked" to higher kinetic energies, yet they (Cl^-, O_2^-, ClO^-) appear at our minimum scan energy (6 eV), suggesting an upper limit of 6 V on magnitude of the hypothetical negative surface charge.

Furthermore, it is difficult to account for the dramatic increase in signal above the nominal BCA energy for these lighter species — this would require that most of the beam spot is charged to strong negative potentials (∼−20 V). Together, these observations allow us to reject the negative charging hypothesis in favor of the more plausible explanation, that the O^- signal is dominated by scattering from Pt, with the peak being "smeared" to lower kinetic energies by charging to positive potentials.

Since we know inelasticity (s) for this process, we can attempt to extract information about the surface potential (V_s). We assume that the scattering angle is independent of the surface charge, which assumption is stronger for $E_0 \gg V_s$. Thus, the BCA peak is shifted to a new exit energy by the double action of the surface potential:

$$E_{out} = (E_0 - V_s)K(O \to Pt \to O) - s - V_s \qquad 3\text{-}2$$

The incident energy is reduced by V_s prior to impact, and the exit energy of the product negative ion is shifted by $-V_s$. With this linear mapping of V_s to E_{out}, the problem can be framed as a deconvolution, subject to some caveats. The peak widening due to multiple Pt isotopes, for instance, must be ignored. But, as discussed before, the effect is negligible at these energies. We expect that some portion of our O^- energy distribution comes from collisions of O^- with Cl and Na. So that the signal from O−Cl scattering is not misattributed to O−Pt scattering at large positive potentials, we exponentially taper the O^- signal for $E < E_0 K\left(m_{^{37}Cl}/m_o, \theta_T\right) + FWHM/2$, effectively limiting the maximum surface potential.

We deconvolute the truncated data energy distribution using the generalized gaussian peak shape from the Au target, with a constant shape parameter (n) of 1.5 and a scale parameter (c) that varies linearly with E_0 to capture widening. Tikhonov regularization is necessitated by noise in the experimental data, but unfortunately introduces ringing artifacts, like negative probability density. Nevertheless, the charge distributions (Figure 3-9) reproduce the O^- signal shapes well. As E_0 increases, so does the mean voltage and the voltage distribution transitions from right-skewed to left-skewed.

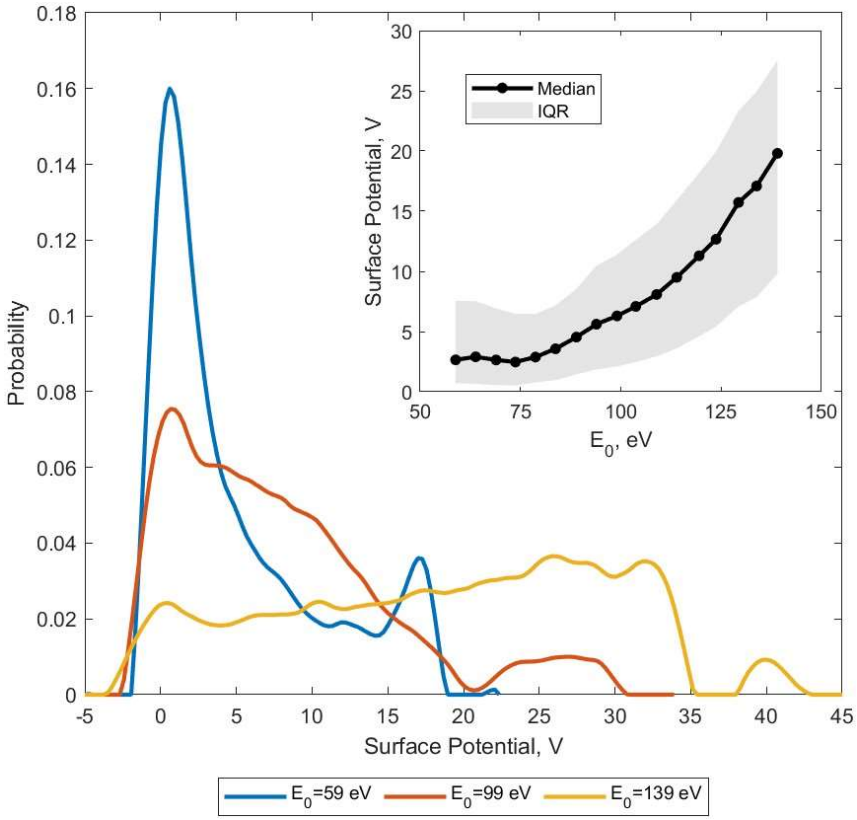

Figure 3-9. Surface charge distributions for three beam energies (regularization factor = 1), with inset showing the how the distributions summary statistics vary with incident energy.

Now that we have quantified the distribution of surface potential, we can address the interesting kinematics of the Cl^-, O_2^-, and ClO^-. First, we obtain the peak O_2^- product energy (Figure 3-10). As seen in Figure 3-7, the dynamic O_2 peak begins to split around E_0= 99 eV due to surface charging, complicating this exercise. Below the splitting, we fit a single gaussian; above, we fit a gaussian to the left and right shoulder of the widened peak. The higher energy mode (E_{pk1}) continues to scale approximately linearly with E_0, whereas the lower energy mode appears to plateau in energy almost immediate after appearing, which we attribute to the increasingly large positive surface potentials developed at high E_0. Additionally, we compute an amplitude-weighted average of E_{pk1} and E_{pk2}. To the extent that the surface charge distributions can be approximated as linear, this midpoint (E_{mid}) is representative of average surface charging conditions. This approximation provides a relatively simple correction to the far-field incident and exit energy: $E_0' = E_0 - \bar{V}_s$ and $E_{out}' = E_{out} + \bar{V}_s$, where $\bar{V}_s$ is the mean surface potential. Here, E_0' and E_{out}' are the energies point of collision, the energies to which BCA applies. After the correction, the linearity of the midpoint

data (E_{mid} adj.) is much improved. The kinematic factor for O abstracting adsorbed O from Pt at our scattering angle is 0.7050. A linear fit to the adjusted data yields a kinematic factor of 0.73 (0.71 0.76), for an error of 3.6%. Since the negative ion signal is not only a function of the surface potential, but also the surface coverage and work function (and we expect our sample to have dramatic local variations in all these), there is certainly no guarantee that the O_2^- energy distribution is convolved with the same voltage distribution as the O^-. Yet the accuracy of the experimental kinematic factor suggests that this is the case. Dynamic O_2^- production has been reported in hyperthermal H_2O^+ impacts with oxidized Pt surfaces, proceeding through an excited oxywater precursor state.[31] In that case, the formation of O_2^- is plausibly facilitated dissociative electron attachment (DEA). This pathway is not available for the O^+ impactor system, so that survival of rovibrationally hot O_2 following electron attachment seems unfavorable. Resonant electron transfer, however, channels the EA into translational rather than vibrational degrees of freedom, perhaps accounting for the survival of the molecular ion at abundances of 0.5% relative to O^-.

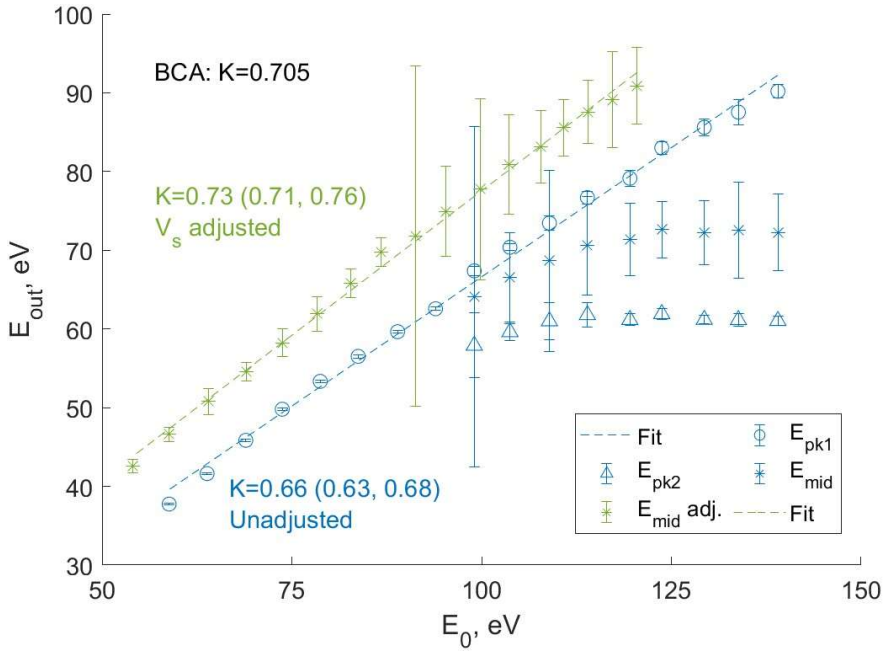

Figure 3-10. Exit energy for the O_2^- product as a function of the incident O^+ energy, E_0. See text for discussion of the fitting. E_{mid} is the amplitude weighted average of E_{pk1} and E_{pk2}, with fit uncertainty propagated. The green data are the E_{mid} after correction by the mean V_s as described in the text. The slopes, K, of unweighted linear fits (--) to E_{pk1} and the adjusted E_{mid} is provided with the 95% CI. For reference, the theoretical kinematic factor for the calculated scattering angle is provided. For the V_s adjusted data, the ordinate and abscissa are actually E'_{out} and E'_0, as described in the text.

3.4.4 Energetics of OCl^-

We now turn to discussion of ClO^- and Cl^-. The ion energy distributions for these two products are quite similar. Like O_2^-, ClO^- shows a high energy peak which plateaus at high E_0, suggesting similar mechanics, that is, an Eley-Rideal abstraction reaction with kinematics obscured by surface charging (Figure 3-11). The Cl^- exhibits the similar behavior. The energetic Cl^- and ClO^- peaks do not however show the same splitting/broadening behavior as the O^- and O_2^- ions, which implies that fast Cl^- and ClO^- production may be correlated with a particular surface charge state. This is not unexpected — an abstraction reaction leading to either would require intimate mixing of Pt and Cl atoms, which is likeliest at the interface between the intact Pt film and the exposed NaCl. From the fractal erosion pattern of the Pt film, we infer that charging of exposed NaCl diverts O^+ flux to the nearby Pt, enhancing the flux to this interface. The interfacial region may be prone to developing a strong positive surface charge as noncontiguous patches of Pt form, with the current conducted to ground across narrow sections of bare NaCl. Furthermore, stronger surface potentials will trap more of the sputtered Cl^- ions, potentially enhancing the Cl surface coverage.

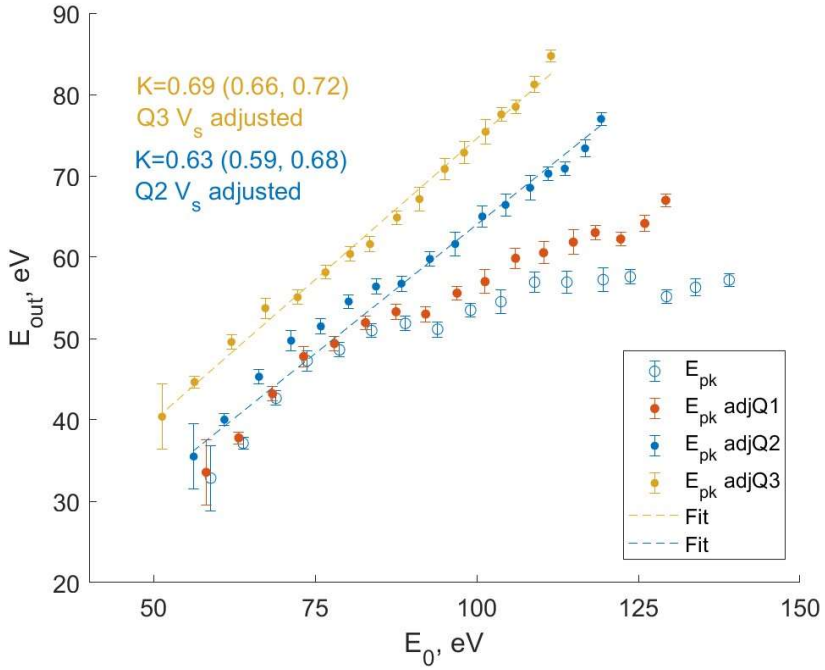

Figure 3-11: Peak exit energy for the fast OCl^- populations with (solid) and without (open) adjustment by the by the 1st, 2nd, and 3rd quartiles of the surface potential distribution (red, blue, and yellow, respectively). Linear fits to the V_s-adjusted data are also shown, with the slopes (with 95% CI) annotated. For the V_s adjusted data, the ordinate and abscissa are actually E'_{out} and E'_0, as described in the text.

For the ClO^- product we attempt the same surface voltage correction as before but find that using the mean surface voltage does not entirely restore linearity, although it does provide excellent agreement to the Cl-abstraction kinematic factor (0.635). The data are better linearized if we correct by the third quartile V_s, which produces a kinematic factor 9% above the theoretical value for Cl abstraction from Pt. The regions producing most of the OCl^- signal may therefore be charged to higher-than-average positive potentials.

Table 3-2: Maximum fractional Cl^- and OCl^- exit energies for various mechanisms at the total scattering angle of this experiment ($\theta_T = 120^o$). For the Cl^- product, the mechanisms are as depicted in Figure 4.3.4, but with the Ag surface atom replaced by Pt. For the ClO^- product, mechanisms 1–3 are identical to Cl^-, except that the Cl^- product is replaced by ClO^-. For the ClO^- product, mechanisms 5 and 4 become partial dissociation and non-dissociation, respectively, of the ER product.

Mechanism	Cl^- K_{max}	OCl^- K_{max}
1A	0.054	0.052
1B	0.009	0.012
2A	0.245	0.207
2B	0.677	0.571
3A	0.391	0.330
3B	0.686	0.579
3C	0.735	0.620
4	0.436	0.635
5	0.307	0.447

In contrast to the O_2^- data, the ClO^- energy distributions show a relatively large low-energy population. Without the introduction of Pt atoms, at our highest incident energy (139 eV), we could expect to see the OCl^- signal (mech. 4) peaking below 17 eV for a Cl substate atom/ion and 4 eV for a Na substrate atom/ion, where they would be essentially indistinguishable from sputtered products. In light of this ambiguous low-energy signal, it would seem that the fast ClO^- energetics could also be due to a single-knockon sputtering process, namely (see Table 3-2), a double scattering on Pt atoms followed by a nearly head-on collision with adsorbed OCl, resulting in its ejection along the bearing of detector. The most efficient geometry for this process results in a kinematic factor of 0.620, very close to that of the abstraction reaction. Under the conditions of our experiment, ClO surface coverage should be insignificant due to spontaneous dissociation on the Pt surface, making this explanation unlikely. ClO^- is also accessible via the formation and partial

dissociation of ClO_2 (mech. 5), but the observed kinematics disfavor this mechanism. The ER abstraction of Cl from Pt is thus the favored explanation for the energetic ClO^-.

3.4.5 Energetics of Cl^-

Cl^- exhibits similar energetics to OCl^- but there are important contrasts (Fig. 4.4.8). The first is that the Cl^- peak energy is higher than that of OCl^- for E_0>90 eV. The second, related observation is that whatever correction we apply for surface charging, so long as it is the same for both OCl^- and Cl^-, we obtain a larger kinematic factor for Cl^-. Both observations are inconsistent with hypothesis that Cl^- is a due to dissociation of scattered OCl^-. If this were the case, the Cl^- would share the exit velocity of OCl^-, or, equivalently, the fraction m_{Cl}/m_{OCl} of the OCl^- exit energy. Here we have made two assumptions, which we will revisit shortly. Now, we consider the possibility that the fast Cl^- are ejected via a well-defined single-knockon process. In any case, it seems reasonable to assume that OCl^- and Cl^- are sourced from the same regions of the surface, which is to say that their energy distributions have been influenced by the same surface potential (for the reasons discussed earlier).

For the sake of clarity, we begin by fixing the surface potential correction. For O abstracting Cl from Pt, the best agreement to the theoretical K (0.6354) is obtained at the 50^{th} percentile of the charge distribution. Applying the same correction to Cl^- yields kinematic factor of 0.67 (0.65, 0.70). The simplest single-knockon process producing comparable kinematic factor is ejection of Cl by the projectile after backscattering from Pt (mech. 2B). A quasi-double process involving a single Pt atom and glancing (θ=10°) scattering from Cl followed by Cl knock out (mech 3B) yields a similar K. Both mechanisms are in good agreement with the observed value. Higher order processes are also possible, producing faster products, but at diminishing probabilities. We can certainly rule out processes that do not involve a Pt surface atom (e.g. double scattering from Na and Cl).

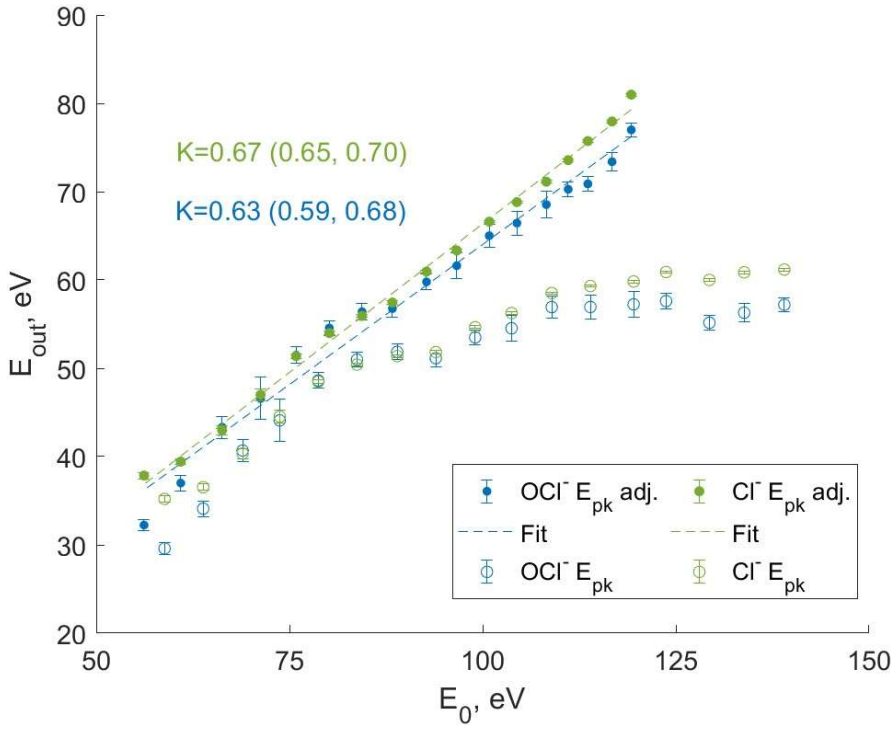

Figure 3-12: Peak exit energy for the fast Cl^- (green) and OCl^- (blue) populations with (solid) and without (open) adjustment by the mean surface potential. Linear fits to the V_s-adjusted are also shown, with the slopes annotated. For the V_s adjusted data, the ordinate and abscissa are actually E'_{out} and E'_0, as described in the text.

Since the fast ClO^- appears to be an ER reaction product, a more thorough assessment is needed before throwing out the hypothesis of a ClO parent for Cl^-. There remain a couple of potential explanations for the higher exit energy and the large kinematic factor of Cl^-. One possible explanation for this behavior is that the parent molecule of Cl^- dissociates with an excess of kinetic energy (E_d) in its center of mass frame. Because of the narrow acceptance angle of our detector, this excess should result in splitting of the scattered peak: higher energy (E_{obs}) when the fragment is "kicked" toward the detector, lower when "kicked" back toward the surface:

$$E_{obs} = \frac{m_{Cl}}{2}\left(\sqrt{\frac{2E_{pre}}{m_{OCl}}} \pm \sqrt{\frac{2E_d m_O}{m_{OCl} m_{Cl}}}\right)^2 \qquad 3\text{-}3$$

Such a dissociation would be attended by a severe drop in signal intensity since most of the fragments would fail to enter the detector. Depending on the magnitude of the excess and the lab-frame kinetic energy of the parent (E_{pre}), the low energy peak may be obscured by the sputtered

population or trapped by the surface potential. Assuming that ClO^- and Cl^- are related as parent-daughter, the difference in exit energy between them provides an indication of the excess. We compute the excess dissociation energy, E_d, from the difference between these peak positions by solving:

$$E_{obs} - E_{OCl} = \frac{2\,m_{Cl}}{m_{OCl}}\sqrt{\frac{E_d E_{pre} m_O}{m_{Cl}}} + \frac{E_d m_O}{m_{OCl}} + \frac{E_{pre} m_{Cl}}{m_{OCl}} - E_{pre} \qquad 3\text{-}4$$

Here, the kinetic energy of the predissociation state COM (E_{pre}) is calculated from the theoretical kinematic factor, neglecting the scattering inelasticity, and after the V_s correction to the incident beam energy. If the dissociation occurs immediately after ionization, we need not include the effect to V_s on the exit energies because it is the same for both species. If dissociation is delayed by a microsecond or so, much of the surface potential's work will have been done, and E_{pre} reduced. In the former case, E_d increases linearly with E_0 from around 2 eV to 9 eV. In the latter case, E_d is slightly lower, by ~1.5 eV at high E_0. The corresponding peak splitting is:

$$\Delta E_{obs} = 4\frac{m_{Cl}}{m_{OCl}}\sqrt{E_d E_{pre} m_O / m_{Cl}} \qquad 3\text{-}5$$

At the highest E_{pre}, the peak splitting is >40 eV, plenty large enough to bury the slow peak in the sputtering signal. The salient problem with this explanation has to do with the experimental kinematic factors. If the dissociation is immediate, we should apply the same V_s correction to Cl^- as to ClO^-, which results in an unaccountably large kinematic factor (for the ER-parent hypothesis). If our observed signal comes from an energetic dissociation, we do expect a somewhat steeper slope:

$$\frac{dE_{obs}}{dE'_0} = K\frac{m_{Cl}}{m_{OCl}}\left(1 + \sqrt{\frac{m_o}{m_{Cl}}\frac{E_d}{(KE'_0 - s)}}\right) \qquad 3\text{-}6$$

However, to bring our Cl^- slope from the anticipated $K_{ER}(O,Cl,Pt,\theta_T)\times m_{Cl}/m_{OCl} = 0.4360$ to this magnitude would require E_d of several tens of eV, which is inconsistent with our previous estimate and generally unrealistic. We can thus reject the hypothesis of prompt dissociation from a ClO^- parent. For the same reason, we can also reject dissociation of ClO_2^- as the source.

To this point we have assumed that the putative Cl^- parent is retarded by the surface potential. If the parent is neutral and ionization after a delay of some microseconds, the measured kinetic energy reflects E'_{out} directly. In this situation, the OCl^- and Cl^- energies are no longer at variance. Because the freezing distance for resonant charge transfer is on the order of a few angstroms,[32] far smaller than plausible Debye lengths at the target surface, the ionization would have to be occurring by some other mechanism (i.e. dipolar dissociation) to be consistent with reactive scattering. If one is willing to overlook the dramatic knee in $E_{out}(Cl^-)$ vs E_0, the data above E_0=75 eV suggest a kinematic factor of 0.33 (0.28, 0.37). This would seem to be in better agreement with a ClO_2 parent (K=0.3069, whether dissociation occurs in one step or two) than a ClO parent (K = 0.4360), although the uncertainty is quite large. In the absence of some explanation for the knee, we reject this hypothesis in favor of single knock-on processes (mech. 2B, 3B).

3.5 Conclusion

Scattering of hyperthermal water ions and O^+ on AgCl results in emission of energetic Cl^- ions in addition to the collision-cascade sputtered population. We have identified several near-threshold sputtering processes that produce kinematics consistent with the experimental data. These are kinetic mechanisms involving heavy surface atoms, rather than an effect of potential sputtering (coulomb explosion). Double-scattering trajectories are sufficient to account for the high energy tail. We probed scattering on a more recalcitrant halide, NaCl, mitigating surface charging via a platinum coating and high surface temperature. By deconvolving a reference scattering peak from the O^- energy distribution, we obtained a surface charge distribution which enabled the extraction of useful kinematics for O_2^-, ClO^-, and Cl^- secondary ions. For each product, the high exit energies were mediated by Pt surface atoms. The energetic O_2^- and ClO^- appear to be products of Eley-Rideal reactions, abstraction of adsorbed O and Cl by impinging O^+. The behavior of the fast Cl^- population is inconsistent with dissociation of scattered ClO, but, as for AgCl, can be explained by single knockon sputtering processes.

3.6 References

1. McCord, T. B. *et al.* Salts on Europa's Surface Detected by Galileo's Near Infrared Mapping Spectrometer. *Science* **280**, 1242–1245 (1998).
2. Trumbo, S. K., Brown, M. E. & Hand, K. P. Sodium chloride on the surface of Europa. *Sci. Adv.* **5**, eaaw7123 (2019).
3. Desai, R. T. *et al.* Hybrid Simulations of Positively and Negatively Charged Pickup Ions and Cyclotron Wave Generation at Europa. *J. Geophys. Res. Space Phys.* **122**, (2017).
4. Volwerk, M., Kivelson, M. G. & Khurana, K. K. Wave activity in Europa's wake: Implications for ion pickup. *J. Geophys. Res. Space Phys.* **106**, 26033–26048 (2001).
5. Rabalais, J. W. Sputtering of Metals and Insulators with Hyperthermal Singly and Doubly Charged Rare-Gas Ions. in *Low energy ion-surface interactions* 355–386 (J. Wiley & sons, Chichester New York Brisbane [etc.], 1994).
6. Postawa, Z. Desorption of alkali halides stimulated by ion bombardment. *Radiat. Eff. Defects Solids* **128**, 107–125 (1994).
7. Szymoński, M., Overeijnder, H. & De Vries, A. E. The sputtering processes during 6 kev Xe ion beam bombardment of halides. *Radiat. Eff.* **36**, 189–196 (1978).
8. Miyagawa, S. Energy spectrum of Na+ ions sputtered from NaCl crystals. *J. Appl. Phys.* **44**, 5617–5618 (1973).
9. Varga, P. *et al.* Sputter yields of insulators bombarded with hyperthermal multiply charged ions. *Phys. Scr.* **1997**, 307 (1997).
10. Hayderer, G. *et al.* Threshold for Potential Sputtering of LiF. *Phys. Rev. Lett.* **83**, 3948–3951 (1999).
11. Seifert, N., Husinsky, W., Betz, G., Yan, Q. & Tolk, N. H. Sputtering of LiF films induced by low-energy Ar + impact. *Phys. Rev. B* **51**, 12202–12208 (1995).
12. Neidhart, T. *et al.* Secondary ion emission from lithium fluoride under impact of slow multicharged ions. *Nucl. Instrum. Methods Phys. Res. Sect. B Beam Interact. Mater. At.* **98**, 465–468 (1995).
13. Hayderer, G. *et al.* Kinetically Assisted Potential Sputtering of Insulators by Highly Charged Ions. *Phys. Rev. Lett.* **86**, 3530–3533 (2001).
14. Thompson, M. W., Colligon, J. S., Smith, R., Aumayr, F. & Winter, H. Potential sputtering. *Philos. Trans. R. Soc. Lond. Ser. Math. Phys. Eng. Sci.* **362**, 77–102 (2003).
15. Shi, Y. *et al.* Observation of significant electron loss in grazing scattering of negative ions off a LiF(100) surface. *Appl. Surf. Sci.* **487**, 116–126 (2019).
16. Miraglia, J. E. Mechanism for electron emission and exciton formation during collisions of neutral hydrogens with a LiF(001) surface. *Phys. Rev. A* **90**, 062715 (2014).
17. Winter, H., Auth, C. & Borisov, A. G. Formation of negative ions in grazing scattering from a LiF(100) surface. *Nucl. Instrum. Methods Phys. Res. Sect. B Beam Interact. Mater. At.* **115**, 133–136 (1996).
18. Kudo, T. & Fueki, K. *Solid State Ionics*. (Kodansha ; VCH, Tokyo, Japan : Weinheim, F.R.G. ; New York, NY, USA, 1990).
19. Tubandt, C. & Lorenz, E. Molekularzustand und elektrisches Leitvermögen kristallisierter Salze. *Z. Für Phys. Chem.* **87U**, 513–542 (1914).

20. Ray, M. P., Lake, R. E. & Sosolik, C. E. Energy transfer in quasibinary and collective scattering events at a Ag(001) surface. *Phys. Rev. B* **79**, 155446 (2009).
21. DiRubio, C. A., McEachern, R. L., McLean, J. G. & Cooper, B. H. Energy transfer, trapping, and the interaction potential in hyperthermal Na + scattering from Cu(001). *Phys. Rev. B* **54**, 8862–8881 (1996).
22. Gnaser, H. *Low-Energy Ion Irradiation of Solid Surfaces*. (Springer, Berlin ; New York, 1999).
23. Bringa, E. M. & Johnson, R. E. Coulomb Explosion and Thermal Spikes. *Phys. Rev. Lett.* **88**, 165501 (2002).
24. Tosi, M. P. Cohesion of Ionic Solids in the Born Model. in *Solid State Physics* vol. 16 1–120 (Elsevier, 1964).
25. Thompson, M. W. Atomic collision cascades in solids. *Vacuum* **66**, 99–114 (2002).
26. Zhou, X. W., Wadley, H. N. G. & Sainathan, S. Low energy sputtering of nickel by normally incident xenon ions. *Nucl. Instrum. Methods Phys. Res. Sect. B Beam Interact. Mater. At.* **234**, 441–457 (2005).
27. Yamamura, Y., Takiguchi, T. & Kimura, H. Ion-induced desorption in the near-threshold regime. *Nucl. Instrum. Methods Phys. Res. Sect. B Beam Interact. Mater. At.* **78**, 337–341 (1993).
28. Szymonski, M. *et al.* Electron stimulated desorption of neutral species from (100) KCl surfaces. *Surf. Sci.* **260**, 295–303 (1992).
29. Dou, Q., Lync, D. W. & Bevolo, A. J. Electron-irradiation-induced structural and compositional changes on alkali halide surfaces. *Surf. Sci.* **219**, L623–L627 (1989).
30. Hooton, I. E. & Jacobs, P. W. M. Ionic conductivity of pure and doped sodium chloride crystals. *Can. J. Chem.* **66**, 830–835 (1988).
31. Yao, Y. & Giapis, K. P. Dynamic molecular oxygen production in cometary comae. *Nat. Commun.* **8**, 15298 (2017).
32. Winter, H. Collisions of atoms and ions with surfaces under grazing incidence. *Phys. Rep.* **367**, 387–582 (2002).

Chapter 4

REACTIVE SCATTERING OF WATER GROUP IONS ON ICE SURFACES

Content for this chapter is adapted with permission of Elsevier from published work:
Grayson, R. W., Goddard, W. A. & Giapis, K. P. Reactive scattering of water group ions on ice surfaces with relevance to Saturn's icy moons. *Icarus* **379**, 114967 (2022).

4.1 Introduction

Collisions of hyperthermal water group ions (10−300 eV) with ices are known to occur in many solar system environments and are frequently associated with observation of volatiles like O_2 and CO_2. For example, the largest ion fluxes onto Saturn's icy moons Rhea and Dione come from the co-rotating plasma, which consists primarily of water group ions (O^+, OH^+, H_2O^+, and H_3O^+, collectively abbreviated W^+) with thermal energies less than the corotational energy.[1] The plasma corotational velocity is ~40 km s^{-1} and ~50 km s^{-1} for Dione and Rhea, respectively,[1] notably faster than the orbital velocity of these moons. In the moon's rest frames, these speeds correspond to H_2O kinetic energies of ~150 eV and ~230 eV, respectively. Unfortunately, experimental studies at these energies are scarce. Experiments have instead focused on ion bombardment of water ice at much higher kinetic energies (>1 keV) and/or with less-relevant nonreactive ions, where physical sputtering and radiolysis dominate.[2–7] Hyperthermal ions are weak drivers of radiolysis, since their primary collisions frequently fail to transmit enough energy for bond dissociation.[2] Despite their abundance, such ions are consequently regarded as a relatively inert component of the radiation environment at Saturn's moons.

In contrast, the effect of hyperthermal atomic oxygen bombardment on spacecraft materials has been studied in great depth for decades. Materials in low Earth orbit (LEO) are readily oxidized by atomic oxygen sourced from Earth's upper atmosphere, and the resulting erosion comprises an important engineering consideration. More recently, research motivated by the detection of molecular oxygen in the coma of comet 67P by the Rosetta orbiter[8] demonstrated a similar effect on geological materials. In the coma of 67P, outgassing and photoionization generate a population of water group ions that are accelerated back toward the nucleus by the solar wind and ultimately impact the surface at hyperthermal energies. Collisions of such H_2O^+ pick-up ions (PUIs) with silica and iron oxide surfaces were shown to produce O_2^- and HO_2^- by an Eley-Rideal (ER) reaction

mechanism, that is, a direct reaction between gas phase projectiles and surface atoms/adsorbates that proceeds without an intervening adsorption step for the projectile.[9] Although the PUI flux to the 67p nucleus is insufficient to produce the O_2 abundance reported,[10] follow up work confirmed that O_2 formation by hyperthermal water-ion bombardment is a rather general phenomenon for oxygen bearing surfaces, proceeding even on man-made materials covering the spacecraft.[11]

In view of the above and in order to provide motivation for experimental studies, we report here results from reactive molecular dynamics (RMD) simulations of ion-surface scattering under conditions relevant to Saturn's moons Dione and Rhea. These simulations focus on collisions between water group molecules and single-crystalline, hexagonal water-ice (1h phase) surfaces at velocities around 20 km s^{-1}.

4.2 Methods

The ReaxFF reactive force field[12] is implemented in LAMMPS[13] using the QEq charge equilibration method[14] to describe the dynamic charge distribution.[15] The ReaxFF formalism can describe bond breaking and forming processes dynamically through a bond order/bond distance relationship, generally fitted to DFT calculations, and has been applied successfully to a variety of reactive systems.[16] We use the force-field parameterization developed by van Duin *et al.* to describe proton transfer reactions in water.[17] Their parameter optimization included dissociation of H_2, O_2, and H_2O_2, as well as binding of ice 1h and $OH^-[H_2O]_n$ and $H_3O^+[H_2O]_n$ clusters. Except where noted, our simulations use a periodic slab of ice 1h 15 Å thick and approximately 40×39 Å in the x and y dimensions.[18] This leads to a total of 720 H_2O molecules. A vacuum headspace of 105 Å is included above the surface to prevent the slab from interacting with its images in the z direction. After energy minimization, the structures are equilibrated for 10 picoseconds at a temperature of 70 K using a Nose-Hoover thermostat with damping constant of 50 fs and a timestep of 0.1 fs. The equilibrium lattice parameters in the periodic directions (x, y) were adjusted as needed so that the principal x and y components of the virial pressure term were near zero (within 50 atm). Finally, the structure was equilibrated at 70 K for 20 ps.

For each condition (temperature, velocity, angle, etc.), we performed many (≥300) independent collision simulations. For a given type of surface (basal or prism face), each simulation begins from the same periodic ice structure but with all atomic velocities assigned randomly according to a Maxwell-Boltzmann distribution (Gaussian) and rescaled to the target temperature. The projectile (O, OH, or H_2O) center of mass (COM) is randomly assigned over the x-y plane while z is fixed at 5.5 Å above the highest atom in the ice slab. For molecular projectiles, the projectile is also

randomly rotated about its COM. The projectile trajectory is then initialized at a given angle θ_{in} (relative to the surface plane, where θ_{in}=90º is normal incidence) and velocity magnitude $|\mathbf{V}_{in}|$ in the range of 10 to 35 km s^{-1} (8 to 102 eV for O). The azimuthal angle φ_{in} of the projectile trajectory is also randomized for each simulation. All simulations use a 0.05 fs time step. We follow a small number of simulations (300) for 2 ps in order to understand the time evolution of the ice. We run a larger number of simulations (≥500) at each condition for a shorter duration to facilitate ensemble averaging. We run these shorter simulations for 215 fs plus the amount of time for the projectile to transit 5.5 Å in the z direction. For example, at θ_{in} = 45º and $|\mathbf{V}_{in}|$=20 km/s, the projectile takes 35 fs to reach the ice surface, so we run the simulation for 250 fs. Under different conditions of θ_{in} and $|\mathbf{V}_{in}|$ this results in different total simulation durations but a constant time for ice evolution after the impact, which is critical because these shorter simulations end before the ice has reached equilibrium.

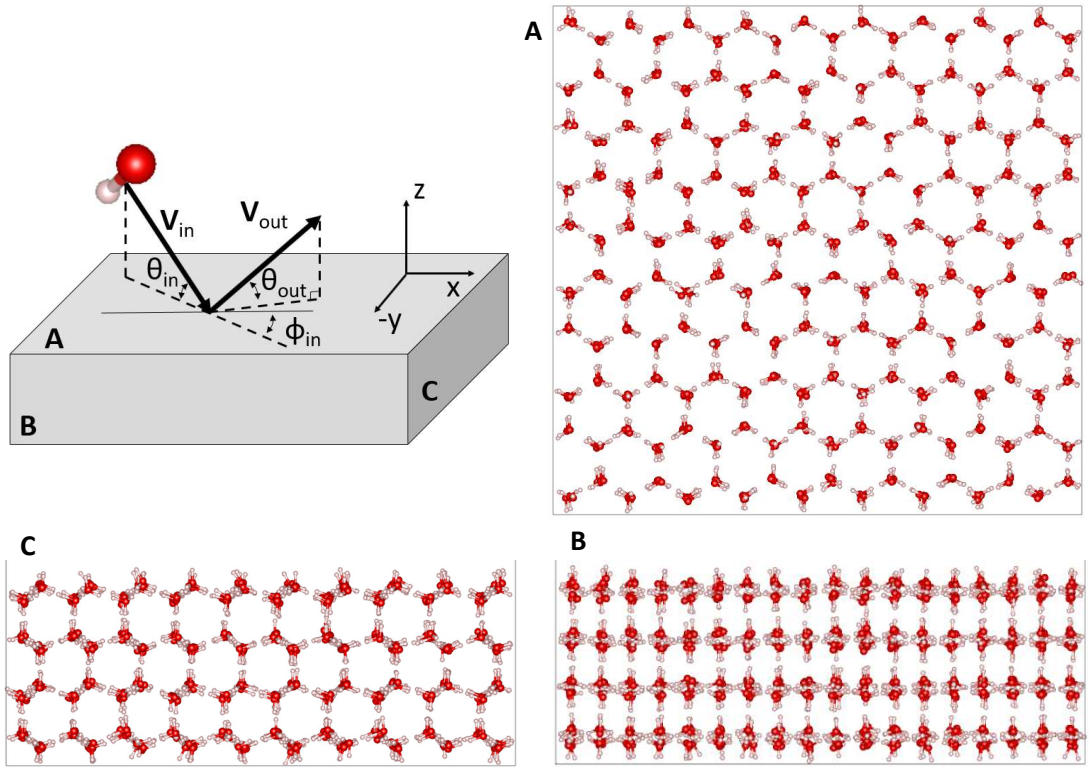

Figure 4-1: Schematic of collision geomery and visualization of the basal-plane ice 1h slab used in the simulations. Each image (A,B,C) of the slab is shown as viewed perpendicular to the corresponding face in the schematic. The headspace is excluded.

In the physical system, molecules leaving the ice slab are lost to the vacuum and can no longer influence the ice. For the long-duration simulations, there is enough time for fast moving species

to traverse the headspace and impact the slab from below. We prevent these molecules from influencing the ice evolution by freezing in place any molecules that enter the region between 65 and 85 Å above the ice slab. These molecules are still included in our analysis, as though they moved off ballistically into the vacuum. Preliminary simulations revealed a substantial amount of penetration of the 15 Å thick ice slab at impact velocities above 20 km s^{-1}. To mitigate this issue, we use a slab of double thickness (29 Å), but similar volume (27×31 Å width), for simulations with $|\mathbf{V}_{in}| \geq 25$ km s^{-1} (Supplemental Fig. A-1). Penetration is thus limited to <1% over the 10−35 km s^{-1} range.

In these simulations, we use the QEq charge equilibration method[14,15,19] to relax the charge distribution for the entire simulation cell by minimizing the electrostatic energy at every time step subject to the constraint of net charge neutrality. The charge state of the projectile is thus assumed to be equilibrated with the ice slab at all times, rather than being explicitly treated as an ion on the inbound trajectory. These simulation results are applicable to the fraction of impinging W+ ions that are Auger neutralized (or resonant neutralized and deexcited) during the surface interaction.

For each collision simulation, bond order (BO) data is analyzed to determine the chemical composition. For the short-duration simulations, this analysis follows energy minimization of the final structure. We use a simple bond order threshold of 0.3 to identify molecules. In the disturbed ice structure following impacts we find many strong hydrogen bonds which meet the bond order threshold, so that further discrimination is needed in computing yields of some species. In reporting yields, clusters are treated according to their net excess/deficit of hydrogen atoms relative to the neutral cluster. For instance, the cluster $O[H_2O]_2$ is counted toward the yield of atomic oxygen, and $H_3O[H_2O]$ is counted toward the yield of H_3O. Although clusters as large as $[H_2O]_4$ were observed, clusters involving more than solvating water were rare.

4.3. Results

4.3.1 Ice evolution

For each collision simulation, velocity data are processed to determine an approximate temperature by species using equipartition theorem for the translational degrees of freedom of the molecular COM. Although clusters are considered in determining the yield, they are excluded from the temperature computation. We use a simple z-position threshold to assign molecules to the solid or gas phase. Molecules with COM above the highest atom in the ice (as determined at t=0) are regarded as being in the gas phase. Yield for each species is determined by averaging the final count (irrespective of phase, except where otherwise noted) across the relevant set of simulations. Figure

4-2 shows the yield of several product molecules as a function of time for an atomic oxygen projectile impacting the basal plane of a 70 K ice-1h slab at 45° angle of incidence and $|\mathbf{V}_{in}|$=20 km s^{-1}.

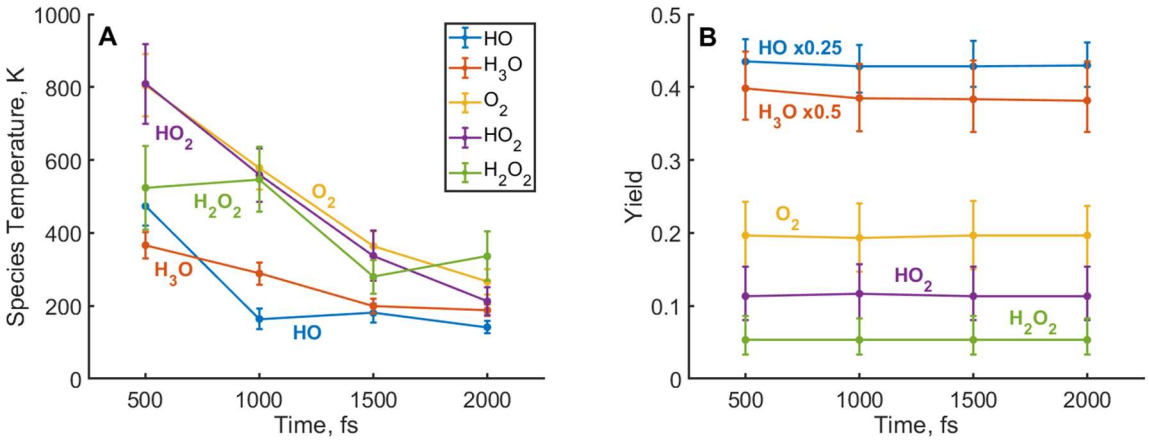

Figure 4-2. Time evolution of ice temperature and composition. **A**: Approximate temperature by species vs time averaged across 300 simulations at each timestep. Only molecules within the slab are considered. Error bars represent the sample standard deviation. **B**: Yield by species vs time for the same set of 300 simulations. The yields for HO and H_3O are rescaled by factors of 0.25 and 0.5, respectively, for readability. Here and in later figures describing yields, the error bars are the wider limits of bootstrapped 95% CI or ±1/(number of simulations).

In a large fraction (35%) of simulations an oxygen-oxygen bond is formed immediately on impact between the atomic oxygen projectile and an ice molecule in the slab. Frequently, one or both hydrogens are ejected from the molecule, resulting in formation of a mixture of molecular oxygen, hydroperoxyl radicals, and hydrogen peroxide (in order of decreasing prevalence). These products are formed early in the trajectory via inelastic collisions, which preserve much of the initial kinetic energy of the projectile. Consequently, the HO_2, H_2O_2, and O_2 formed are very hot. Consistent with their immediate formation, the yield for these molecules seems to be relatively stable over time as the system relaxes. In contrast, H_3O and OH are formed, destroyed, and accommodated in water complexes throughout the collision cascade, after much of the initial kinetic energy has been dispersed, resulting in lower temperatures for these species and more variable yield through time.

Hyperthermal ions are typically inefficient drivers of radiolysis because only a fraction of their kinetic energy is ultimately available for breaking bonds. For O^+, the fraction of energy available for radiolysis has been estimated to be less than half of the incident kinetic energy at 100 eV.[2] According to this estimate, an oxygen projectile at 20 km/s should contribute only a few eV toward

dissociation, falling short of the 5.4 eV OH bond dissociation energy in water. At 30 km s^{-1}, enough energy is available to dissociate around 5 of these bonds. Our simulations show radiolysis yields roughly consistent with these expectations, except that at the lowest impact velocities OH yield is buoyed to the order of unity by the projectile reactivity.

The O_2, HO_2, and H_2O_2 molecules created in our simulation form by an Eley-Rideal mechanism; that is, they are formed between a gas phase atom and a surface atom without intermediate adsorption and thermalization. We discuss these promptly formed species further by examining a larger number of short simulations.

4.3.2 Prompt reactions with atomic oxygen

As discussed above, the initial kinetic energy of the projectile is important to the O–O bond formation mechanism. In order to elucidate the role of impact velocity, we carried out 500 short impact simulations for an atomic oxygen projectile impacting the basal plane of ice-1h at 10–35 km s^{-1}. To facilitate our investigation of the O_2 formation mechanism, we simulated a total of 1900 impacts at $|\mathbf{V}_{in}|$ = 20 km s^{-1}.

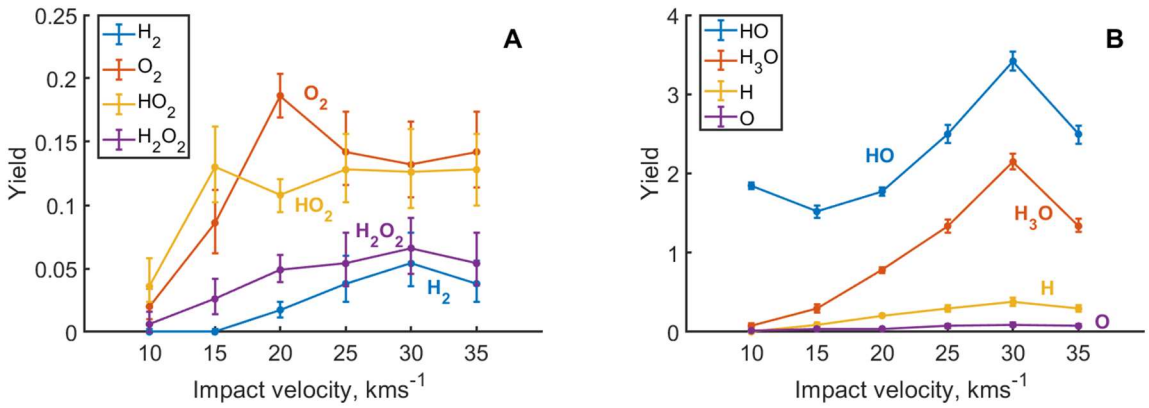

Figure 4-3: Yield of several product molecules as a function of $|\mathbf{V}_{in}|$ for an atomic oxygen projectile impacting the basal plane of a 70 K ice-1h slab at 45° angle of incidence. Species are separated into **A** and **B** subplots for readability. Each data point is an average over 500 simulations, except at 20 km s^{-1} where 1900 runs are averaged. The atomic oxygen yield is not netted against the O projectile.

At 10 km s^{-1}, we find that in most cases the oxygen projectile abstracts one or two hydrogen atoms from the ice to form hydroxyl radical or H_2O. A small fraction of trajectories results in molecular oxygen (2%) or surviving atomic oxygen (1%). As the impact velocity is increased, survival of the incident atomic oxygen becomes more frequent, largely at the expense of H_2O formation.

Fragmentation of the ice target also increases at higher impact velocities, producing an abundance of OH and H. In addition, a substantial amount of sputtering occurs. At $|\mathbf{V}_{in}|$= 20 km s^{-1} an average of 2.1 water molecules are ejected from the surface per impact with velocities averaging 2.1 km s^{-1}. Notably, O_2, HO_2, and H_2O_2 formation peaks at 20 km s^{-1}, with the yield for oxygen-oxygen bond formation reaching 35%.

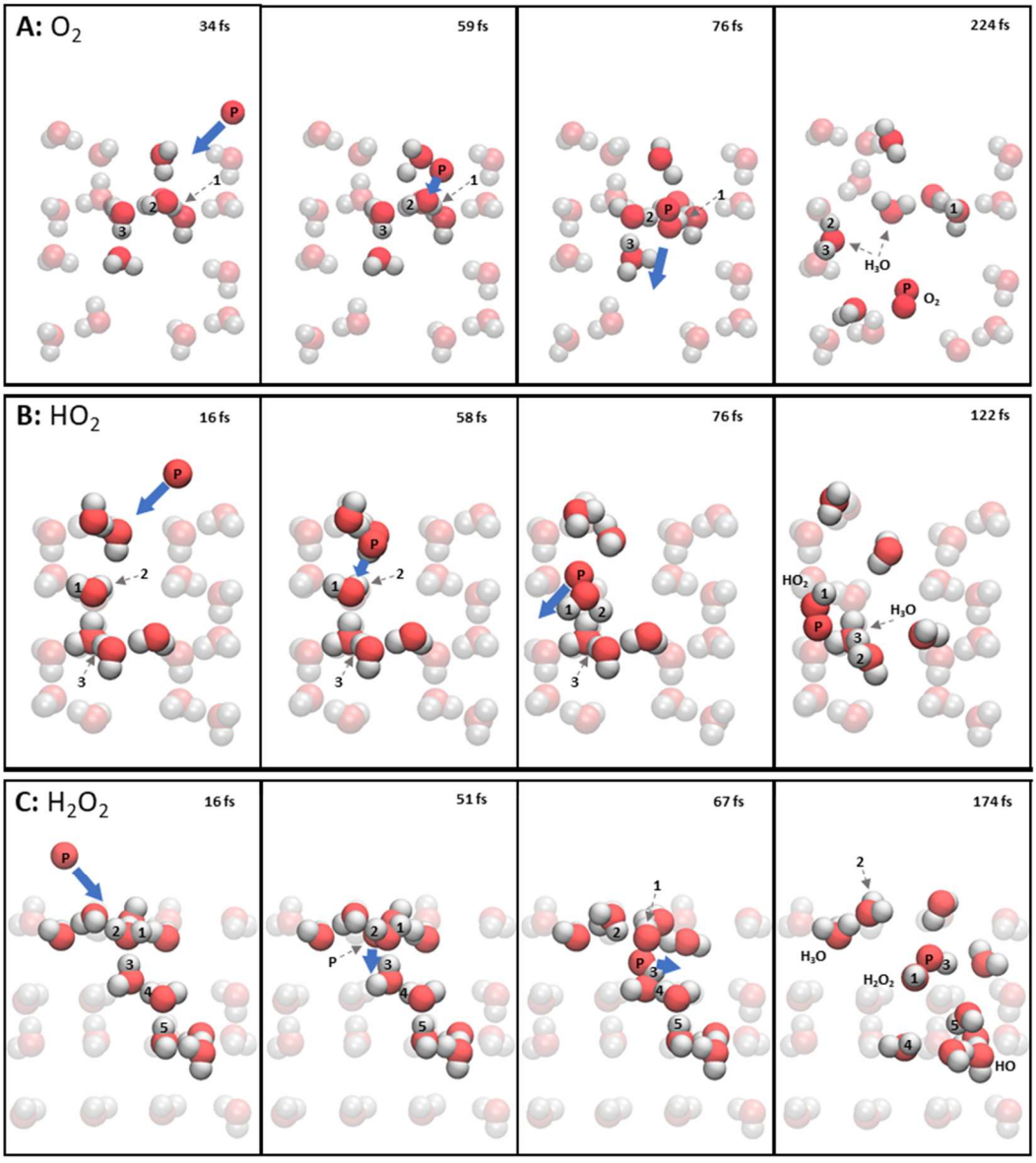

Figure 4-4: Snapshots from simulations of an atomic oxygen projectile (**P**) impacting ice at 20 km s^{-1} and 45° showing formation of O_2 (**A**), HO_2 (**B**), and H_2O_2 (**C**). Most spectator molecules have been omitted and some atoms are numbered, in no particular order, to clarify their movements. The blue arrows indicate the projectile's direction of motion approximately.

Molecular oxygen dominates the O−O bonded products. At 20 km s^{-1}, O_2 is typically formed during the first or second collision of the projectile with a water molecule. In the single collision mechanism, which accounts for the majority of reactions, the formation of a stable O_2 molecule involves nearly simultaneous ejection of both hydrogen atoms. In the double collision mechanism, the projectile glances off a first water molecule before colliding with a second and ejecting the hydrogens to form O_2 (Figure 4-4 A). In either case, the resulting O_2 molecule retains much of the projectile's kinetic energy, and a relatively violent collision with H_2O follows. Occasionally, O_2 is hydrogenated during this interaction, with <2% of O_2 being converted to HO_2 and <1% to H_2O_2. At higher collision energies (v = 30 km s^{-1}), water dissociation alone can no longer dissipate enough kinetic energy to stabilize the O_2 bond, and O_2 formation proceeds via two or more projectile-water collisions.

Hydrogen peroxide and HO_2 form via a similar mechanism, although the single and double collision processes occur with roughly equal frequency. In most cases, HO_2 forms through the dissociation of a single OH bond in the projectile-water collision (Figure 4-4 B). In the balance of cases, the collision partner dissociates completely, and a formerly hydrogen-bonded neighbor immediately transfers one hydrogen atom. The hydrogen atoms in the H_2O_2 product belonged initially to different water molecules, except in very rare cases. Hydrogen peroxide formation thus involves abstraction of H from water prior to O–O bond formation (in the double collision mechanism) or prompt hydrogenation of HO_2 (in the single collision mechanism, depicted in Figure 4-4 C). In any case, most hydrogen atoms liberated by the projectile are accommodated by the ice as H_3O and displaced by the Grotthuss mechanism as seen in Figure 4-4 A–C.[20] A smaller portion of H remain free (26 per 100 H_3O), and >99% of these escape the ice slab within the simulation duration.

Since the collision is very fast relative to thermal motion, the outcome of each impact is primarily determined by the collision geometry set by the initial trajectory, not by the stochasticity of thermal motion. By binning trajectories based on the direction of the initial impactor velocity vector we can ascertain the correlation between collision geometry and O_2 formation at 250 ps. Figure 5 shows the O_2 yield for trajectories binned over 3° intervals. The angular coordinate is the angle between the positive x axis and the projection of $\mathbf{V}_{in}$ onto the surface plane. We mod the angle by 60 and fold the resulting 60° range in half to account for the symmetry of the oxygen sublattice.

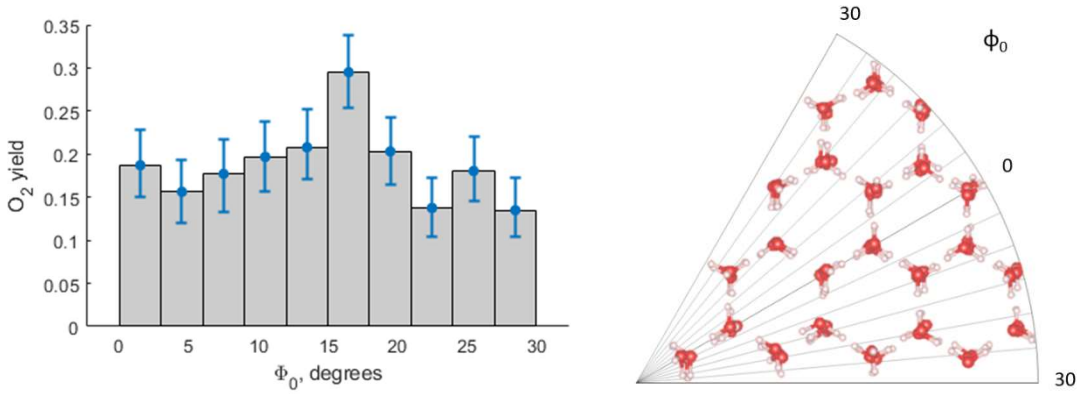

Figure 4-5. O_2 yield vs the angle between the positive x axis and the projection of V_0 onto the x−y plane for 1900 impacts of 20 km s^{-1} O at 45°. The angular coordinate was reduced into the 0−30° range using the symmetry of the oxygen lattice (6-fold symmetry resulting in 60° wedges that each have mirror symmetry). The yield was computed as the number of trajectories that produced O_2 divided by the total number of trajectories within 3° bins on the reduced coordinate.

Molecular oxygen formation through the single collision mechanism is independent of the orientation of $\mathbf{V}_{in}$ relative to the crystal, contributing to relatively uniform O_2 yield. There is a peak in the yield near 15°, where $\mathbf{V}_{in}$ misaligns with rows of oxygen atoms. This orientation preference reflects O_2 formation in two or more collisions, after small deflection of the projectile out of the plane of incidence. Along this direction, the first and second nearest neighbor oxygen atoms in the surface plane are accessible by 45° or 15° deflections from the POI. At alignments close to 0 and 30°, the second nearest neighbor is only accessible by 0 or 60° deflections from POI, lowering the probability of the two-collision process.

In light of the orientation preference seen in Figure 4-5, we expect different crystal faces of ice 1h to produce O_2 at different rates. To examine this effect, we simulated collisions of atomic oxygen ($|\mathbf{V}_{in}|$=20 km s^{-1}, θ_{in} = 45°) with the prism face of hexagonal ice (Supplemental Fig. A-2) to compare with results from basal face (Figure 4-1 A) scattering. We find that product yields are not strongly affected by the change in surface structure (Supplemental Fig. A-3), except that on the prism face survival of atomic oxygen increased at the expense of water and O_2 formation. The decrease in O−O bond formation events for prism face scattering might be explained by the absence of staggered rows of oxygen atoms in the x-y projection of the surface.

4.3.3 Gas phase products

A flux of ions normal to the surface at a topographical length scale will actually sample a range of θ_{in} due to surface roughness. In order to probe the effect of surface roughness, we simulated atomic oxygen impacts at three angles (θ_{in} = 22.5, 45, and 67.5°) with $|\mathbf{V}_{in}|$ fixed at 20 km s^{-1} (see Supplemental Fig. A-4). Production of O_2 peaks at 45°, dropping to 14.6% at 22.5° and 11.6% at 67.5°. This is likely due to obstruction of the incoming trajectory by OH bonds protruding from the ice surface for 22.5 and 67.5° angles of incidence. By contrast, at θ_{in} = 45° the O projectile is least impeded by dangling hydrogens.

For simulations at 45° and 67.5° incidence, no dioxygen emerges from the surface. Instead, it is implanted in the first several molecular layers of the ice where from it can escape the surface quickly due to its kinetic energy and shallow implantation depth (3 to 10 Å). Indeed, 3% of O_2 formed has escaped the ice by 2 ps. Although we expect all of these molecules to escape the ice eventually (due to the volatility of O_2 at the temperature of our simulation), our simulation duration is not sufficient to capture this process.

We find that at θ_{in} = 22.5°, 45% of the O_2 molecules formed rebound from the ice surface with velocities greater than 1.5 km s^{-1}. The relative abundance of fast O_2 bonded products at θ_{in} = 22.5° makes it possible to resolve the θ_{out} distribution coarsely. Fast O_2 products are seen sharply peaked around θ_{out} = 45° with a corresponding peak in the product velocity (Figure 4-6). Fast products are of particular interest for several reasons. Experimentally, scattered products display a "memory" of the incident energy to provide confirmation of an ER reaction mechanism. These O_2 molecules rebound at an average velocity of 4.1 km s^{-1} (min: 1.55 km s^{-1}, max: 7.78 km s^{-1}, standard deviation: 1.47 km s^{-1}), easily exceeding the escape velocity of Dione (0.51 km s^{-1})[21] and Rhea (0.64 km s^{-1})[22], so they could be detectable by orbiting spacecraft and may constitute a significant mass loss channel.

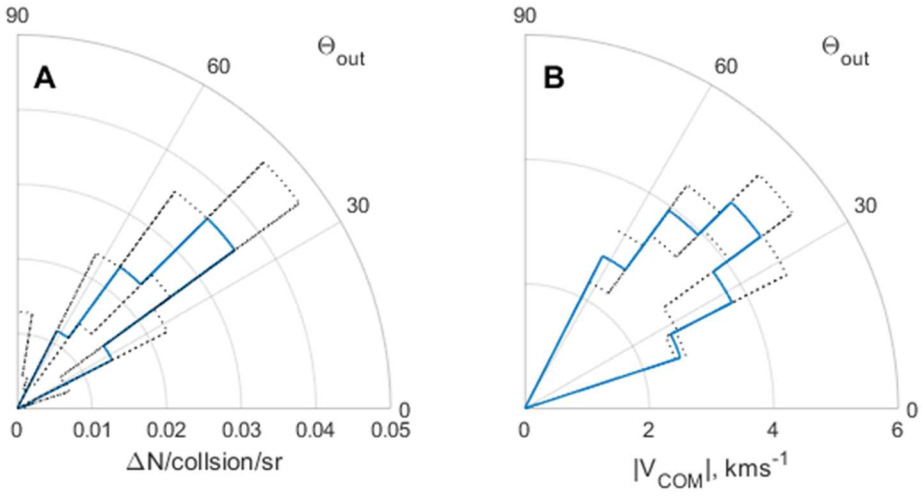

Figure 4-6. O_2 product angular distributions for atomic oxygen projectiles at θ_{in} = 22.5° and 20 km s^{-1}. **A**- Differential yield of gas-phase O_2 products (out of n = 1000 trajectories) vs outgoing angle. θ_{out} is the angle between the product COM velocity and the ice surface at the end of the simulation (90° is normal to the surface), so that the bin limits define an open spherical sector. Data are binned by θ_{out} in 9° intervals. The dotted traces are the wider limits of bootstrapped 95% CI or ±1/(number of simulations)/sr. **B**- Velocity of the same (averaged over the bin) vs θ_{out}. The dotted traces are error bars at ± the bin standard error.

The temperature dependence for reactive scattering at hyperthermal energies should be small because thermal velocities are on the order of one hundredth of the projectile velocity. We tested different initial temperature conditions by cooling/warming the 70 K basal plane ice slab over 5 ps and equilibrating at the new temperature for 20 ps without regard for thermal expansion. We ran 500 collision simulations with the atomic oxygen projectile incident at θ_{in} = 45° and 20 km s^{-1} on the basal face of ice 1h at each temperature. As expected, the effect of the temperature on the yield is small compared to effects of other variables (See supplemental Fig. A-5).

4.3.4 Other water group projectiles

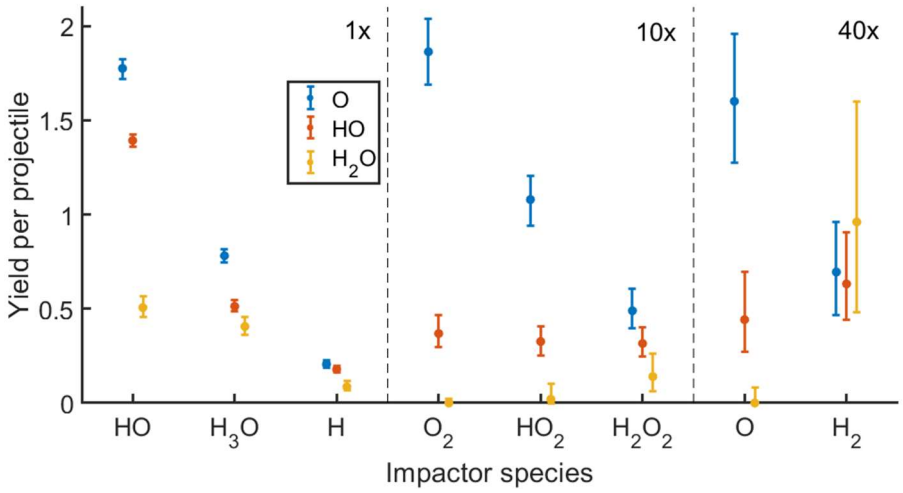

Figure 4-7. Product yield for various chemical species (x-axis) for different projectile molecules (O, HO, H_2O) for 45° incidence at 20 km s^{-1} with randomized azimuthal angle. For readability, the y scale is magnified by 10× for O_2, HO_2, and H_2O_2 species and by 40× for O and H_2. The O and OH yields are not netted against the projectile.

Although the atomic oxygen projectile is a useful and relevant starting case for beginning to understand reactive scattering on ice, the hyperthermal ion flux onto Dione and Rhea is comprised of a mixture of several water group ions. The fraction of O^+ in the magnetospheric plasma varies with radial distance from Saturn, but at the orbit of Dione, H_2O^+, OH^+, and O^+ abundances are approximately equal.[23] We expect different reactivity for each of these projectiles, so we conducted additional collision simulations for OH (1000 impacts) and H_2O (500 impacts) projectiles under the same conditions ($|\mathbf{V}_{in}|$= 20 km s^{-1}, θ_{in} = 45°, basal plane). The product yields are plotted in Figure 4-7. Under these conditions, atomic oxygen impactors produce O_2 an order of magnitude more efficiently than radiolysis (<0.02 O_2/O^+ impactor).[2] However, the yield of O_2, HO_2, and H_2O_2 drops dramatically as the projectile is increasingly hydrogenated. Survival of H_2O becomes the most likely outcome for H_2O projectiles, with dissociation products accounting for most of the balance. O_2 yield drops from 18.6% for the O projectile to 2.8% for OH impactors. The reactivity of the OH radical instead contributes to O–H bond formation, resulting in higher yield of H_2O. The sharp drop in O_2 yield for OH relative to O is owed to steric effects, with O_2 formation hindered in hydrogen-led trajectories.

As for the O projectile, H atoms displaced by HO and H_2O impactors are more frequently accommodated as H_3O than liberated from the ice slab, with fewer hydrogens escaping as the

projectile is increasingly hydrogenated. Assuming equal abundances for each of the three impactors and accounting for the volatility of H_2, around 8 H are accommodated for every 10 impactors, resulting in a net shift to oxygen rich stoichiometry.

4.4 Discussion

The mechanism of O_2 formation observed here is distinct from the usual radiolytic mechanism. It is well known that radiolytic O_2 yields depend on the exposure history of the sample, with steady state yields reached after a saturation dose on the order of 1×10^{15} ions/cm^2.[2] This saturation effect arises from the accumulation of oxygen rich precursors near the surface, where hydrogen is irreversibly lost from the ice. At the onset of ion exposure and, at steady state, deep (>30 Å) in the ice, H and H_2 facilitate the destruction of O_2 by successive hydrogenation and decrease the availability of reactive oxygen species by recombining with water fragments.[2,24] The notion of an oxygen rich surface layer facilitating O_2 synthesis is supported by the projectile range dependence found across the studies aggregated by Teolis.[2] The precursor concentrations near the surface are controlled by the interplay of surface erosion, radiolysis, radical reactions, and hydrogen out-diffusion, and it is the nature of the steady state concentration profile of precursors that ultimately dictates the O_2 yield. Recent efforts to model the source rates of O_2 exospheres at Dione and Rhea (Refs [21,22]) and Europa (Refs[7,25–28]) have relied on linear superposition of laboratory yields for steady state radiolysis by relatively monoenergetic ion beams. This approach predicts O_2 source rates at Dione and Rhea 50 and 300 times larger, respectively, than the observed source rates.[21] The discrepancy led researchers to speculate that an angstroms thick refractory lag layer sits at the ice surface and suppresses both radiolysis and secondary sputtering.[21] Alternatively, the discrepancy could be taken as evidence that there are significant co-exposure effects making the superposition approach invalid. Application of the laboratory steady state O_2 yields in this way is only accurate if the governing reaction-diffusion system is linear. It is difficult to rationalize such a scenario considering the physical and chemical complexities; even a linearizing approximation seems unlikely given that magnetospheric ion energies span several orders of magnitude.

As an illustration, consider the ion energy distribution at Dione, where half of W^+ impactors have energies below ~400 eV. At these low energies, ions are inefficient at radiolysis due to the relatively large dissociation energy of water. They do however remain quite effective at sputtering (since the surface binding energy, 0.52 eV,[29] is much smaller than the bond-dissociation energy, 5.15 eV).[2,6,30] These ions, therefore, increase the rate of surface erosion without contributing substantially to generation of radical precursors, enhancing apparent advection of unprocessed ice to the surface.

The hyperthermal flux thus decreases the residence time of ice through the heavily irradiated near-surface region, depressing the steady state concentration of O_2 and its precursors. By interfering with formation of an oxygen rich surface layer, simultaneous exposure of the ice to large low-energy ion fluxes may reduce the O_2 yield of higher energy ions, which is not anticipated by superposition. A more complete kinetic model is required to evaluate the linearity assumption.

Although radiolytic O_2 synthesis is hindered in this scenario, the ER reaction mechanism proceeds on such a surface. Moreover, the ER reaction forms O_2 at depths less than a few monolayers, so that O_2 should escape the ice surface quickly and consequently be less vulnerable to chemical destruction by hydrogen. Using the O_2 yield for O impactors at 10−35 km s^{-1} and neglecting the effects of temperature, crystallinity, and angle of incidence, we can crudely estimate the contribution of the ER reaction to the observed O_2 source rate at Dione and Rhea. Assuming O^+ comprises one third of the W^+ flux and the surface is entirely pure water ice, the direct oxidation of the ice by O^+ ions up to 35 km s^{-1} (102 eV) can supply roughly 22−32% of the observed O_2 source rate at Dione and 11−16% at Rhea, based on the W^+ energy distributions given in Teolis and Waite (2016). The uncertainty of this estimate is based solely on the confidence intervals of the simulated yields. In reality, many factors complicate the application of simulation results like these, and the uncertainty is much larger.

For instance, the interplay of plasma absorption and photoelectric emission creates a diurnal cycle of non-uniform surface charging on the trailing hemispheres of Saturn's icy moons. Generally negative surface potentials are expected, with extremes of −130 V (−50 V) predicted for Rhea and Dione.[31] A more accurate estimate of the O_2 source from direct oxidation must account for large distortions of the impactor energy distribution caused by variable surface charging. Additionally, the ER O_2 mechanism will be extremely sensitive to surface composition, since, at these energies, penetration is limited to the top few molecular layers. By analogy to the projectile hydrogenation effect (Figure 4-7), it should become more efficient at a hydrogen depleted surface. Distributed trace impurities are unlikely to affect yields strongly because of the highly local nature of the ER reaction (involving impacts with generally only one or two water molecules). On the other hand, it would be completely suppressed if impurities are concentrated into a continuous non-ice surface layer, even angstroms thick, like the one proposed by Teolis & Waite for Rhea and Dione.[21] Although, if such a surface can be oxidized, O_2 formation may proceed by a similar mechanism, as observed for hyperthermal H_2O^+ bombarded silica, iron oxide, and titania.[9] Direct oxidation of impure and mixed ice surfaces is a compelling subject for further research.

Although more complicated, similar considerations apply to Europa, where a corotating plasma of O^{n+} and S^{n+} (O/S ≈ 2−4)[32] overtakes the moon at a relative velocity of 76 km s^{-1}.[33] Eddy currents flowing in and around Europa perturb the plasma flow in its vicinity, diverting a large portion of low energy ions around the moon (estimated at 80% by Vorburger and Wurz 2018).[33,34] Large areas of Europa's surface are dominated by non-ice material, likely hydrated sulfuric acid or frozen brine.[35] Future studies should assess whether these hydrates behave similarly to pure water ice under O^+ bombardment.

4.5 Conclusion

Simulations of collisions of hyperthermal water group molecules with water ice surfaces demonstrate that molecular oxygen forms via an Eley-Rideal mechanism, with yields as high as 18% under some conditions. Dioxygen production is maximized for atomic oxygen projectiles (at 20 km s^{-1}) and drops sharply for more hydrogenated projectiles. At low angles of incidence (nearer normal incidence), the O_2 formed remains implanted within a few molecular layers of the surface, where it can desorb thermally or be sputtered to populate an exosphere. At high angles of incidence (nearer grazing incidence), a large portion of O_2 formed rebounds from the surface with hyperthermal velocities and will escape the weak gravity of Saturn's icy moons. This mechanism may be relatively important to maintaining the O_2 exospheres of Dione and Rhea, where the hyperthermal W^+ dose rate from the co-rotating plasma far exceeds the observed O_2 source rate.[21] In contrast to radiolytic O_2 production, accumulation of oxygen rich water fragments is not a prerequisite for O_2 synthesis via the ER mechanism, making it a viable source of O_2 on fresh ice. This mechanism may therefore become dominant in environments where high rates of resurfacing or erosion interfere with the accumulation of an oxygenated surface layer.

4.6 References

1. Howett, C. J. A. *et al.* Ring and Magnetosphere Interactions with Satellite Surfaces. in *Enceladus and the Icy Moons of Saturn* (The University of Arizona Press, 2018). doi:10.2458/azu_uapress_9780816537075-ch017.
2. Teolis, B. D., Plainaki, C., Cassidy, T. A. & Raut, U. Water Ice Radiolytic O2, H2, and H2O2 Yields for Any Projectile Species, Energy, or Temperature: A Model for Icy Astrophysical Bodies. *J. Geophys. Res. Planets* **122**, 1996–2012 (2017).
3. Muntean, E. A. *et al.* A laboratory study of water ice erosion by low-energy ions. *Mon. Not. R. Astron. Soc.* **462**, 3361–3367 (2016).
4. Galli, A., Vorburger, A., Wurz, P., Cerubini, R. & Tulej, M. First experimental data of sulphur ions sputtering water ice. *Icarus* **312**, 1–6 (2018).

5. Galli, A., Vorburger, A., Wurz, P. & Tulej, M. Sputtering of water ice films: A re-assessment with singly and doubly charged oxygen and argon ions, molecular oxygen, and electrons. *Icarus* **291**, 36–45 (2017).
6. Famá, M., Shi, J. & Baragiola, R. A. Sputtering of ice by low-energy ions. *Surf. Sci.* **602**, 156–161 (2008).
7. Cassidy, T. A. *et al.* Magnetospheric ion sputtering and water ice grain size at Europa. *Planet. Space Sci.* **77**, 64–73 (2013).
8. Bieler, A. *et al.* Abundant molecular oxygen in the coma of comet 67P/Churyumov–Gerasimenko. *Nature* **526**, 678–681 (2015).
9. Yao, Y. & Giapis, K. P. Dynamic molecular oxygen production in cometary comae. *Nat. Commun.* **8**, 15298 (2017).
10. Heritier, K. L. *et al.* On the origin of molecular oxygen in cometary comae. *Nat. Commun.* **9**, 2580 (2018).
11. Yao, Y. & Giapis, K. P. Reply to "On the origin of molecular oxygen in cometary comae". *Nat. Commun.* **9**, 2581 (2018).
12. Chenoweth, K., van Duin, A. C. T. & Goddard, W. A. ReaxFF Reactive Force Field for Molecular Dynamics Simulations of Hydrocarbon Oxidation. *J. Phys. Chem. A* **112**, 1040–1053 (2008).
13. Thompson, A. P. *et al.* LAMMPS - a flexible simulation tool for particle-based materials modeling at the atomic, meso, and continuum scales. *Comput. Phys. Commun.* **271**, 108171 (2022).
14. Rappe, A. K. & Goddard, W. A. Charge equilibration for molecular dynamics simulations. *J. Phys. Chem.* **95**, 3358–3363 (1991).
15. Aktulga, H. M., Fogarty, J. C., Pandit, S. A. & Grama, A. Y. Parallel reactive molecular dynamics: Numerical methods and algorithmic techniques. *Parallel Comput.* **38**, 245–259 (2012).
16. Senftle, T. P. *et al.* The ReaxFF reactive force-field: development, applications and future directions. *Npj Comput. Mater.* **2**, 15011 (2016).
17. van Duin, A. C. T., Zou, C., Joshi, K., Bryantsev, V. & Goddard, W. A. CHAPTER 6. A Reaxff Reactive Force-field for Proton Transfer Reactions in Bulk Water and its Applications to Heterogeneous Catalysis. in *Catalysis Series* (eds. Asthagiri, A. & Janik, M. J.) 223–243 (Royal Society of Chemistry, Cambridge, 2013). doi:10.1039/9781849734905-00223.
18. Hayward, J. A. & Reimers, J. R. Unit cells for the simulation of hexagonal ice. *J. Chem. Phys.* **106**, 1518–1529 (1997).
19. Nakano, A. Parallel multilevel preconditioned conjugate-gradient approach to variable-charge molecular dynamics. *Comput. Phys. Commun.* **104**, 59–69 (1997).
20. Cukierman, S. Et tu, Grotthuss! and other unfinished stories. *Biochim. Biophys. Acta BBA - Bioenerg.* **1757**, 876–885 (2006).
21. Teolis, B. D. & Waite, J. H. Dione and Rhea seasonal exospheres revealed by Cassini CAPS and INMS. *Icarus* **272**, 277–289 (2016).
22. Teolis, B. D. *et al.* Cassini Finds an Oxygen-Carbon Dioxide Atmosphere at Saturn's Icy Moon Rhea. *Science* **330**, 1813–1815 (2010).

23. Smith, H. T. *et al.* Enceladus and Its Influence on Saturn's Magnetosphere. in *Enceladus and the Icy Moons of Saturn* (The University of Arizona Press, 2018). doi:10.2458/azu_uapress_9780816537075-ch011.
24. Loeffler, M., Raut, U., Vidal, R., Baragiola, R. & Carlson, R. Synthesis of hydrogen peroxide in water ice by ion irradiation. *Icarus* **180**, 265–273 (2006).
25. Plainaki, C. *et al.* The role of sputtering and radiolysis in the generation of Europa exosphere. *Icarus* **218**, 956–966 (2012).
26. Teolis, B. D., Wyrick, D. Y., Bouquet, A., Magee, B. A. & Waite, J. H. Plume and surface feature structure and compositional effects on Europa's global exosphere: Preliminary Europa mission predictions. *Icarus* **284**, 18–29 (2017).
27. Plainaki, C. *et al.* Exospheric O2 densities at Europa during different orbital phases. *Planet. Space Sci.* **88**, 42–52 (2013).
28. Johnson, R. E. *et al.* The Origin and Fate of O 2 in Europa's Ice: An Atmospheric Perspective. *Space Sci. Rev.* **215**, 20 (2019).
29. Haynes, D. R., Tro, N. J. & George, S. M. Condensation and evaporation of water on ice surfaces. *J. Phys. Chem.* **96**, 8502–8509 (1992).
30. Rumble, J. R., ed. Bond Dissociation Energies in Polyatomic Molecules. in *CRC Handbook of Chemistry and Physics, 102nd Edition (Internet Version 2021)* (CRC Press/Taylor & Francis, Boca Raton, FL).
31. Roussos, E., Krupp, N., Krüger, H. & Jones, G. H. Surface charging of Saturn's plasma-absorbing moons. *J. Geophys. Res. Space Phys.* **115**, (2010).
32. Bagenal, F. *et al.* Plasma conditions at Europa's orbit. *Icarus* **261**, 1–13 (2015).
33. Margaret G. Kivelson, Krishan K. Khurana, & Martin Volwerk. Europa's Interaction with the Jovian Magnetosphere. in *Europa* 545–570 (University of Arizona Press, Tucson, 2009).
34. Vorburger, A. & Wurz, P. Europa's ice-related atmosphere: The sputter contribution. *Icarus* **311**, 135–145 (2018).
35. Carlson, R. W. *et al.* Europa's Surface Composition. in *Europa* 283–328 (University of Arizona Press, Tucson, 2009).

Chapter 5

METHANOL FORMATION IN HYPERTHERMAL OXYGEN BOMBARDMENT OF CARBON-BEARING CLATHRATE HYDRATES

5.1 Introduction

The presence and origin of organics at airless icy bodies is a topic of critical importance in planetary science. Methanol is an important precursor to complex organics with prebiotic significance (e.g. amino acids), common in cometary comae (typical abundance of 2% relative to water) and detected on Enceladus' surface and in its plume.[1–4] In the cometary context, methanol is presumed to be formed mostly prior to accretion, through successive hydrogen addition reactions. For example, in dense molecular clouds and, to a lesser extent, the protoplanetary disk[5] methanol can be synthesized via exposure of pure CO or mixed CO−H_2O ice grains to cold atomic hydrogen.[6–10] Comets are widely regarded as relatively pristine environments, presumed to closely resemble their initial compositions, and are used to infer conditions in the solar system's distant past.[11] Similarly, the composition of Enceladus' plume can indicate the composition of its interior ocean and thus its habitability. In both cases, it is vital to understand how the composition is modified by the radiation environment.

Since an overview of the radiation environment of Saturn's moons has been provided in preceding chapters, we will forgo a discussion of it here, except to mention that plume environment is quite different and covered in detail in Chapter 7. Instead, we will provide some brief introduction to the cometary system. Within their reservoirs, comets are indeed minimally processed, although methanol synthesis can continue over the lifetime of the comet due to radiolytic processing of CO−H_2O ice grains by cosmic rays[12] or through photolysis of CH_4−H_2O ices by UV photons.[13] New sources of radiation emerge with decreasing heliocentric distance, however. The coma evolves through interaction with the solar wind into an ionosphere, introducing energetic heavy ion bombardment. The Rosetta mission revealed this process in detail, following the evolution of Comet 67P's dynamic ionosphere starting from ~3.6 AU through perihelion, and beyond.[14] Among its discoveries was a population of water group ions accelerated by interaction with the solar wind to a mean energy of several hundred eV. These pick-up ions (PUIs) impinge on the nucleus' surface at fluxes comparable to or even exceeding the solar wind flux,[15] potentially altering the ice and coma composition.

Cometary ices comprise predominately water with widely varying abundances of volatile carbon-bearing species: CO_2 (4−30%, relative to water), CO (0.4−30%), and CH_4 (0.4−1.6%).[11] Although hypervolatiles such as CH_4 and CO are abundant, they are among the first species to be lost with decreasing heliocentric distance. These species can, however, be preserved by enclathration into water ice during the amorphous to crystalline transition[16] and, for short period comets, survive at the nucleus surface during periods of high activity.[17] Indeed, the presence of CH_4 and C_2H_6 clathrates has been inferred at 67P on the basis its outgassing pattern.[18] Carbon bearing clathrate hydrates are thus made available for processing by accelerated water group ions.

Ions in the hyperthermal energy regime are relatively radiolytically inert because much of the collision cascade fails to meet the threshold for bond dissociation, and the energy is dissipated thermally. When the impinging ions are reactive, however, the excess kinetic energy can drive unexpected chemistry, as we demonstrated in the previous chapter.[19] But, the literature sheds little light on how reactive hyperthermal impactors modify the organic inventory of ices. Most research on ion irradiation of ices is generally limited to much higher kinetic energies (>5 keV), where radiolysis is the primary driver of chemistry (see [20]). The problem is not less acute for the subtopic of formation/destruction of organics. Ennis et al. (2011) irradiated methane ice with 5 keV O^+ and detected methanol sublimation from the sample upon warming.[21] Unfortunately, methanol eluded their primary analytical technique (FTIR spectroscopy), so that they could not quantify its abundance or ascertain the formation mechanism. Here, we perform reactive molecular dynamics (RMD) simulations of low energy water-group molecule bombardment of carbon bearing ices to investigate whether it presents an alternative mechanism for methanol formation.

5.2 Methods

5.2.1 Single impacts

The simulation methodology for this work is very similar to that of Grayson et al. (2022), presented in the previous chapter, but with some slight differences. Again, we use the ReaxFF formalism to model dynamic bond breaking and formation during the impact simulations, implemented in the Large-scale Atomic/Molecular Massively Parallel Simulator (Lammps).[22–24] Although ReaxFF has proven accurate and useful in simulating a wide variety of chemical phenomena,[25] it does not explicitly handle electronic states of atoms or molecules, neither their spin state nor charge state. Its accuracy relies largely on a set of parameters optimized to replicate energies from relevant density functional theory (DFT) calculations. We use a published set of forcefield parameters developed to describe glycine tautomerization in water,[26] which is an augmentation of an earlier

parameterization for oxidation of hydrocarbons.[24] This ReaxFF uses a parameterization for water trained to capture, among other phenomena, autoionization, proton transfer reactions, and the structure of hexagonal ice.[27] Without modification, these parameters adequately describe the binding energy of enclathrated methane.

The starting structure for impact simulations was generated as follows. A simulation cell of 23x23x35 Å was produced by tiling a published clathrate phase I unit cell structure derived from DFT (B3LYP).[28] We subject the structure to energy minimization and a 20 ps equilibration at 50 K (or another temperature of interest) with periodic boundary conditions. The cell dimensions were then relaxed isotropically over 10 ps to bring the principal components of the virial stress tensor near zero. After another 20 ps equilibration, the cell was sliced to produce a slab. This was achieved using a simple upper and lower Z threshold to remove molecules before adding back water molecules needed to complete the twenty member cages of all remaining enclathrated molecules. The resulting slab, with ~90 Å of added headspace, was again energy minimized and equilibrated 20 ps before relaxing the cell dimensions to bring the magnitude of the in-plane normal stress components below 50 atm. Finally, the slab was equilibrated for 20 ps using a Nose-Hoover thermostat with a damping constant of 50 fs and a timestep of 0.1 fs. For our simulations using a pure water ice (1h) surface, we follow a similar procedure, beginning with a 29 Å thick slab of width 27 Å and length 31 Å produced by tiling the unit cell of Hayward and Reimers (1997).[29]

We ran at least 300 impact simulations for each given set of conditions (velocity, projectile, temperature, etc.) in order to calculate yields from the ensemble average. Among a set of simulations, each begins with an identical surface structure, prepared as described above. To avoid a shift in temperature due to random fluctuation when switching to the microcanonical ensemble (NVE), at the start of each run, the velocities of atoms in the surface are normalized to reproduce the slab equilibration temperature exactly. The projectile molecule or atom (e.g. H_2O), the projectile, is positioned so that its center of mass (COM) lies 10 Å above the highest atom in the slab (z_{max}+10 Å) and its X,Y coordinates are randomized uniformly over the width of the simulation cell. For molecular projectiles, the orientation is also randomized by rotating about three orthogonal axes through the COM. The COM is given an initial velocity ($|V_{in}|$) with fixed angle of incidence from the surface plane (θ_{in}) and uniformly randomized azimuthal angle (ϕ). We run each simulation under the microcanonical ensemble with a timestep of 0.05 fs for 1 ps after the impactor is projected to reach the surface. This simulation duration provides adequate time for the composition of the slab to stabilize after impact (see later discussion).

Our simulations use the QEq charge equilibration methodology to determine the electron distribution dynamically under the condition of net neutrality.[30] This framework provides for polarization of bonds according to electronegativity but does not adequately describe all ionization phenomena that might occur under these impact conditions (e.g. collisional autoionization).[31] Furthermore, the projectile charge is at all times equilibrated with the surface, so that the results are only applicable to neutral projectiles or the subset of ion impacts in which the projectile is neutralized during approach (i.e. via resonant charge transfer or Auger neutralization).

Because of the artificial periodicity in the z direction, it is possible for a sputtered or scattered particle to traverse the headspace and impact the ice slab from below. To prevent this, we exclude any molecules/clusters that enter a 20 Å thick region (beginning ~45 Å above the slab) from further time integration and from pairwise interactions. A simple bond distance threshold of 2 Å is used to identify the clustered atoms so that they can be frozen on the same timestep. This procedure preserves the bond topology and velocity of ejected molecules as though they continued ballistically into the vacuum.

In the chemical analysis, species are identified by using a bond order (BO=0.55) threshold following energy minimization to determine covalent connectivity. Simple bond order thresholding can misidentify strongly hydrogen-bonded clusters as a single molecule, which is especially problematic for alcohols. A more sophisticated approach than that of Chapter 4 is required. In the following analysis, we break clusters by attributing overcoordinated hydrogen atoms to which ever molecule has the higher bond order. The yield of a given species is computed as the difference between the starting and ending quantity of the molecule in each simulation, averaged across the relevant set of simulations. Unless otherwise noted, the yields are for the whole simulation cell, without differentiation by phase. Where we do differentiate between species in the gas phase and the solid phase, we use a simple Z threshold. Molecules with COM above the highest atom in the slab, as determined at the start of the simulation, and below the upper limit of the freeze region are regarded as being in the gas phase.

5.2.2 Consecutive impacts

To probe the steady-state ice chemistry, it is necessary to accumulate considerable projectile doses in the slab, which requires consecutive impact simulations. The finite size of the simulation cell poses a problem in this situation, as each impact deposits a large amount of kinetic energy into the ice. In the physical scenario, this excess kinetic energy is conducted away thermally into the semi-

infinite ice. This effect would be ordinarily included by simulating in the canonical ensemble (NVT) with a thermostat, but this must be done with care in our case to avoid prematurely removing kinetic energy from the projectile or the collision cascade. Our solution is to cycle between been NVE dynamics, a thermostat-enforced cooling ramp back to the initial temperature, and a subsequent NVT equilibration phase, with the effect that the slab temperature is reset between impacts. This NVE-NVT alternation protocol is similar to that used by Aussems et al. (2017) for ReaxFF simulations of graphite etching by hyperthermal atomic hydrogen.[32]

A single impact cycle begins with initializing the projectile as described in §5.2.1, followed by NVE dynamics for a duration of 500 fs plus the nominal projectile transit time. The transition to NVT dynamics cannot be made for the entire simulation cell because doing so would artificially cool sputtered/scattered species which are no longer in thermal communication with the solid phase. To differentiate phases, we define a spherical region centered at the initial slab COM (the "ice cluster basis", see Figure 5-1). Any molecules that belong to the same cluster (as defined by a 4 Å interatomic distance threshold) as a molecule in the spherical region are regarded as being part of the ice. For these molecules, the thermostat is applied to ramp linearly the temperature back to the initial 50 K over 1 ps, after which the temperature is held constant for 500 fs. Other molecules (the vapor) are excluded and continue inertially into the headspace. Again, in order to prevent these molecules from impacting the slab from below, they are frozen upon entering a predefined region at the top of the headspace.

At the end of the ~2 ps cycle, a new projectile is initialized in the plane of the original. To prevent the interference of slow vapor with the next impact trajectory, the vapor is translated upward 15 Å before beginning the dynamics (clearing the 15 Å above the ice). As a result of this "sweeping" procedure, gas-phase molecules are deleted at most 3 to 4 impacts after they enter the headspace (depending on their initial z position). The ice COM position and velocity are also reset every iteration to prevent drift from accumulated projectile momentum. This cycle is run for 100 consecutive impacts, equivalent to a dose 1.9×10^{15} cm^{-2} for our CH_4 clathrate slab.

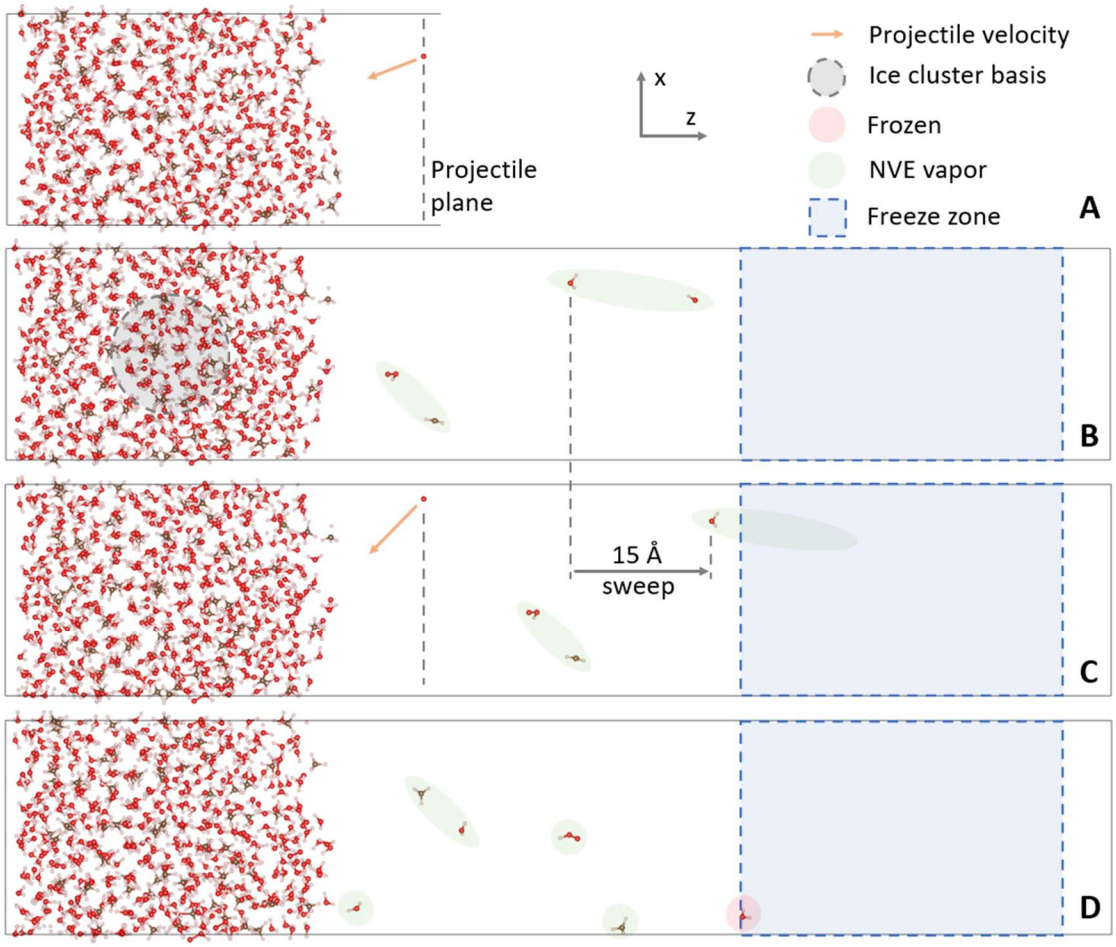

Figure 5-1: Start (A,C) and end (B,D) states for two consecutive impact cycles, illustrating the simulation protocol. A) a projectile (atomic oxygen) is initialized in the "projectile plane" at z_{max} + 10 Å with random XY coordinates and a velocity vector (fixed $|V_{in}|$, θ_{in} ; randomized ϕ). B) When the simulation transitions from NVE to NVT dynamics, the "ice cluster basis" region is used to differentiate between solid and vapor phases (highlighted in green), the latter of which is not thermostatted. Between B and C, the vapor is translated upward 15 Å so as not to interfere with the next projectile. Any molecules in the freeze region (blue) after this step are deleted. C) A new projectile is initialized. D) Any molecules reaching the freeze region, like the red-highlighted H_2O, are omitted from time integration and pairwise interactions, until they are removed at the end of the iteration. The visualization was created using the VESTA software.[33]

5.3 Results and Discussion

5.3.1 CH_4 Clathrate, O impacts

Here, we investigate the chemistry produced by bombardment of carbon bearing ices by water group molecules, starting with atomic oxygen impacting a methane clathrate surface. As a preliminary test we assess time evolution of ice composition following impact. The yield vs time

for a subset of species of interest is shown in Figure 5-2 for 20 km s^{-1} atomic oxygen impacting methane clathrate. Yields are computed at each time point as the number of molecules of a given species averaged across the ensemble of 300 trajectories. The yields stabilize by ~300 fs following the impact. We choose a generous simulation duration of 1 ps (after the impact) to ensure that the dynamics are sufficiently captured.

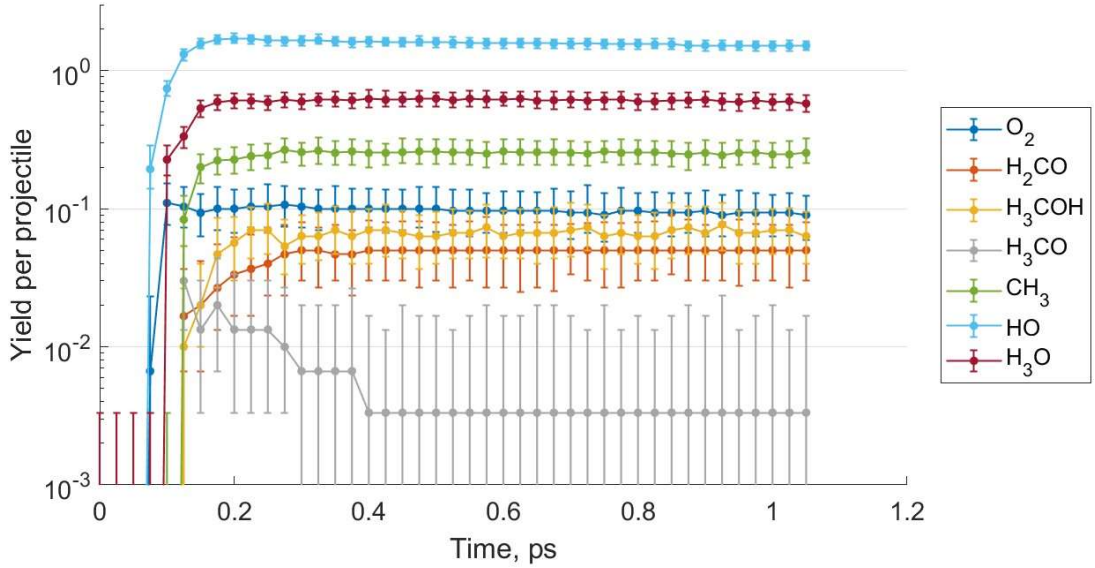

Figure 5-2: Yield of various species vs time for 300 impacts of atomic oxygen with methane clathrate at 20 km s^{-1}. Error bars are bootstrapped 95% confidence intervals from resampling the whole set of simulations (n = 300) at each time point with replacement. Yields of methanol and formaldehyde include their protonated forms.

As we hypothesize that the impactor velocity plays a driving role in the surface chemistry, we run an ensemble of collisions (n = 300) at each of several velocities spanning 5 to 25 km s^{-1} (2 to 52 eV). As expected, we find formation of O_2, HO_2, and H_2O_2 at increasing abundance as the impactor velocity increases. The results are in general agreement with previous ReaxFF simulations of atomic oxygen impacting a pure water ice (1h) slab,[19] although our yields are slightly lower because of the lower water density in the clathrate and the competitive carbon oxidation reactions (Figure 5-3).

With the presence of methane in the surface, we now find a variety of carbon bearing products, including HCO, H_2CO, H_3CO, H_2COH, and H_3COH. Among the carbon bearing products, methanol dominates at all energies, followed in abundance by formaldehyde. As observed for dioxygen products, the methanol yield increases with increasing impact energy. The highest yield of both formaldehyde (5%) and methanol (10%) is reached at an impact velocity of 25 km s^{-1}.

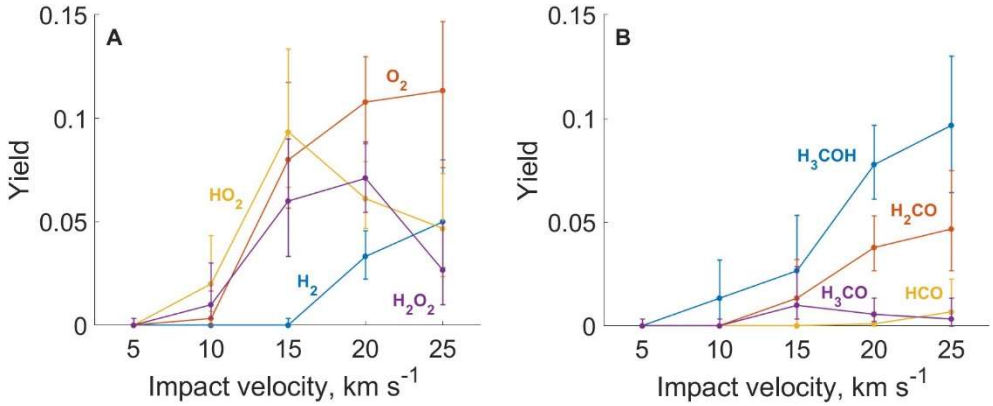

Figure 5-3: Yield of various species vs impact velocity for an atomic oxygen projectile impacting methane clathrate at 45 degrees (n = 300). Error bars are bootstrapped 95% confidence intervals from resampling the whole set of simulations at each condition with replacement. The yield for methanol and formaldehyde includes their protonated forms.

Based on analysis of the methanol producing trajectories, two main formation mechanisms emerge. The dominant, hot atom (HA) mechanism, accounting for 75% of cases, is a direct reaction between an enclathrated methane molecule and the projectile oxygen atom (hereafter denoted by O'), following one or more primary collisions with water molecules, such that the product methanol molecule contains the projectile atom. Within this set of reactions, we can further differentiate between two main subcases. Within the HA channel, 74% of trajectories proceed through abstraction of a hydrogen atom from CH_4 by the projectile to form a hydroxyl radical and a methoxy radical. This is followed by a prompt association of these radicals to form a vibrationally hot methanol molecule, which is stabilized by third body interactions with the ice cage. The probability of radical association to form methanol is high due to trapping of ·O'H and ·CH_3 as a contact pair in the clathrate cage. Henceforth, we will refer to this mechanism as HA_M. In the remainder of HA cases (which we will call HA_X), the projectile first abstracts a hydrogen atom from H_2O in the clathrate (most often from the molecules comprising the inner wall of the cage) to form a pair of hydroxyl radicals. Methanol formation then can occur in a couple of ways. One possibility is that the O'H formed in the abstraction from water retains much of the projectile kinetic energy and collides violently with CH_4 to eject a hydrogen atom, which is likely to be ultimately accommodated in the ice as H_3O^+, while the methanol is formed during this collision. Formally, all bond dissociation in ReaxFF is homolytic, so that 2 H_2O → HO· + ·H_3O results in formation of an unstable H_3O radical. QEq delocalizes the electron instantaneously to favorable, preexisting sites in the ice structure to form H_3O^+. Conceptually, this is similar to the spontaneous autoionization of

microhydrated H_3O molecules[34] or the prehydration of excess electrons in water.[35] Attachment of the presolvated electron to the HO· is favorable, but likely hindered by the displacement of the radical during dissociation (due to momentum transferred efficiently from the projectile), which disturbs its coordination to the hydrogen bond network. Our simulations do not capture this possible passivation — the reactivity of the HO moiety toward carbon is that of the radical.

Alternatively, methanol formation can proceed through the sequential reactions $\cdot OH + CH_4 \rightarrow \cdot CH_3 + H_2O$ and $\cdot OH + \cdot CH3 \rightarrow CH_3OH$. Depending on whether there is an intermediate hydrogen exchange between H_2O and ·OH, the oxygen atom incorporated into CH_3OH can be either the projectile atom or one that is native to the ice surface. These latter cases are similar to the radiolytic mechanism,[13,36] although notably here structural ·OH diffusion occurs only over the shortest possible distance. Additionally, the reaction does not depend on the availability of accumulated intermediates (e.g. OH), which is required in radiolytic synthesis of molecular oxygen from water ice.[20]

The HA reaction comprises a two-step process, abstraction followed by association. A single-step insertion of the singlet oxygen atom (^1D) into the methane C−H bond is a known pathway to methanol formation,[37–39] although insertion of the ground state oxygen atom radical is spin-forbidden. Bergner et al., for instance, induced photolysis of O_2 in mixed O_2:CH_4 ice using UV light, and found oxygen insertion into CH_4 leading to formation of methanol and formaldehyde.[39] Although this mechanism should be active during energetic O atom/ion bombardment, experimental evidence has not yet been produced. Ennis et al. irradiated methane ice with 5 keV O^+ and produced evidence for methanol formation, but its abundance was not quantifiable and the formation mechanism could not be ascertained.[21] Neither do we observed this mechanism here. The ReaxFF forcefield parameterization used in our simulations was trained on partial optimization DFT calculations of C−O bond dissociation, with the goal of reproducing the energy of the lowest spin state.[24] That is, reactions are presumed to occur along the lowest potential energy surface (PES). Consequently, ReaxFF does not explicitly penalize the spin-forbidden oxygen insertion reaction.

5.3.2 Contrasting clathrate and pure CH_4 target

Analysis of the mechanism for methanol formation under these conditions reveal that the water ice matrix actively contributes to methanol formation through the radiolytic and HA_X pathways, but in the dominant mechanism, the role of the water ice matrix appears to be limited to accommodating

excess kinetic energy. To shed more light on the role of the water ice matrix, we prepared a slab of pure methane ice and subjected it to 20 km s^{-1} bombardment of atomic oxygen.

Table 5-1: Yield of various product species for atomic oxygen projectiles (20 kms^{-1}) impacting methane clathrate (50 K, n = 900) compared to impacting a pure methane target (20 K, n = 300). O' designates the projectile atom.

	CH_4 Clathrate		CH_4 pure	
Species	yield, %	95% CI	yield, %	95% CI
H_2O'	62.4	(59.3,65.3)	64	(59.0,69.7)
H'	20.3	(17.8,23.0)	84	(76.0,92.2)
H_3COH	7.8	(6.1,9.6)	13.3	(9.7,17.3)
H_2CO	3.8	(2.6,5.1)	12.7	(9.3,16.7)
HO'	3.4	(2.3,4.9)	4.3	(2.7,6.7)
H_2	3.3	(2.3,4.7)	14.7	(11.0,18.3)
H_3CO	0.6	(0.2,1.2)	4.0	(2.3,6.7)
O'	0.6	(0.2,1.2)	0.0	(0.0,0.3)
OC	0.1	(0.0,0.6)	0.0	(0.0,0.3)
HCO	0.1	(0.0,0.6)	0.3	(0.0,1.7)
H_3O'	0.1	(0.0,0.6)	1.0	(0.3,2.6)

These simulations confirm that the production of methanol proceeds on pure methane ices. The production of methanol is ~2× greater for the pure methane target (Table 5-1), despite there being no contribution from the water-radiolytic mechanism. Several competing factors govern this change in methanol yield. The increase is due mostly to the larger density of methane in the pure CH_4 target compared with the clathrate, since a large portion of trajectories do not see the impactor interacting directly with a methane molecule; in a sample of 300 clathrate impacts, the median distance of closest approach between projectile and a carbon atom was 2.27 Å. In pure CH_4 ice case consecutive hydrogenation resulting in H_2O formation is a very effective sink for the reactive oxygen species (ROS). This is the outcome for 64% of simulated trajectories. Such consecutive hydrogen abstractions and collisional dissociation leave methane-fragment radicals (overwhelmingly $\cdot CH_3$), which associate to form H_xC_2 in 6% of impacts. In the clathrate structure, the H_2O matrix also provides a sink for reactive oxygen via formation of O_2 and H_2O_2, but this process is less efficient (18% of impacts). The cage structure of the clathrate favors methanol production by trapping OH and CH_3 as a contact pair. In contrast, the contact pair in pure methane ice is more easily broken.

Instances of CH_3OH formation from the CH_4 ice are differentiable, again, into two mechanism subtypes: one a rearrangement as in the HA_M case described above, and the other resembling the HA_X case, where methanol formation is preceded by hydrogen abstraction from a second methane molecule. The latter comprises 57% of events observed. Thus, the third body tends to play a more passive role in the clathrate case.

5.3.3 Other clathrate guest species

In the HA_X mechanism, the water matrix of the clathrate contributes a hydrogen atom to the methanol product. This introduces the possibility that the projectile kinetic energy might facilitate the hydrogenation of oxocarbon guests by the clathrate water matrix. To examine this possibility, we ran simulations of O impacts (n = 300) on CO_2 and CO clathrates at 20 km s^{-1}. Like CH_4, these species also preferentially form Structure I clathrates.[40,41] We found that hydrogenation was rare for these more abundant carbon sources (Figure 5-4). The hydrocarboxyl radical formed in just 4 impacts with the CO_2 clathrate and a single instance of HCO· formation occurred for both the CO and CO_2 clathrate (0.3% yield).

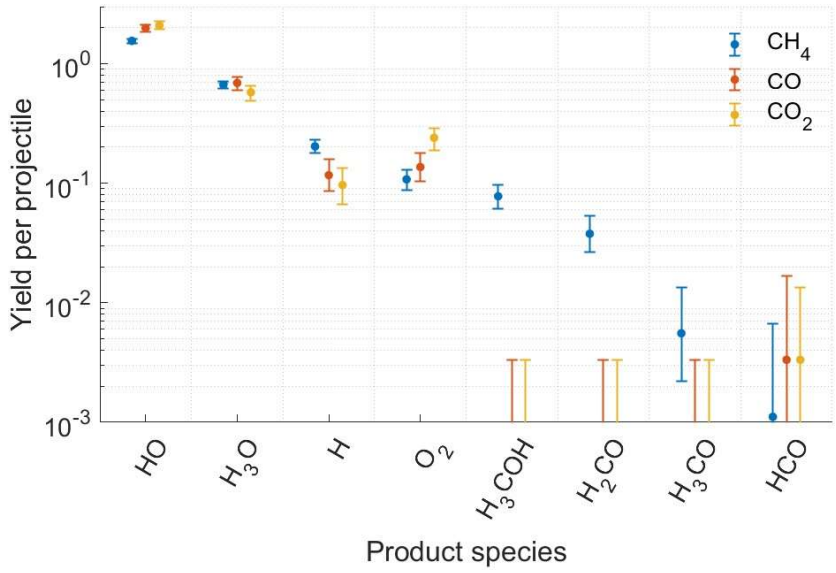

Figure 5-4: Yield of various product species for atomic oxygen projectiles (20 km s^{-1}) impacting clathrate with different guest molecules (CH_4, CO, CO_2) (50 K). For the methane clathrate, n = 900. Otherwise, n = 300.

The yield of O_2 increases substantially as the oxidation state of the guest molecule increases. This is attributable to carbon oxidation competing with O_2 formation. In the case of the methane

clathrate, the primary ROS sink is methanol formation, while for CO clathrate it is CO_2. This is also reflected in the yield of ·OH, which is significantly lower for the CH_4 clathrate.

5.3.4 Other impactors

In the cometary environment, where the projectile ions are produced through ionization of water vapor, the population of accelerated ions will include other water group ions (OH^+, H_2O^+). To determine to what extent the chemistry is influenced by hydrogenation of the projectile, we ran impact simulations (n = 300) for OH and H_2O impactors at 20 km s^{-1}.

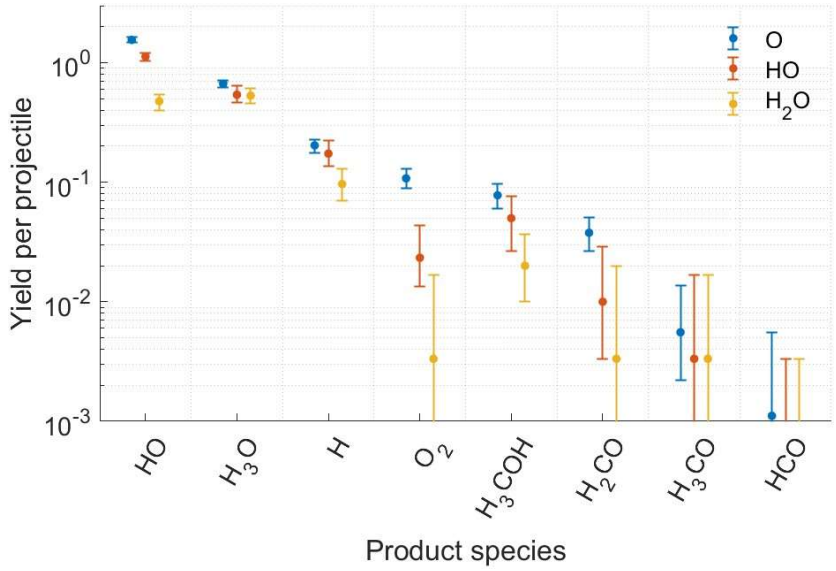

Figure 5-5: Yield of various product species for different projectiles (O, HO, H_2O) impacting the methane clathrate slab at 45° incidence and 20 km s^{-1}.

The yield of major dioxygen and methane oxidation products decreases as the projectile is increasingly hydrogenated. The yield of O_2 decreases more sharply than the yield of methanol, which we attribute to the activity of a second mechanism for methanol formation, the radiolytic pathway, that is negligible for O_2 synthesis at this energy.[19] Formaldehyde production is also sustained at diminished yields.

In the interest of generalizing our findings and providing more insights into the mechanism, we now consider bombardment of pure CH_4 ice by water group impactors and compare to the symmetric system (See Appendix Fig. A-10 and accompanying discussion), bombardment of water ice by the homologous series of CH_x impactors (x=0−4). Experimental and theoretical studies of C^+ impacting water ice in the literature have not reported formation of methanol.[42–45] To the best of

our knowledge, only a single study has reported on CH_x projectiles, that of Bag et al. (2013), which observed hydrogen isotope exchange at impact energies of 2−7 eV but does not report C−O bond formation.[46]

For atomic carbon impactors the dominant product by far is CO, followed by the formyl radical (HCO·). McBride et al. studied single collisions of C^+ with water ice clusters at lower energies (11 and 1.7 eV) using first-principles MD and found COH· and CO to be the dominant products, with CO being the more abundant product at 11 eV.[45] The preference for the isoformyl isomer in the simulations of McBride et al may be an electronic effect related to the projectile charge state. Experimental investigations of C^+ irradiation of water ice films at energies in the keV range report CO_2 as the dominant product.[42–44] The absence of CO_2 formation in our simulations is attributable to the difference in impact energy and irradiation dose — few ROS are created during a single impact, limiting the extent of oxidation. At higher energies and irradiation doses, such as are covered by experiments, the ice slab stoichiometry will become oxygen rich, facilitating further carbon oxidation. Finally, we note that for CH_x impacts there is an apparent preference for products that preserve the initial number of C−H bonds in the projectile.[1]

5.3.5 Consecutive impacts of O

To this point we have addressed single impacts of pristine clathrate surfaces. Now we attempt to address the high-dose limit corresponding to steady state ice conditions by running consecutive impact simulations. For atomic oxygen bombardment, we expect severely oxidizing conditions from the accumulation of reactive oxygen species and the depletion of hydrogen from the near surface region. These factors will eventually be balanced by sputtering and chemical erosion (by formation of volatile O_2 and CO) to establish a steady-state surface composition, although steady state conditions have evidently not been reached by our maximum simulated dose of 1.9×10^{15} cm^{-2} (Figure 5-6).

[1] For instance, the yield of HCO peaks for x=1, and the yield of CH_3OH and OCH_3 peak for x=3. This suggests that, for molecular projectiles, the relevant reactions proceed according to the following general outline: the projectile partially dissociates during the impact, subsequently abstracts or ejects a hydrogen atom from one of the ice molecules, and the resulting radical pair associates, forming the C−O bond.

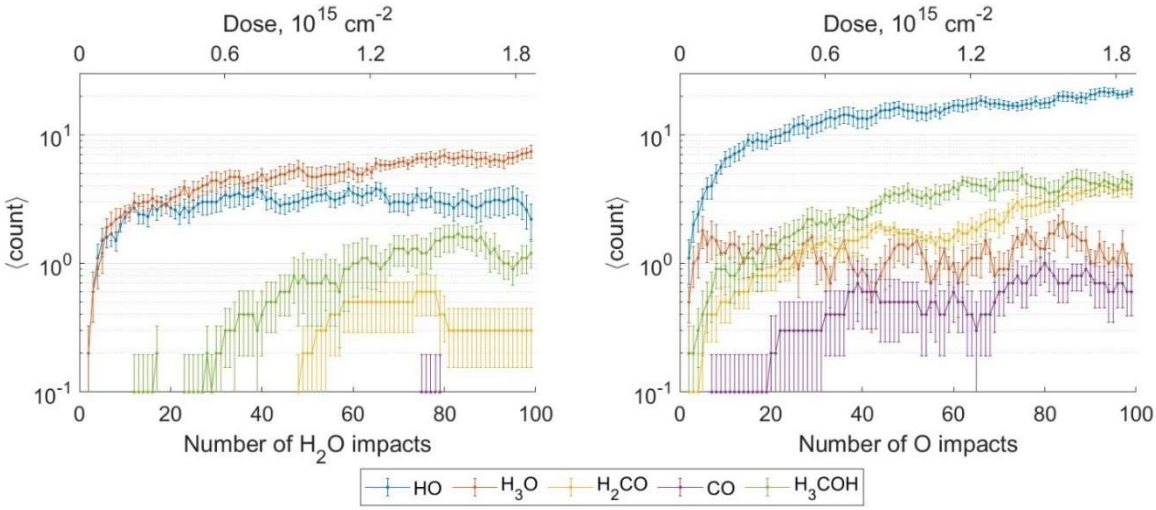

Figure 5-6: Abundances for several products (HO, H_3O, H_2CO, CO, H_3COH) as a function of the dose for H_2O impactors (left) and O impactors (right). The abundance only includes molecules remaining in the simulation cell. Since gas-phase molecules are deleted at most 3 impacts after they enter the headspace, the plotted abundances effectively represent the solid phase. The error bars are the standard error across 10 independent simulations for each impactor species (H_2O, O). The abundance for methanol includes protonated methanol.

There are several important limitations of these simulations. One is that we cannot simulate realistic fluxes. Dose rate simulated here is $\sim 4\times10^{24}$ cm^{-2} s^{-1}, some 17 orders of magnitude greater than, for instance, the solar wind flux at 1 AU.[47] This cannot be helped — simulating an interval of many tens of hours between impacts is computationally intractable. This can have important implications for the solid-phase chemistry.[32] Because of the very low temperature of these simulations, molecular mobility is severely constrained and vertical diffusion of carbon bearing species should be negligible between impacts. The same cannot be said for structural diffusion of OH and H_3O through the ice hydrogen bond network, which has a much lower activation energy barrier and is enabled at very low temperatures by tunnelling. This is liable to mitigate, to some extent, reactivity related to accumulation of OH and H_3O.

Much of the chemistry we observe however is does not depend on the accumulation of these species, however. The formation of molecular oxygen, for instance, shows no evidence of nonlinearity (Figure 5-7, right) because it is formed almost exclusively via the Eley−Rideal/hot-atom reaction described in Chapter 4. The formation of H_2CO, H_3COH, and CO, do however exhibit nonlinearities, as expected. Notably though, the oxidation rate, that is, the change carbon oxidation state per impact, is apparently independent of the dose (Figure 5-7, left). This suggests that the

nonlinearity of the carbon oxidation chemistry is due to the accumulation of oxidized carbon species, rather than the accumulation of reactive oxygen species, which makes it somewhat more robust to changes in the flux.

As second, related issue is the accumulation of hypervolatile species (O_2 and CO) and the reduced ice density near the surface. The CO adsorption lifetime on amorphous water ice is on the order milliseconds.[48,49] Over realistic inter-impact timescales, therefore, CO and O_2 (of similar volatility) are likely to desorb at the temperature of our simulation (50 K). Also, over realistic timescales, structural relaxation will promote densification of the impact-amorphized surface, although it seems improbable that this process will substantially alter the observed chemistry.

Still, there are several conclusions that we can draw with relatively high confidence, despite the unrealistic flux. One is that the non-radiolytic O_2 formation mechanism described in Chapter 4 is not strongly influenced by accumulated compositional changes in the ice. A second is that the anticipated near-surface hydrogen depletion occurs mostly due to direct ejection of atomic hydrogen, rather than via formation and loss of H_2, which is a minor product (yield of 2.1%).

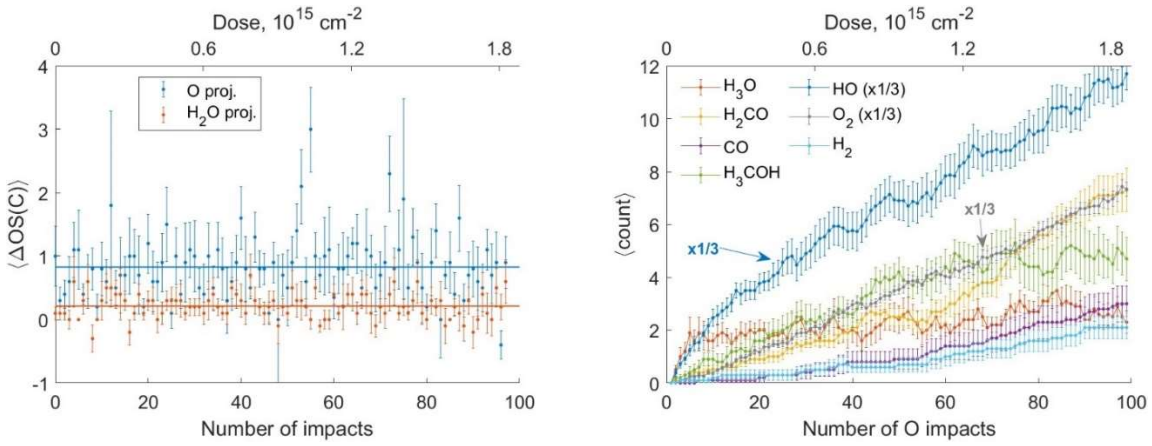

Figure 5-7: Left) Change in the net carbon oxidation state ($\Delta OS(C)$) for all carbon atoms versus the number of impacts for O (blue) and H_2O projectiles (orange). Molecules lost to the headspace are included. The error bars are standard error across 10 independent simulations. For each impactor species, the mean of all data is plotted as a horizontal solid line. Oxidation states for carbon were calculated based on Lewis structures.[50] As an illustration, if a single impact converted one methane molecule (OS=−4) into methanol (OS=−2), but no other carbon bearing molecules were affected, the $\Delta OS(C)$ would be +2. Right) Cumulative abundances for several products as a function of the dose for O impactors, as in Figure 5-6, except that here we have included molecules lost to the headspace. For readability, the O_2 (gray) and HO (blue) traces have been rescaled by a

factor of 1/3. Note the linearity of O_2 production, and the nonlinearity of H_3COH, H_2CO, and CO production.

5.4 Conclusion

Reactive MD simulations of water group molecules impacting methane clathrate at hyperthermal energies show formation of methanol via two distinct mechanisms: a dominant hot atom mechanism and a secondary radiolytic mechanism. The hot atom mechanism is a two-step process, an initial hydrogen abstraction reaction followed by association of OH and CH_3 radicals. Insertion of oxygen into the C−H bond of the enclathrated methane is not observed. This novel two-step pathway to formation of methanol and formaldehyde may be important at airless icy bodies in the solar system, particularly comets. Our simulation results support the notion that low-energy ions play a unique role in modifying the organic composition of ices. Consequently, abundances of these molecules measured during periods of high activity may belie primordial solar system conditions.

In addition to outgassing from the cometary nucleus, some production of formaldehyde and methanol within the coma is needed to account for their radial distribution at some comets.[1,51] The thermal degradation of polyoxymethylene (POM) trapped in ice grains has been proposed as a potential extended source for formaldehyde, but results from the Rosetta mission did not support the presence of POM at comet 67P,[52] casting doubt on this explanation. The production mechanism we observed here could contribute to an extended source, since grains entrained in the coma would present high specific surface area to solar wind PUIs. The fluxes are quite low, however, and we leave it to other to determine whether the contribution is substantial.

5.4 References

1. McKay, A. J. & Roth, N. X. Organic Matter in Cometary Environments. *Life* **11**, 37 (2021).
2. Hodyss, R. *et al.* Methanol on Enceladus. *Geophys. Res. Lett.* **36**, L17103 (2009).
3. Peter, J. S., Nordheim, T. A. & Hand, K. P. Detection of HCN and diverse redox chemistry in the plume of Enceladus. *Nat. Astron.* **8**, 164–173 (2024).
4. Waite Jr, J. H. *et al.* Liquid water on Enceladus from observations of ammonia and 40Ar in the plume. *Nature* **460**, 487–490 (2009).
5. Booth, A. S. *et al.* An inherited complex organic molecule reservoir in a warm planet-hosting disk. *Nat. Astron.* **5**, 684–690 (2021).
6. Watanabe, N. & Kouchi, A. Efficient Formation of Formaldehyde and Methanol by the Addition of Hydrogen Atoms to CO in H[TINF]2[/TINF]O-CO Ice at 10 K. *Astrophys. J.* **571**, L173–L176 (2002).

7. Hidaka, H., Watanabe, N., Shiraki, T., Nagaoka, A. & Kouchi, A. Conversion of H_2CO to CH_3OH by Reactions of Cold Atomic Hydrogen on Ice Surfaces below 20 K. *Astrophys. J.* **614**, 1124–1131 (2004).
8. Watanabe, N., Nagaoka, A., Shiraki, T. & Kouchi, A. Hydrogenation of CO on Pure Solid CO and CO-H_2O Mixed Ice. *Astrophys. J.* **616**, 638–642 (2004).
9. Hiraoka, K. *et al.* Formation of formaldehyde and methanol from the reactions of H atoms with solid CO at 10–20 K. *Chem. Phys. Lett.* **229**, 408–414 (1994).
10. Fuchs, G. W. *et al.* Hydrogenation reactions in interstellar CO ice analogues: A combined experimental/theoretical approach. *Astron. Astrophys.* **505**, 629–639 (2009).
11. Mumma, M. J. & Charnley, S. B. The Chemical Composition of Comets—Emerging Taxonomies and Natal Heritage. *Annu. Rev. Astron. Astrophys.* **49**, 471–524 (2011).
12. Hudson, R. L. & Moore, M. H. Laboratory Studies of the Formation of Methanol and Other Organic Molecules by Water+Carbon Monoxide Radiolysis: Relevance to Comets, Icy Satellites, and Interstellar Ices. *Icarus* **140**, 451–461 (1999).
13. Hodyss, R., Johnson, P. V., Stern, J. V., Goguen, J. D. & Kanik, I. Photochemistry of methane–water ices. *Icarus* **200**, 338–342 (2009).
14. Nilsson, H. *et al.* Birth of a comet magnetosphere: A spring of water ions. *Science* **347**, aaa0571 (2015).
15. Nilsson, H. *et al.* Evolution of the ion environment of comet 67P/Churyumov-Gerasimenko: Observations between 3.6 and 2.0 AU. *Astron. Astrophys.* **583**, A20 (2015).
16. Bar-nun, A., Herman, G., Laufer, D. & Rappaport, M. L. Trapping and release of gases by water ice and implications for icy bodies. *Icarus* **63**, 317–332 (1985).
17. Marboeuf, U., Mousis, O., Petit, J.-M. & Schmitt, B. CLATHRATE HYDRATES FORMATION IN SHORT-PERIOD COMETS. *Astrophys. J.* **708**, 812–816 (2010).
18. Luspay-Kuti, A. *et al.* The presence of clathrates in comet 67P/Churyumov-Gerasimenko. *Sci. Adv.* **2**, e1501781 (2016).
19. Grayson, R. W., Goddard, W. A. & Giapis, K. P. Reactive scattering of water group ions on ice surfaces with relevance to Saturn's icy moons. *Icarus* **379**, 114967 (2022).
20. Teolis, B. D., Plainaki, C., Cassidy, T. A. & Raut, U. Water Ice Radiolytic O_2, H_2, and H_2O_2 Yields for Any Projectile Species, Energy, or Temperature: A Model for Icy Astrophysical Bodies: Ice O_2, H_2, and H_2O_2 Radiolysis Yields. *J. Geophys. Res. Planets* **122**, 1996–2012 (2017).
21. Ennis, C., Yuan, H., Sibener, S. J. & Kaiser, R. I. On the chemical processing of hydrocarbon surfaces by fast oxygen ions. *Phys. Chem. Chem. Phys.* **13**, 17870 (2011).
22. Aktulga, H. M., Fogarty, J. C., Pandit, S. A. & Grama, A. Y. Parallel reactive molecular dynamics: Numerical methods and algorithmic techniques. *Parallel Comput.* **38**, 245–259 (2012).
23. Nakano, A. Parallel multilevel preconditioned conjugate-gradient approach to variable-charge molecular dynamics. *Comput. Phys. Commun.* **104**, 59–69 (1997).
24. Chenoweth, K., van Duin, A. C. T. & Goddard, W. A. ReaxFF Reactive Force Field for Molecular Dynamics Simulations of Hydrocarbon Oxidation. *J. Phys. Chem. A* **112**, 1040–1053 (2008).

25. Senftle, T. P. *et al.* The ReaxFF reactive force-field: development, applications and future directions. *Npj Comput. Mater.* **2**, 15011 (2016).
26. Rahaman, O., van Duin, A. C. T., Goddard, W. A. & Doren, D. J. Development of a ReaxFF Reactive Force Field for Glycine and Application to Solvent Effect and Tautomerization. *J. Phys. Chem. B* **115**, 249–261 (2011).
27. van Duin, A. C. T., Zou, C., Joshi, K., Bryantsev, V. & Goddard, W. A. CHAPTER 6. A Reaxff Reactive Force-field for Proton Transfer Reactions in Bulk Water and its Applications to Heterogeneous Catalysis. in *Catalysis Series* (eds. Asthagiri, A. & Janik, M. J.) 223–243 (Royal Society of Chemistry, Cambridge, 2013). doi:10.1039/9781849734905-00223.
28. Lenz, A. & Ojamäe, L. Structures of the I-, II- and H-Methane Clathrates and the Ice−Methane Clathrate Phase Transition from Quantum-Chemical Modeling with Force-Field Thermal Corrections. *J. Phys. Chem. A* **115**, 6169–6176 (2011).
29. Hayward, J. A. & Reimers, J. R. Unit cells for the simulation of hexagonal ice. *J. Chem. Phys.* **106**, 1518–1529 (1997).
30. Rappe, A. K. & Goddard, W. A. Charge equilibration for molecular dynamics simulations. *J. Phys. Chem.* **95**, 3358–3363 (1991).
31. Jaramillo-Botero, A. *et al.* Hypervelocity Impact Effect of Molecules from Enceladus' Plume and Titan's Upper Atmosphere on NASA's Cassini Spectrometer from Reactive Dynamics Simulation. *Phys. Rev. Lett.* **109**, 213201 (2012).
32. Aussems, D. U. B., Bal, K. M., Morgan, T. W., Van De Sanden, M. C. M. & Neyts, E. C. Atomistic simulations of graphite etching at realistic time scales. *Chem. Sci.* **8**, 7160–7168 (2017).
33. Momma, K. & Izumi, F. *VESTA 3* for three-dimensional visualization of crystal, volumetric and morphology data. *J. Appl. Crystallogr.* **44**, 1272–1276 (2011).
34. Uhlig, F., Marsalek, O. & Jungwirth, P. From a localized H3O radical to a delocalized H3O+···e− solvent-separated pair by sequential hydration. *Phys. Chem. Chem. Phys.* **13**, 14003 (2011).
35. Migus, A., Gauduel, Y., Martin, J. L. & Antonetti, A. Excess electrons in liquid water: First evidence of a prehydrated state with femtosecond lifetime. *Phys. Rev. Lett.* **58**, 1559–1562 (1987).
36. Wada, A., Mochizuki, N. & Hiraoka, K. Methanol Formation from Electron-irradiated Mixed H_2O/CH_4 Ice at 10 K. *Astrophys. J.* **644**, 300–306 (2006).
37. Carder, J. T., Ochs, W. & Herbst, E. Modelling the insertion of O(1D) into methane on the surface of interstellar ice mantles. *Mon. Not. R. Astron. Soc.* **508**, 1526–1532 (2021).
38. Chang, A. H. H. & Lin, S. H. A theoretical study of the O(1D)+CH4 reaction II. *Chem. Phys. Lett.* **384**, 229–235 (2004).
39. Bergner, J. B., Öberg, K. I. & Rajappan, M. Methanol Formation via Oxygen Insertion Chemistry in Ices. *Astrophys. J.* **845**, 29 (2017).
40. Sloan, E. D. Fundamental principles and applications of natural gas hydrates. *Nature* **426**, 353–359 (2003).
41. Zhu, J. *et al.* Encapsulation kinetics and dynamics of carbon monoxide in clathrate hydrate. *Nat. Commun.* **5**, 4128 (2014).

42. Dawes, A. *et al.* Low energy 13C+ and 13C2+ ion irradiation of water ice. *Phys. Chem. Chem. Phys.* **9**, 2886 (2007).
43. Mejía, C., Barros, A. L. F. de, Rothard, H., Boduch, P. & Silveira, E. F. da. Radiolysis of Ices by Cosmic-Rays: CH4 and H2O Ices Mixtures Irradiated by 40 MeV 58Ni11+ Ions. *Astrophys. J.* **894**, 132 (2020).
44. Hunniford, C. A. *et al.* Irradiation of water ices by 2 keV carbon ions. *J. Phys. Conf. Ser.* **163**, 012078 (2009).
45. McBride, E. J., Millar, T. J. & Kohanoff, J. J. Irradiation of Water Ice by C+ Ions in the Cosmic Environment. *J. Phys. Chem. A* **118**, 6991–6998 (2014).
46. Bag, S., Bhuin, R. G. & Pradeep, T. Distinguishing Amorphous and Crystalline Ice by Ultralow Energy Collisions of Reactive Ions. *J. Phys. Chem. C* **117**, 12146–12152 (2013).
47. Verscharen, D., Klein, K. G. & Maruca, B. A. The multi-scale nature of the solar wind. *Living Rev. Sol. Phys.* **16**, 5 (2019).
48. Collings, M. P., Dever, J. W., Fraser, H. J. & McCoustra, M. R. S. Laboratory studies of the interaction of carbon monoxide with water ice. *Astrophys. Space Sci.* **285**, 633–659 (2003).
49. Al-Halabi, A., Fraser, H. J., Kroes, G. J. & Dishoeck, E. F. van. Adsorption of CO on amorphous water-ice surfaces. *Astron. Astrophys.* **422**, 777–791 (2004).
50. 'oxidation state'. in *The IUPAC Compendium of Chemical Terminology: The Gold Book* (ed. Gold, V.) (International Union of Pure and Applied Chemistry (IUPAC), Research Triangle Park, NC, 2019). doi:10.1351/goldbook.
51. Cottin, H. & Fray, N. Distributed Sources in Comets. *Space Sci. Rev.* **138**, 179–197 (2008).
52. Altwegg, K. *et al.* Organics in comet 67P – a first comparative analysis of mass spectra from ROSINA–DFMS, COSAC and Ptolemy. *Mon. Not. R. Astron. Soc.* **469**, S130–S141 (2017).

Chapter 6

SCATTERING ON ICE

6.1 Introduction

Although heavy-ion irradiation of ices has a long history of study, published experiments have focused on chemically inert projectiles (noble gas ions) and/or high kinetic energies (>keV). In the latter category, Giovanni Strazzulla (INAF-Osservatorio Astrofisico di Catania) and associates have reported on ice irradiation with relevant reactive ions (C, N, S, O), although at high KE (15−105 keV).[1–3] With new observations of Europa forthcoming (viz. *Juice*, *Europa Clipper*), there has been a more recent surge of interest in implantation of sulfur ions into ices, with experiments at ≥105 keV.[4–6]

Despite the ubiquity low-energy interactions, there are, to our knowledge, perhaps two research groups conducting experiments with reactive hyperthermal ions. The first, that of Heon Kang (a Caltech graduate) at Seoul National University, conducts RIS studies (Cs^+ projectiles) of spontaneous, thermal reactions[7–13] at ice surfaces and studies of RIS itself (the method) as applied to ice.[14–17] The second is that of Thalappil Pradeep at the Indian Institute of Technology Madras, which has reported on two interesting reactions: H_2 formation in very low energy (10 eV) H^+ bombardment of ice via an ER mechanism[18] and the isotope exchange of CH_2^+ with D_2O ice.[19] The reader is referred to their coauthored review for a thorough, though now somewhat outdated, overview of prior art in hyperthermal ion exposure of ices.[20]

When it comes to reactive hyperthermal ions as drivers, rather than observers, of ice chemistry, the literature is essentially a vacuum.[20] Galli et al. (2017) are the exception, reporting on irradiation of water ice with O^+ and O_2^+ at energy as low as 100 eV, although these were strictly measurements of the sputtering yields via microbalance.[21] Additionally, a few simulation efforts have been published ([22–26]) in addition to our own.[27] By and large, the space remains unexplored. In this chapter we describe the extension of our MIBSA platform to accommodate ice targets.

6.2 Methods

6.2.1 Apparatus

Our experiments with ice surfaces use the same molecular ion beam and scattering apparatus as earlier described, except that the sample holder has been modified to accommodate cryogenic

targets. The cryogenic sample stage was constructed around a two-stage, closed-cycle helium cryocooler (CTI Cryogenics), capable of bringing the target to temperatures as low as 24 K in its final configuration. In addition to temperature control, several features were required to perform the targeted experiments: an electron flood gun for neutralizing surface charge, a dosing system for depositing ice, and an interferometry system for monitoring ice thickness during deposition.

The sample stage consists of an aluminum (6061) cold finger (Figure 6-1) affixed on the second stage of the cryocooler. The cold finger itself is a modular assembly, with a flanged cylindrical base and flat rectangular extension with one face aligned to the cryocooler axis ("the target flat," see Figure 6-1). A molybdenum retaining ring clamps the scattering surface into a recess in the target flat, with electrical isolation provided by a sapphire ring (above) and disc beneath. The target surface itself is a high purity gold foil with an underlying copper disc, which is grounded through an ammeter during scattering experiments. Indium foil enhances thermal contact between the aluminum cold finger and the sapphire disc, and between the sapphire disc and copper foil. Because of the ductility of gold and the mechanical pressure provided by the molybdenum holding ring, we tolerate dry thermal contact between the Au scattering surface and underlying Cu.

A 20 W cartridge heater press-fit just above the target flat provides control over the surface temperature. The heater can be overdriven to for temperature control up to 170 K with the cryocooler on. Steady ramps ($\geq 4\times10^{-1}$ K/min) to higher temperatures can be produced by passive warming of the unpowered cryocooler. The thermal contact between the cold finger and the stainless steel cryocooler is not substantially throttled. Consequently, we are able to tolerate large parasitic heat loads (Figure 6-2), while reaching satisfactorily low cold finger temperatures. This allowed us to forgo radiative shielding, which considerably simplified design and integration with the scattering apparatus. A drawback of this choice is that the thermal equilibration times are long for high heating powers because the temperature of the stainless steel cryocooler must adjust. Diode thermometry is used to monitoring the target temperature, with the silicon diode (Lakeshore Cryotronics) mounted on the back side of the cold finger, opposite the target surface. The baseline cold finger temperature after installation is 24 K, which suggests a total parasitic heat load of roughly 15W at the second cooling stage.

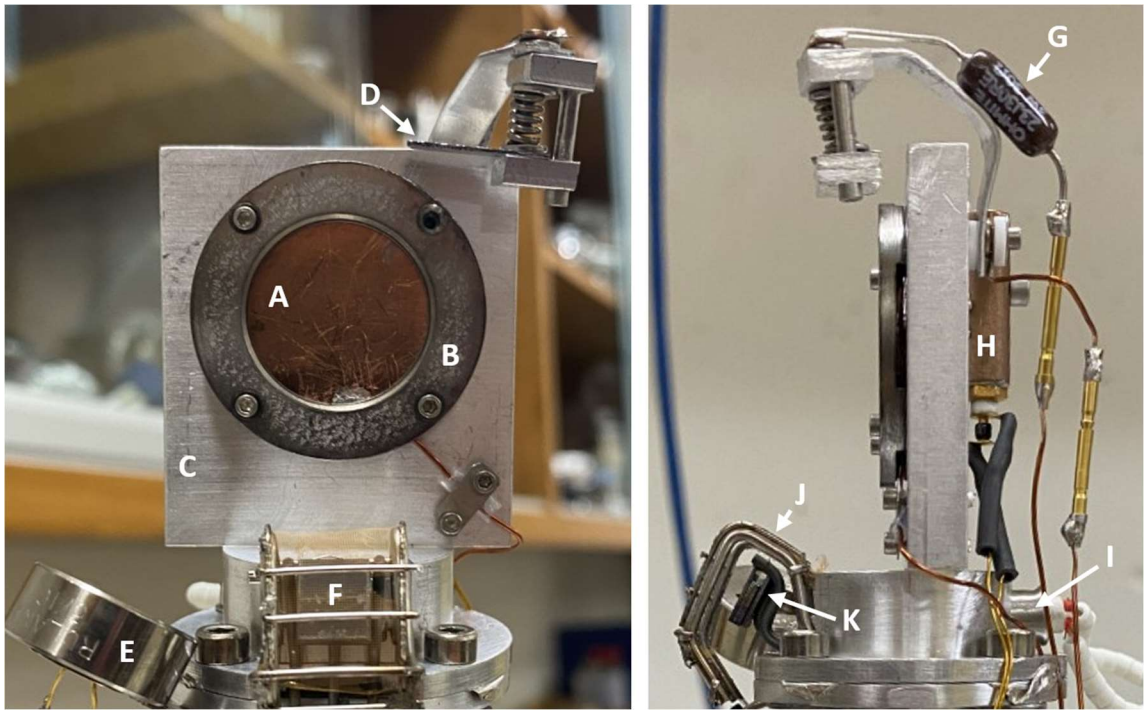

Figure 6-1: Photos of the assembled cold finger before installation and without the gold target surface in place. The main features are shown: A) Cu plate to ground target surface. B) Molybdenum retaining ring. C) Aluminum cold finger body. D) Silicon mirror. E) Photodiode holder/thermal ballast. F) Electron flood gun assembly. G) wire wound resistor for mirror deicing. H) Silicon diode thermometer housing. I) cartridge heater. J) Electron gun subassembly – ground grid. K) Electron gun subassembly – Repeller and filament.

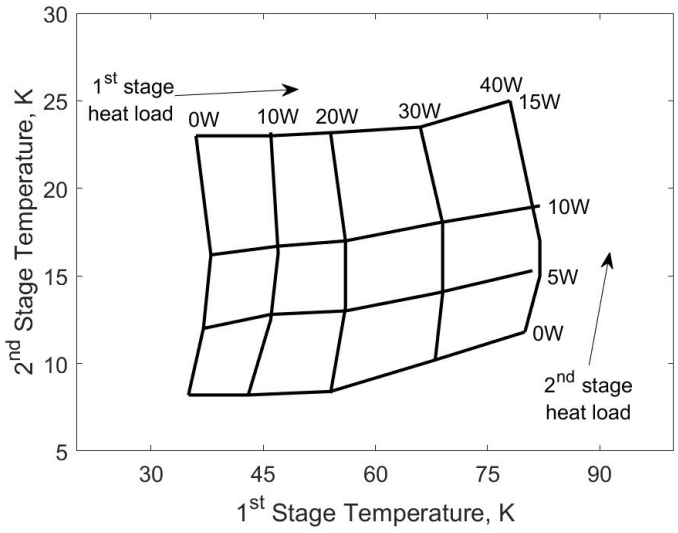

Figure 6-2: Nominal performance characteristics of the cryocooler. (CTI Cryogenics, private correspondence).

The ice deposition is monitored via interferometry. Because of tight geometrical constraints in and around the scattering chamber, the laser (5 mW HeNe, 632.8 nm) is introduced via optical viewport, and modulation of the reflected beam is recorded in the open-circuit voltage of a photodiode mounted internally on the cold finger itself. This has the benefit that signal to noise ratio is improved at the by cooling to the ice deposition temperature. The diode is mounted using a stainless-steel shaft collar, which provides thermal ballast against temperature changes that might occur during ice deposition and propagate to changes in the voltage baseline. The incoming laser light is redirected to the surface and specularly (half angle 53^{o}) into the photodiode using a silicon mirror also mounted on the cold finger. Ice deposition on this mirror is prevented by heating with a vitreous enamel coated, wire-wound resistor (3W). Ceramic washers provide thermal insulation between the mirror-heater assembly at the mounting point, and the power leads are noninductively wound on a spool at the first cold stage to reduce thermal load on the tip. With the de-ice resistor driven at 2W, which is sufficient to prevent deposition of water ice onto the mirror, surface temperatures as low as 31K can be achieved. The laser beam spot is not precisely aligned with the ion beam spot. The intention of this interferometric measurement is not to provide a quantitative measurement of the ice thickness at the location of beam exposure, but to enable repeatable depositions.

To combat surface charging by the positive ion beam, we included an electron flood gun mounted on the cold finger above the target flat. The electron gun comprises an emissive tungsten filament with a U-shaped reflecting electrode behind and a fine gold mesh in front, grounded to shield the surface from stray electric fields. The electron gun is thermally and electrical isolated from the cold finger via a thick ceramic spacer, and its power leads are noninductively wound on a heat sinking post at the first cold stage of the cryocooler, which has a much greater cooling power than the tip. Thus, large currents (3−5 A) can be driven with tolerable thermal load on the cold finger. The electron energy is controlled via the floating bias of the gun filament (Figure 6-3) and the repeller electrode is biased to direct emission toward the surface. In pre-installation testing the electron gun could supply tens of microamps to the target surface (Figure 6-4), enough to compensate for the ion currents typical of our experiments (1 to 20 μA).

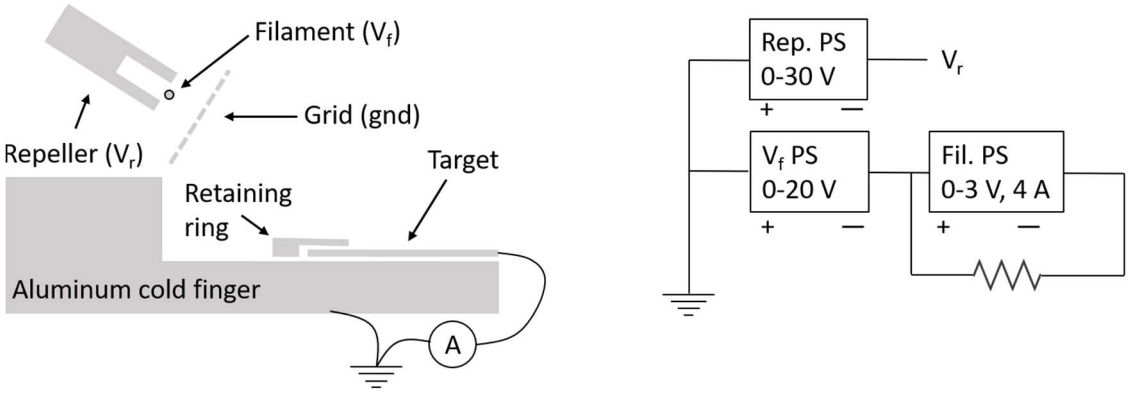

Figure 6-3: Electron gun configuration. Left) Schematic (longitudinal cross-section, not to scale) of the electron flood gun and target arrangement. The connection to the cryocooler is made at the left-hand side. The distal tip of the cold finger is cut off in this view to better depict the electrical connectivity. Right) Power supply bias scheme for the flood gun. V_f – the floating bias of the e-gun filament, V_r – repeller electrode bias.

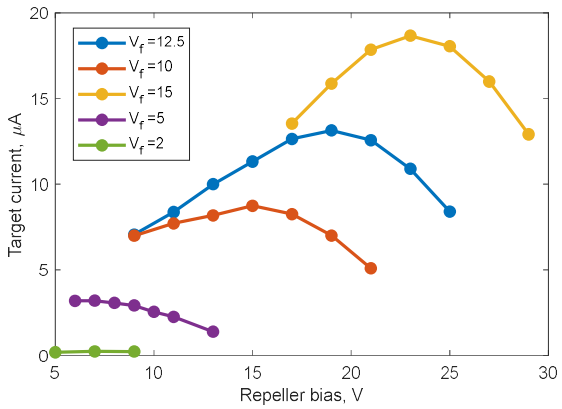

Figure 6-4: Performance of the electron flood gun at different repeller, and filament floating biases, prior to installation in the scattering apparatus and without cooling (no ice).

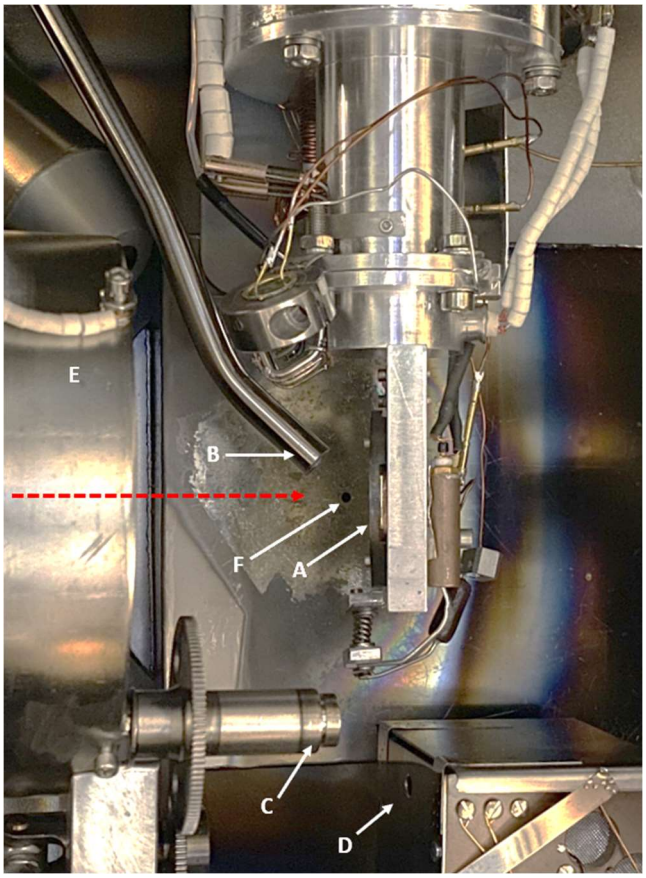

Figure 6-5: Photo of installed cold finger with target arranged for ice deposition. The red broken red arrow indicated the path of incident ions (the beamline axis), which scatter from the target into the page. A) target surface. B) Doser tube at full insertion. C) mounting point for rotatable beam flag (removed in this photo). D) Miniaturized EEA for measurement of beam energy. E) Beamline terminal ground shield. F) Detector entrance aperture.

Gas for ice deposition is introduced via a leak valve and directed toward the target surface by a retractable, open-ended, stainless-steel dosing tube (0.18” ID). This results in a nonuniform deposition profile on the target, which was centered on the target visually. Deposition of water ice at a temperature of 30 K followed by rapid heating to 50 K renders the ice film visible. The conductivity of our ice coating abruptly increases around this temperature. Both phenomena are due to the freezing of residual N_2 and O_2 gas as an insulating film at <34 K (prior to H_2O dosing) and its sublimation on warming, which fractures the overlying water ice (see Appendix Fig. A-12 for a demonstration of N_2 condensation). The prototype assembly underwent testing in separate vacuum chamber and iterative improvements, while custom fittings were fabricated for its integration into the existing scattering apparatus.

6.2.2 Procedural

Two different ion beams (Ar^+ and O^+) are used in the following experiments. Ions are extracted from an inductively coupled plasma (ICP) with feed gas consisting of oxygen (industrial grade, Airgas), neon (research plus grade, Air Liquide), and argon (UHP grade, Airgas). The Ar^+ beam is sourced from a 500 W or 600 W ICP with pure Ar feed gas. For the O^+ beam we use a mixed feed gas comprising a mixture of Ar (48%), O_2 (50.5%), and Ne (1.5%) and drive the ICP at 600 W. For experiments involving ice films, we dose vapor from degassed deionized water. The water is degassed inside of the dosing manifold via two freeze-thaw cycles with rough pumping before each thaw. Residual gas analysis during dosing of water prepared in this way showed an increase in H_2O partial pressure without increase in partial pressure for atmospheric species (N_2, O_2, Ar, CO_2). Ice deposition was conducted at a surface temperature of 31 K by dosing to a chamber pressure of 4×10^{-7} torr for a period of 10 minutes, during which time the film thickness was monitored via interferometry. For the evaluation surface charging in §3.2.2, the surface temperature was raised to 50 K after deposition. The actual surface temperature was somewhat variable depending on additional heat load from the electron gun. For measurements of secondary ion energetics and mass distribution in §3.2.1 and §3.2.2, the electron gun was operated under fixed conditions in a constant current mode (V_f=−12.5 V, V_r=0 V, filament current 4.1 A), and the surface temperature was 57−58 K during beam exposure. The filament voltage drop was 1.9 to 2.2 V, so the electron energy was between 12.5−14.7 eV at ground.

For the demonstration of TPD in §3.2.3, the ice deposition was as above. Following deposition, the target surface was rotated toward the 2 mm detection aperture (labelled F in Figure 6-5) so that the detector line of sight was nearer to surface-normal (12° off). The detector system was configured for SNMS, with the electron impact ionizer operating at 70 eV and an emission current of 0.49−0.77 mA. The cold finger temperature was then ramped at roughly 2 K/min by manually adjusting the cryocooler power and cartridge heater power (see Appendix Fig. A-13C). Analog mass spectra (6 to 63 amu) were collected twice per minute by sweeping the QMS at a fixed EEA pass energy (ion kinetic energy) of 15 eV for the duration of the temperature ramp. Simultaneously, the gas partial pressure in the scattering chamber was monitored for a number of masses via residual gas analyzer (RGA 200, Stanford Research Systems) operating at the same electron energy.

6.3 Preliminary results

6.3.1 Ar^+ scattering results

After installation the total scattering angle was assessed using an Ar^+ beam scattering from the uncooled gold target surface (Appendix Fig. A-11). As described in earlier sections, a scattering angle of 79.0° is extracted from the measured kinematic factor (0.7157) for Ar^+ scattering from single gold atoms. Due to the small distances between the target surface and the flag aperture, small displacements of the target surface, such as are accrued from assembly tolerances, propagate to substantial changes in the scattering angle.

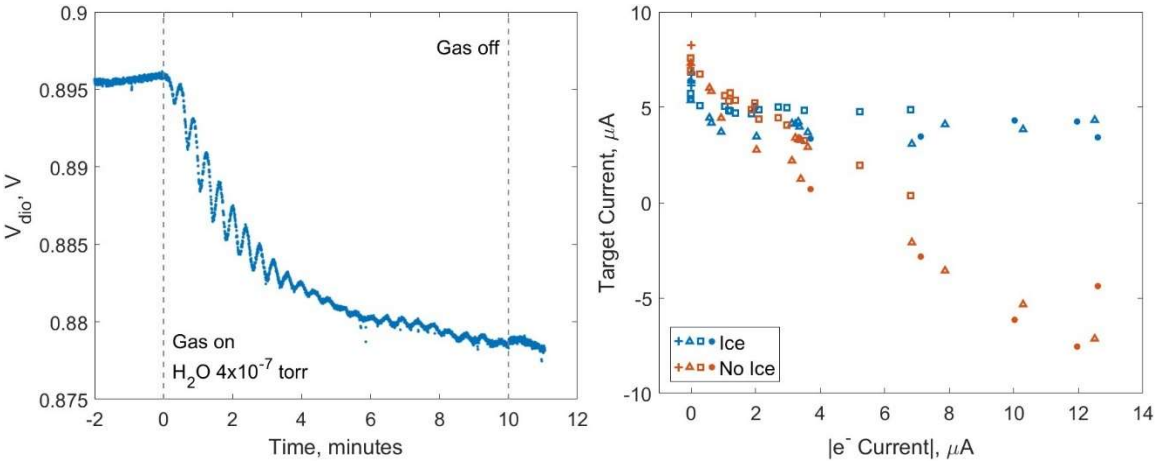

Figure 6-6: Deposition and charging of ASW film. Left) Photodiode voltage during 10-minute ice deposition at 31 K. The fringe shows 23 maxima, corresponding to a thickness of 6.4 μm. Right) Target current vs on-target electron current with (blue) and without (red) water ice (~50 K) during exposure to a 109 eV Ar^+ beam at 6−8 μA. Different marker shapes designate different filament currents for the electron gun (0A +, 3.8A □, 4.2A Δ, 4.4A •), with on-target emission current adjusted via the repeller and filament floating bias.

Following deposition of a 6.4 μm H_2O ice film (Figure 6-6 Left), we explored the surface charging dynamics of the ice film at 50 K under exposure to the Ar^+ beam by monitoring the target current after as electron gun parameters were varied (Figure 6-6 Right). A follow-up experiment measured the target current without ice deposition for the same operating parameters, without and without simultaneous ion exposure. With no ice on the surface the net target current (constant ion beam current plus varied electron flood current) decreases linearly with the electron flood current, as expected. With ice deposited, an initial 2−3 μA drop in target current is observed when the filament is turned on, larger than the corresponding electron current to the bare (neutral) surface, indicating collection of the flood electrons by a positive surface potential. Interestingly, after this initial drop,

further increases in the electron current do not lower the target current. This indicates the presence of a negative surface potential, yet the net current through the base of the film remains positive. These observations can be explained by the development of a surface dipole due to accumulation of electrons at the surface and implantation of O^+ at greater depth.

The secondary ion signal intensities and peak energies were also functions of the electron flood conditions. Secondary negative ions were not detected with the filament off, due presumably to trapping by large positive surface potentials. Under these conditions, the energy distribution for the most abundant secondary ion, H_3O^+, peaked at 42 eV. When electron flooding is supplied, the secondary negative ions become detectable and the positive ion peak exit energies are reduced, consistent with the partial neutralization of surface charge.

To evaluate the secondary ion energetics and product mass distributions, we fix the electron gun parameters and vary the incident energy. For the most abundant positive ions, H_2O^+ and H_3O^+, we observe symmetric distributions peaking at energies of 25−35 eV (Figure 6-7). Neither the peak energy nor the symmetry is expected for sputtered products. Indeed, although negative ions were detectable, their signals were very faint, too weak to resolve the energy distributions, but sufficient to evaluate the mass distribution (Figure 6-8). O^- and OH^- are the most abundant anion products. The halide peaks are fluorine and chlorine sputtered from within of the EEA by the large scattered neutral flux. Notably, the O_2^+ signal is barely above the noise floor, with an intensity 4 decades lower than H_3O^+ and one decade lower than the $(H_2O)H_3O^+$ cluster. Production of O_2 via radiolysis is expected under Ar^+ bombardment, and a yield of 0.5 O_2/impact has been measured under similar conditions (206 eV, 12 K).[28] Lacking a measurement of the neutral O_2 flux and angular distribution, our data cannot be quantitatively converted to a yield. However, given that the positive ion fraction is a sharply decreasing function of the ionization energy[29] and that the IE is considerably larger for argon (15.76 eV) than for O_2 (12.07 eV),[30] the ion abundances (3.8:1 Ar^+:O_2^+) in Figure 6-8 suggest a very inefficient production of O_2.

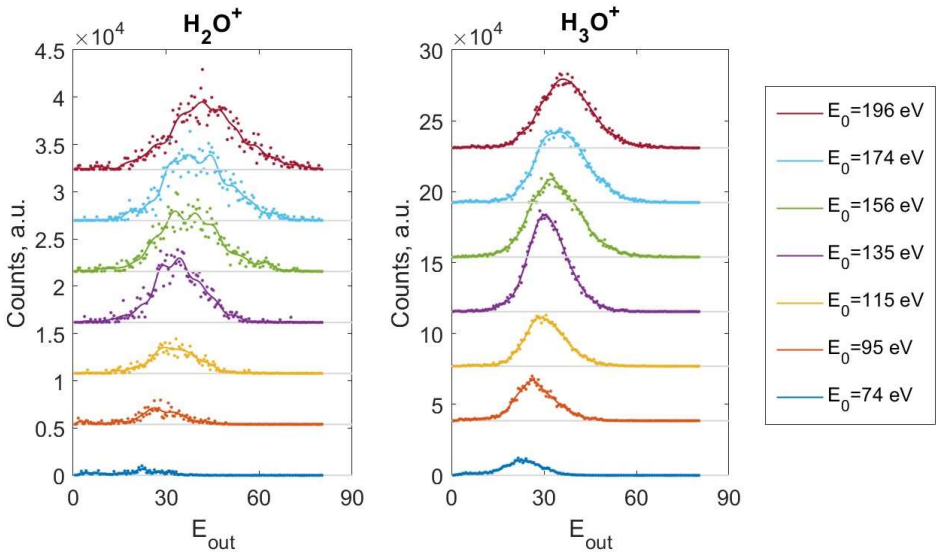

Figure 6-7: Secondary positive ion energy distributions at different Ar^+ incident energies for an ASW target. The baselines are staggered for readability. The data are plotted as points. The solid lines are these data low-pass filtered at 0.1 Hz to remove some noise.

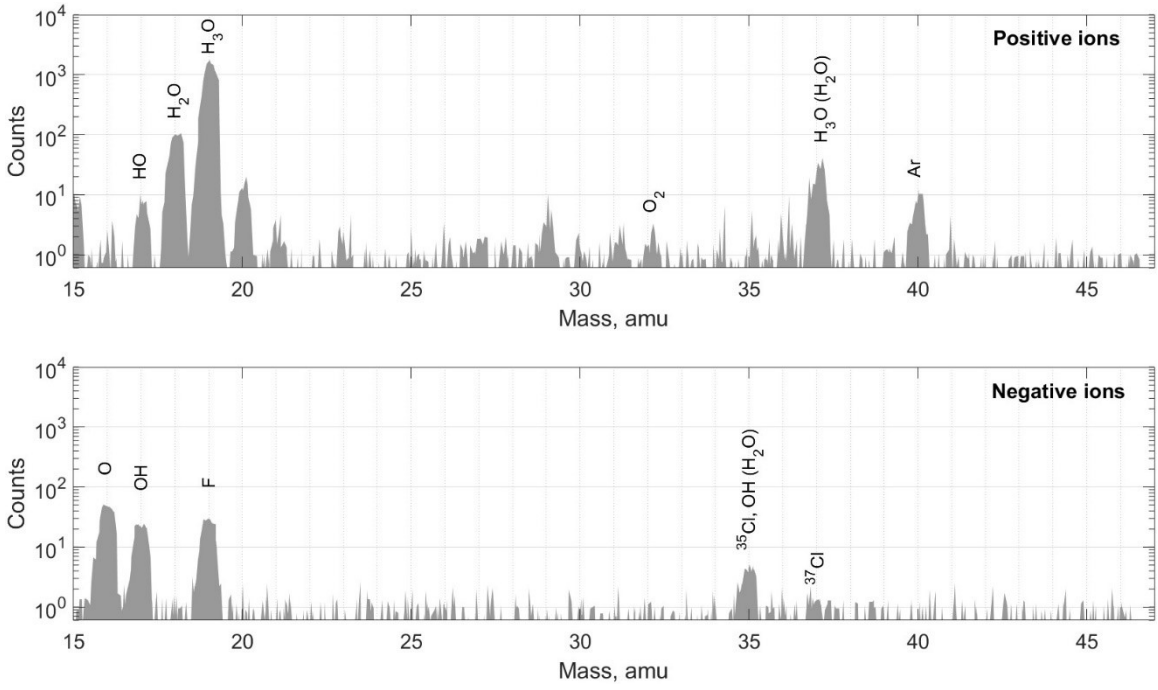

Figure 6-8: Mass spectra for positive (top) and negative (bottom) product ions from amorphous water ice (58K) under exposure to Ar^+ (116 eV). Each scan is conducted at fixed product kinetic energy as in §3.4.1, where the caveats of this approach are adressed. The product kinetic energies are 26 and 32 eV for positive and negative ions, respectively.

6.3.2 O^+ scattering results

The experiments of §6.3.1 with an Ar^+ beam confirm that the electron flood gun partially neutralizes surface charging at the beam spot, allowing us to measure secondary negative ions. Under exposure to a O^+ beam, the ice film shows similar sputtering behavior, except that O^+ becomes the second most abundant positive ion (Figure 6-9). Besides the water group ions, the positive ion distribution shows, again, several other peaks. The strongest of these correspond to O_2 and the $H_3O(H_2O)^+$ cluster with abundances comparable to HO^+. The O_2^+ abundance relative to H_2O^+ is ~3× greater than under argon exposure, perhaps indicating an enhancement of the O_2 production due to implantation of reactive atomic oxygen or the Eley-Rideal mechanism described in Chapter 4.[27] Further experiments are needed to ascertain the significance and mechanism for the O_2^+ enhancement.

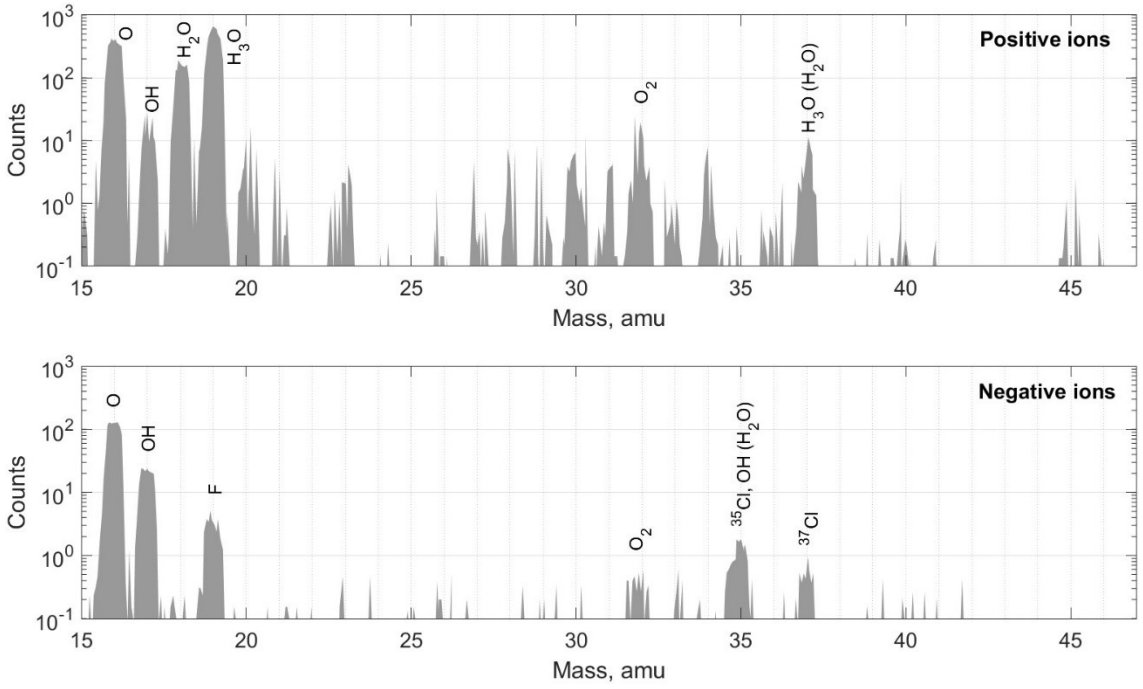

Figure 6-9: Preliminary mass spectra for positive (top) and negative (bottom) product ions from amorphous water ice (58K) under exposure to O^+ (118 eV). The product kinetic energies are 20 and 26 eV for positive and negative ions, respectively.

Besides these water-derived ions, there is evidence of impurities in the ice or contamination of the detector system. The signal at 20 amu, for instance, is likely neon due to crossover flux from the plasma feed gas. At 23 amu, we have signal from sodium. Alkali metal ions are known to be emitted from heated tungsten filaments, such as the one supplying the neutralizing current in this

experiment.[31] However, they are emitted at thermal energies and cannot reach the target surface due to the floating bias of the filament (−12.5 V). More likely the signal at 23 amu is due to sputtering of Na inside of the EEA by the scattered neutral flux. More puzzling is the relatively strong signal at 30 amu, which did not appear for the Ar^+ projectile. The nitric oxide cation (NO^+) is a possibility given its relatively low IE (9.26 eV)[30] and that N_2 trapping would be possible at our ice deposition temperature.[32] Other identifications (e.g. H_2CO, DCO) are more difficult to rationalize.

Fluoride and chloride ions appear in the negative ion mass distribution for the same reason as in §6.3.1. These possible sources of contamination do not interfere with our measurements of the most abundant secondary and scattered ions (excepting the cluster ion OH $(H_2O)^-$), but they will be an obstacle in planned work with ices of mixed composition. Further work should begin by identifying and mitigating the contamination source. Apart from halides, only O^-, OH^-, and O_2^- are detected as negative ions. The first hydroxide cluster ion OH $(H_2O)^-$ is ambiguous with $^{35}Cl^-$, so that we can only provide an upper limit of 1% relative to O^-.

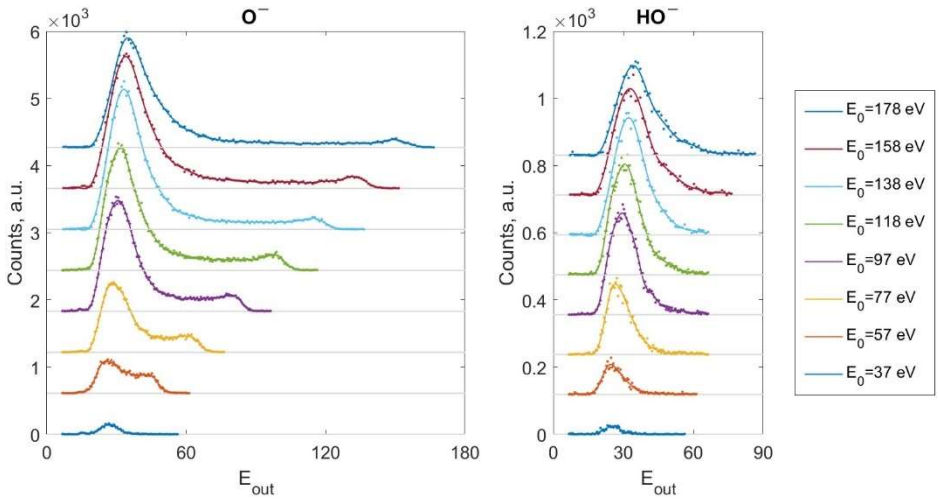

Figure 6-10: Secondary negative ion energy distributions at different O^+ incident energies for an ASW target. The baselines are staggered for readability. The data are plotted as points. The solid lines are these data low-pass filtered at 0.1 Hz to remove some noise.

At all beam energies, the onset of the O^- and OH^- signals is approximately 18 eV. The O_2^- ion appears at kinetic energy around 12 eV lower. The onset exit energy of O^- was to some extent controllable by adjusting the e-gun parameters, moving to higher energies for higher electron energies and currents. The positive ion energy distributions do not show these large onset energies

(Figure 6-11), suggesting that the surface is, in this experiment, charged to negative potentials. Indeed, the positive ion signals show evidence of truncation at low energies (especially obvious for H_3O^+), consistent with surface trapping. The electron gun parameters were the same in this experiment and the Ar^+ beam experiment, so this change in the surface charge polarity is pressing concern. It may be due to the beam current being lower for O^+ (~2 μA for these ICP conditions) than for Ar^+ (as much as 8.3 μA in §6.3.1). In the present experimental configuration, it is not possible to dynamically balance electron flood and beam current with any precision.

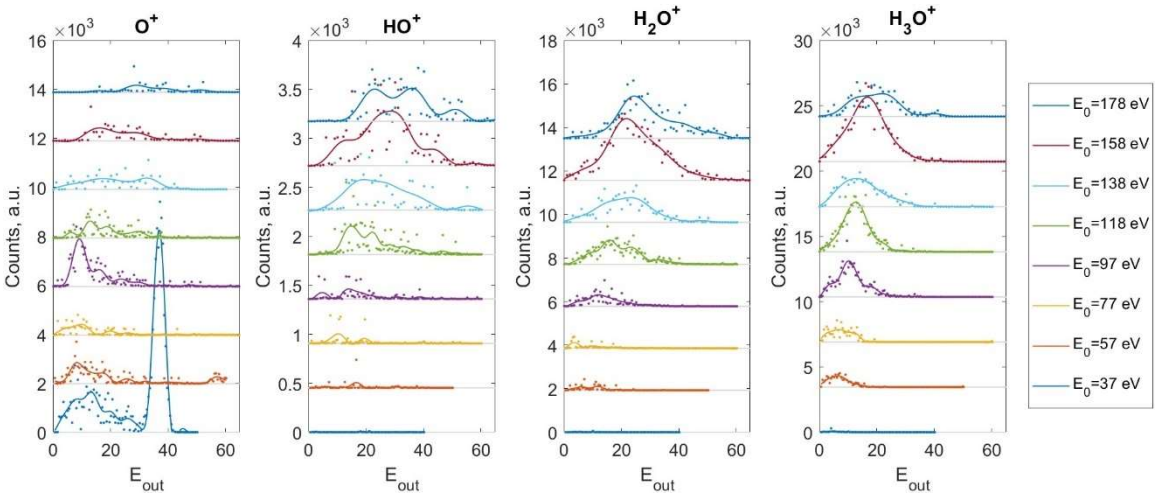

Figure 6-11: Secondary positive ion energy distributions at different O^+ incident energies for an ASW target. The baselines are staggered for readability. The data are plotted as points. The solid lines are these data low-pass filtered at 0.1 Hz to remove some noise. The sharp peak at $E_0=E_{out}=37$ eV for the O^+ subplot is due to deflection of primary ions into the detector by electric field conditions near the target.

6.3.3 Temperature programmed desorption

We did not see direct evidence for the ER water oxidation reaction observed in our Reactive MD simulations (Chapter 4). This was the anticipated outcome given the scattering geometry in our preliminary experiment — due to the low surface density and near unity projectile-surface mass ratio, rebounding of O_2 from the surface should be very rare. Indeed, in the simulations we only observe scattered O_2 at higher angles of incidence (nearer to grazing incidence).[27] More importantly, the charge equilibration formalism (QEq[33]) employed in our simulations does not capture important ionization processes, such as resonant charge transfer. The simulation results do not shed light on the charge state of O_2. Our scattering system is equipped for SNMS, which may be critical in confirming the simulated reaction mechanism. In the case that the reaction kinematics cannot be ascertained from scattered products, indirect evidence for the reaction may be provided

by temperature programmed desorption, provided that the ER product can be distinguished from the radiolytic product, for instance via isotopic labelling. Looking beyond studies of pure water ice toward more complex chemistries (as in Chapters 5 and 8), TPD is a potentially a vital asset. For this reason, we provide a basic demonstration of the capability here (Figure 6-12).

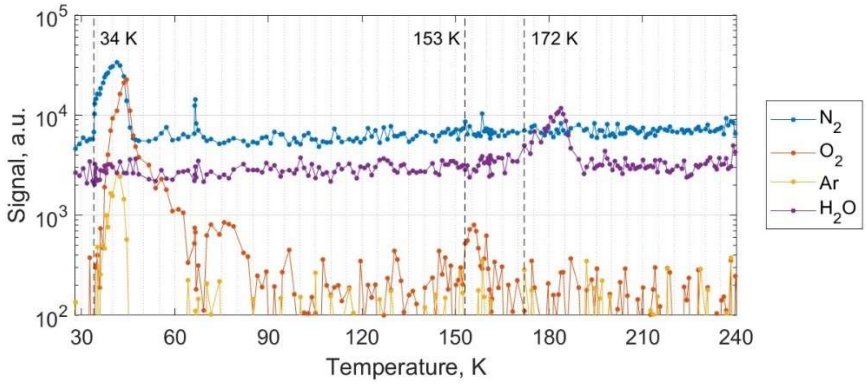

Figure 6-12: A demonstration of temperature programmed desorption for water ice deposited at 31K. The onset temperatures are called out for three events: N_2 desorption, a high-temperature desorption of O_2, and water desorption.

Our apparatus' SNMS-capable scattered product detector is readily repurposed for TPD. Following deposition of a water ice film at 31 K, we monitor the SNMS signal during a heating ramp. By conducting this test at a low deposition temperature, we are creating a rather extreme test of the TPD system. At 31 K, the entire cold finger and second stage of the cryocooler condenses N_2, O_2, and Ar residual to the vacuum chamber.

Three events are apparent in the TPD data (Figure 6-12). Beginning around 34 K, N_2, O_2, and Ar condensed prior to H_2O deposition sublimate. The high-temperature (153 K) desorption of O_2 is coincident with the temperature for the amorphous to crystalline phase transition,[34] which is typically marked by desorption of trapped volatiles.[32] The trapped O_2 in this case is likely from the condensed residual O_2, although further investigation is warranted to determine if more thorough degassing of the water is necessary. Around 172 K, the bulk water-ice begins to sublime. This is somewhat higher a temperature than expected,[32] which is due to the high H_2O background in the ionizer obscuring the onset of H_2O sublimation.

The most important result of this experiment is to demonstrate that the product detector system provides excellent surface specificity. A residual gas analyzer (RGA) running simultaneously in the scattering chamber logged partial pressure excursions of four orders of magnitude for the hyper-

volatiles and three for water (Appendix Fig. A-13A), as gas desorbed from various surfaces of the cold finger and cryocooler. Relatively large power adjustments occurred at 66 K and 161 K, resulting in large pressure changes in the scattering chamber, which are reflected as very narrow spikes in the N_2 signal. There is clearly much room for improvement in the dynamic range, especially for N_2 and H_2O. A more thorough bakeout of the ionizer assembly and optimization of the ionization conditions are expected to provide large improvements.

6.4 Conclusion and Outlook

Although a great deal of experimental effort has been mustered toward understanding radiolysis and sputtering of water ice in the past few decades, studies with relevant hyperthermal reactive ions are extremely rare. To our knowledge, the experimental capability we have developed in the foregoing sections is utterly unique, and the preliminary results are the first of their kind. Still, our results to date are more diagnostic of experimental challenges than exciting surface chemistry/dynamics. There is much work to be done toward refining the platform and the results. The first and most pressing is to resolve the issue of surface charging, which distorts the energy distributions of scattered products and complicates their interpretation, as discussed in Chapter 3 (§3.4.3). The electron flooding parameters require further optimization to prevent the overcompensation evident in §6.4. This will require a method of measuring the surface potential, ideally one that can provide dynamic feedback for closed loop control. At the least, there is hope that surface charge distribution can be ascertained by the method demonstrated in §3.4.3. This method requires foreknowledge of the scattering peak shape and a peak which is well separated from zero kinetic energy and from other scattering/sputtering signals. In the case of O^+ scattering on pure water ice, we meet none of these criteria. However, co-deposition of H_2O with a heavy inert gas (Kr or Xe) potentially resolves both problems.

With the charging issue corrected, exploration of the low-energy ion-ice interaction can begin in earnest, ideally beginning with a verification of our simulation results. At higher angles of incidence, we may find direct kinematic evidence for the Eley-Rideal O_2 formation mechanism seen in Chapter 4. Indirect evidence may be obtained from the onset energy for H_3O^+ emission. For Cs^+ bombardment, preformed H_3O^+ can be emitted at energies as low as 19 eV, whereas H_3O^+ is formed by collision-induced secondary ionization processes at energies over 60 eV.[8] H_3O^+ is frequently a by-product of the ER water oxidation, even at impact energies of 8.3 eV, the lowest simulated in Chapter 4. A comparison of O^+ and Ne^+ bombardment will provide the most direct

separation between radiolytic and non-radiolytic O_2 formation. The platform developed in this chapter is general — a virtually unlimited space of projectile-ice combinations is now accessible. We will provide some further suggestions for future work in Chapter 8.

6.5 References

1. Strazzulla, G., Leto, G., Gomis, O. & Satorre, M. A. Implantation of carbon and nitrogen ions in water ice. *Icarus* **164**, 163–169 (2003).
2. Strazzulla, G., Palumbo, M. E., Boduch, P. & Rothard, H. Ion Implantation and Chemical Cycles in the Icy Galilean Satellites. *Earth Moon Planets* **127**, 2 (2023).
3. Martinez, R. *et al.* Production of Hydronium Ion $(H_3O)^+$ and Protonated Water Clusters $(H_2O)_n H^+$ after Energetic Ion Bombardment of Water Ice in Astrophysical Environments. *J. Phys. Chem. A* **123**, 8001–8008 (2019).
4. Ruf, A. *et al.* Sulfur ion irradiation experiments simulating space weathering of Solar System body surfaces - Organosulfur compound formation. *Astron. Astrophys.* **655**, A74 (2021).
5. Bouquet, A. *et al.* Sulfur Implantation into Water Ice with Propane: Implications for Organic Chemistry on the Surface of Europa. *Planet. Sci. J.* **5**, 102 (2024).
6. Mifsud, D. V. *et al.* Energetic electron irradiations of amorphous and crystalline sulphur-bearing astrochemical ices. *Front. Chem.* **10**, (2022).
7. Park, S.-C., Moon, E.-S. & Kang, H. Some fundamental properties and reactions of ice surfaces at low temperatures. *Phys. Chem. Chem. Phys.* **12**, 12000–12011 (2010).
8. Kang, H. Chemistry of Ice Surfaces. Elementary Reaction Steps on Ice Studied by Reactive Ion Scattering. *Acc. Chem. Res.* **38**, 893–900 (2005).
9. Kang, H. Reactive Ion Scattering of Low Energy Cs+ from Surfaces. A Technique for Surface Molecular Analysis. *Bull. Korean Chem. Soc.* **32**, 389–398 (2011).
10. Bang, J., Shoaib, M. A., Choi, C. H. & Kang, H. Efficient Thermal Reactions of Sulfur Dioxide on Ice Surfaces at Low Temperature: A Combined Experimental and Theoretical Study. *ACS Earth Space Chem.* **1**, 503–510 (2017).
11. Bang, J., Lee, D. H., Kim, S.-K. & Kang, H. Reaction of Nitrogen Dioxide with Ice Surface at Low Temperature (≤170 K). *J. Phys. Chem. C* **119**, 22016–22024 (2015).
12. Kim, S.-K. & Kang, H. Efficient Conversion of Nitrogen Dioxide into Nitrous Acid on Ice Surfaces. *J. Phys. Chem. Lett.* **1**, 3085–3089 (2010).
13. Park, S.-C., Maeng, K.-W., Pradeep, T. & Kang, H. Unique Chemistry at Ice Surfaces: Incomplete Proton Transfer in the H3O+–NH3 System. *Angew. Chem.* **113**, 1545–1548 (2001).
14. Shin, T.-H., Han, S.-J. & Kang, H. Efficient hydration of Cs+ ions scattered from ice films. *Nucl. Instrum. Methods Phys. Res. Sect. B Beam Interact. Mater. At.* **157**, 191–197 (1999).
15. Lee, C.-W., Lee, P.-R., Lahaye, R. J. W. E. & Kang, H. Effect of adsorbate mass on an Eley–Rideal reaction. Reactive scattering of Cs+ from noble gases and N2 adsorbed on Ru(0001) surfaces at hyperthermal energy. *Phys. Chem. Chem. Phys.* **11**, 2268 (2009).
16. Kim, J.-H., Lahaye, R. J. W. E. & Kang, H. Evidence for Eley-Rideal abstraction mechanism in reactive ion scattering of Cs+ from Pt(111) adsorbed with CO and CO2. *Surf. Sci.* **601**, 434–440 (2007).

17. Lahaye, R. J. W. E. & Kang, H. Reactive Ion Surface Scattering as an Eley–Rideal Process: A Molecular Dynamics Study into the Abstraction Reaction Mechanism by Low Energy Cs+ From Pt(111). *ChemPhysChem* **5**, 697–705 (2004).
18. Bag, S., McCoustra, M. R. S. & Pradeep, T. Formation of H2+ by Ultra-Low-Energy Collisions of Protons with Water Ice Surfaces. *J. Phys. Chem. C* **115**, 13813–13819 (2011).
19. Bag, S., Bhuin, R. G. & Pradeep, T. Distinguishing Amorphous and Crystalline Ice by Ultralow Energy Collisions of Reactive Ions. *J. Phys. Chem. C* **117**, 12146–12152 (2013).
20. Cyriac, J., Pradeep, T., Kang, H., Souda, R. & Cooks, R. G. Low-Energy Ionic Collisions at Molecular Solids. *Chem. Rev.* **112**, 5356–5411 (2012).
21. Galli, A., Vorburger, A., Wurz, P. & Tulej, M. Sputtering of water ice films: A re-assessment with singly and doubly charged oxygen and argon ions, molecular oxygen, and electrons. *Icarus* **291**, 36–45 (2017).
22. McBride, E. J., Millar, T. J. & Kohanoff, J. J. Irradiation of Water Ice by C+ Ions in the Cosmic Environment. *J. Phys. Chem. A* **118**, 6991–6998 (2014).
23. Jaramillo-Botero, A. *et al.* Hypervelocity Impact Effect of Molecules from Enceladus' Plume and Titan's Upper Atmosphere on NASA's Cassini Spectrometer from Reactive Dynamics Simulation. *Phys. Rev. Lett.* **109**, 213201 (2012).
24. Jaramillo-Botero, A., An, Q., Theofanis, P. L. & Goddard, W. A. Large-scale Molecular Simulations of Hypervelocity Impact of Materials. *Procedia Eng.* **58**, 167–176 (2013).
25. Kohanoff, J. & Artacho, E. Water radiolysis by low-energy carbon projectiles from first-principles molecular dynamics. *PLOS ONE* **12**, e0171820 (2017).
26. Kohanoff, J. & Artacho, E. First-principles molecular dynamics simulations of the interaction of ionic projectiles with liquid water and ice. *AIP Conf. Proc.* **1080**, 78–87 (2008).
27. Grayson, R. W., Goddard, W. A. & Giapis, K. P. Reactive scattering of water group ions on ice surfaces with relevance to Saturn's icy moons. *Icarus* **379**, 114967 (2022).
28. Teolis, B. D. *et al.* Cassini Finds an Oxygen-Carbon Dioxide Atmosphere at Saturn's Icy Moon Rhea. *Science* **330**, 1813–1815 (2010).
29. Gnaser, H. Chapter 5: Ionization Processes of Sputtered Atoms and Molecules. in *Low-energy ion irradiation of solid surfaces* 205–250 (Springer, Berlin ; New York, 1999).
30. Lias, S. G. Ionization Energy Evaluation. in *NIST Chemistry WebBook, NIST Standard Reference Database Number 69* (eds. Linstrom, P. J. & Mallard, W. G.) (National Institute of Standards and Technology, Gaithersburg MD).
31. Craig, J. H. & Hock, J. L. Construction and performance characteristics of a low cost energy prefilter. *J. Vac. Sci. Technol.* **17**, 1360–1363 (1980).
32. Bar-nun, A., Herman, G., Laufer, D. & Rappaport, M. L. Trapping and release of gases by water ice and implications for icy bodies. *Icarus* **63**, 317–332 (1985).
33. Rappe, A. K. & Goddard, W. A. Charge equilibration for molecular dynamics simulations. *J. Phys. Chem.* **95**, 3358–3363 (1991).
34. Jenniskens, P. & Blake, D. F. Crystallization of Amorphous Water Ice in the Solar System. *Astrophys. J.* **473**, 1104 (1996).

CHAPTER 7

MOLECULAR HYDROGEN IN THE ENCELADUS PLUME

[The contents of this chapter are temporarily embargoed.]

Chapter 8

CONCLUDING REMARKS AND FUTURE WORK

8.1 Introduction

In this final chapter, we will briefly recapitulate the main conclusions of this dissertation and then offer an opinion as to future directions for this line of research. To motivate future studies, we will also provide some preliminary simulation results for mixed-composition ice surface.

8.2 Summary

Broadly speaking, this thesis has been directed at understanding the chemical weathering astrophysical surfaces by low-energy plasma. Specifically, we have taken a mixed experimental-theoretical approach focusing on hyperthermal water group ion/molecule bombardment. Experimentally, we have presented brief case studies of two systems, carbonaceous surfaces (Chapter 2) and chloride surfaces (Chapter 3), focusing on secondary negative ion emission and reactive scattering. The results provide some important context for the interpretation of negative PUI signatures found in the Saturn system. In Chapter 6, we describe the modification of our scattering apparatus to accommodate cryogenic ice targets and report preliminary results scattering on amorphous water ice.

On the side of theory, we undertaken Reactive MD simulations of ices under hyperthermal water group molecule bombardment, beginning with a study of pure, hexagonal water ice (Chapter 4). The simulations reveal an efficient, non-radiolytic pathway to formation of molecular O_2, which is relevant to the maintenance of O_2 exospheres at icy moons. Building on these results, we explore the oxidation of enclathrated methane, focusing on the production of methanol, which again occurs via a non-radiolytic pathway (Chapter 5). These simulations suggest that low-energy reactive impactors may play an important role in modifying the organic inventory of airless icy bodies. In this chapter, we will report a further extension of the simulation work to more elaborate ice chemistry. Finally, in Chapter 7, we addressed *Cassini's* observation of abundant molecular hydrogen in the Enceladus plume, specifically, whether exposure of ice grains to plasma in the "plume ionosphere" can account for the measured mixing ratio. We developed a model for H_2 production (by both radiolysis and Eley-Rideal reactions) and transport in the plume, which shows

that the plasma-surface interaction does not produce a sufficient quantity of H_2. This conclusion, we note, is particularly sensitive to the grain flux at the plume source, which is badly constrained at present.

In brief, we have attempted to repair some of the research deficit for astrophysical low-energy plasma-surface interactions, while addressing some lingering questions from past missions (i.e. *Cassini*) and anticipating some from future missions (*Juice* and *Europa Clipper*). Although chapter to chapter, the work has been somewhat disparate, an overarching conclusion does emerge: low-energy reactive ions play a unique role in modifying the composition of airless bodies and in populating the gas/plasma phases. These scattering systems show reactivity and physics that is not adequately captured by extrapolation from higher energy regimes. We hope, at least, to have demonstrated this point and provided some motivation for further study. But a second, inescapable conclusion follows, that their role in astrochemistry is still largely unknown. As a final illustration, the next section will present simulation of more complex chemistry driven by hyperthermal impacts.

8.3 Hyperthermal CHON Ice chemistry

The presence and source of surface organics are key and timely questions in planetary science because of their implications for habitability and the search for life beyond Earth. They are particularly important at Ocean Worlds (e.g. Enceladus, Europa), where they can provide markers of prebiotic or biogenic chemistry beneath the ice. At the plasma-processed surface of these bodies, however, organics may be created, modified, or destroyed through surface chemistry. Although vigorous research efforts have already exposed the role of radiolysis in synthesis (see [1] and references therein) and destruction of organics (especially biomarkers[2–5]) by energetic (>1 keV) charged particle interactions, the contribution of much more abundant low-energy plasma ions (<1 keV) is scarcely studied. Our previous Reactive MD simulations with methane clathrate surfaces revealed that the organic inventory is expanded by Eley-Rideal reactions and implanted reactive species.

Nitrogen bearing-species, including ammonia and hydrogen cyanide, are also associated with ices throughout the solar system. Hydrated ammonia and hydrazine monohydrate are present, for instance, in the ices of Saturn's icy moons. Hydrogen cyanide is an common parent molecule in cometary comae[6] and has recently been reported in the Enceladus plume.[7] In combination with a carbon source, these molecules make a variety of CHON molecule accessible, including, in

principle, amino acids and peptides. As an exploration of hyperthermal impact induced CHON chemistry, we have simulated atomic oxygen bombardment of a mixed H_2O−HCN−CH_4 ice. A variety of surface structures are conceivable for this system. We have chosen a phase 1 clathrate structure of mixed cage occupancy for our simulation, not because it is a realistic or relevant surface structure, but because it is a convenient experimental construct. This construct simplifies the preparation of a homogenous surface tremendously and supports facile tuning of the ice composition (different guest molecules and different ratios), making a quick exploration of the chemical space possible.

The surface is prepared as in Chapter 5, except that the occupant of each clathrate cage in the tiled structure has been chosen by coin-flip as either HCN or CH_4. The final slab dimensions are here 34.7×34.7×35.9 Å and the surface temperature is 110 K. The simulation protocol is identical to that described in §5.2.2 and the chemical analysis method also follows Chapter 5. Our forcefield parameters are, as in Chapter 5, those of Rahaman et al. (2011), essentially an augmentation of the parameterizations we used in Chapters 4,[8] optimized to describe tautomerization of glycine in aqueous solution.[9] It bears noting that forcefield parameters are optimized to provide an accurate description of molecules (relative to QM), and the fact that this forcefield has been trained on glycine conformers does not bias our simulations toward the production of glycine. We found that a single modification, reduction of N−O sigma bond distance parameter by 13%, was needed to correct spurious geometries (in e.g. $HONH_2$). We have run 19 independent simulations to a dose of 100 atomic oxygen impacts at 20 km s^{-1} and angle of incidence 45°.

8.3.1. Preliminary simulation results for a ternary ice

The mixed clathrate system shows much the same chemistry of the of the methane clathrate, with a linear increase in the number of O−O and C−O bonds (Figure 8-1). But we have new contributions from the HCN-ice chemistry and, more rarely, reactions between guest molecules. In the former category we have frequent hydrogenation of HCN to HCNH (13%), dehydrogenation to CN (2.3%), conversion to hydrogen iso-cyanide (1.3%), and formation of isocyanic acid (OCNH, 2.3%). Accumulated hydrogenation results eventually in methylene imine (H_2CNH, 0.7%) and methylamine (H_3CNH_2, 0.1%), both of which are precursors to glycine formation (see Figure 8-3).[10,11] The cyanogen motif only occurred in one instance (as HNCCN, 0.05%). Reactions between disparate guest molecules were rare but did occur, even after as few as 4 impacts. These formed a variety of $H_xNC_2H_y$ species with the −NCC− backbone motif, with a yield collectively of 0.2%. Single instances of $HNC(H)C(OH)H_2$ (0.05%, see Figure 8-2) and the H_2NCCO radical

(0.05%) were formed. The latter is a single hydrogen addition from aminoketene ($H_2NC(H)CO$), which has lately been implicated in peptide synthesis in the ISM.[12] Although at the meager yield of this system, the requisite aminoketene polymerization is certainly unlikely.

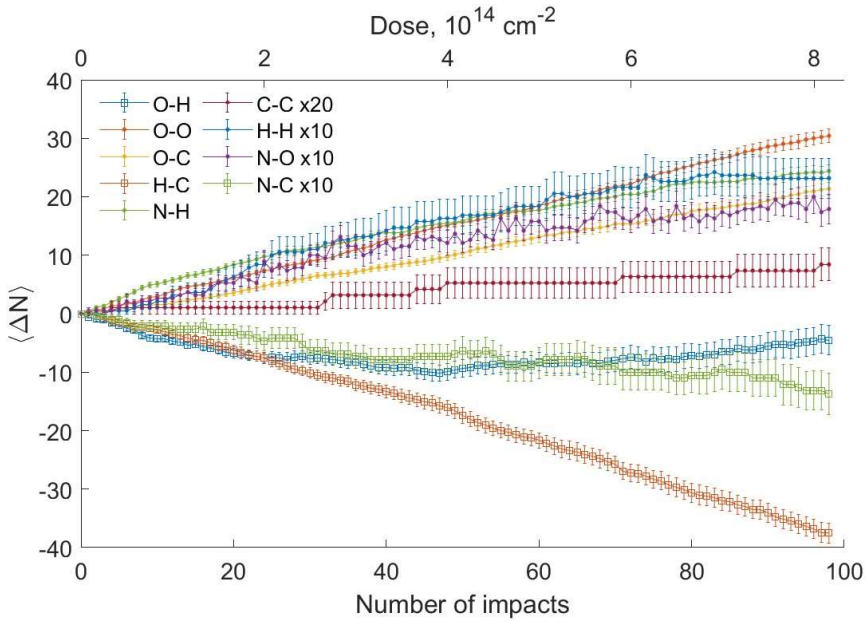

Figure 8-1: Cumulative change in the number of bonds of a given type (BO>0.55) vs the accumulated impact dose. Hydrogen bonded clusters have been broken apart at over-coordinated hydrogen atoms as described in §5.2.1. The bond tally ΔN includes molecules that were lost to the headspace. Error bars are standard error across the 19 replicates.

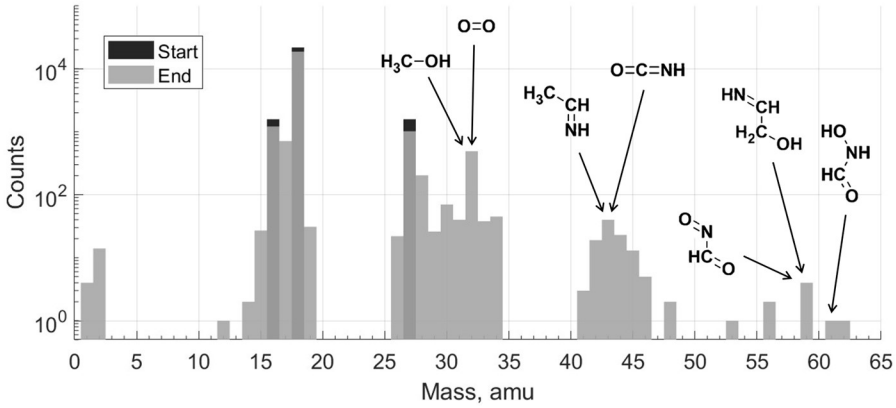

Figure 8-2. Mass spectrum of the simulation before (black) and after 100 O impacts (gray). Where the two spectra overlap, the color is darker. The data are aggregated across the 19 replicates, and species lost to the headspace are not included, so the mass spectrum is representative of the solid phase. Annotations show a selection of molecules contributing to several peaks, but these are not an exhaustive catalog.

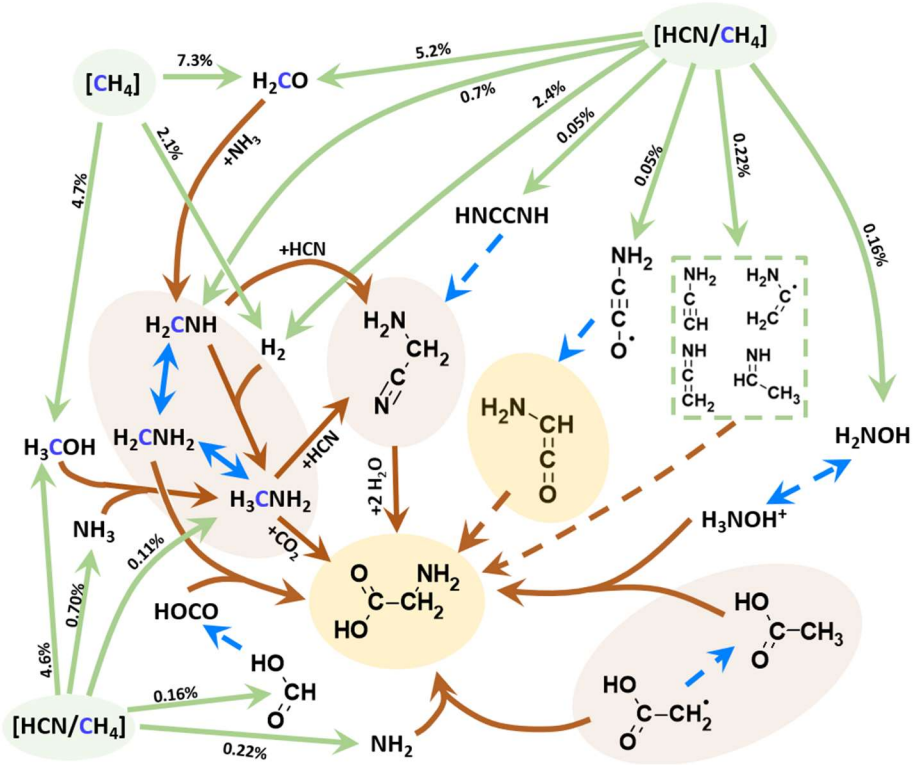

Figure 8-3: A schematic of reaction pathways potentially leading from oxygen-bombarded mixed ices (green bubbles) to two prebiotically significant organics (yellow bubbles), glycine and aminoketene. Maroon bubbles highlight important intermediates in literature abiotic glycine formation pathways. Maroon arrows indicate reactions in these pathways (see Aponte et al. 2017 and Joshi & Lee 2022), some but not all of which have been confirmed experimentally. Blue arrows indicate hydrogen addition/removal reactions specifically and green arrows show reactions actually observed in our simulations, along with yields on a per impactor basis. Broken arrows represent putative paths, not explicitly described in the two cited papers. The HCN/CH_4 clathrate is represented twice to avoid circuitous arrows. These results include a 20th simulation, which only went to 93 impacts.

8.4 Directions

The importance of the subject (the thesis topic) will only grow in coming decades as search for life shifts its focus from Saturn's moons to Jupiter's and back again. NASA's *Europa Clipper* is soon to launch, and the ESA's *Juice* already en route to the Galilean moons. With the National Academies' Decadal Survey and the ESA's recent Expert Committee Report both marking an Enceladus lander as a high-priority mission, a return to Saturn's airless icy moons is likely not far off.[13,14] Until an Enceladus lander is realized, however, we will have to rely on remote observations

to constrain the surface and interior composition of these bodies. The dearth of research on the relevant low-energy plasma-surface interactions jeopardizes our ability to interpret these remote observations in the prioritized terms (habitability).

Saito et al. (2008), to my knowledge, were the first to point out the analogy between LEIS as an analytical technique and LEIS as an astrophysical phenomenon.[15] Extending this analogy to RIS, the native plasma-surface interaction at airless icy bodies, while driving compositional changes, may also become a novel remote sensing asset. Since gas phase and sputter yields of negative ions fail to reproduce the observed negative ion abundances at Saturn's icy moons, it is plausible that the bulk of the negative ions here are due to surface scattering processes. At the kinetic energies relevant to Saturn and Jupiter's moons, plasma-surface scattering can sample surface composition through abstraction of atoms/molecules from the top few monolayers of the surface and through the ionization mechanism (RCT), which is sensitive to electronic structure of the surface. In contrast, currently used remote spectroscopy techniques sample the surfaces of icy moons to optical depths in the micrometer to centimeter range. Important surface properties can be obscured due to the sampling depth, which results in uncertainty and deficiencies in our understanding of icy moons. The carbonaceous lag layer speculated to protect the surface of Rhea from sputtering, for instance, would be practically undetectable by remote spectroscopy.[16] In addition, some postulated moon surface components (e.g., many salts, some organics, Europa's abundant non-ice surface material) do not have spectroscopic features that are detectable by existing and currently planned spectrometers. Negative PUIs thus carry surface-selective compositional information that cannot be resolved by existing remote sensing techniques. A key thrust for future work should be the maturation of astrophysical LEIS and RIS as a remote probe of surface composition for icy bodies. It has been a secondary objective of this thesis to provide some preliminary development toward this end, but many more laboratory experiments are needed to clarify how the surface composition is modified and translated into the gas phase by relevant impactors.

There is lately a push to understand how radiolysis of ice is influenced by the presence of impurities — no doubt a critical question. An equally important, although perhaps underappreciated question, is how to translate laboratory measurements with monoenergetic beams to a physical system where impact energies are spread over many orders of magnitude. We have tried to draw attention to this problem at several points in this dissertation. How does co-exposure at disparate energies alter yields relative to superposition? Do abundant hyperthermal ions, for instance, interfere with or reinforce the oxygenated near-surface layer that facilitates radiolytic O_2 formation?

Multi-component ices provide a rich and highly relevant vein of unexplored chemistry. With the habitability of Ocean Worlds presently under scrutiny, abiotic mechanisms for synthesis of organics, especially amino acids, are of particular importance. In the absence of abiotic formation pathways, the presence of these species at the ice surface may indicate their availability in the subsurface ocean. The simulations of §8.3.1 provide a glimpse of unknown prebiotic chemistry and caution against some potential habitability false positives. Many questions still remain unanswered: what does the ice surface look like at steady state? How do other basic ice chemistries (e.g. NH_3+CO+H_2O) evolve under hyperthermal bombardment?

8.5 References

1. Rothard, H. *et al.* Modification of ices by cosmic rays and solar wind. *J. Phys. B At. Mol. Opt. Phys.* **50**, 062001 (2017).
2. Gerakines, P. A. & Hudson, R. L. Glycine's Radiolytic Destruction in Ices: First *in situ* Laboratory Measurements for Mars. *Astrobiology* **13**, 647–655 (2013).
3. Gerakines, P. A., Hudson, R. L., Moore, M. H. & Bell, J.-L. *In situ* measurements of the radiation stability of amino acids at 15–140 K. *Icarus* **220**, 647–659 (2012).
4. Evans, N. L., Bennett, C. J., Ullrich, S. & Kaiser, R. I. ON THE INTERACTION OF ADENINE WITH IONIZING RADIATION: MECHANISTICAL STUDIES AND ASTROBIOLOGICAL IMPLICATIONS. *Astrophys. J.* **730**, 69 (2011).
5. Kminek, G. & Bada, J. L. The effect of ionizing radiation on the preservation of amino acids on Mars. *Earth Planet. Sci. Lett.* **245**, 1–5 (2006).
6. Bockelee-Morvan, D., Crovisier, J., Weaver, H. A. & Mumma, M. J. The Composition of Cometary Volatiles. in *Comets II* (eds. Festou, M., Keller, H. U. & Weaver, H. A.) 391–424 (University of Arizona press, Tucson, 2004).
7. Peter, J. S., Nordheim, T. A. & Hand, K. P. Detection of HCN and diverse redox chemistry in the plume of Enceladus. *Nat. Astron.* **8**, 164–173 (2024).
8. van Duin, A. C. T., Zou, C., Joshi, K., Bryantsev, V. & Goddard, W. A. CHAPTER 6. A Reaxff Reactive Force-field for Proton Transfer Reactions in Bulk Water and its Applications to Heterogeneous Catalysis. in *Catalysis Series* (eds. Asthagiri, A. & Janik, M. J.) 223–243 (Royal Society of Chemistry, Cambridge, 2013). doi:10.1039/9781849734905-00223.
9. Rahaman, O., van Duin, A. C. T., Goddard, W. A. & Doren, D. J. Development of a ReaxFF Reactive Force Field for Glycine and Application to Solvent Effect and Tautomerization. *J. Phys. Chem. B* **115**, 249–261 (2011).
10. Aponte, J. C. *et al.* Pathways to Meteoritic Glycine and Methylamine. *ACS Earth Space Chem.* **1**, 3–13 (2017).
11. Joshi, P. R. & Lee, Y.-P. A chemical link between methylamine and methylene imine and implications for interstellar glycine formation. *Commun. Chem.* **5**, 1–7 (2022).
12. Krasnokutski, S. A., Chuang, K.-J., Jäger, C., Ueberschaar, N. & Henning, T. A pathway to peptides in space through the condensation of atomic carbon. *Nat. Astron.* **6**, 381–386 (2022).

13. Martins, Z. *et al. Report of the Expert Committee for the Large-Class Mission in ESA's Voyage 2050 Plan Covering the Science Theme "Moons of the Giant Planets"*. https://cosmos.esa.int/documents/1866264/1866292/ESA_L4_Expert_Committee_report_Voyage_2050_Moons_of_the_Giant_Planets.pdf (2024).
14. Committee on the Planetary Science and Astrobiology Decadal Survey, Space Studies Board, Division on Engineering and Physical Sciences, & National Academies of Sciences, Engineering, and Medicine. *Origins, Worlds, and Life: A Decadal Strategy for Planetary Science and Astrobiology 2023-2032*. 26522 (National Academies Press, Washington, D.C., 2022). doi:10.17226/26522.
15. Saito, Y. *et al.* Solar wind proton reflection at the lunar surface: Low energy ion measurement by MAP-PACE onboard SELENE (KAGUYA). *Geophys. Res. Lett.* **35**, (2008).
16. Teolis, B. D. & Waite, J. H. Dione and Rhea seasonal exospheres revealed by Cassini CAPS and INMS. *Icarus* **272**, 277–289 (2016).

Appendix A

A.1 Chapter 4 Supplementary Information

A.1.1 Figures

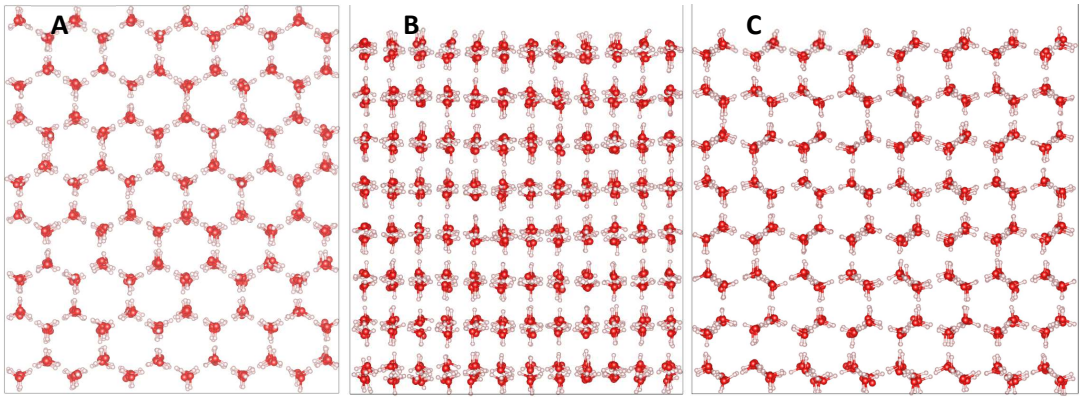

Figure A-1: Visualization of the thick basal-plane ice 1h slab used in simulations with $|\mathbf{V}_{in}| \geq 25$ kms^{-1}. Each image (A,B,C) of the slab is shown as viewed perpindicular to the corresponing face in the schematic in Fig. 4-1 of the main text. The headspace is excluded. The slab is 27 Å x 31 Å in width and 29 Å thick, containing 768 molecules.

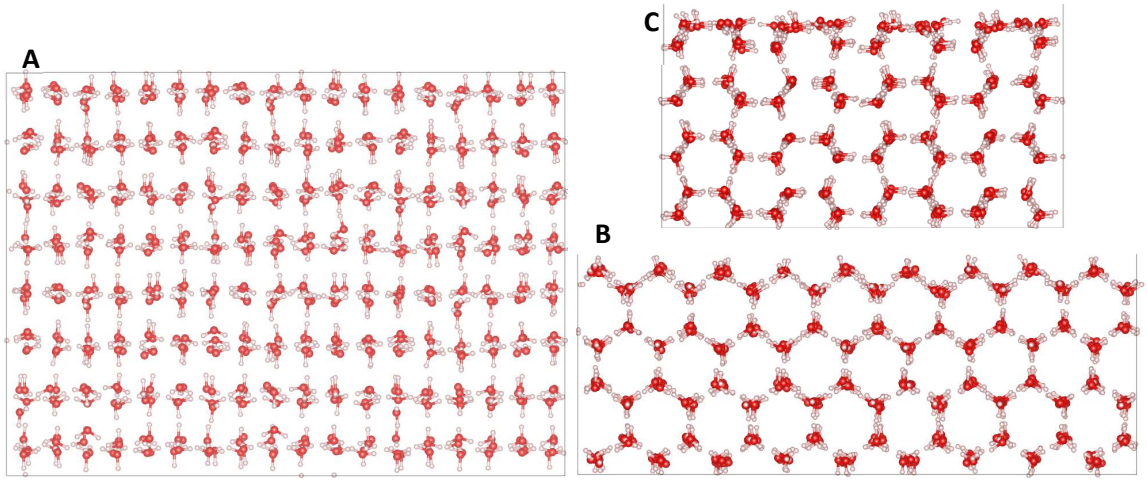

Figure A-2: Visualization of the prism-plane ice 1h slab used in some simulations. Each image (A,B,C) of the slab is shown as viewed perpindicular to the corresponing face in the schematic in Fig. 4-1 of the main text. The headspace is excluded. The slab is 40 Å x 29 Å in width and 16 Å thick, containing 576 molecules.

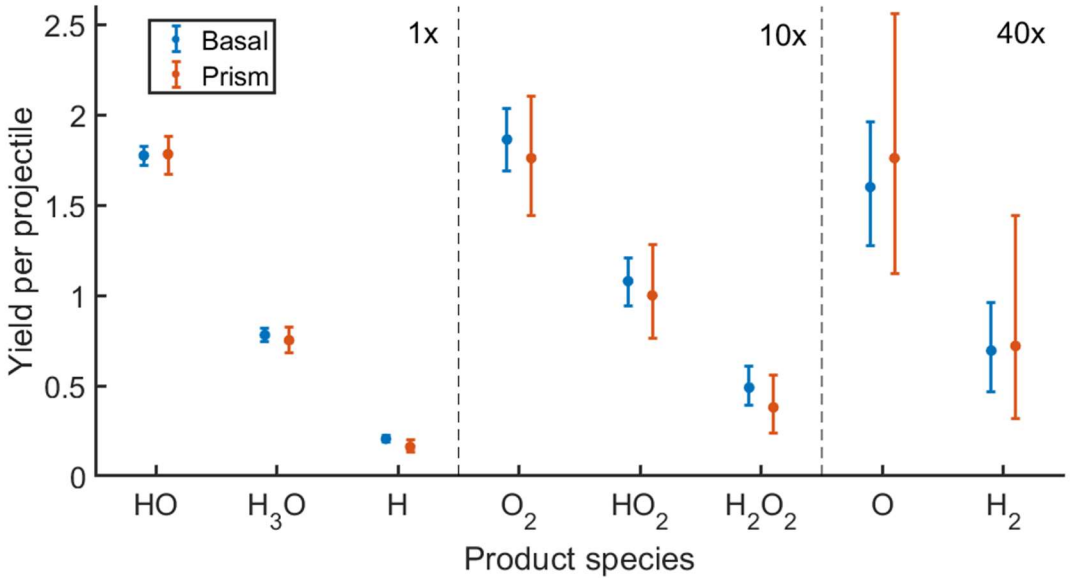

Figure A-3. Yield for various species vs surface structure of the ice slab. Yields are averaged across 1900 simualtions for the basal-plane target and 500 for the prism-plane target. Here and in further figures, the error bars are the wider limits of bootstrapped 95% CI or ±1/(number of simulations).

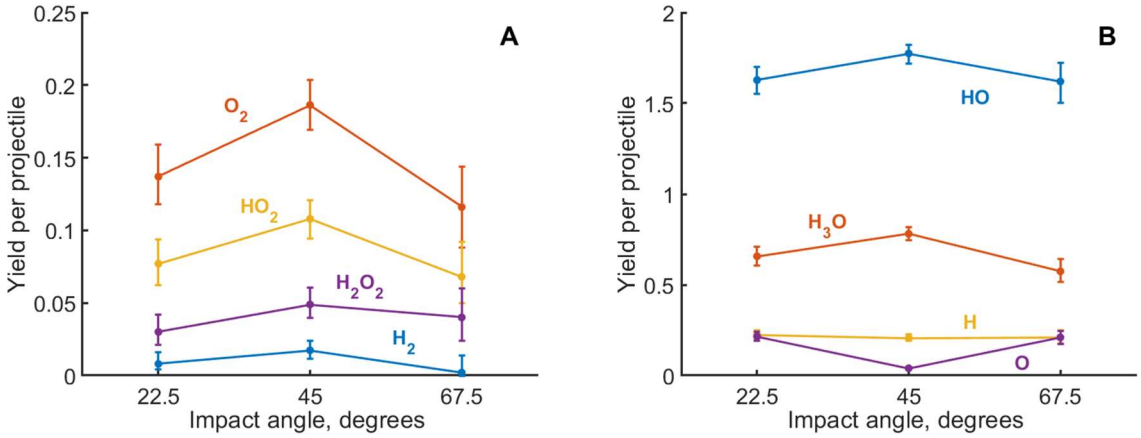

Figure A-4: Yield per projectile vs impact angle (measured from the surface plane) for 1000, 1900, and 500 simulations of O impacts at 20 kms^{-1} at 22.5, 45, and 67.5 degrees, respectively. Species are separated into **A** and **B** subplots for readability.

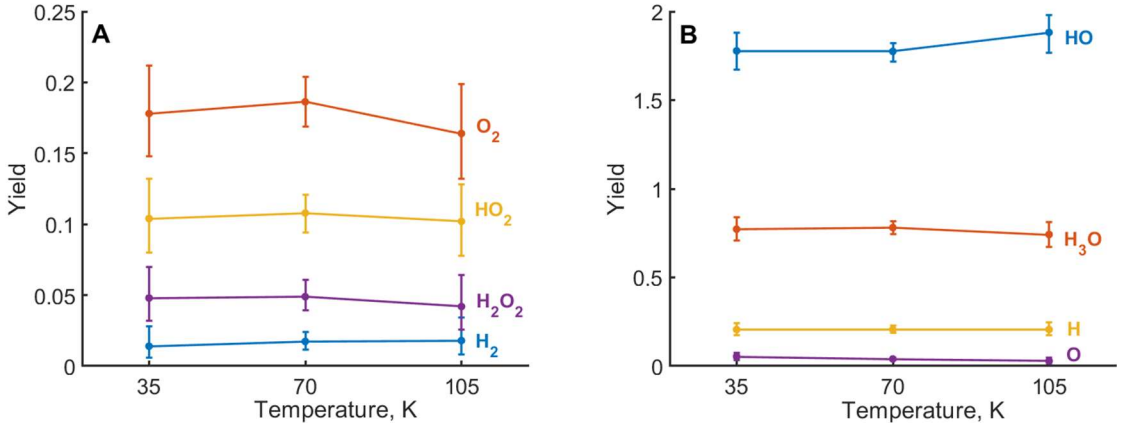

Figure A-5. Yield for various species vs initial temperature of the ice slab. Yields are averaged across 500, 1900, and 500 for simulations at 35, 70, and 105 K, respectively. Species are separated into **A** and **B** subplots for readability.

A.1.2 Tables

Table A-1. Comparison of equilibrium bond distances for the ReaxFF forcefield used in the MD simulations[2] vs CCCBDB (NISTs Computational Chemistry Comparison and Benchmark DataBase)

	ReaxFF, Å			CCCBDB[1], Å			Error, %		
Species	rOH	rOO	rHH	rOH	rOO	rHH	rOH	rOO	rHH
H_2O_2	1.00	1.41		0.95	1.48		-5.11	4.18	
O_2		1.20			1.21			0.66	
OH	0.92			0.97			5.27		
H_2O	0.95			0.96			0.89		
H_2			0.76			0.74			-2.66
HO_2	1.03	1.32		0.97	1.33		-5.79	0.59	
H_3O	1.03			0.98			-5.42		

Table A-2. Comparison of atomization energies for CCCBDB vs this forcefield[2]

	Atomization energy (0 K), eV		
Species	ReaxFF	CCCBDB[1]	Error, %
H_2O_2	12.86	10.94	-17.56
O_2	5.38	5.12	-5.17
OH	5.52	4.41	-25.0
H_2O	10.69	9.51	-12.3
H_2	4.71	4.48	-5.27
HO_2	8.19	7.20	-13.8

A.1.3 Forcefield Parameters

Reactive MD-force field
39 ! Number of general parameters
50.0000 !Comment here
9.5469 !Comment here
26.5405 !Comment here
1.7224 !Comment here
6.8702 !Comment here
60.4850 !Comment here
1.0588 !Comment here
4.6000 !Comment here
12.1176 !Comment here
13.3056 !Comment here
-51.3259 !Comment here
0.0000 !Comment here
10.0000 !Comment here
2.8793 !Comment here
33.8667 !Comment here
6.0891 !Comment here
1.0563 !Comment here
2.0384 !Comment here
6.1431 !Comment here
6.9290 !Comment here
0.3989 !Comment here
3.9954 !Comment here
-2.4837 !Comment here
5.7796 !Comment here

```
 10.0000 !Comment here
  1.9487 !Comment here
 -1.2327 !Comment here
  2.1645 !Comment here
  1.5591 !Comment here
  0.1000 !Comment here
  2.1365 !Comment here
  0.6991 !Comment here
 50.0000 !Comment here
  1.8512 !Comment here
  0.5000 !Comment here
 20.0000 !Comment here
  5.0000 !Comment here
  0.0000 !Comment here
  2.6962 !Comment here
 2    !Nr of atoms; cov.r; valency;a.m;Rvdw;Evdw;gammaEEM;cov.r2;
         alfa;gammavdW;valency;Eunder;Eover;chiEEM;etaEEM;n.u.
         cov r3;Elp;Heat inc.;n.u.;n.u.;n.u.;n.u.
         ov/un;val1;n.u.;val3,vval4
H    0.8930   1.0000   1.0080   1.3550   0.0930   0.8203  -0.1000   1.0000
     8.2230  33.2894   1.0000   0.0000 121.1250   3.7248   9.6093   1.0000
    -0.1000   0.0000  61.6606   3.0408   2.4197   0.0003   1.0698   0.0000
   -19.4571   4.2733   1.0338   1.0000   2.8793   0.0000   0.0000   0.0000
O    1.2450   2.0000  15.9990   2.3890   0.1000   1.0898   1.0548   6.0000
     9.7300  13.8449   4.0000  37.5000 116.0768   8.5000   8.3122   2.0000
     0.9049   0.4056  59.0626   3.5027   0.7640   0.0021   0.9745   0.0000
    -3.5500   2.9000   1.0493   4.0000   2.9225   0.0000   0.0000   0.0000
 3     ! Nr of bonds; Edis1;LPpen;n.u.;pbe1;pbo5;13corr;pbo6
                 pbe2;pbo3;pbo4;n.u.;pbo1;pbo2;ovcorr
 1  1 153.3934   0.0000   0.0000  -0.4600   0.0000   1.0000   6.0000   0.7300
       6.2500   1.0000   0.0000   1.0000  -0.0790   6.0552   0.0000   0.0000
 1  2 160.0000   0.0000   0.0000  -0.5725   0.0000   1.0000   6.0000   0.5626
       1.1150   1.0000   0.0000   0.0000  -0.0920   4.2790   0.0000   0.0000
 2  2 142.2858 145.0000  50.8293   0.2506  -0.1000   1.0000  29.7503   0.6051
       0.3451  -0.1055   9.0000   1.0000  -0.1225   5.5000   1.0000   0.0000
 1    ! Nr of off-diagonal terms; Ediss;Ro;gamma;rsigma;rpi;rpi2
 1  2   0.0283   1.2885  10.9190   0.9215  -1.0000  -1.0000
 6    ! Nr of angles;at1;at2;at3;Thetao,o;ka;kb;pv1;pv2
 1  1  1   0.0000  27.9213   5.8635   0.0000   0.0000   0.0000   1.0400
 1  1  2   0.0000   8.5744   3.0000   0.0000   0.0000   0.0000   1.0421
 1  2  1  85.8000   9.8453   2.2720   0.0000   2.8635   0.0000   1.5800
 1  2  2  75.6935  50.0000   2.0000   0.0000   1.0000   0.0000   1.1680
```

```
2  1  2   0.0000  15.0000   2.8900   0.0000   0.0000   0.0000   2.8774
2  2  2  80.7324  30.4554   0.9953   0.0000   1.6310  50.0000   1.0783
6    ! Nr of torsions;at1;at2;at3;at4;;V1;V2;V3;V2(BO);vconj;n.u;n
0  1  1  0  62.2304  12.4120   3.4647   0.5000   1.4224   0.0000   1.8517
0  1  2  0   0.0000   0.2044   1.7494   0.0000   1.2268   0.0000   3.1652
0  2  2  0  70.0000  25.0000   1.0000   0.0000   1.0000   0.0000   1.2500
1  2  2  1   0.0000   0.1000   0.0200  -2.5415   0.0000   0.0000   0.0000
1  2  2  2   0.0000  50.0000   0.3000  -4.0000  -2.0000   0.0000   0.0000
2  2  2  2  -0.0555  -5.0000   0.1515  -2.2056   0.0000   0.0000   0.0000
1    ! Nr of hydrogen bonds;at1;at2;at3;Rhb;Dehb;vhb1
2  1  2   2.1200  -3.5800   1.4500  19.5000
```

A.1.4 References

1) NIST Computational Chemistry Comparison and Benchmark Database, NIST Standard Reference Database Number 101. Release 21, August 2020, Editor: Russell D. Johnson III. http://cccbdb.nist.gov/
2) van Duin, A. C. T., Zou, C., Joshi, K., Bryantsev, V. & Goddard, W. A. CHAPTER 6. A Reaxff Reactive Force-field for Proton Transfer Reactions in Bulk Water and its Applications to Heterogeneous Catalysis. in *Catalysis Series* (eds. Asthagiri, A. & Janik, M. J.) 223–243 (Royal Society of Chemistry, 2013). doi:10.1039/9781849734905-00223.

A.2 Chapter 5 Supplementary Information

A.2.1 Figures

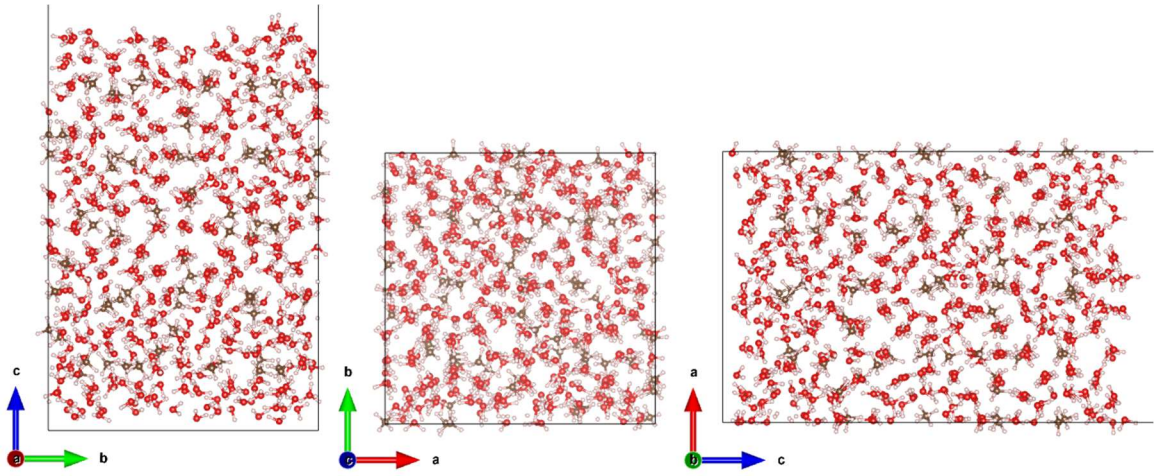

Figure A-6: Orthogonal views of the mixed CH_4 clathrate slab used in simulations. Visualized with VESTA software.

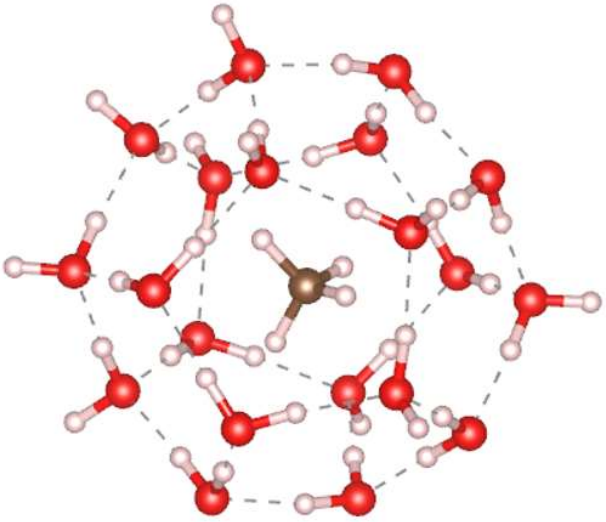

Figure A-7: Isolated 20-member cage structure of the CH_4 clathrate. Trapping of the CH_4 is favorable by 0.3 eV. Visualized with VESTA software.

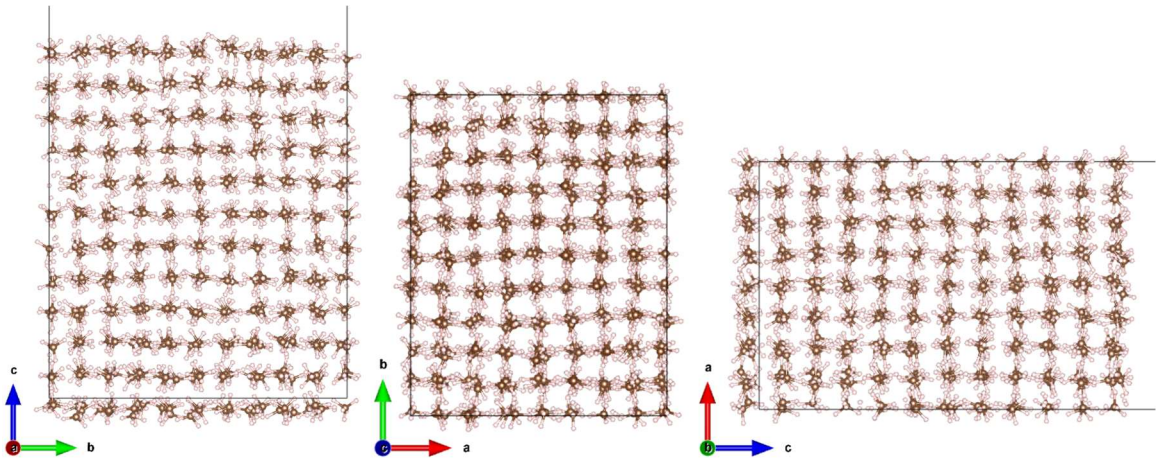

Figure A-8: Orthogonal views of the CH_4 ice slab used in simulations. Visualized with VESTA software.

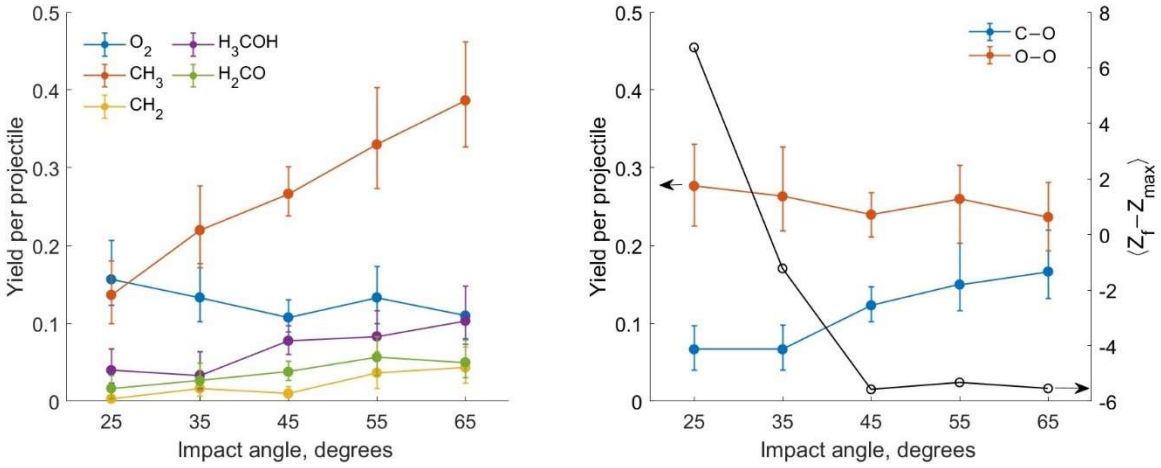

Figure A-9: Angular dependence for reactive scattering O on CH_4 clathrate. Left) Yield vs impact angle (relative to the surface plane) for several species. Right) Total yield to C−O and O−O bond formation (left axis) and, on the right axis, average final projectile z-position (Z_f) relative to the top of the slab (Z_{max}).

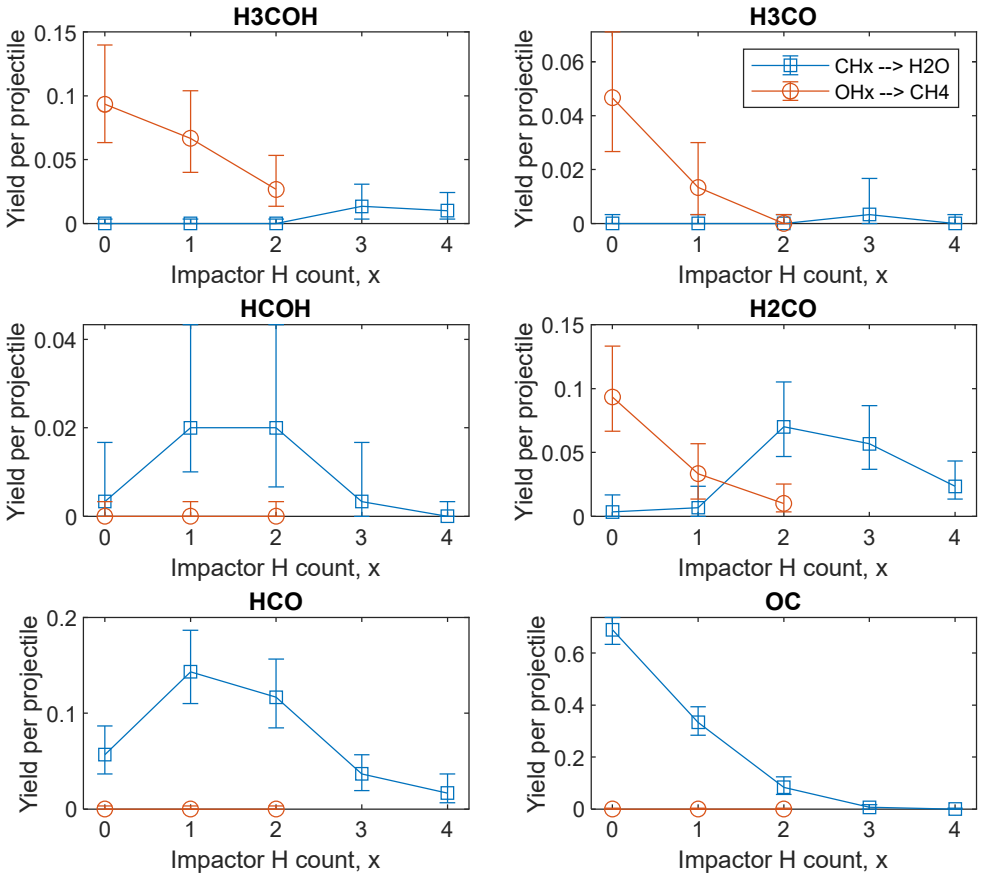

Figure A-10: Yield of various product species for symmetric projectile-surface systems (20 km s^{-1}, n=300). The abscissa is the number of hydrogen atoms in the projectile molecules. Each subplot gives yields for a single species, indicated by the title. The blue traces are for simulations of CH_x impacting hexagonal water ice. The orange traces are for OH_x impacting methane ice.

The total probability of forming a C-O bond (PC-O) is much higher for the CH_x impactors than for the OH_x impactors for equal x (220% increase for C vs O). This is because access to the carbon is more hindered by sterics in the methane ice. At the same degree of undersaturation, where the steric hindrance to C−O bond formation is similar, P_{C-O} is still larger for the CH_x projectile, although the difference is more moderate (37% increase for CH_2 vs O, 19% increase for CH_3 vs OH). The increased probability is due to facilitation of H_2O dissociation by the hydrogen bond network. P_{C-O} increases with the degree of undersaturation. Projectiles with more bonds are able to accommodate more of the impact energy in vibrational degrees of freedom without bond dissociation, especially at these energies where the impact timescale is comparable to the timescale for bond vibrations. Steric hinderance for the bulkier projectiles also contributes to this trend. Because the projectile kinetic energy is well above the BDE for all the projectile molecules, saturation does not preclude C−O bond formation.

A.2.2 Forcefield parameters

Reactive MD-force field: Glycine November 21 Rahaman 2011 Glycine Tautomerization, RG decrease N-O rsigma
```
 39       ! Number of general parameters
  50.0000 !Overcoordination parameter
   9.5469 !Overcoordination parameter
   1.6725 !Valency angle conjugation parameter
   1.7224 !Triple bond stabilisation parameter
   6.8702 !Triple bond stabilisation parameter
  60.4850 !C2-correction
   1.0588 !Undercoordination parameter
   4.6000 !Triple bond stabilisation parameter
  12.1176 !Undercoordination parameter
  13.3056 !Undercoordination parameter
 -40.0000 !Triple bond stabilization energy
   0.0000 !Lower Taper-radius
  10.0000 !Upper Taper-radius
   2.8793 !Not used
  33.8667 !Valency undercoordination
   6.0891 !Valency angle/lone pair parameter
   1.0563 !Valency angle
```

```
  2.0384 !Valency angle parameter
  6.1431 !Not used
  6.9290 !Double bond/angle parameter
  0.3989 !Double bond/angle parameter: overcoord
  3.9954 !Double bond/angle parameter: overcoord
 -2.4837 !Not used
  5.7796 !Torsion/BO parameter
 10.0000 !Torsion overcoordination
  1.9487 !Torsion overcoordination
 -1.2327 !Conjugation 0 (not used)
  2.1645 !Conjugation
  1.5591 !vdWaals shielding
  0.1000 !Cutoff for bond order (*100)
  1.7602 !Valency angle conjugation parameter
  0.6991 !Overcoordination parameter
 50.0000 !Overcoordination parameter
  1.8512 !Valency/lone pair parameter
  0.5000 !Not used
 20.0000 !Not used
  5.0000 !Molecular energy (not used)
  0.0000 !Molecular energy (not used)
  0.7903 !Valency angle conjugation parameter
 4    ! Nr of atoms; cov.r; valency;a.m;Rvdw;Evdw;gammaEEM;cov.r2;#
        alfa;gammavdW;valency;Eunder;Eover;chiEEM;etaEEM;n.u.
        cov r3;Elp;Heat inc.;n.u.;n.u.;n.u.;n.u.
        ov/un;val1;n.u.;val3,vval4
C    1.3817   4.0000  12.0000   1.8903   0.1838   0.6544   1.1341   4.0000
     9.7559   2.1346   4.0000  34.9350  79.5548   5.4088   6.0000   0.0000
     1.2114   0.0000 202.2908   8.9539  34.9289  13.5366   0.8563   0.0000
    -2.8983   2.5000   1.0564   4.0000   2.9663   0.0000   0.0000   0.0000
H    0.8930   1.0000   1.0080   1.3550   0.0930   0.8203  -0.1000   1.0000
     8.2230  33.2894   1.0000   0.0000 121.1250   3.7248   9.6093   1.0000
    -0.1000   0.0000  55.1878   3.0408   2.4197   0.0003   1.0698   0.0000
   -19.4571   4.2733   1.0338   1.0000   2.8793   0.0000   0.0000   0.0000
O    1.2450   2.0000  15.9990   2.3890   0.1000   1.0898   1.0548   6.0000
     9.7300  13.8449   4.0000  37.5000 116.0768   8.5000   8.3122   2.0000
     0.9049   0.4056  68.0152   3.5027   0.7640   0.0021   0.9745   0.0000
    -3.5500   2.9000   1.0493   4.0000   2.9225   0.0000   0.0000   0.0000
N    1.2333   3.0000  14.0000   2.2403   0.1102   0.9928   1.1748   5.0000
     9.8276  12.0698   4.0000  30.2790 100.0000   6.1112   6.6645   2.0000
     1.0433   0.1000 119.9837   0.7382   6.7108   2.7268   0.9745   0.0000
    -2.0000   4.0000   1.0183   4.0000   2.8793   0.0000   0.0000   0.0000
```

```
10      ! Nr of bonds; Edis1;LPpen;n.u.;pbe1;pbo5;13corr;pbo6
                  pbe2;pbo3;pbo4;Etrip;pbo1;pbo2;ovcorr
 1  1 158.2004  99.1897  78.0000  -0.7738  -0.4550   1.0000  37.6117   0.4147
      0.4590  -0.1000   9.1628   1.0000  -0.0777   6.7268   1.0000   0.0000
 1  2 169.4760   0.0000   0.0000  -0.6083   0.0000   1.0000   6.0000   0.7652
      5.2290   1.0000   0.0000   1.0000  -0.0553   6.9316   0.0000   0.0000
 2  2 153.3934   0.0000   0.0000  -0.4600   0.0000   1.0000   6.0000   0.7300
      6.2500   1.0000   0.0000   1.0000  -0.0790   6.0552   0.0000   0.0000
 1  3 100.9167 136.3836  65.3877   0.3895  -0.3906   1.0000  18.8159   0.6674
      1.1202  -0.3411   9.1099   1.0000  -0.1966   5.6975   0.0000   0.0000
 3  3 142.2858 145.0000  50.8293   0.2506  -0.1000   1.0000  29.7503   0.6051
      0.3451  -0.1055   9.0000   1.0000  -0.1225   5.5000   1.0000   0.0000
 1  4 165.1874 148.6965  87.7249  -1.3237  -0.3504   1.0000  27.5446   0.1473
      0.1449  -0.2871   7.2074   1.0000  -0.2565   4.4890   1.0000   0.0000
 3  4 130.8596 169.4551  40.0000   0.3837  -0.1639   1.0000  35.0000   0.2000
      1.0000  -0.3579   7.0004   1.0000  -0.1193   6.8773   1.0000   0.0000
 4  4 157.9384  82.5526 152.5336   0.4010  -0.1034   1.0000  12.4261   0.5828
      0.1578  -0.1509  11.9186   1.0000  -0.0861   5.4271   1.0000   0.0000
 2  3 160.0000   0.0000   0.0000  -0.5725   0.0000   1.0000   6.0000   0.5626
      1.1150   1.0000   0.0000   0.0000  -0.0920   4.2790   0.0000   0.0000
 2  4 208.1369   0.0000   0.0000  -0.3949   0.0000   1.0000   6.0000   0.3340
      6.0174   1.0000   0.0000   1.0000  -0.1026   5.5235   0.0000   0.0000
 6    ! Nr of off-diagonal terms; Ediss;Ro;gamma;rsigma;rpi;rpi2
 1  2   0.1239   1.4004   9.8467   1.1210  -1.0000  -1.0000
 2  3   0.0283   1.2885  10.9190   0.9215  -1.0000  -1.0000
 2  4   0.1275   1.3000   9.8924   1.0418  -1.0000  -1.0000
 1  3   0.0647   2.0109  10.0105   1.3177   1.2052   1.0682
 1  4   0.1952   1.8813   9.7734   1.3434   1.2545   1.1533
 3  4   0.1201   2.4775   9.0171   1.3285   1.0682   1.2716
42    ! Nr of angles;at1;at2;at3;Thetao,o;ka;kb;pv1;pv2
 1  1  1  59.0573  30.7029   0.7606   0.0000   0.7180   6.2933   1.1244
 1  1  2  65.7758  14.5234   6.2481   0.0000   0.5665   0.0000   1.6255
 2  1  2  70.2607  25.2202   3.7312   0.0000   0.0050   0.0000   2.7500
 1  2  2   0.0000   0.0000   6.0000   0.0000   0.0000   0.0000   1.0400
 1  2  1   0.0000   3.4110   7.7350   0.0000   0.0000   0.0000   1.0400
 2  2  2   0.0000  27.9213   5.8635   0.0000   0.0000   0.0000   1.0400
 1  1  3  66.0686  28.5756   1.4793   0.0000   2.9950  58.6562   1.0000
 3  1  3  84.3310  21.5172   5.4724  -1.0000   1.5183   0.0000   2.9776
 1  1  4  66.8437  45.0000   1.2491   0.0000   1.1834   0.0000   3.0000
 3  1  4  82.7022  45.0000   0.5769   0.0000   1.1019   0.0000   1.0000
 4  1  4  90.0000  43.1792   0.5055   0.0000   1.1155   0.0000   1.0204
 2  1  3  64.3088  32.5434   2.1997   0.0000   0.1000   0.0000   1.2995
```

```
 2  1  4  63.9629  41.6246   1.4921   0.0000   0.2000   0.0000   2.8070
 1  2  4   0.0000   0.0019   6.3000   0.0000   0.0000   0.0000   1.0400
 1  3  1  68.4903  45.0000   1.3617   0.0000   2.8294   0.0000   1.0000
 1  3  3  80.6161  45.0000   1.4073   0.0000   1.0572  68.1072   1.4451
 1  3  4  69.5983  45.0000   1.4248   0.0000   2.9000   0.0000   2.3286
 3  3  3  89.9934  17.9465   1.7798   0.0000   2.9881   0.0000   1.0538
 3  3  4  83.5202  33.7933   1.0337   0.0000   2.9000   0.0000   1.3398
 4  3  4  67.1317  42.3748   1.7873   0.0000   3.0072   0.0000   1.5832
 1  3  2  90.0000   7.1513   7.5000   0.0000   1.3111   0.0000   3.0000
 2  3  3  75.6935  50.0000   2.0000   0.0000   1.0000   0.0000   1.1680
 2  3  4  72.7348  20.1071   7.5000   0.0000   0.1000   0.0000   1.0746
 2  3  2  85.8000   9.8453   2.2720   0.0000   2.8635   0.0000   1.5800
 1  4  1  70.6778  12.3495   3.0486   0.0000   2.8702   0.0000   1.0000
 1  4  3  73.9745  21.1329   2.3337   0.0000   2.8701   0.0000   1.7170
 1  4  4  71.4579  14.0942   2.8540   0.0000   2.8701   0.0000   1.0631
 3  4  3  74.2613  20.9008   2.8607 -18.0069   3.0701   0.0000   1.3874
 3  4  4  74.2615  27.8669   1.6736  -0.9193   3.0117   0.0000   1.4381
 4  4  4  73.3189  24.9685   2.2561   0.0000   2.9983   0.0000   2.1573
 1  4  2  70.2498  13.6111   2.6311   0.0000   0.2025   0.0000   1.0000
 2  4  3  74.5739  45.0000   1.4078   0.0000   0.3956   0.0000   3.0000
 2  4  4  79.7136  45.0000   0.5316   0.0000   0.5437   0.0000   1.0000
 2  4  2  80.2201   6.8385   7.5000   0.0000   0.1000   0.0000   1.0000
 1  2  3   0.0000   8.9481   0.5983   0.0000   0.0000   0.0000   1.0000
 1  2  4   0.0000   0.2694   2.1363   0.0000   0.0000   0.0000   1.8036
 1  2  5   0.0000  15.0000   3.0000   0.0000   0.0000   0.0000   1.0400
 3  2  3   0.0000  15.0000   2.8900   0.0000   0.0000   0.0000   2.8774
 3  2  4   0.0000   1.0574   0.1000   0.0000   0.0000   0.0000   2.7676
 4  2  4   0.0000   0.0100   1.0929   0.0000   0.0000   0.0000   2.1728
 2  2  3   0.0000   8.5744   3.0000   0.0000   0.0000   0.0000   1.0421
 2  2  4   0.0000   0.0019   6.0000   0.0000   0.0000   0.0000   1.0400
41    ! Nr of torsions;at1;at2;at3;at4;;V1;V2;V3;V2(BO);vconj;n.u;n
 1  1  1  1  -0.2500  34.7453   0.0288  -6.3507  -1.6000   0.0000   0.0000
 1  1  1  2  -0.2500  29.2131   0.2945  -4.9581  -2.1802   0.0000   0.0000
 2  1  1  2  -0.2500  31.2081   0.4539  -4.8923  -2.2677   0.0000   0.0000
 1  1  1  3  -0.5740  22.4215   0.8787  -2.7603  -1.1000   0.0000   0.0000
 2  1  1  3   1.8164  18.8479   0.5134  -7.0513  -1.0978   0.0000   0.0000
 3  1  1  3  -2.5000  56.1599  -1.0000  -4.3607  -0.8614   0.0000   0.0000
 1  1  3  1   2.5000  14.6490   1.0000  -2.5209  -0.9000   0.0000   0.0000
 1  1  3  2  -2.2946  11.6826  -1.0000  -2.5000  -0.9000   0.0000   0.0000
 2  1  3  1  -1.0402  26.8401   0.6384  -2.5000  -0.9000   0.0000   0.0000
 2  1  3  2  -1.0000  66.0304   0.7580  -5.4593  -1.1000   0.0000   0.0000
 1  1  3  3   1.0182   5.3409   0.1292  -4.3356  -2.0544   0.0000   0.0000
```

```
 2  1  3  3   2.1531  45.9655   1.0000  -2.5000  -2.8274   0.0000   0.0000
 3  1  3  1   0.6706  80.0000  -0.2443  -4.7181  -3.0437   0.0000   0.0000
 3  1  3  2  -1.0000  91.6742  -0.5000  -3.9849  -3.0476   0.0000   0.0000
 3  1  3  3  -1.9346   5.0000   0.6401  -3.3416  -2.7174   0.0000   0.0000
 1  3  3  1   1.0469   4.3827   0.8149  -3.4434  -2.7536   0.0000   0.0000
 1  3  3  2  -2.5000  -0.5181   0.0268  -5.4085  -2.9498   0.0000   0.0000
 2  3  3  2  -2.1995 -25.0000  -1.0000  -2.6000  -0.9921   0.0000   0.0000
 1  3  3  3   2.4118 -24.8219   0.9706  -2.5004  -0.9972   0.0000   0.0000
 2  3  3  3  -2.5000  43.1840  -0.6826  -6.6539  -1.2407   0.0000   0.0000
 3  3  3  3  -2.5000 -25.0000   1.0000  -2.5000  -0.9000   0.0000   0.0000
 1  1  4  2  -1.0000  71.4280  -0.5000  -8.0000  -1.9825   0.0000   0.0000
 2  1  4  2  -1.0000  63.9914   0.7449  -8.0000  -2.1051   0.0000   0.0000
 3  1  4  2  -1.0000  24.9527   1.0000  -4.6063  -2.5261   0.0000   0.0000
 3  1  1  4   1.0000  25.3373   1.0000  -4.1453  -0.9511   0.0000   0.0000
 4  1  1  4  -1.0000  21.8427   1.0000  -4.0686  -1.7241   0.0000   0.0000
 1  1  4  1   1.0000  83.8750   1.0000  -6.5279  -1.6589   0.0000   0.0000
 3  1  4  1  -1.0000  48.6477   1.0000  -8.0000  -1.8038   0.0000   0.0000
 2  1  1  4   1.0000  98.8297  -0.2745  -4.9954  -1.9000   0.0000   0.0000
 4  1  4  2   0.5000   2.8273  -0.1650  -7.9605  -2.0202   0.0000   0.0000
 2  1  4  1  -1.0000  92.9120  -0.4541  -7.7688  -1.5996   0.0000   0.0000
 0  1  2  0   0.0000   0.0000   0.0000   0.0000   0.0000   0.0000   0.0000
 0  2  2  0   0.0000   0.0000   0.0000   0.0000   0.0000   0.0000   0.0000
 0  2  3  0   0.0000   0.1000   0.0200  -2.5415   0.0000   0.0000   0.0000
 0  1  1  0   0.0000  50.0000   0.3000  -4.0000  -2.0000   0.0000   0.0000
 0  3  3  0   0.5511  25.4150   1.1330  -5.1903  -1.0000   0.0000   0.0000
 0  1  4  0   0.2176  40.4126   0.3535  -3.9875  -2.0051   0.0000   0.0000
 0  2  4  0   0.0000   0.1032   0.3000  -5.0965   0.0000   0.0000   0.0000
 0  3  4  0   1.1397  61.3225   0.5139  -3.8507  -2.7831   0.0000   0.0000
 0  4  4  0   0.7265  44.3155   1.0000  -4.4046  -2.0000   0.0000   0.0000
 4  1  4  4  -0.0949   8.7582   0.3310  -7.9430  -2.0000   0.0000   0.0000
 4    ! Nr of hydrogen bonds;at1;at2;at3;Rhb;Dehb;vhb1
 3  2  3   2.1200  -3.5800   1.4500  19.5000
 3  2  4   2.1215  -7.5000   1.4500  19.5000
 4  2  3   1.7500  -4.3286   1.4500  19.5000
 4  2  4   2.4000  -2.3575   1.4500  19.5000
```

A.3 Chapter 6 Supplementary Information

A.3.1 Figures

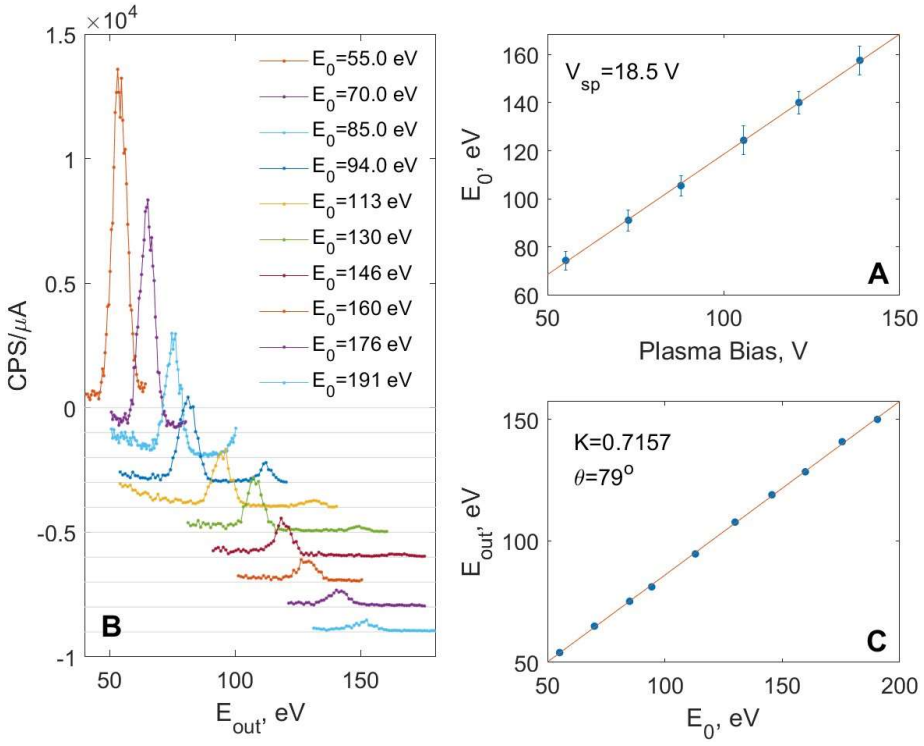

Figure A-11: Determination of scattering geometry. A) Regression of primary ion energy vs plasma bias to obtain the plasma self-bias. B) Energy distribution for scattered Ar^+ on staggered baselines. C) Regression of peak exit energies vs incident energy, yielding slope K, which corresponds to a scattering angle of 79°.

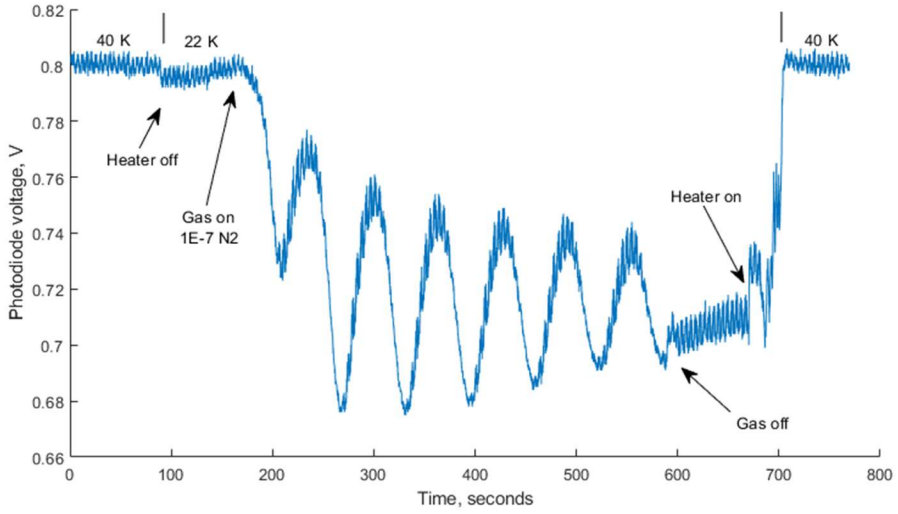

Figure A-12: Illustrative interferometry fringes for N_2 deposition, obtained prior to integration with the MIBSA. See §6.2.1 for context.

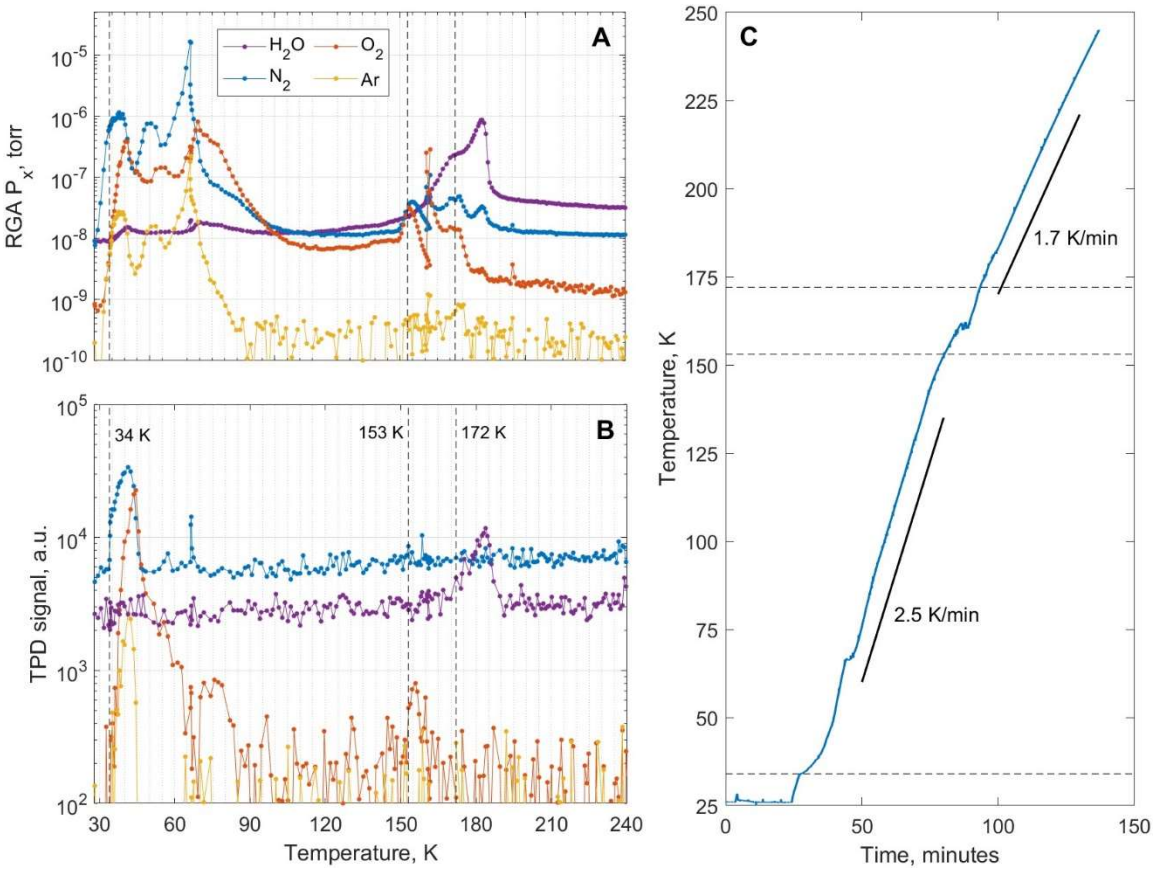

Figure A-13: Temperature ramp and background gas rejection for TPD. A) RGA partial pressures in the scattering chamber for several masses as a function of temperature. B) Simultaneous TPD signal acquired by our SNMS detector as in Fig. 6-13. A and B subplots share a common legend and x-axis. C) The manually executed temperature ramp for this experiment (blue), with two slopes depicted for comparison (solid black trace). Three temperatures of interest (34, 153, 172 K) are marked across all three subplots with black dashed lines.

A.4 Chapter 7 Supplementary Information

A.4.1 Figures

Figure A-14. Alternative rendering of the data in Figure 7-12 courtesy of Gennady Gorin.

A.4.2 Tables

Table A-3. H_2 yields for the non-radiolytic mechanism from ReaxFF simulations of H impacts

Impact energy, eV	H_2 yield, molecules per impact
0.02	0
0.06	0
0.20	0.008
0.61	0.024
1.92	0.018
5.00	0.014

A.5 Chapter 8 Supplementary Information

A.5.1 Figures

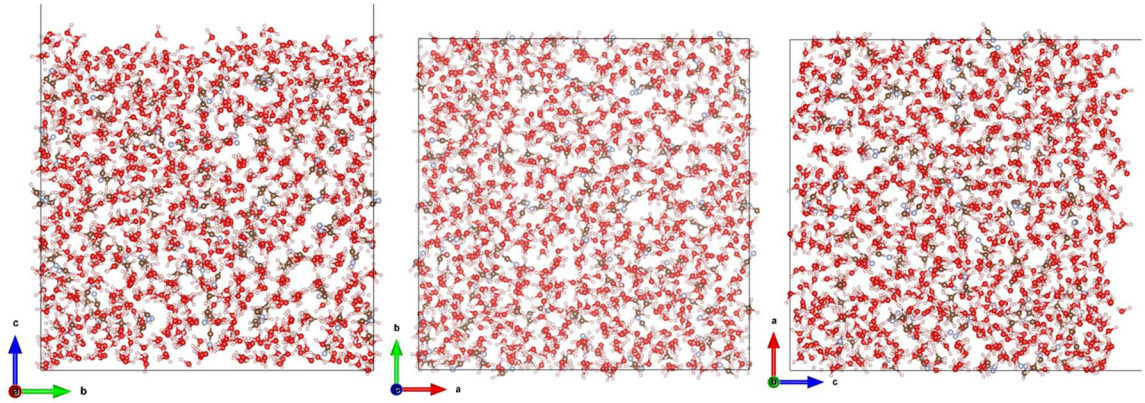

Figure A-15: Orthogonal views of the mixed HCN− CH_4−H_2O ice used in simulations. Visualized with VESTA software.